I MEASUREMENT AND ANALYSIS, BASED ON THE ASSUMPTION OF THREE NUCLEON PICK-UP, OF SOME (p,α) REACTIONS ON VARIOUS NUCLEI

II MEASUREMENT AND ANALYSIS, USING A COMPOUND NUCLEAR STATISTICAL MODEL, OF (p,α) ENERGY SPECTRA FROM ^{197}Au AT VARIOUS ANGLES AND PROTON ENERGIES

A Thesis

Submitted to the

Faculty of Graduate Studies,

University of Manitoba,

in partial fulfillment of the

requirements of the degree of

Doctor of Philosophy

By

Cornelis Jan Kost

Winnipeg, Canada

December, 1968

CONTENTS

ACKNOWLEDGEMENTS

The author would like to express his sincere thanks to Dr. B. Hird for his valuable advice, patient guidance and constant encouragement throughout the course of this work.

The author is much obliged and grateful to Mr. C. A. Miller for the developement of the Statistical Model computor program as well as his constant assistance throughout much of this research.

Thanks are also due Dr. R. M. Craig, Dr. T. Y. Li and Dr. G. A. Moss for their assistance in the collection and numerical analysis of some of the experimental data.

The author is also indebted to:
All the members of the Electronic and Mechanical work shops for the building and maintenance of the electronics and associated apparatus required for the experiments;
Those members of the Cyclotron Technical Staff who assisted in operating the cyclotron;
Dr. D. G. Douglas for his assistance in the determination of certain target impurities;
Mr. R. R. Kawchuk and members of the Manitoba Department of Computor Science for their assistance in the seemingly endless number of hours of running time required on the IBM-360-65;
Mrs. W. Weiss, Mrs. M. A. Orves and Miss A. Loney for adding a more humane element to this work.

Acknowledgement is also accorded Dr. T. Y. Li and Dr. B. Hird for the calculation of the theoretical spectro-

scopic factors used in this work.

Finally the author would like to express his immeasurable indebtedness to his wonderful parents whose moral support made the struggle for this degree bearable.

This work was performed under the auspices of the Atomic Energy Control Board of Canada.

ABSTRACTS

Differential cross-section measurements have been made of the (p,α) reactions on ^{23}Na, ^{27}Al, ^{58}Ni and ^{59}Co. The systematic use of the DWBA code, incorporating a finite range correction (in the local energy approximation) was developed. Satisfactory fits and agreements between the theoretical and experimental spectroscopic factors were obtained for the (p,α) reactions on ^{23}Na and ^{27}Al.

A study, based on a statistical model of nuclear reactions, has been made of the importance of this mechanism in the emission of alpha particles resulting from the bombardment of ^{197}Au with protons in the energy range 20-60 MeV and of the importance of multiple particle emission to the theoretical evaporation spectra for this reaction. The experimental measurements were not found to be in accord with this model.

INTRODUCTION

One of the objects of this work is to study the nature of the mechanism for (p,α) reactions on light nuclei. Previously measurements[2] have been made at this laboratory on ^{7}Li, ^{12}C and ^{19}F. The conclusion reached upon the analysis of that work was a strong indication of the predominant role played by a reaction mechanism consisting of three-nucleon pick-up. This was in agreement with (p,α) measurements performed in other laboratories[55,58] at lower proton energies. It is the intention of this work to extend the (p,α) reaction measurements to other targets in order to add more weight to this conclusion.

Two other targets having the property like ^{19}F, in having a structure which can be considered as a core plus three outer nucleons are $^{23}Na = {}^{20}Ne$ core+3 nucleons and $^{27}Al = {}^{24}Mg$ core +3 nucleons. The shell-model configuration of these nuclei are well known so that if the reaction does proceed by the triton pick-up mechanism one can readily make a comparison between the experimental and theoretical spectroscopic factors. Agreement would tend to confirm the validity of the assumption of the pick-up reaction mechanism. The main possible competing reaction mechanism is likely to be the knockout of a virtual alpha (cluster) by the incident proton with the resultant capture of the latter into a bound state of the residual nucleus. Unfortunately comparible theoretical calculations have not as yet been made. However, comparible calculations have been per-

formed for (d,p) reactions[78] with the conclusion that the contribution from the knockout mechanism was negligible in comparison to the pick-up (stripping) mechanism.

For these two targets then one would expect reasonable quantitative fits to the data using a three-nucleon pick-up DWBA theory.

The second object of this work is to study certain aspects of (p,α) reactions where the final states are not resolvable.

When a proton, having an energy of $\approx$50 MeV, strikes a heavy target nucleus many processes can take place. Grazing collisions may result in the knockout or stripping of the outer nucleons. As the collision distance decreases it becomes possible for the proton to be captured and be amalgamated into a compound system in which the identity of the method by which the system was formed is lost as the energy of the proton is shared among the target nucleons. The energy spectra of the emitted particles are then usually delt with in terms of the evaporation theory[34]. A comparison of the energy spectra with the statistical evaporation theory can then provide a check of the assumed reaction mechanism. However for excitation energies of the order of 50 MeV it is possible for more than one particle to be "evaporated" from such a highly excited compound nucleus. In order to take account of this effect a computor program, which can calculate the emission spectra resulting from the evaporation of up to three

particles, has been prepared[44]. To account for multiple emission one must integrate over the energy spectra of all the particles that could be emitted in each of the previous stages. In practice the calculation can be done analytically only up to about the third stage on present day computors.

Specifically, the purpose of this work is to study the importance of the compound nuclear evaporation mechanism to the observed alpha particle energy spectrum resulting from a 20-60 MeV proton bombardment of ^{197}Au. In addition we will study the theoretical importance of each of the successive emissions to the alpha spectrum.

CHAPTER I

EXPERIMENTAL ARRANGEMENT AND PROCEDURES

1.1 The Cyclotron and Beam Optics.

The proton beam used to obtain the results described in this work was provided by the University of Manitoba 42" sector-focussed cyclotron. All measurements made use of the variable energy facilities, whereby one varies the cyclotrons extracted proton beam energy by simply moving the stripping foil to an appropriate radius and azimuthal angle [1] so that the combination magnet (adjacent to the Cyclotron main magnet) guided the proton beam down a fixed beam line when the magnetic field was correspondingly adjusted.

For the measurement of the $^{23}Na(p,\alpha)^{20}Ne$ reaction the general beam layout consisted of a single straight beam line [2] (Figure 1.1) while for all our subsequent measurements the beam transport was as shown in Figure 16, the chief difference being the installation of a switching magnet which yielded a better energy resolution than was provided by the raw beam. This was obtained through the use of appropriate object and image slits placed respectively before and after the switching magnet.

Figure 17 shows a series of typical views of the energy structure in the raw proton beam for various settings of the main magnetic field. This measurement was made by obtaining a series of curves, each corresponding to a fixed value of the main magnetic field, which were a measure of the beam current intersecting a fine probe placed downstream

Figure 1.1

Beam Layout for $^{23}Na(p,\alpha)^{20}Ne$ reaction measurements

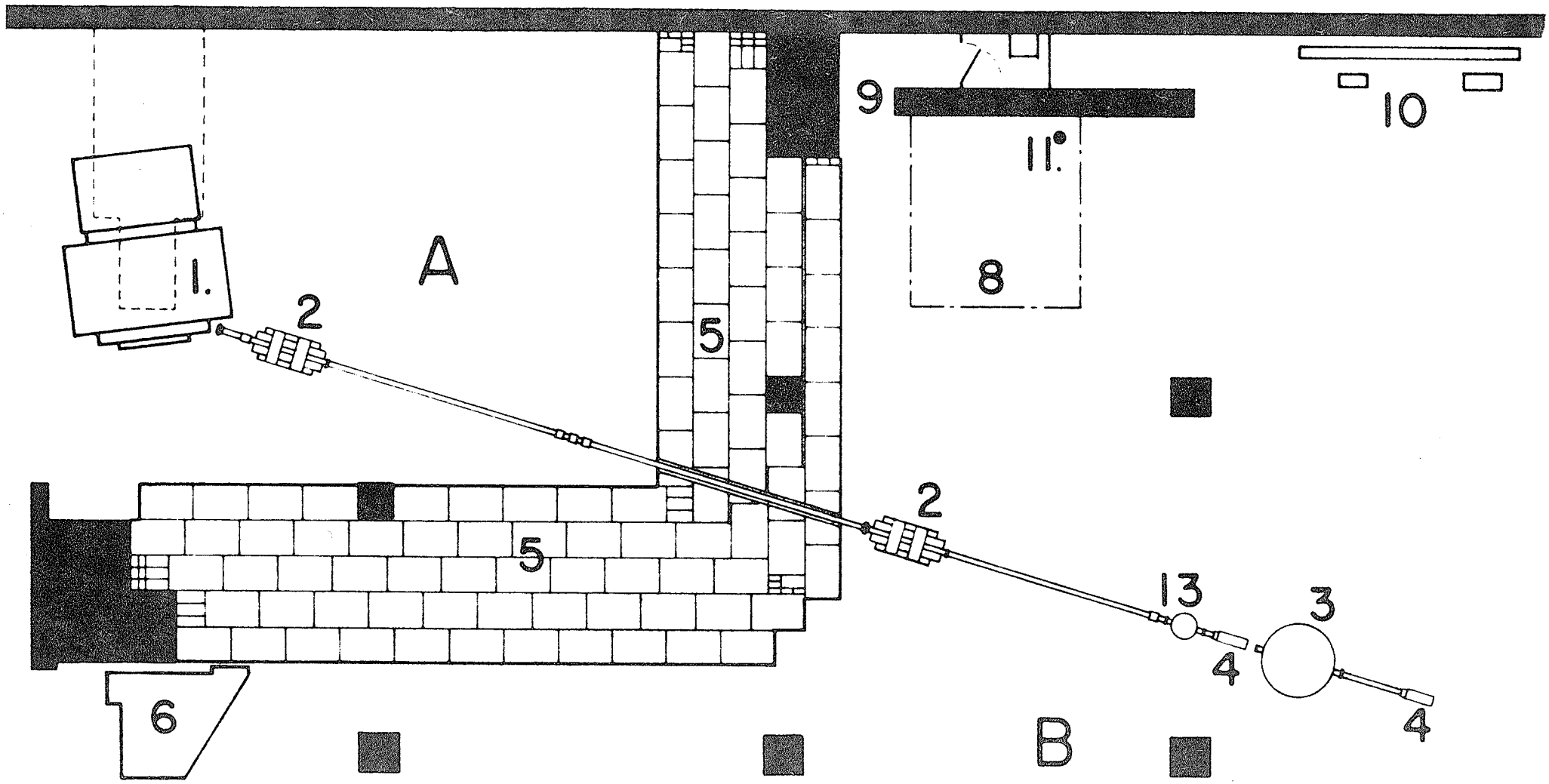

BEAM LAYOUT

Figure 16

General Beam Layout

Fig. 16

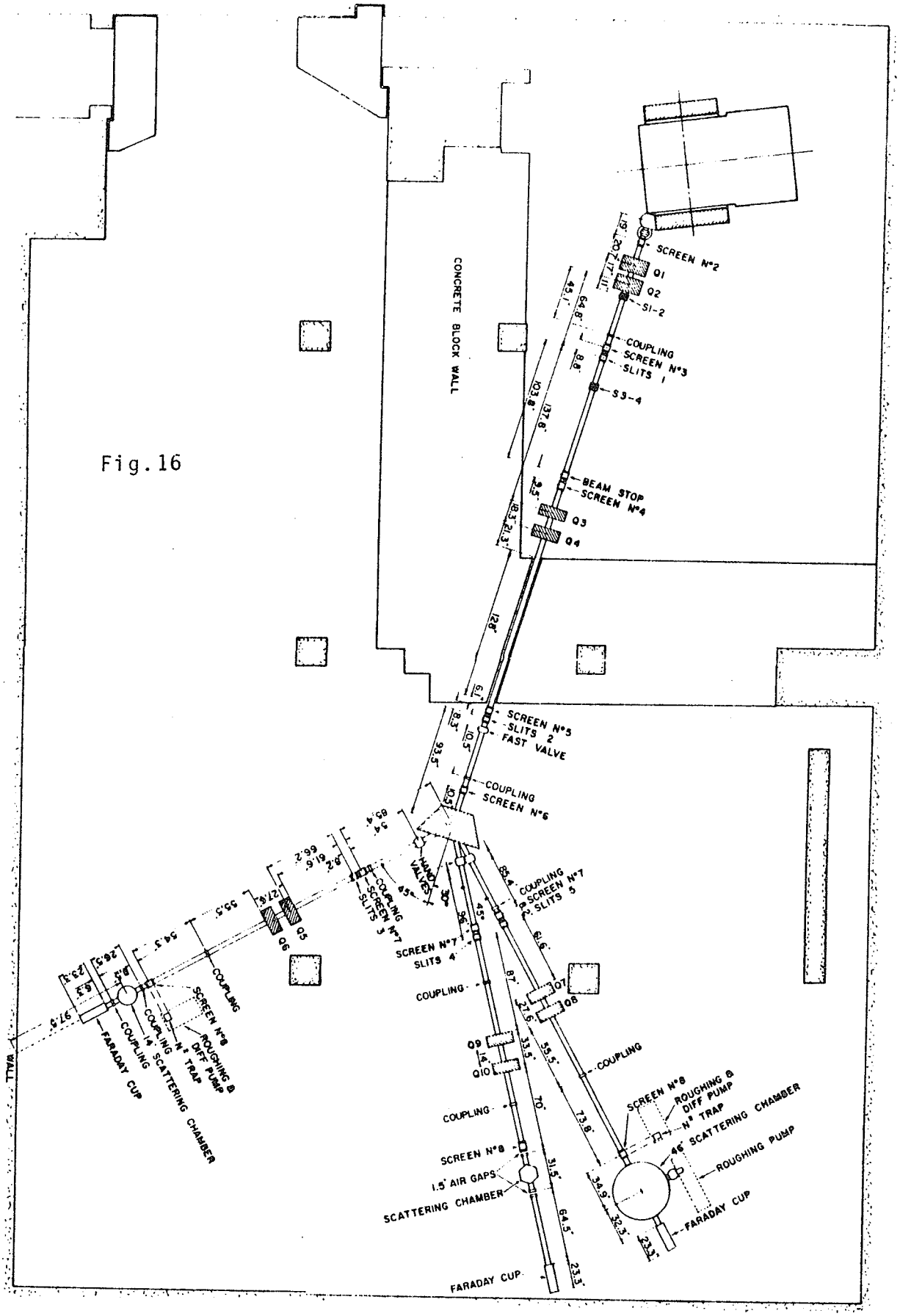
CONCRETE BLOCK WALL
SCREEN N°2
Q1
Q2
SI-2
COUPLING
SCREEN N°3
SLITS 1
S3-4
BEAM STOP
SCREEN N°4
Q3
Q4
SCREEN N°5
SLITS 2
FAST VALVE
COUPLING
SCREEN N°6
HAND VALVES
COUPLING
SCREEN N°7
SLITS 3
SCREEN N°7
SLITS 4
COUPLING
Q5
Q6
COUPLING
SCREEN N°8
ROUGHING & DIFF PUMP
N² TRAP
SCATTERING CHAMBER
FARADAY CUP
COUPLING
Q9
Q10
COUPLING
SCREEN N°8
1.5" AIR GAPS
SCATTERING CHAMBER
FARADAY CUP
COUPLING
SCREEN N°8
ROUGHING & DIFF PUMP
N² TRAP
46" SCATTERING CHAMBER
ROUGHING PUMP
FARADAY CUP
WALL

Figure 17

Typical energy structure of extracted proton beam

Fig. 17

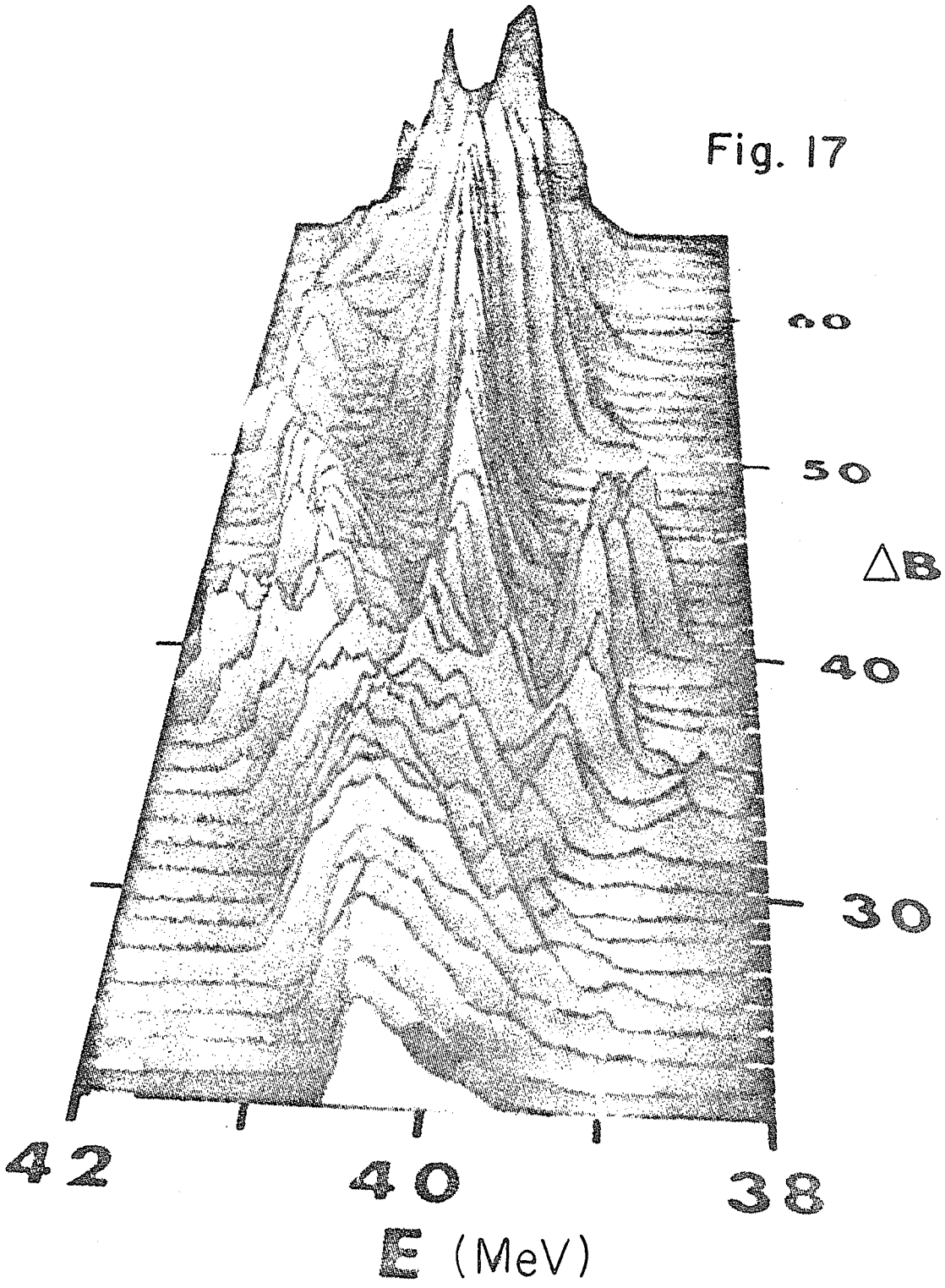

of the switching magnet, as one varied the magnetic field in this switching magnet. In effect we were using the switching magnet as an energy analyzer of the raw beam and measuring the intensity as a function of the energy. Of course this whole beam structure was also a function of many other machine parameters but it serves to illustrate the typical beam structure one obtains from the cyclotron. Clearly there exist values of the main magnetic field where one obtains a considerably smaller energy spread in the raw beam, with most of the beam intensity being concentrated into a single energy peak. This point of the resonance in the main magnet was the one which gave the best energy resolution of the raw beam and corresponded to the setting used for the $^{23}Na(p,\alpha)^{20}Ne$ measurement. It should be pointed out that Figure 17 was made through the use of the switching magnet which was installed subsequent to the completion of the $^{23}Na(p,\alpha)^{20}Ne$ measurement. However, this beam characteristic had already been previously encountered by us in earlier measurements [2], being observed as energy structure in well separated ground state (p,α) reactions. The precise origin of this beam structure is still unknown, but undoubtedly when eliminated will result in substantially higher beam currents being transported through the beam transport system.

With the advent of the switching magnet one would expect, and we did obtain, the best beam transport through the energy analysis system when one operated in the above mentione

mode. Under such circumstances one could expect between 10 - 20% transmission of the beam from the stripping foil, through a pair of .1" gap slits and an .1" diameter entrance collimator situated in front of the scattering chamber, to the Faraday Cup placed immediately downstream of the 14" diameter scattering chamber.

Typical beam currents in the Faraday Cup were between 50 and 500 nanoamperes. In order to prevent the beam entering the scattering chamber from having too large a divergence in the reaction plane we placed a carbon collimator, restricting the beam to a 1" width and a 2" height, at the exit point of the last pair of quadrupoles. This effectively gave us an angular spread of approximately 1.5^{o}, thus keeping the kinematic energy spread, due to this, negligible in proportion to the inherent energy spread of the proton beam coming from the energy analysis system. The loss in beam intensity, due to the insertion of this collimator, was usually negligible, provided one "tuned" the optics properly.

The beam spot size at the target as observed with a zinc-sulphide screen and as measured by the "burn" spot on the target, was generally found to be .1" in height and .2" in width.

1.2 Scattering Chamber and Charge Collection.

Figure 1.3 gives a rough scale sketch of the scattering chamber used for all the measurements presented in this work. It consists basically of manually rotatable

Figure 1.3

Schematic side-view of 14" scattering chamber

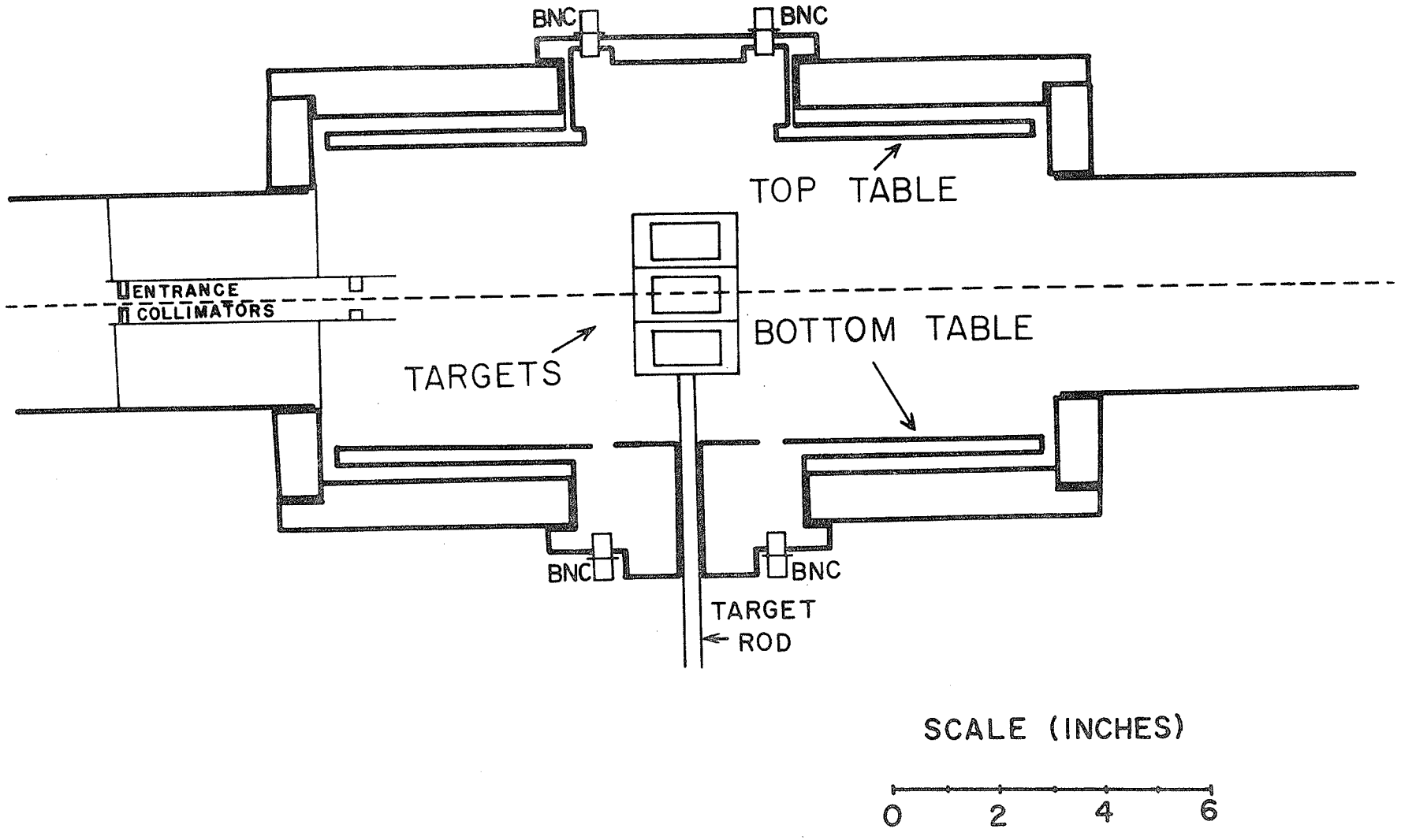
BNC
BNC
TOP TABLE
ENTRANCE
COLLIMATORS
TARGETS
BOTTOM TABLE
BNC
BNC
TARGET
ROD
SCALE (INCHES)
0
2
4
6

top and bottom platforms on which are mounted the appropriate detectors whose "zero" angle was determined by simple optical means as previously described elsewhere [2]. The chamber alignment and rotational axis accuracy with respect to the beam axis have also been previously described [2]. The angle of a detector assembly mounted on either platform could be calibrated and read out to an accuracy of $\pm$ .2 degrees. Selection of any of the three targets which were mounted on the target ladder, as well as its angular setting was done simply by the proper vertical placement and rotation of the target rod which projected out through a vacuum seal in the bottom of the scattering chamber. The collimators placed immediately in front of the scattering chamber served to restrict the beam spot on the target to an acceptable size and consisted of a .1" diameter beam limiting carbon collimator and a .2" diameter anti-scattering collimator.

The vacuum in the chamber and associated beam lines was maintained by oil diffusion pump facilities which generally kept the pressure below 10^{-5} mm of mercury.

Beam currents, typically around 100 nanoamperes in the Faraday Cup, were measured and integrated through the use of a precision charge integrator which was periodically calibrated using a high impedance precision resistor (approximately 10 megΩ) and a standard cell (1.01859 volts). The correction to the calibration never amounted to more than 1%.

1.3 Beam Energy Calibration.

Energy calibration procedures have also been previously described [2] and the technique consisted, for our work, in the use of one of these methods. This method consisted of using standard alpha sources and comparing their pulse heights to those obtained from the $^{12}C(p,\alpha)^{9}B_{G.S.}$ reaction measured at angles of approximately 60^{o} and 150^{o}. Kinematic tables were then used to calculate the proton energy. A pulser was used to extrapolate the energy calibration we obtained from the standard alpha sources (5.477 MeV alphas from ^{241}Am; 6.047,8.778 MeV alpha from Th). The reasons why we choose ^{12}C were that the target is readily available (in the form of polyethelene) and moreover the Q value is highly negative (-7.55 MeV) so that the energy of the alphas from the $^{12}C(p,\alpha)\ ^{9}B_{G.S}$ reaction, in the backward angles, were not too far removed energetically from those obtained by the above standard alpha sources, thus lending a greater accuracy to this technique. The uncertainty in the energy calibration using the above procedure usually amounted to about $\pm$ 300 KEV.

For those measurements where a single run on the cyclotron did not suffice to complete an angular distribution the energy was reproduced (to within $\pm$ 200 KEV) by using the same value of the magnetic field (as determined by Nuclear Magnetic Resonance Measurements) in the switching magnet. This procedure turned out to be expedient since it required only a measurement of the N.M.R. frequency while the corresponding beam energy could be measured at some

later date.

1.4 Detectors.

Since the maximum energies that can be deposited in a 1 mm silicon surface barrier detector are 12, 16 and 19 MeV for proton, deuterons and tritons respectively and since the Q values for (p, ^{3}He) reactions on the nuclei studied are approximately -11. MeV while those for (p,α) reactors are approximately +1. MeV this means that from a practical standpoint one such single detector could suffice to study the (p,α) reactions at least up to the first 10 MeV of excitation since no interference can take place from the other reaction products.

However it was found that the continued use of the particle identification system [3] used in previous (p,α) measurement [2] helped reduce the background in some of the higher excited states (due to the preponderance of singly charged reaction products) even though the particle identifier window was set to reject only singly charged particles. A direct comparison of results obtained with and without the use of the particle identifier showed the difference in overall detection efficiency to be less than 1%. The detectors of the E +ΔE telescope system consisted of an 150μm surface barrier detector an a 1 mm surface barrier detector.

A special case was the measurement of the ^{197}Au(p,α) reaction where we were interested in observing the alpha particles having energies between 10 and 40 MeV. This required the use of a thinner ΔE detector so as not

to completely absorb the alpha particle in this energy range and thus have the event rejected by the ΔE -E coincidence requirement. The Silicon detector of the required thickness ($30\mu m$) was purchased from the Institute of Nuclear Science in Jugoslavia. This allowed us to identify double charged particles down to alpha particle energies of approximately 7MeV. Due to the small signal levels involved with the ΔE detector the pick-up of electronic noise, especially from relay signal originating throughout the cyclotron installation, presented many difficulties. In fact over 80% of the events recorded during initial measurements of the (p,α) reaction on ^{197}Au were traced to such electrical pick-up. With appropriate grounding of signal cables and filtering of relay noise this problem was eliminated to a point where it made a negligible contribution to the measured alpha particle energy spectrum. To ensure that we had eliminated this problem we made the identical measurement with a blank target frame.

1.5 Electronics.

Short lengths of low capacity cable connected the detector to the charge sensitive Tennellec 100B preamplifier, while 75Ω cable, terminated in the control room, connected the preamplier output to the Berkeley 11 x 1982-B-1A (ORTEC MODEL 220 LINEAR PULSE ANALYSIS SYSTEM EQUIVALENCE) Amplifiers. The analogue circuitry produced the particle identification signal which was used to gate the summed energy from the E and ΔE detector into a 4096 CHANNEL

NUCLEAR DATA pulse-height analyser operated in the 4 groups of 1024 channel mode.

A block diagram of the circuitry is shown in Figure 1.4 while one giving more detail is shown in Figure 1.5. It should be remarked that the pre-amplifiers have accounted for the majority of our electronic problems, mainly on account of their susceptibility to radiation damage. Preamplifiers incorporating pentodes were especially sensitive so we finally settled for the triode based Tennelec 100B units.

1.6 Targets.

A) ^{23}Na

This target was prepared by pressing a pellet of natural sodium metal between two steel plates, one of which had a wide grove machined to a depth roughly corresponding to the desired target thickness. The plates were first covered with a thin layer of silicon vacuum grease. The pellet was then placed between the plate and a pressure between 2000-6000 lbs/in.^{2} applied. The plates were separated while immersed under kerosene. The target was then briefly washed in benzene and mounted on a target frame. While still wet, the target was mounted on the target ladder and the scattering chamber promptly evacuated. The target oxidation was thus kept to a minimum. In any case, any oxidation that did occur was not detrimental to the ground state (p,α) measurement since the Q value for $^{23}Na(p,\alpha)^{20}Ne_{G.S}$ is + 2.377MeV while

Figure 1.4

General Block Diagram of Particle Identification System

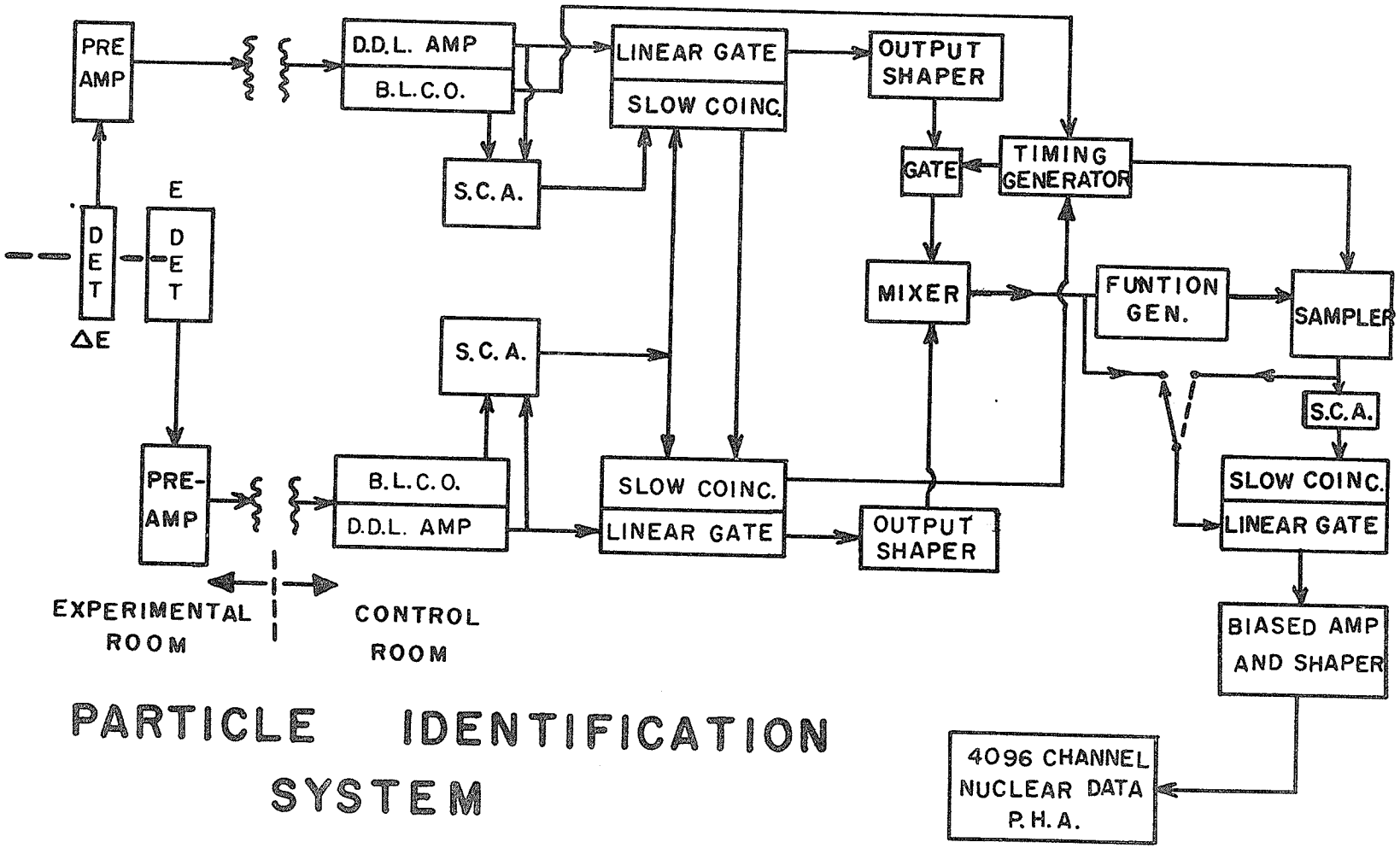

PARTICLE IDENTIFICATION SYSTEM

Figure 1.5

Detailed Block Diagram of Particle Identification System

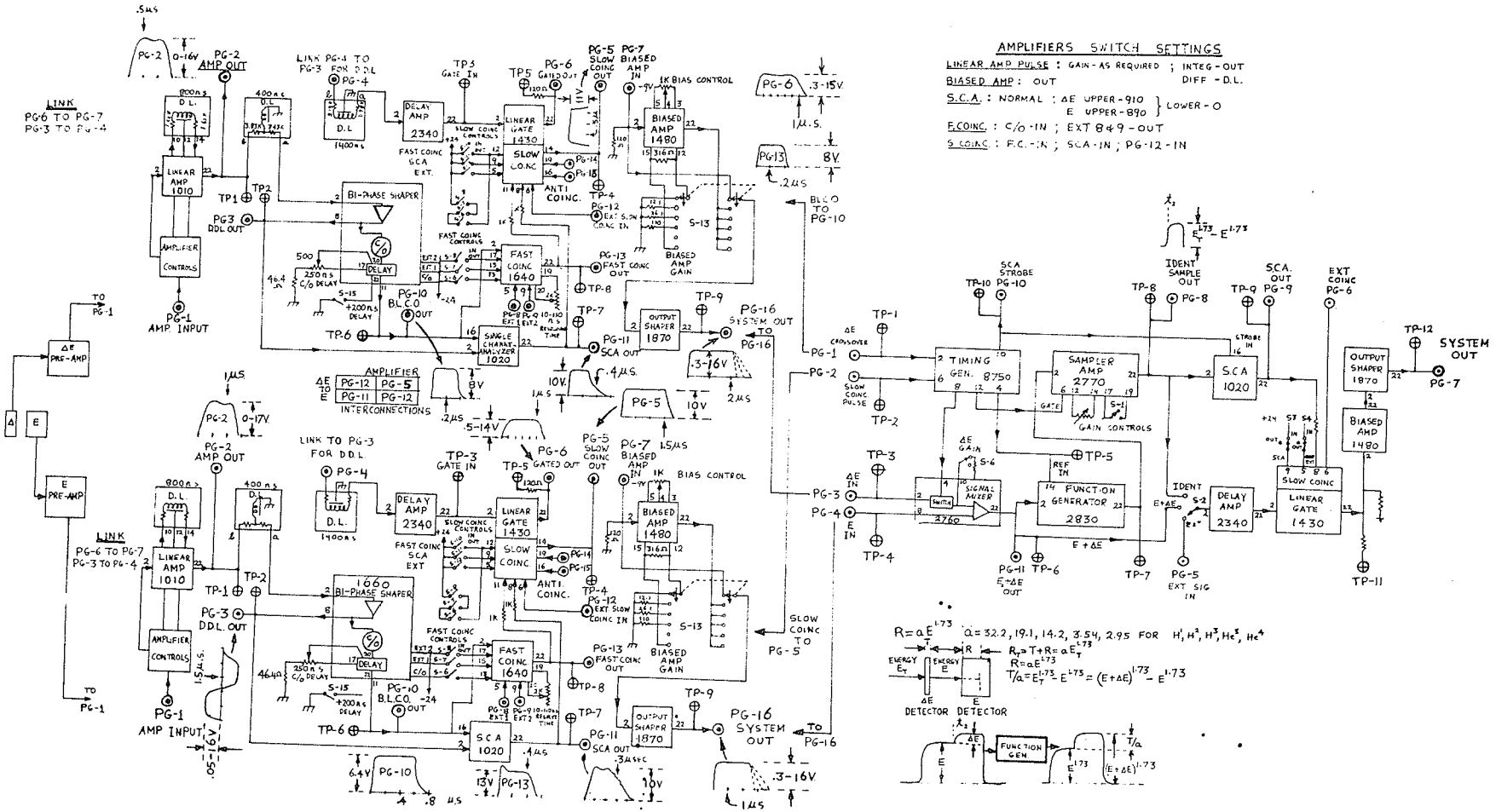
AMPLIFIERS SWITCH SETTINGS
LINEAR AMP PULSE : GAIN - AS REQUIRED ; INTEG - OUT
BIASED AMP : OUT DIFF - D.L.
S.C.A. : NORMAL : ΔE UPPER - 910 E UPPER - 890 } LOWER - 0
F.COINC. : C/O - IN ; EXT 849 - OUT
S COINC : F.C. - IN ; SCA - IN ; PG-12 - IN
LINK PG-6 TO PG-7 PG-3 TO PG-4
LINK PG-4 TO PG-3 FOR DDL
LINK PG-6 TO PG-7 PG-3 TO PG-4
LINK TO PG-3 FOR DDL
PG-2 AMP OUT
PG-1 AMP. INPUT
PG-3 DDL OUT
PG-10 B.L.CO. OUT
PG-16 SYSTEM OUT
PG-5 SLOW COINC OUT
PG-6 GATED OUT
PG-12 EXT SLOW COINC IN
PG-13 FAST COINC OUT
PG-11 SCA OUT
TP-1
TP-2
TP-3 GATE IN
TP-4
TP-5
TP-6
TP-7
TP-8
TP-9
TP-10
TP-11
TP-12 SYSTEM OUT
PG-7
ΔE PRE-AMP
E PRE-AMP
LINEAR AMP 1010
AMPLIFIER CONTROLS
BI-PHASE SHAPER
1660
DELAY AMP 2340
LINEAR GATE 1430
SLOW COINC
FAST COINC 1640
BIASED AMP 1480
OUTPUT SHAPER 1870
SINGLE CHANNEL ANALYZER 1020
SCA 1020
TIMING GEN. 8750
SAMPLER AMP 2770
SIGNAL MIXER
FUNCTION GENERATOR 2830
AMPLIFIER INTERCONNECTIONS
PG-12 PG-5
PG-11 PG-12
R = aE^1.73
a = 32.2, 19.1, 14.2, 3.54, 2.95 FOR H, H², H³, He³, He⁴
ENERGY E
ENERGY E+ΔE
ΔE DETECTOR
E DETECTOR
FUNCTION GEN

that for $^{16}O(p,\alpha)^{13}N_{G.S}$ is -5.218 Mev. The angular kinematic variation increases this separation. A single target of about 7.5 mg. cm^{-2} thick was used to obtain the entire angular distribution while two separate ^{23}Na targets, having measured thicknessess of 7.15 and 9.85 mg. cm^{-2} were used to normalize the data at 30° and 50°. The latter targets were prepared by rolling, while covered with kerosene, instead of pressing since it was felt these would be more uniform in thickness. The target thickness was measured using a precision micrometer. An error of $\pm$ 10% was assigned due to target non-uniformity.

B) ^{27}Al

A self-supporting aluminium foil 1.73 mg. cm^{-2} thick, as measured by weighing a known area, was used for the $^{27}Al(p,\alpha)^{24}Mg$ reaction measurements. Uncertainty in the thickness due to non-uniformity was estimated to be $\pm$ 7%.

C) ^{58}Ni

A self-supporting, isotopically enriched (99.95%) nickel foil purchased from O.R.N.L., having a thickness of $1.02 \pm .04$ mg. cm^{-2} was used for the $^{58}Ni(p,\alpha)^{55}Co$ reaction measurements. The measurement of its thickness was a result of an average being taken between the value as obtained by weight/area and that obtained from range-energy relationship using the energy loss suffered by alpha particles of known incident energies which have traversed the target. The first method yielded $T = 1.04 \pm .02$ mg. cm^{-2}. The second method, which made use of the 6.047 and 8.778 MeV alphas from a Thorium source yielded $T = 1.01 \pm .02$ mg. cm^{-2}

It seems worthwhile to describe the latter method in more detail. The technique was as follows:

i) The alpha source was placed in the evacuated scattering chamber-diagonally opposite to the detector. With a blank target frame we recorded the voltage V_1 and V_2 of the pulser (which was fed into the "test" input of the pre-amplifier) that corresponded to the same channel number of the P.H.A. as those produced by the 6.047 and 8.778 MeV alphas respectively.

ii) By the technique described in reference 2 we can use V_1 and V_2 to determine the dead layer thickness of the face of the detector. Call this dead layer thickness D mg. cm^{-2}. Hence V_1 and V_2 really correspond to $6.047 - \left(\frac{dE}{dx}\right)_{6.05}.D$ MeV and $8.778 - \left(\frac{dE}{dx}\right)_{8.78}.D$ MeV respectively, where $\left(\frac{dE}{dx}\right)_{E_1}.D$ is the energy loss suffered by an alpha particle of energy E_1 traversing D mg. cm^{-2} of silicon.

iii) With the target in the same location as when the actual angular distribution was taken, so that the alpha particles would traverse the same spot bombarded by the proton beam, we again record the pulser voltages V_1' and V_2' which overlap their respective alpha peaks in the P.H.A.

iv) Assuming pulser linearity and that the insertion of the target does not significantly change $(dE/dx)_{E_1}$ (in other words we only make a first order correction

for D) then from $V_1 - V_1'$ and $V_2 - V_2'$ we know the energy loss for both the 6.047 and 8.778 MeV alphas when they traverse the target. From this we can readily extract the target thickness.

v) Slight rotation of the platform on which the alpha source was mounted, as well as vertical displacements of the target ladder allowed us to "scan" various locations of the target. Variations in energy losses were easily detected and for our Ni target amounted to $\pm$ 4% and accounted for nearly all the error in the thickness quoted for the ^{58}Ni target.

D) ^{59}Co

A self-supporting cobalt foil, purchased from O.R.N.L., having a thickness of 2.00 $\pm$ .20 mg. cm^{-2}, as determined by weight/area was used for the ^{59}Co (p,α)^{56}Fe reaction measurement.

E) ^{197}Au

Initial (p,α) measurements were made using 200 ugm. cm^{-2} "Hastings" 23K Gold Leaf. The resulting alpha particle spectra were highly unsatisfactory; there were too many low energy alpha particles, which was indicative of a low Z impurity in the target. An analysis of the target, using X-ray phosphorescence techniques indicated the presence of impurities in region of Z = 47 $\pm$ 1, which we attributed to Ag contamination. Figure 1.6 shows the results of the target analysis by comparing the X-rays observed from the Gold Leaf and those from a sample of silver.[4]

Figure 1.6

Characteristic X-ray spectrum resulting from irradiation of target foils with standard X-ray sources.

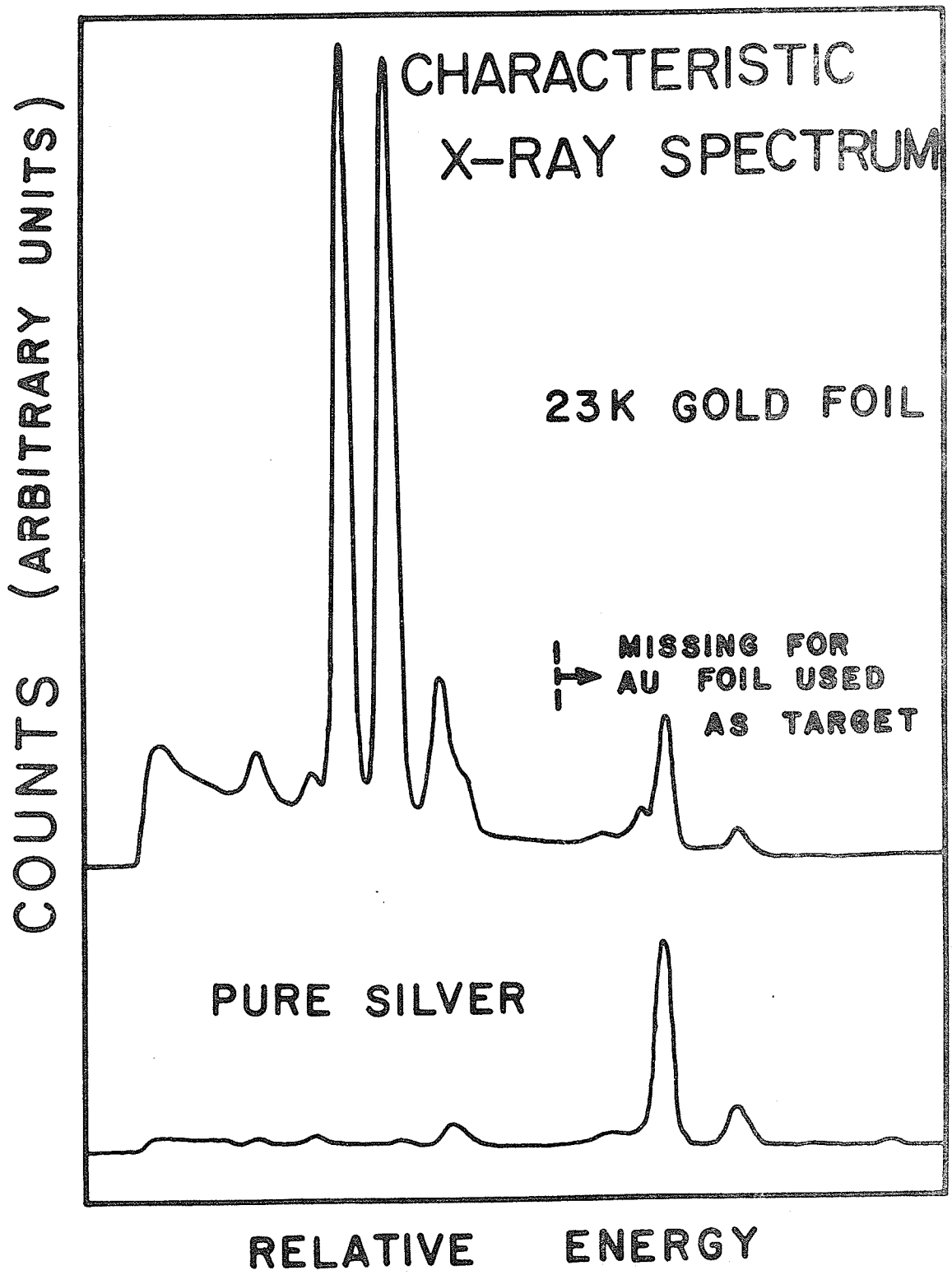
CHARACTERISTIC
X-RAY SPECTRUM
23K GOLD FOIL
MISSING FOR
AU FOIL USED
AS TARGET
PURE SILVER
COUNTS (ARBITRARY UNITS)
RELATIVE ENERGY

Use was thereafter made of a 99.9% pure Au foil whose thickness, as determined by using alpha sources (see section 1.6C) was $7.8 \pm .5$ mg. cm^{-2}.

1.7 Absolute Normalization of Cross sections.

The relationship between the differential cross-section $(d\sigma/d\Omega)_{LAB}$, the number of detected events N_D, the number of protons N_p which traversed the target, the solid angle Ω subtended by the detector and the number of atoms/cm^2 as seen by the incident proton beam is given by

$$\left(\frac{d\sigma}{d\Omega}\right)_{lab} = \frac{N_D}{N_p\left(\frac{\text{ATOMS}}{\text{CM2}}\right)\Omega} \qquad \text{hence}$$

$$\left(\frac{d\sigma}{d\Omega}\right)_{lab} = \frac{N_D}{\left(\frac{10^{-9}}{1.602\times10^{-19}}\frac{\text{protons}}{\text{nancoul}}\right)\left(\frac{6.02\times10^{23}\times10^{-3}}{A\sin\theta}\,T\,\frac{\text{nuclei}}{\text{mole}}\,\frac{\text{mg}}{\text{cm2}}\right)\Omega}$$

which for an isotopically pure target becomes

$$\left(\frac{d\sigma}{d\Omega}\right)_{lab} = \frac{A\,N_D\,(2.67\times10^{-1})}{(\text{NANCOUL})(T/\sin\theta)\Omega}\ \mu b/\text{ster}$$

where T is the target thickness in mg. cm^{-2}, θ is the angle of the target with respect to the beam axis (normally 90°), Ω is the solid angle, in steradians, subtended by the detector. NANCOUL is the charge collected in the Faraday Cup (measured in nanocoulombs) and A is the atomic weight of the target. The conversion factors which change $(d\sigma/d\Omega)_{LAB}$ to $(d\sigma/d\Omega)_{c.m.}$ and θ_{LAB} to $\theta_{c.m.}$ were taken from tables which were compiled using a relativistic kinematic program.[2)]

The normalization of the $^{197}Au(p,\alpha)$ reaction deserves some special attention since it differs from the other reactions in that we were not interested in the differential cross-section for a reaction leading to a discrete state but we were now interested in the differential cross-section leading to a certain "energy band" in the alpha particle spectrum; that is we wanted to determine $d^2\sigma/(d\Omega dE)$

The energy scale of the observed alpha spectrum was established by several calibration points, the 6.047 MeV and 8.778 MeV alphas from the Thorium source and forward angle measurements of the $^{12}C(p,\alpha)^{9}B$ reaction leading to the ground state. The resulting energy scale was also corrected for energy losses due to target thickness effect.

The data was recorded using 1024 channels across the energy spectrum, but since this resolution was not required the raw data was later integrated into sections 6 channels in width by using the P.D.P -9 computor which also plotted and typed out the numerical values of the region of interest. Each point of this "smoothed" spectrum was then separately normalized and correlated to an energy, to yield a plot of $d^2\sigma/(d\Omega dE)$ vs E. The area of this curve (as measured by summing counts in all channels) yields $(d\sigma/d\Omega)$ which was used for a comparison with the theoretical value obtained from the Statistical Model Program.

CHAPTER II

EXPERIMENTAL RESULTS

2.1 $^{23}Na(p,\alpha)^{20}Ne$

This differential cross section was measured every 2.5° between 16° and $85^{\circ}_{c.m.}$ and every 5° from 85° to $164^{\circ}_{c.m.}$ using a proton beam energy of $45.5 \pm .5$ MeV. The Q value for this reaction is +2.3774 MeV. Because the target was quite thick and the proton beam quality rather poor, prior to the installation of the beam analysis system, only the ground state angular distribution was obtained. Figure 2.1 shows the energy spectrum obtained for $\theta_L = 30^{\circ}$, while Figure 2.2 and Table 2.1 show the angular distribution of the ground state. Errors shown are those due to statistics only and neglect the overall normalization error of 10%, due mostly to the uncertainty in the target thickness.

2.2 $^{27}Al\ (p,\alpha)^{24}Mg$

This reaction has previously been reported by Shkolnick and Hintz [5] at 39.7 MeV and by S. Micheletti [6] at 38 MeV. Both sets of measurements showed rather poor statistics and were confined to forward angles. Our measurements were taken every 2.5° between 19° and $90^{\circ}_{c.m.}$ and about every 10° between 90° and $160^{\circ}_{c.m.}$, using a proton beam energy of $41.3 \pm .5$ MeV. The Q value for this reaction is + 1.6014 MeV. With the exception of the doublet at 4.12-4.24 MeV, all the levels up to 6.0 MeV were sufficiently well resolved to obtain complete angular distributions.

Figure 2.1

Energy Spectrum for the $^{23}Na(p,\alpha)^{20}Ne$ Reaction

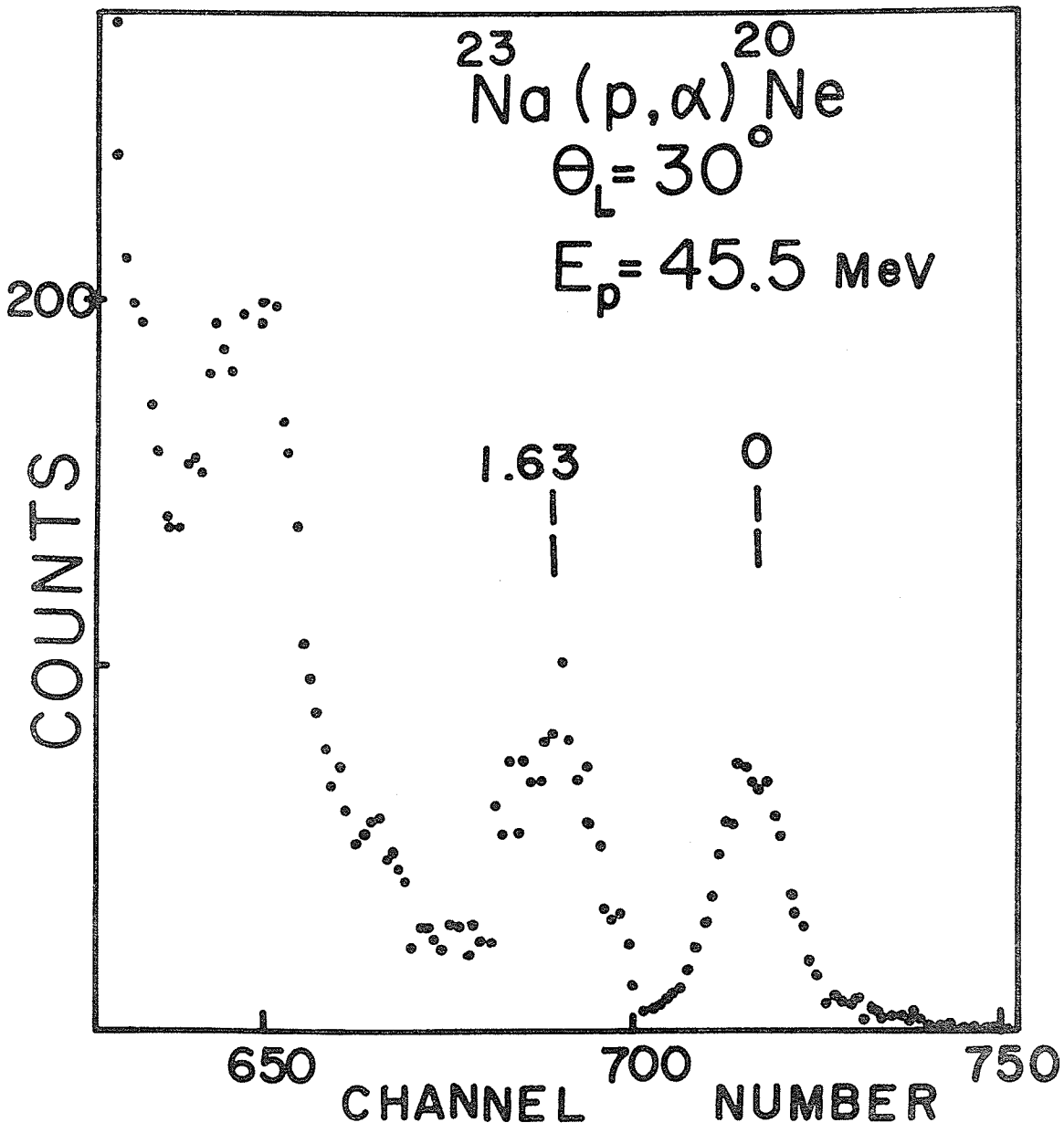
$^{23}Na(p,\alpha)^{20}Ne$
$\theta_L = 30^\circ$
$E_p = 45.5$ MeV
1.63
0
200
COUNTS
650
700
750
CHANNEL NUMBER

Table 2.1

Tabulation of Ground State Angular Distribution of the $^{23}Na\ (p,\alpha)^{20}Ne$ reaction

$^{23}Na(p,\alpha)^{20}Ne_{G.S.}$

$E_p = 45.5 \pm .5$ MeV

$\theta_{c.m.}$ (deg.)	$d\sigma/d\Omega$ (μb/st)	Error (μb/st)	$\theta_{c.m.}$ (deg.)	$d\sigma/d\Omega$ (μb/st)	Error (μb/st)
16.4	82.8	4.0	75.0	2.98	0.15
19.1	78.5	2.1	77.6	3.08	0.2
21.8	63.5	3	80.1	2.86	0.22
24.5	54.7	3	82.7	2.24	0.13
27.3	32.4	1.27	85.2	2.16	0.15
30.6	35.8	2	90.3	1.82	0.2
32.7	25.3	1.4	95.3	1.80	0.2
35.4	19.73	0.6	100.3	1.13	0.2
38.1	13.95	0.65	105.2	1.15	0.1
40.7	12.72	0.4	110.1	0.583	0.08
43.4	9.57	1.3	115.0	0.584	0.08
46.1	10.62	0.4	119.8	0.484	0.05
48.8	8.87	0.35	124.6	0.526	0.063
51.4	9.32	0.3	129.4	0.488	0.07
54.1	8.01	0.22	134.1	0.436	0.08
56.7	7.23	0.23	138.8	0.310	0.09
59.4	6.45	0.29	143.4	0.347	0.048
62.0	6.00	0.3	148.1	0.166	0.04
64.6	4.88	0.16	152.7	0.182	0.04
67.2	4.28	0.23	157.2	0.183	0.06
69.8	4.19	0.16	161.8	0.296	0.05
72.4	3.78	0.16	164.1	0.171	0.04

Figure 2.2

Angular distribution of the $^{23}Na\ (p,\alpha)^{20}Ne_{G.S}$ reaction

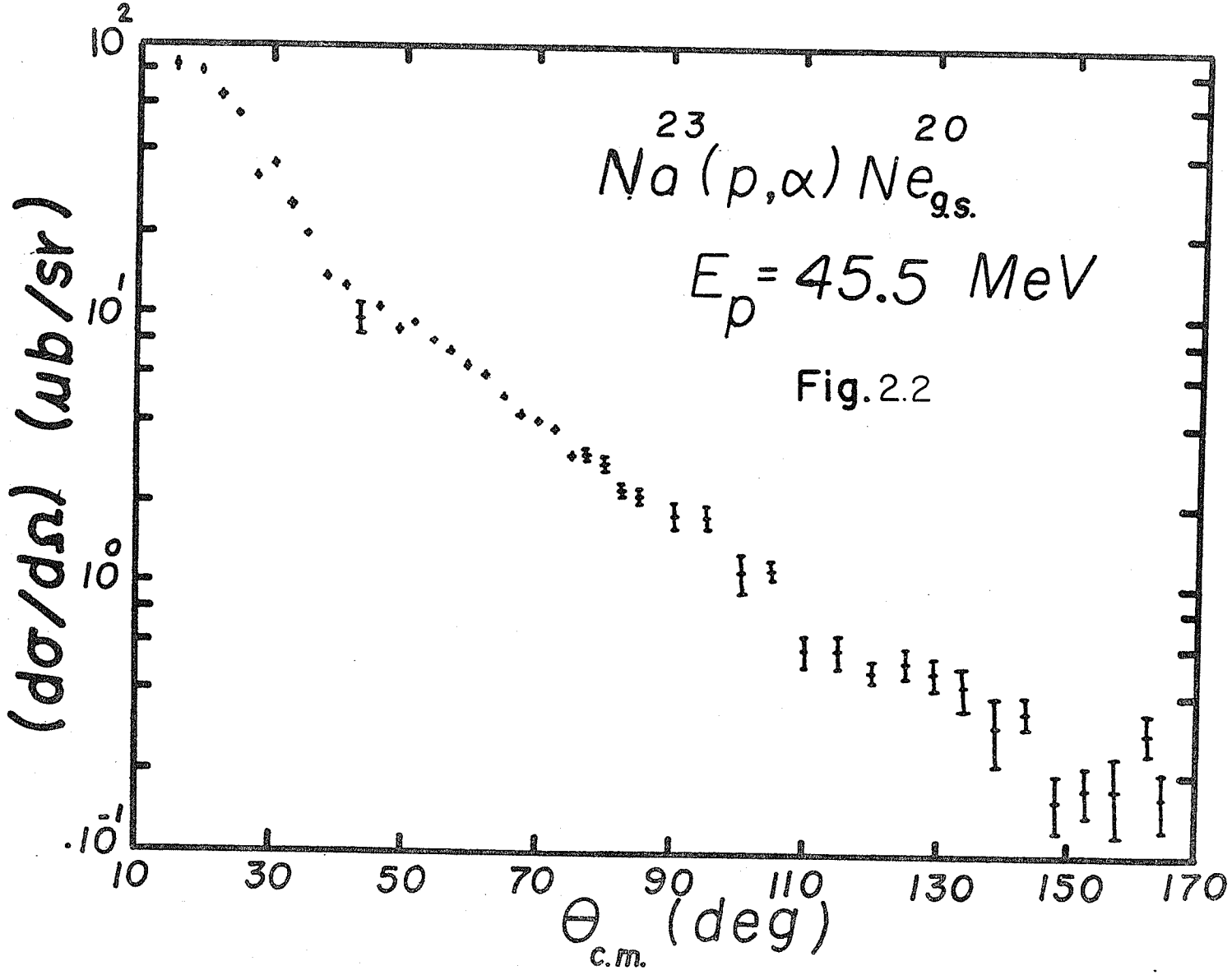
$^{23}Na(p,\alpha)^{20}Ne_{g.s.}$
$E_p = 45.5$ MeV
$(d\sigma/d\Omega)$ (ub/sr)
10^2
10^1
10^0
$.10^{-1}$
10
30
50
70
90
110
130
150
170
$\theta_{c.m.}$ (deg)

Fig. 2.2

A limited angular distribution for the 7.5 MeV level was also obtained.

Figure 2.3 shows the energy spectrum of alpha particles emitted at 30° from ^{27}Al. Figure 2.4-2.6 and Tables 2.2-2.4 show the angular distributions for these levels. An overall normalization error of 10%, due mainly to target thickness uncertainties, has again been neglected.

2.3 $^{58}Ni(p,\alpha)^{55}Co$

This reaction has been previously measured by Cavanagh et al. [7] at E_p = 50 MeV between angle 10-30°$_{LAB}$ and by R. Sherr [14] for E_p = 17.5 MeV.

Measurements of this reaction, using a proton energy of 41.3 ± .3 MeV, were taken at intervals of 2.5° between 18° and 92°$_{C.M.}$ and at 5° intervals for the backward angles. The Q value for this reaction is -1.3498 MeV. Only the ground state angular distribution was extracted from the raw data due to difficulties in clearly separating the other states. The energy spectrum obtained at θ_L = 25° is shown in Figure 2.7, while Figure 2.8 and Table 2.5 give the ground state angular distribution. Again, only statistical errors are indicated, leaving out an overall normalization error of ± 6% of which ± 4% is due to the target thickness uncertainty.

2.4 $^{59}Co(p,\alpha)^{56}Fe$ Q = +.3363 MeV

This reaction has been measured by a Rutherford Laboratory Linear Accelerator group [7] with E_p=50 MeV. They

Figure 2.3
Energy Spectrum from ^{27}Al (p,α) ^{24}Mg. Reaction

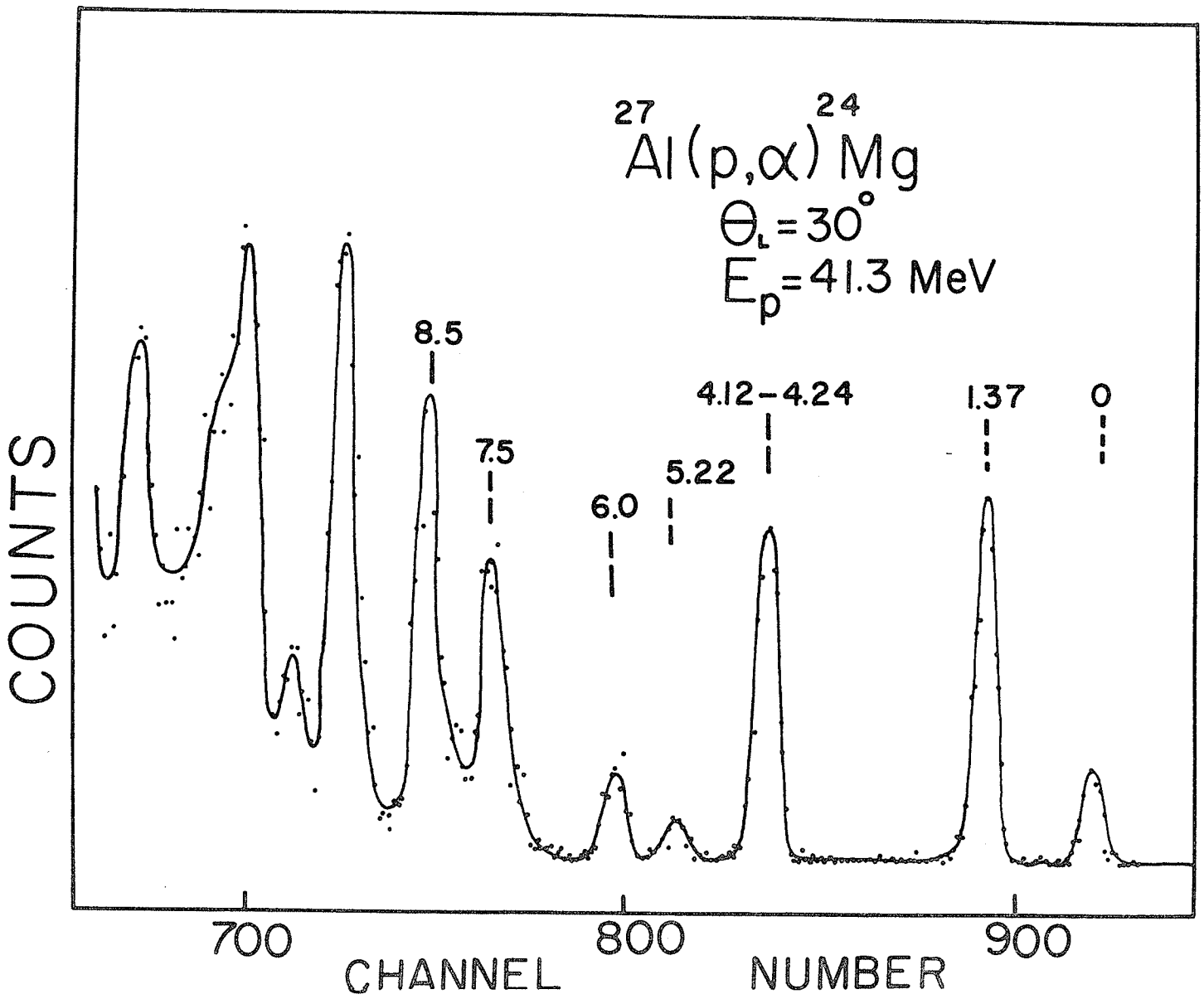
$^{27}Al(p,\alpha)^{24}Mg$
$\theta_L = 30°$
$E_p = 41.3$ MeV
8.5
7.5
6.0
5.22
4.12–4.24
1.37
0
COUNTS
700
800
900
CHANNEL NUMBER

Figure 2.4

The $^{27}Al(p,\alpha)^{24}Mg$ angular distribution leading to the Ground state and first excited state of ^{24}Mg.

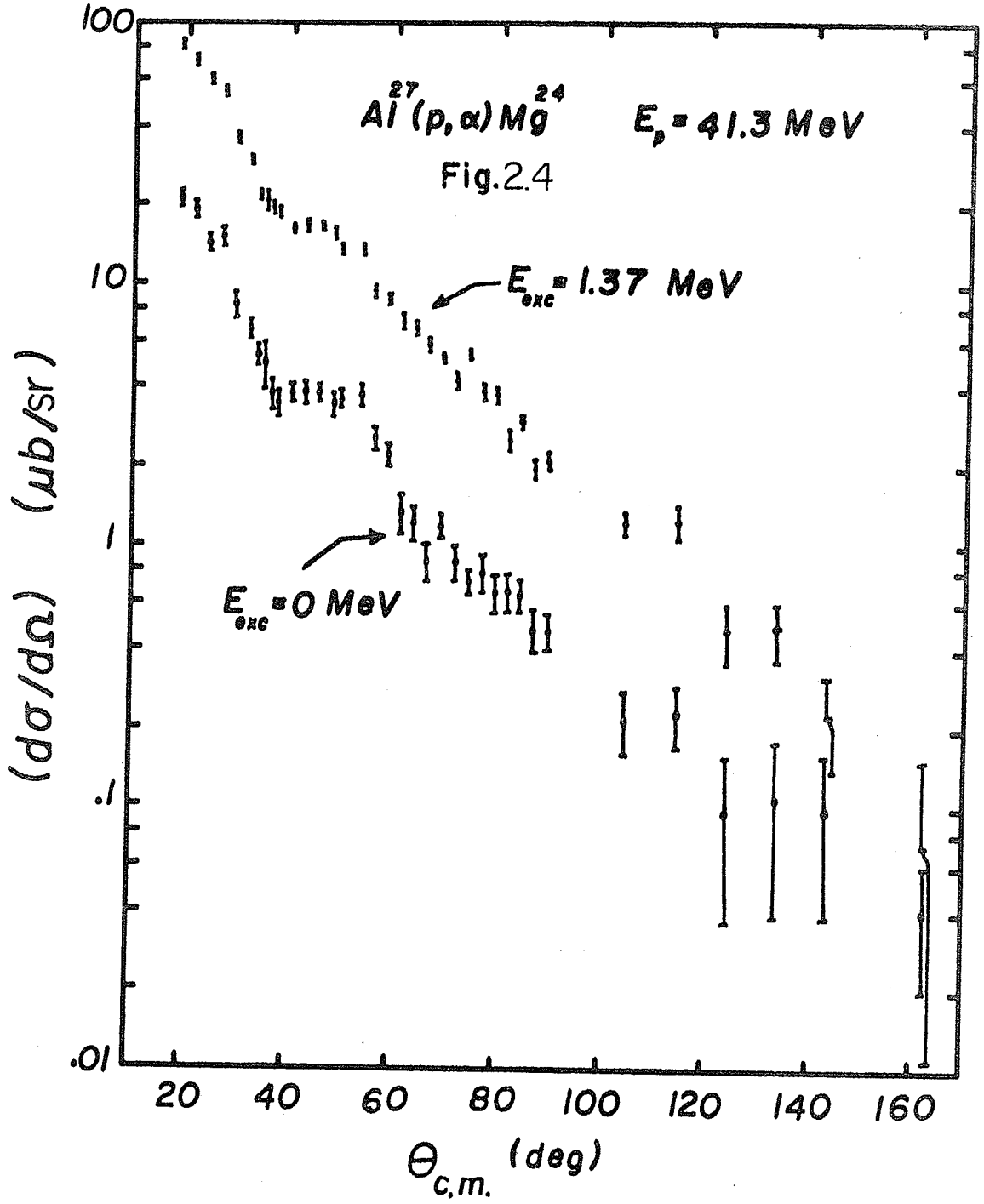
100
10
1
.1
.01
$Al^{27}(p,\alpha)Mg^{24}$
$E_p = 41.3$ MeV
$E_{exc} = 1.37$ MeV
$E_{exc} = 0$ MeV
$(d\sigma/d\Omega)$ $(\mu b/sr)$
20
40
60
80
100
120
140
160
$\theta_{c.m.}$ (deg)

Fig. 2.4

Figure 2.5

The ^{27}Al (p,α) ^{24}Mg. Angular distributions leading to the 4.12-4.24 MeV doublet and the 5.22 MeV levels of ^{24}Mg.

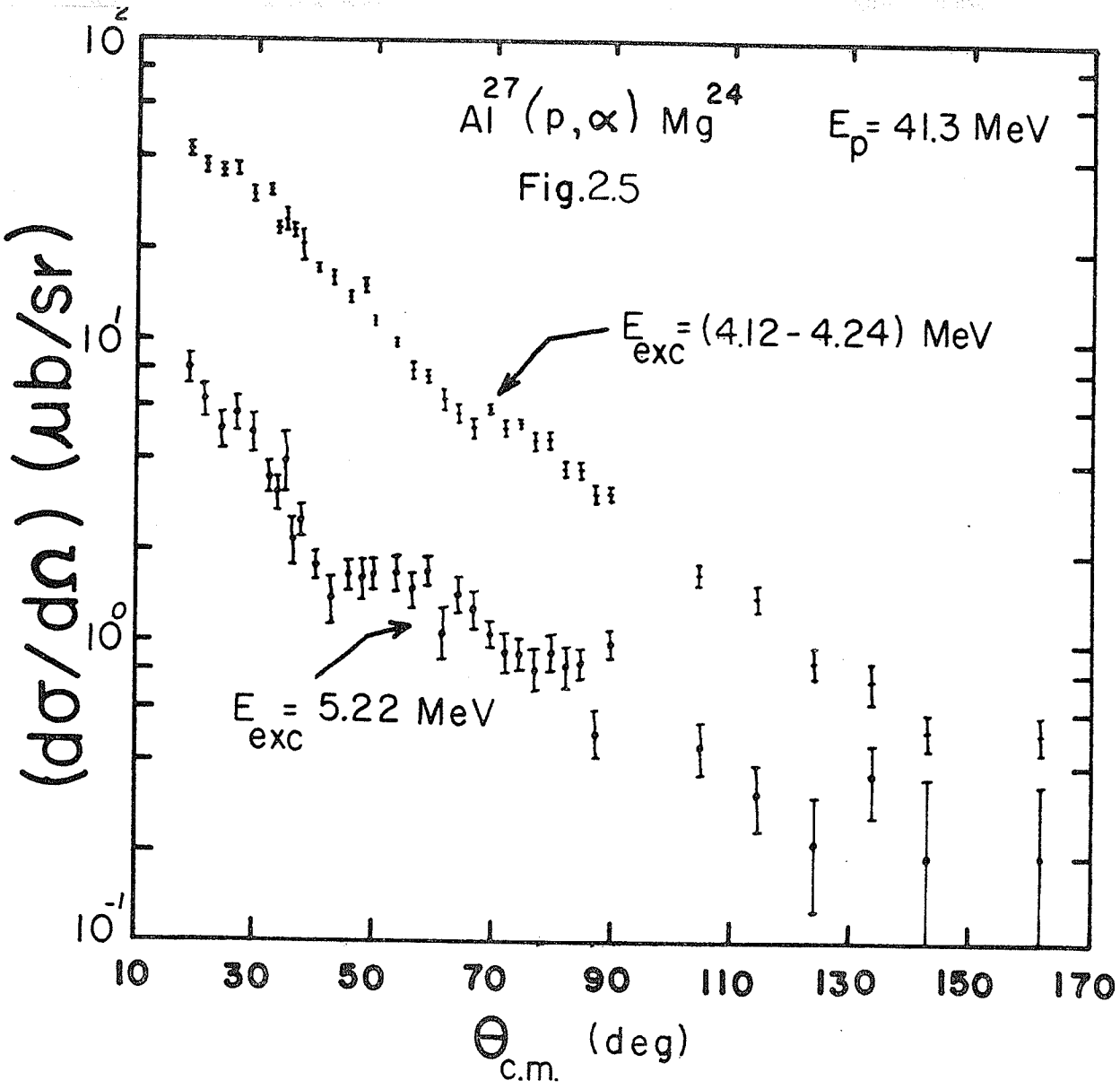
$Al^{27}(p,\alpha)\ Mg^{24}$
E_p= 41.3 MeV
Fig.2.5
E_{exc} = (4.12 - 4.24) MeV
E_{exc} = 5.22 MeV
$(d\sigma/d\Omega)$ (μb/sr)
10^2
10^1
10^0
10^{-1}
10
30
50
70
90
110
130
150
170
$\Theta_{c.m.}$ (deg)

Figure 2.6

The $^{27}Al(p,\alpha)^{24}Mg$ Angular distributions leading to the 6.0 MeV and 7.5 MeV levels in ^{24}Mg.

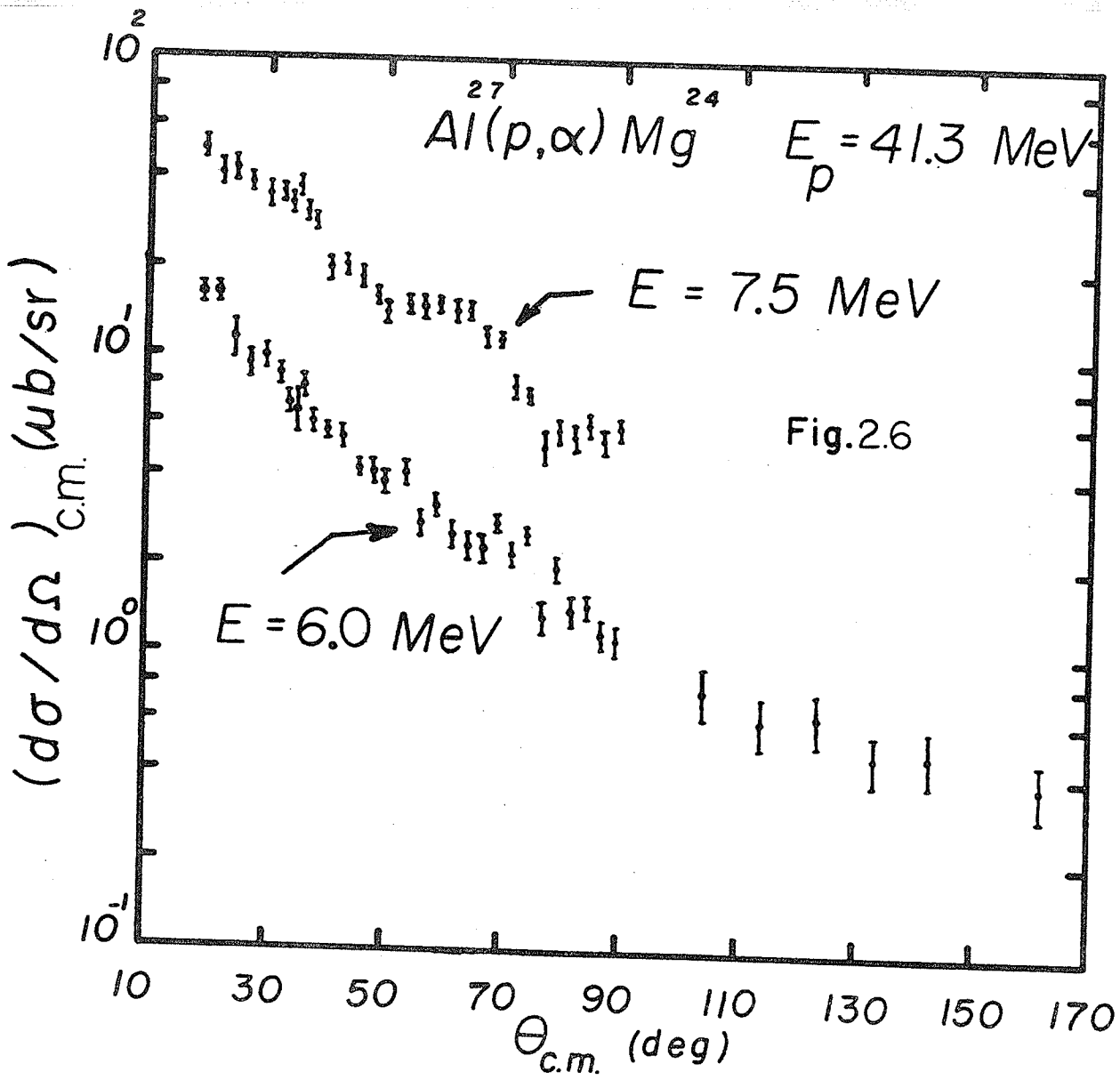
$^{27}Al(p,\alpha)\,^{24}Mg$
$E_p = 41.3$ MeV
$E = 7.5$ MeV
$E = 6.0$ MeV
$(d\sigma/d\Omega)_{c.m.}$ (μb/sr)
$\theta_{c.m.}$ (deg)
10^2
10^1
10^0
10^{-1}
10
30
50
70
90
110
130
150
170

Fig. 2.6

Table 2.2

Tabulations of the $^{27}Al(p,\alpha)^{24}Mg$ angular distributions leading to the ground and first excited state of ^{24}Mg.

$^{27}Al(p,\alpha)^{24}Mg$ $E_p = 41.3 \pm .5$ MeV

$E_{exc} = 0$ MeV			$E_{exc} = 1.37$ MeV		
$\theta_{c.m.}$ (deg.)	$\frac{d\sigma}{d\Omega}_{c.m.}$ $\frac{\mu b}{st}$	Error $\mu b/st$	$\theta_{c.m.}$ (deg.)	$\frac{d\sigma}{d\Omega}_{c.m.}$ $\frac{\mu b}{st}$	Error $\mu b/st$
18.9	21.14	1.51	18.9	81.5	3.0
21.6	19.03	1.43	21.6	71.4	2.8
24.2	14.15	1.17	24.2	60.0	2.4
26.9	15.08	1.25	26.9	54.0	2.4
29.6	8.29	.92	29.6	35.8	1.9
32.3	6.67	.58	32.3	29.2	1.2
33.7	5.30	.51	33.7	21.6	.95
34.9	4.89	.98	35.0	20.7	2.01
36.4	3.74	.49	36.4	19.3	1.12
37.6	3.46	.40	37.6	18.75	.93
40.3	3.80	.29	40.3	16.1	.61
42.9	3.82	.41	42.9	16.4	.86
45.6	3.81	.29	45.6	16.5	.6
48.2	3.44	.37	48.3	15.4	.78
49.8	3.62	.30	49.8	13.4	.57
53.5	3.74	.38	53.5	13.4	.72
56.1	2.57	.26	56.1	9.27	.47
58.7	2.23	.22	58.8	8.67	.44
61.3	1.33	.23	61.4	6.11	.48
63.9	1.22	.18	64.0	6.76	.41
66.5	0.867	.14	66.6	5.85	.38
69.1	1.19	.13	69.2	5.18	.25
71.7	0.863	.135	71.7	4.25	.30
74.3	0.724	.075	74.3	5.34	.21
76.8	0.787	.128	76.9	3.85	.28
79.4	0.657	.107	79.4	3.69	.25
81.9	0.668	.115	82.0	2.53	.22
84.5	0.653	.09	84.5	2.96	.19
87.0	0.476	.086	87.1	1.96	.17
89.5	0.472	.074	89.6	2.10	.16
104.5	0.220	.06	104.5	1.22	.12
114.3	0.230	.06	114.3	1.24	.17
123.9	0.0963	.06	124.0	.477	.12
133.5	0.109	.07	133.5	.485	.12
142.9	0.0980	.06	143.0	.228	.09
161.5	0.0403	.02	161.6	.072	.08

Table 2.3

Tabulation of the $^{27}Al(p,\alpha)^{24}Mg$ angular distributions leading to the 4.12 - 4.24 doublet and the 5.23 MeV states of ^{24}Mg

$^{27}Al(p,\alpha)^{24}Mg$ $E_p = 41.3 \pm .5$ MeV

E_{exc} = (4.12-4.24) MeV			E_{exc} = 5.228 MeV		
$\theta_{c.m.}$ (deg.)	$\frac{d\sigma}{d\Omega}_{c.m.}$ $\frac{\mu b}{st}$	Error μb/st	$\theta_{c.m.}$ (deg.)	$\frac{d\sigma}{d\Omega}_{c.m.}$ $\frac{\mu b}{st}$	Error μb/st
18.9	42.7	2.1	19.0	8.1	.9
21.6	37.8	2.0	21.7	6.3	.8
24.3	36.3	1.9	24.3	5.05	.71
27.0	36.5	1.9	27.0	5.7	.74
29.7	30.4	1.8	29.7	4.95	.69
32.4	31.1	1.2	32.4	3.54	.42
33.8	23.5	1.1	33.8	3.13	.39
35.1	25.2	2.2	35.1	4.02	.88
36.5	23.0	1.2	36.5	2.21	.38
37.7	20.7	2.5	37.8	2.54	.33
40.4	17.2	.6	40.5	1.80	.20
43.1	16.1	.8	43.1	1.40	.25
45.8	13.9	.54	45.8	1.68	.18
48.4	15.2	.8	48.4	1.65	.25
50.0	11.6	.53	50.0	1.69	.20
53.6	9.8	.33	53.7	1.70	.24
56.3	7.95	.53	56.4	1.50	.20
58.9	7.63	.4	59.0	1.74	.19
61.5	6.40	.49	61.6	1.08	.21
64.1	5.74	.38	64.2	1.46	.20
66.7	5.13	.35	66.8	1.29	.18
69.3	5.91	.27	69.4	1.07	.11
71.9	5.12	.33	72.0	.93	.14
74.5	5.35	.22	74.5	.92	.11
77.1	4.67	.31	77.1	.82	.13
79.6	4.74	.28	79.7	.94	.13
82.2	3.8	.27	82.3	.84	.13
84.7	3.75	.25	84.8	.86	.10
87.2	3.15	.22	87.3	.51	.09
89.7	3.15	.19	89.8	1.00	.11
104.7	1.71	.14	104.8	.46	.09
114.5	1.43	.14	114.5	.32	.08
124.1	.88	.10	124.2	.22	.09
133.6	.76	.12	133.7	.37	.10
143.1	.52	.07	143.1	.20	.16
161.6	.51	.07	161.6	.20	.14

Table 2.4

Tabulation of the $^{27}Al(p,\alpha)^{24}Mg$ angular distribution leading to the 6.00 MeV and 7.5 MeV states in ^{24}Mg.

$^{27}Al(p,\alpha)^{24}Mg$ $E_p = 41.3 \pm .5$ MeV

$E_{exc} = 6.00$ MeV			$E_{exc} = 7.5$ MeV		
$\theta_{c.m.}$ (deg.)	$\frac{d\sigma}{d\Omega}_{c.m.}$ $\frac{\mu b}{st}$	Error μb/st	$\theta_{c.m.}$ (deg.)	$\frac{d\sigma}{d\Omega}_{c.m.}$ $\frac{\mu b}{st}$	Error μb/st
19.0	16.00	1.3	19.0	49.5	4.5
21.7	16.17	1.3	21.7	41.6	4.0
24.4	11.37	1.7	24.4	42.5	4.0
27.1	9.32	.98	27.1	38.1	3.2
29.8	9.85	.99	29.8	34.7	3.5
32.5	8.63	.66	32.5	35.2	2.4
33.8	6.93	.58	33.8	32.6	2.8
35.2	6.56	1.1	35.2	26.9	3.1
36.5	7.89	.71	36.5	30.3	2.7
37.8	6.05	.52	37.8	28.2	2.0
40.5	5.66	.36	40.5	19.7	1.8
43.2	5.35	.49	43.2	20.3	1.6
45.9	4.24	.30	45.9	18.5	1.6
48.5	4.14	.41	48.5	16.0	1.1
50.2	3.77	.30	50.2	14.0	1.3
53.8	4.09	.40	53.8	15.0	1.1
56.4	2.77	.27	56.4	14.76	1.4
59.0	3.19	.26	59.0	16.04	1.1
61.7	2.55	.31	61.7	14.40	1.2
64.3	2.35	.24	64.3	14.38	1.1
66.9	2.31	.24	66.9	11.78	.94
69.4	2.80	.19	69.4	11.58	.73
72.0	2.20	.21	72.0	8.09	.73
74.6	2.56	.15	74.6	7.49	.48
77.2	1.36	.17	77.2	5.10	.66
79.7	1.98	.18	79.7	5.75	.53
82.3	1.43	.17	82.3	5.40	.60
84.8	1.47	.14	84.8	6.02	.58
87.4	1.19	.13	87.4	5.31	.50
89.9	1.14	.13	89.9	5.88	.44
104.8	.77	.15			
114.6	.62	.12			
124.2	.64	.13			
133.8	.47	.09			
143.2	.48	.10			
161.7	.38	.08			

Figure 2.7
Energy Spectra for the $^{58}Ni(p,\alpha)^{55}Co$ reaction measured with 41.3 MeV protons

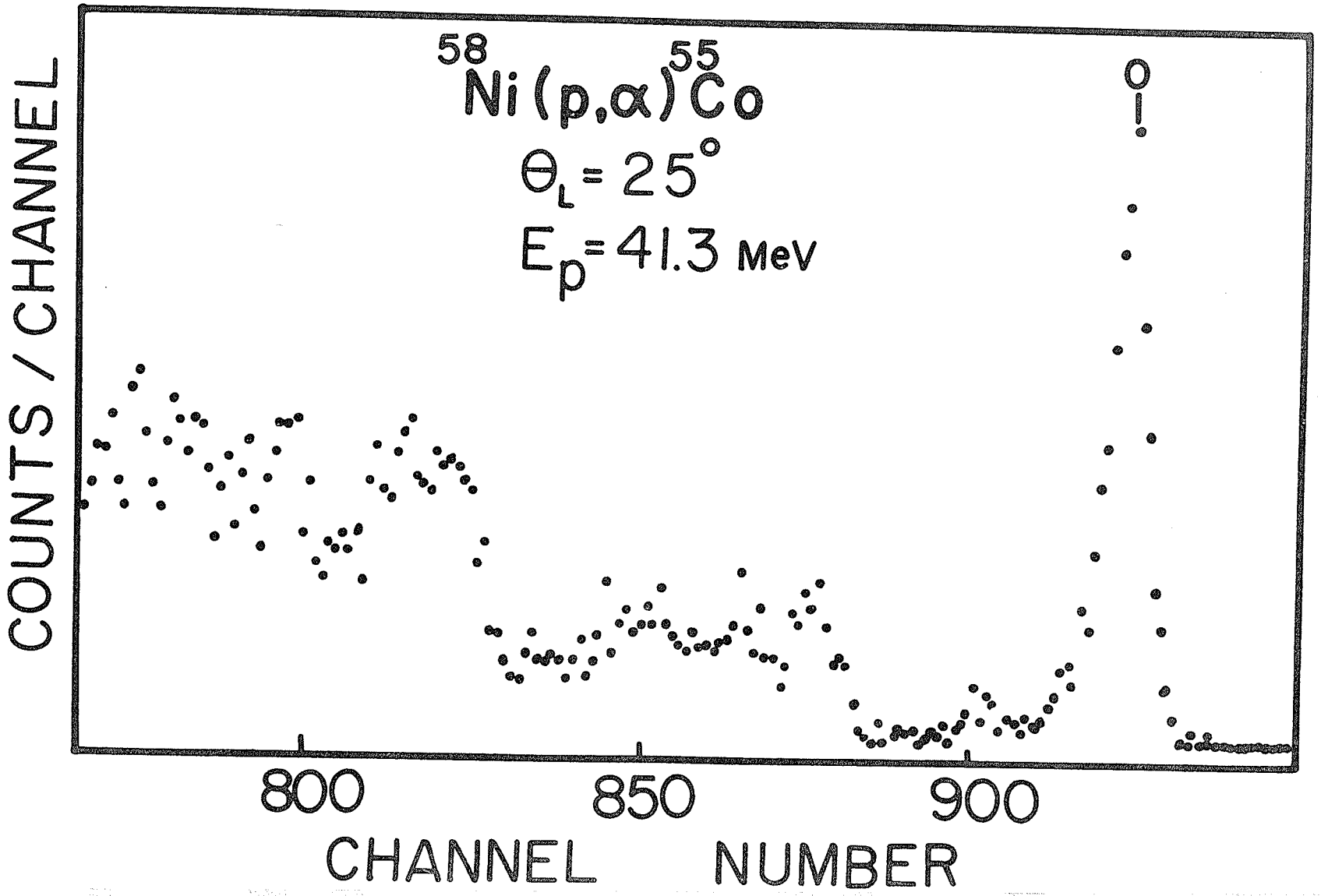
$^{58}Ni(p,\alpha)^{55}Co$
$\theta_L = 25°$
$E_p = 41.3$ MeV
0
COUNTS / CHANNEL
800
850
900
CHANNEL NUMBER

Figure 2.8
Angular distribution for $^{58}Ni(p,\alpha)^{55}Co$ ground state reaction

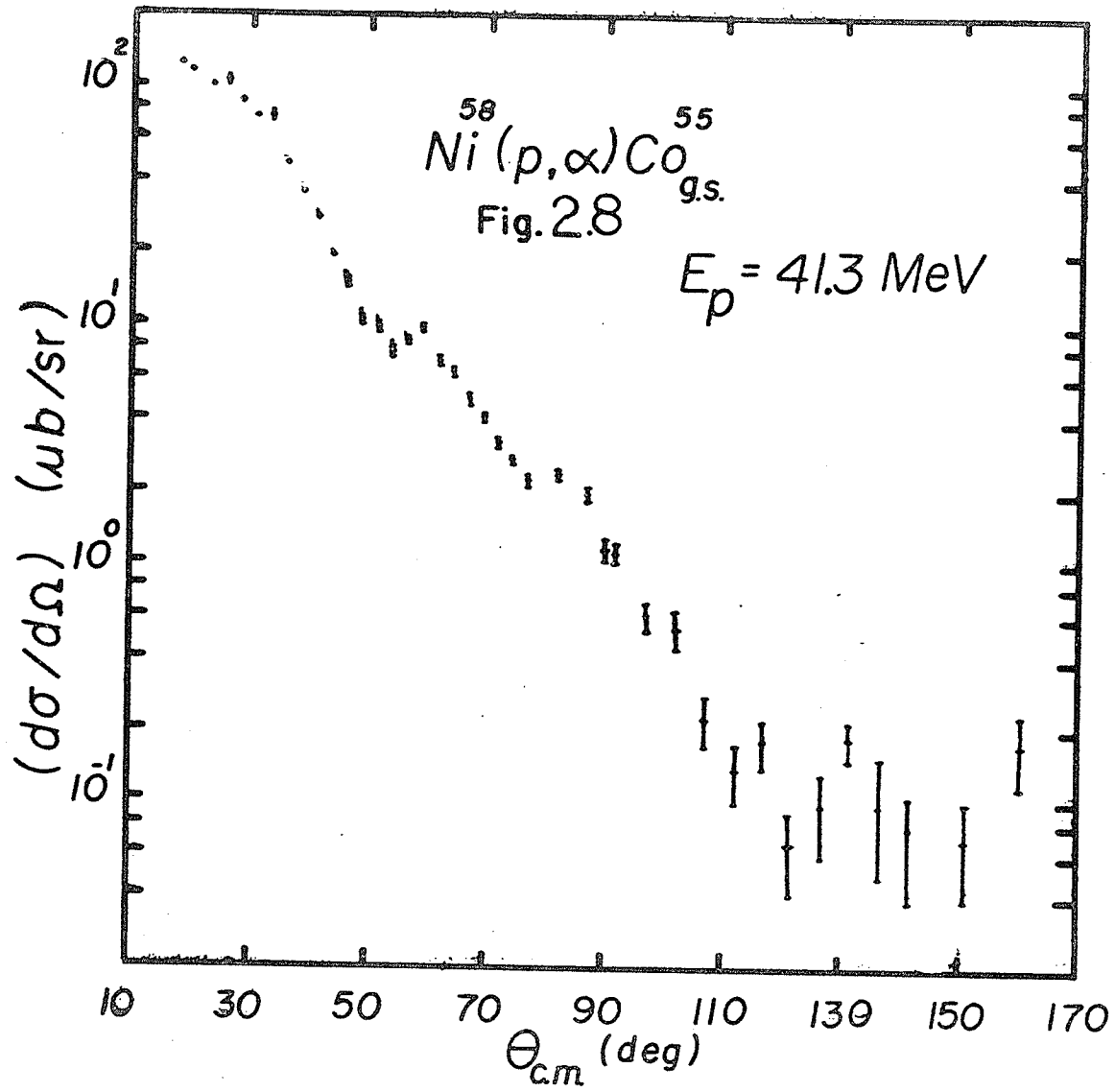
$^{58}Ni(p,\alpha)Co^{55}_{g.s.}$
Fig. 2.8
$E_p = 41.3$ MeV
$(d\sigma/d\Omega)$ $(\mu b/sr)$
10^2
10^1
10^0
10^{-1}
10
30
50
70
90
110
130
150
170
$\theta_{c.m.}$ (deg)

Table 2.5

Tabulation of the $^{58}Ni(p,\alpha)^{55}Co_{G.S}$ Angular distribution

$^{58}Ni(p,\alpha)^{55}Co_{G.S.}$

$E_p = 41.3 \pm .3$ MeV.

$\theta_{c.m.}$ (deg.)	$d\sigma/d\Omega$ (μb/st)	Error (μb/st)	$\theta_{c.m.}$ (deg.)	$d\sigma/d\Omega$ (μb/st)	Error (μb/st)
18.1	123.0	3.9	71.9	3.22	0.20
19.7	115.0	4.3	74.5	2.72	0.14
23.3	99.6	3.6	77.0	2.24	0.16
25.9	103.5	3.5	82.0	2.39	0.14
28.5	86.3	3.5	87.1	1.98	0.14
31.0	74.3	1.5	89.6	1.01	0.12
33.6	75.2	0.9	92.1	1.157	0.128
36.2	47.6	1.4	97.1	0.610	0.084
38.8	35.8	1.0	102.0	0.536	0.098
41.3	28.2	0.9	107.0	0.225	0.053
43.9	19.5	0.7	111.9	0.138	0.038
46.5	15.1	0.7	116.9	0.182	0.041
49.0	10.5	0.5	121.8	0.0679	0.0256
51.6	9.88	0.51	126.7	0.0968	0.0365
54.1	7.77	0.46	131.6	0.1865	0.033
56.7	8.61	0.41	136.5	0.0983	0.0491
59.2	9.68	0.47	141.3	0.0781	0.0294
61.8	7.12	0.40	146.2	-	-
64.3	6.37	0.33	151.0	0.0707	0.0315
66.9	4.92	0.34	160.7	0.1774	0.0591
69.4	4.07	0.20			

found the ground state differential cross-section too small to extract an angular distribution. They did, however, give a limited (10° - 30°_{LAB}) angular distribution, with poor statistics for the 3.5 MeV level in ^{56}Fe.

We measured this reaction using a proton beam energy of $41.3 \pm .3$ MeV at angular intervals of 2.5° between 18° and $74^{\circ}_{C.M.}$. The more backward angles were not measured due to the extraordinary length of time that would be required with the beam currents available in the Faraday Cup (approximately 200 nanoamps). For example, the measurement at 70° lab produced only 6 counts / hr. to the ground state of ^{56}Fe.

The ground and first two excited states were sufficiently well resolved to obtain their angular distribution. A level near 3.5 MeV was also observed and due to its rather large cross-section the corresponding angular distribution was also extracted. This highly populated level has been previously observed [7] and our measurements are in accord with them.

The energy spectrum observed at 27.5°_{LAB} is shown in Figure 2.9, while the angular distributions are shown and tabulated, along with statistical errors, in Figure 2.10 and Table 2.6 respectively. An overall normalization error of 10% due to target thickness uncertainties has not been included.

Figure 2.11 shows the known energy levels pertaining to the residual nuclei discussed in sections 2.1-2.4.

Figure 2.9

ıergy Spectrum resulting from the $^{59}Co(p,\alpha)^{56}Fe$ reaction

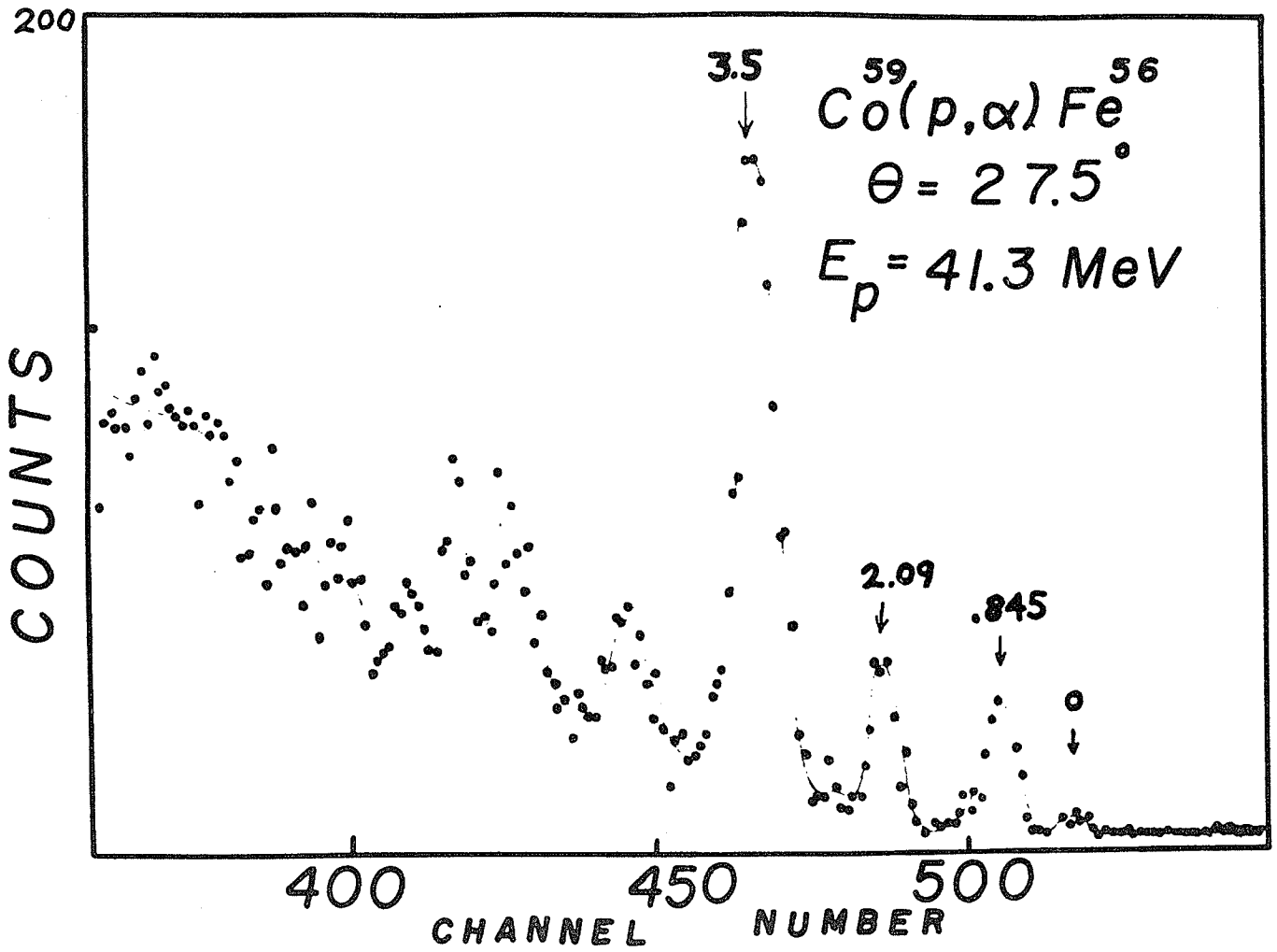
200
COUNTS
3.5
$Co^{59}(p,\alpha)Fe^{56}$
$\theta = 27.5^{\circ}$
$E_p = 41.3$ MeV
2.09
.845
0
400
450
500
CHANNEL NUMBER

Figure 2.10

(p,α) angular distribution to the various states of ^{56}Fe

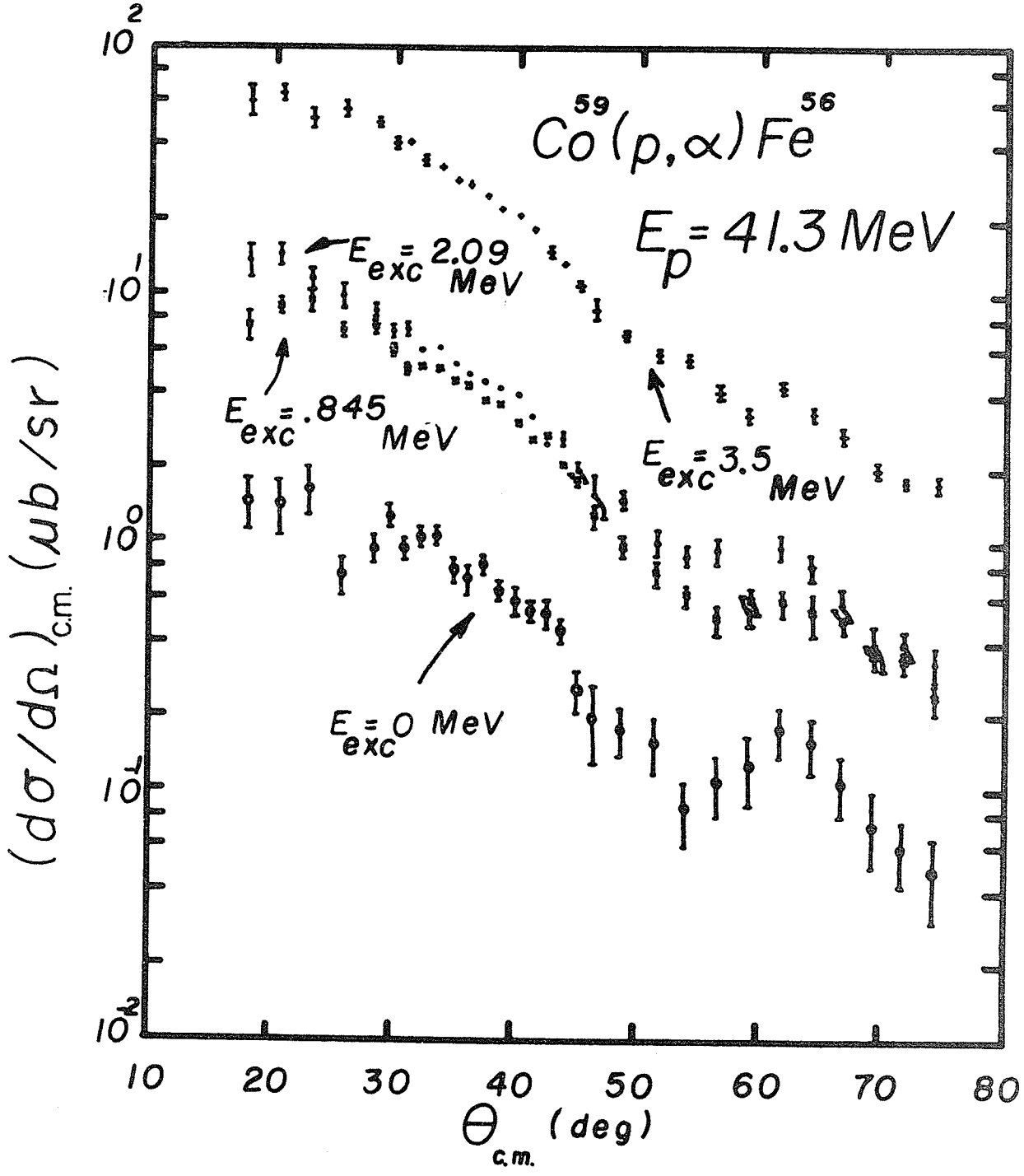
$Co^{59}(p,\alpha)Fe^{56}$
$E_p = 41.3$ MeV
$E_{exc} = 2.09$ MeV
$E_{exc} = .845$ MeV
$E_{exc} = 3.5$ MeV
$E_{exc} = 0$ MeV
$(d\sigma/d\Omega)_{c.m.}$ ($\mu b/sr$)
$\theta_{c.m.}$ (deg)
10^2
10^1
10^0
10^{-1}
10^{-2}
10
20
30
40
50
60
70
80

Table 2.6

Tabulated differential cross-sections for the $^{59}Co(p,\alpha)^{56}Fe$ reaction, leading to several states of ^{56}Fe

$^{59}Co(p,\alpha)^{56}Fe$ $E_p = 41.3 \pm .3$ MeV

$d\sigma/d\Omega(\mu b/st) \pm Error(\mu b/st)$

$\theta_{c.m.}$ (deg.)	G.S.	1st X.S. (-.845 MeV)	2nd X.S. (2.085 MeV)	(3.5 MeV)
18.1	1.47 ±.33	7.5 ±1.0	13.7 ±2.0	60.5 ±9.0
20.7	1.44 ±.36	9.0 ± .7	14.5 ±1.4	65.0 ±4.3
23.2	1.67 ±.37	9.5 ± .9	11.5 ±1.1	51.2 ±4.7
25.8	.75 ±.13	7.2 ± .4	9.9 ±1.1	55.8 ±4.4
28.4	.95 ±.13	7.45± .42	8.6 ± .5	49.3 ±1.9
29.8	1.30 ±.14	6.05± .3	7.15± .43	40.8 ±2.2
31.0	.96 ±.09	4.97± .21	7.25± .42	41.2 ±1.1
32.3	1.07 ±.10	5.17± .25	5.98± .31	35.6 ±1.8
33.6	1.08 ±.09	5.12± .19	6.15± .23	33.0 ±1.1
34.9	.79 ±.09	4.53± .15	5.26± .30	29.2 ±1.0
36.1	.72 ±.10	4.33± .21	4.84± .26	28.0 ±1.0
37.4	.83 ±.07	3.80± .17	4.47± .25	25.3 ± .6
38.7	.65 ±.06	3.66± .12	4.30± .19	22.6 ± .25
40.1	.59 ±.08	3.11± .15	4.00± .10	21.1 ± .5
41.3	.54 ±.05	2.62± .11	3.31± .12	18.6 ± .4
42.6	.53 ±.07	2.72± .14	2.55± .14	15.0 ± .8
43.8	.45 ±.05	2.09± .11	2.67± .16	13.4 ± .4
45.1	.26 ±.05	1.83± .13	1.95± .21	11.9 ± .5
46.4	.20 ±.07	1.29± .14	1.59± .30	8.8 ± .8
48.8	.18 ±.04	.98± .09	1.53± .13	6.9 ± .3
51.5	.16 ±.04	.77± .09	1.02± .13	5.80± .32
54.1	.086±.025	.62± .06	.91± .09	5.50± .25
56.6	.11 ±.03	.50± .07	.95± .12	4.10± .30
59.2	.13 ±.04	.59± .07	.55± .08	3.37± .23
61.7	.18 ±.04	.59± .07	.97± .09	4.28± .20
64.3	.16 ±.04	.53± .10	.82± .10	3.34± .20
66.8	.11 ±.03	.50± .06	.58± .09	2.75± .17
69.4	.074±.025	.36± .04	.39± .08	2.02± .14
71.9	.060±.017	.34± .03	.40± .05	1.77± .10
74.4	.048±.016	.24± .033	.33± .05	1.76± .10

2.5 Partial Cross-Section Calculations

Partial cross-sections were calculated from the experimental data in the usual fashion, by plotting $(d\sigma/d\ )_{c.m.}\ \sin\theta_{c.m.}$ vs. $\theta_{c.m.}$ and integrating the area under the resulting curve. Since in general there was a considerable uncertainty introduced by the lack of data in the extreme forward angles we used, whenever possible, the data of other works, even though they were not measured at the same energy. The justification for this procedure lies in the assumption that the shape of the forward region of the angular distribution changes slowly with energy and hence, with appropriate normalization, the pertinent data should introduce little error.

For $^{27}Al(p,\alpha)^{24}Mg_{G.S.}$ we used data from Minnesota [5] measured for E_p = 39.7 mev between 12° and 36°.

For $^{58}Ni\ (p,\alpha)^{55}Co_{G.S.}$ we used the Proton Linear Accelerator RHEL data [7], measured for E_p = 50.0 MeV at angles between 10° and 20°.

For $^{59}Co\ (p,\alpha)^{56}Fe$ (to 3.5 MeV state in Fe^{56}) we again used the P.L.A. data [7], measured for the same level at E_p = 50Mev for angles between 10° and 19°.

The resulting partial cross-sections of the various angular distributions discussed in this work, together with previous (p,α) measurement on other elements measured on the University of Manitoba Cyclotron are listed in Table 2.7.

Table 2.7

Tabulated (p,α) partial cross-sections

REACTION	ENERGY (MeV)	EXCITATION ENERGY (MeV)	PARTIAL CROSS-SECTION (μb)
$^{7}Li(p,\alpha)^{4}He$	45.2	0.0	580 ± 100
$^{7}Li(p,\alpha)^{4}He$	41.3	0.0	760 ± 100
$^{12}C(p,\alpha)^{9}B$	44.5	0.0	1110 ± 80
$^{12}C(p,\alpha)^{9}B$	41.6	0.0	1600 ± 300
$^{12}C(p,\alpha)^{9}B$	38.6	0.0	2510 ± 80
$^{19}F(p,\alpha)^{16}O$	44.5	0.0	120 ± 20
$^{23}Na(p,\alpha)^{20}Ne$	45.5	0.0	107 ± 24
$^{27}Al(p,\alpha)^{24}Mg$	41.3	0.0	30 ± 7
$^{27}Al(p,\alpha)^{24}Mg$	41.3	1.37	120 ± 19
$^{27}Al(p,\alpha)^{24}Mg$	41.3	4.12 - 4.25	99 ± 11
$^{27}Al(p,\alpha)^{24}Mg$	41.3	5.228	16 ± 4
$^{27}Al(p,\alpha)^{24}Mg$	41.3	6.0	35 ± 3
$^{27}Al(p,\alpha)^{24}Mg$	41.3	7.5	129 ± 14
$^{58}Ni(p,\alpha)^{55}Co$	41.3	0.0	163 ± 13
$^{59}Co(p,\alpha)^{56}Fe$	41.3	0.0	2.4 ± .5
$^{59}Co(p,\alpha)^{56}Fe$	41.3	.845	11.7 ± 1.8
$^{59}Co(p,\alpha)^{56}Fe$	41.3	2.085	18.4 ± 4.3
$^{59}Co(p,\alpha)^{56}Fe$	41.3	3.5	88. ± 11.

2.6 Alpha Particle Energy Spectra from ^{197}Au Bombarded by Protons.

Previous measurements of the alpha particle spectra resulting from the bombardment of ^{197}Au with protons have been measured using E_p= 9.5-23 MeV, 56 MeV and 155 MeV[8,9,10]. None were taken using a solid state detector arrangement. We made measurements using E_p= 23 MeV, 32 MeV and 41.3 MeV. (higher beam energies, although attainable with our cyclotron, did not deliver enough beam current to obtain satisfactory alpha particle yields).

Table 2.8 tabulates the angle and energies at which measurements of the alpha particle energy spectra were taken. Some of them are shown in Figure 2.11-2.15. In order to compare the experimental results with those predicted theoretically we must extract from these spectra only the component which is the result of a statistical compound nuclear process. This was done, on the assumptions that this process was isotropic and also that the yield in the extreme backward angles was due to such a mechanism (ie direct reaction contribution assumed negligible for the backward angle). Figure 2.16 gives the extrapolated cross-section one should obtain for $\theta_L = 180^\circ$ (where we assume we measure only evaporation processes). The result for E_p = 23 MeV (labelled as (b) in both Fig. 2.16 and Table 2.8) makes use of a measurement by FULMER [8] taken at $\theta = 90^\circ$. The result in Figure 2.16 and Table 2.8 labelled as (a) refers to the work of MUTO [9]

Table 2.8

Alpha Particle yield from $^{197}Au(p,\alpha)$ reaction.

ALPHA PARTICLE YIELD FROM PROTON BOMBARDMENT OF ^{197}Au

E_L^p (MeV)	θ_L (deg)	$d\sigma/d\Omega$ ($\mu b/sr$)	σ (mb)
23.0[b]	90	200 ± 10	
23.0	120	107 ± 5	
23.0	150	84 ± 4	
23.0	* 180	76 ± 8	.96 ± .10
32.0	60	1025 ± 100	
32.0	120	290 ± 15	
32.0	140	240 ± 20	
32.0	150	232 ± 15	
32.0	* 180	220 ± 30	2.76 ± .37
41.3	60	1800 ± 200	
41.3	90	820 ± 30	
41.3	110	570 ± 25	
41.3	120	488 ± 15	
41.3	130	440 ± 12	
41.3	140	416 ± 10	
41.3	150	404 ± 10	
41.3	* 180	390 ± 30	4.90 ± .38
56.3[a]			15.0 ± 1.

* EXTRAPOLATED

Figure 2.11

Alpha particle spectra from ^{197}Au bombarded with 41.3 MeV protons.

E_p = 41.3 MeV
^{4}He SPECTRUM
FROM ^{197}Au
30°
60°
90°
150°
E_α (MeV)
15
21
27
33
$d^2\sigma/d\Omega dE$
μb/(sr-MeV)
20
40
60
80
100
120
140

Figure 2.12

Alpha particle spectra from ^{197}Au

bombarded with 41.3 MeV protons.

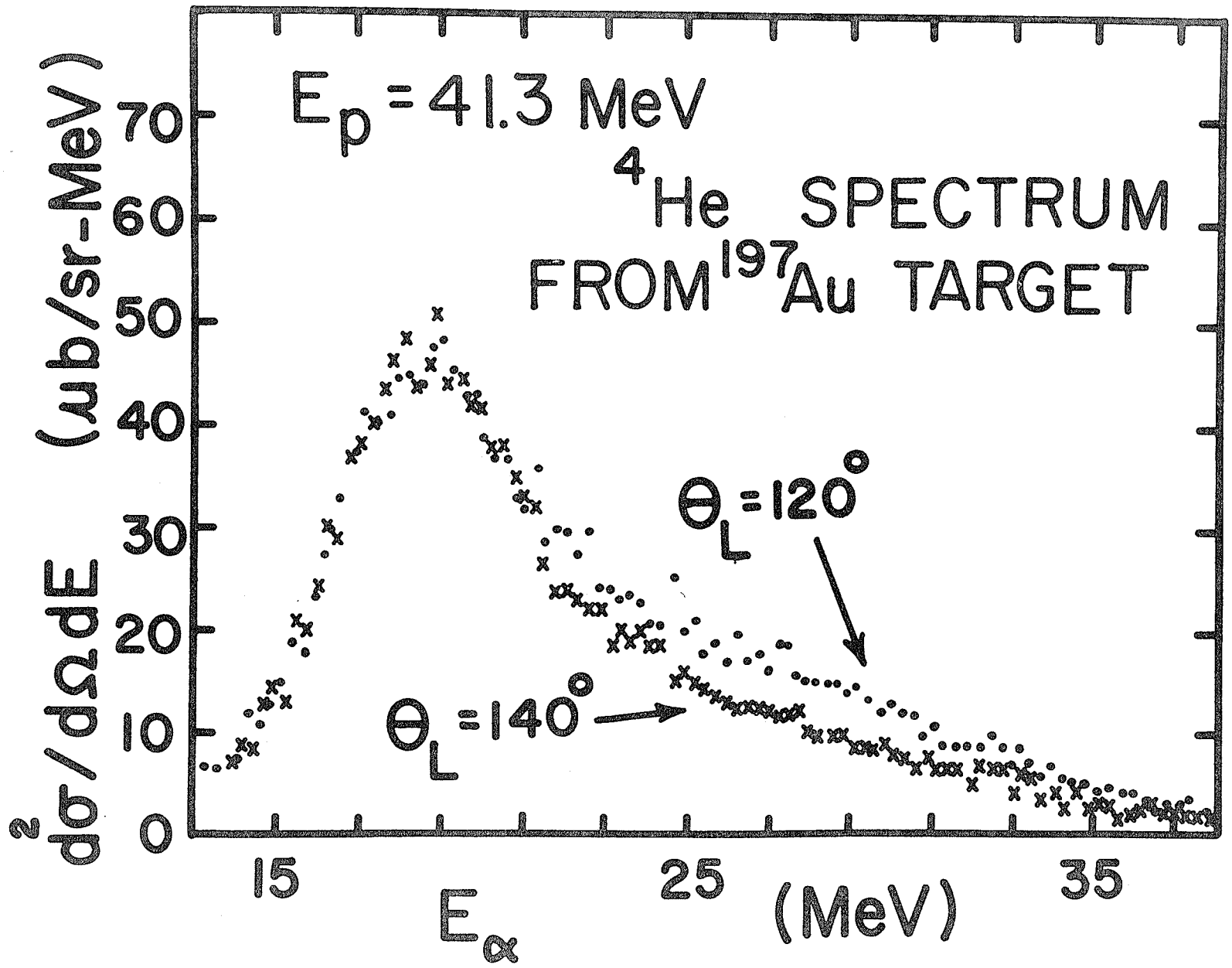
E_p = 41.3 MeV
^{4}He SPECTRUM
FROM ^{197}Au TARGET
θ_L = 120°
θ_L = 140°
$\frac{d^2\sigma}{d\Omega dE}$ (μb/sr-MeV)
0
10
20
30
40
50
60
70
15
25
35
E_α (MeV)

Figure 2.13

Alpha particle spectra from ^{197}Au bombarded with 32.0 MeV protons.

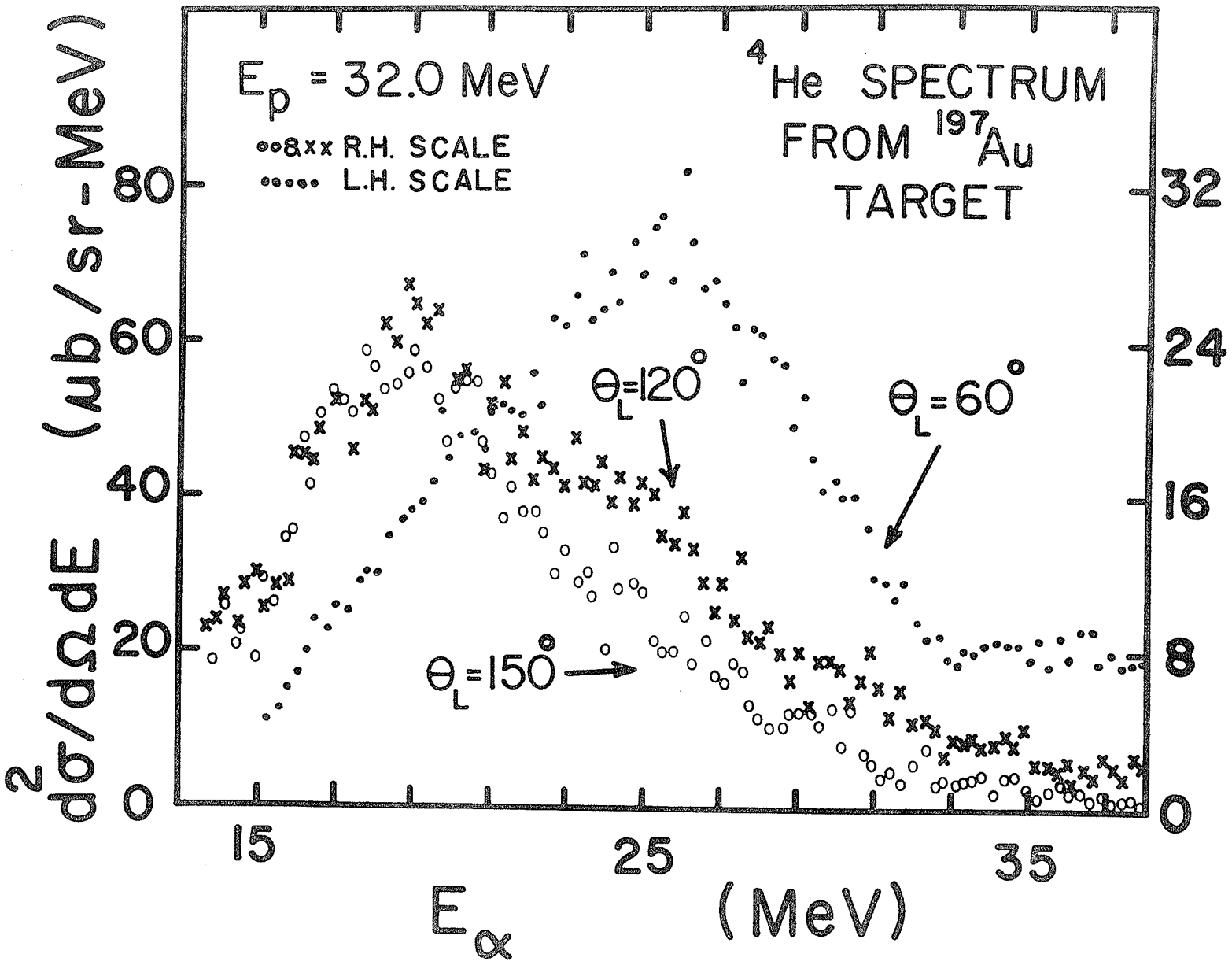
E_p = 32.0 MeV
^{4}He SPECTRUM
FROM ^{197}Au
TARGET
oo8xx R.H. SCALE
ooooo L.H. SCALE
θ_L=120°
θ_L=60°
θ_L=150°
$\frac{d^2\sigma}{d\Omega dE}$ (μb/sr-MeV)
0
20
40
60
80
0
8
16
24
32
15
25
35
E_α (MeV)

Figure 2.14

Alpha particle spectrum from ^{197}Au

bombarded with 23.0 MeV protons

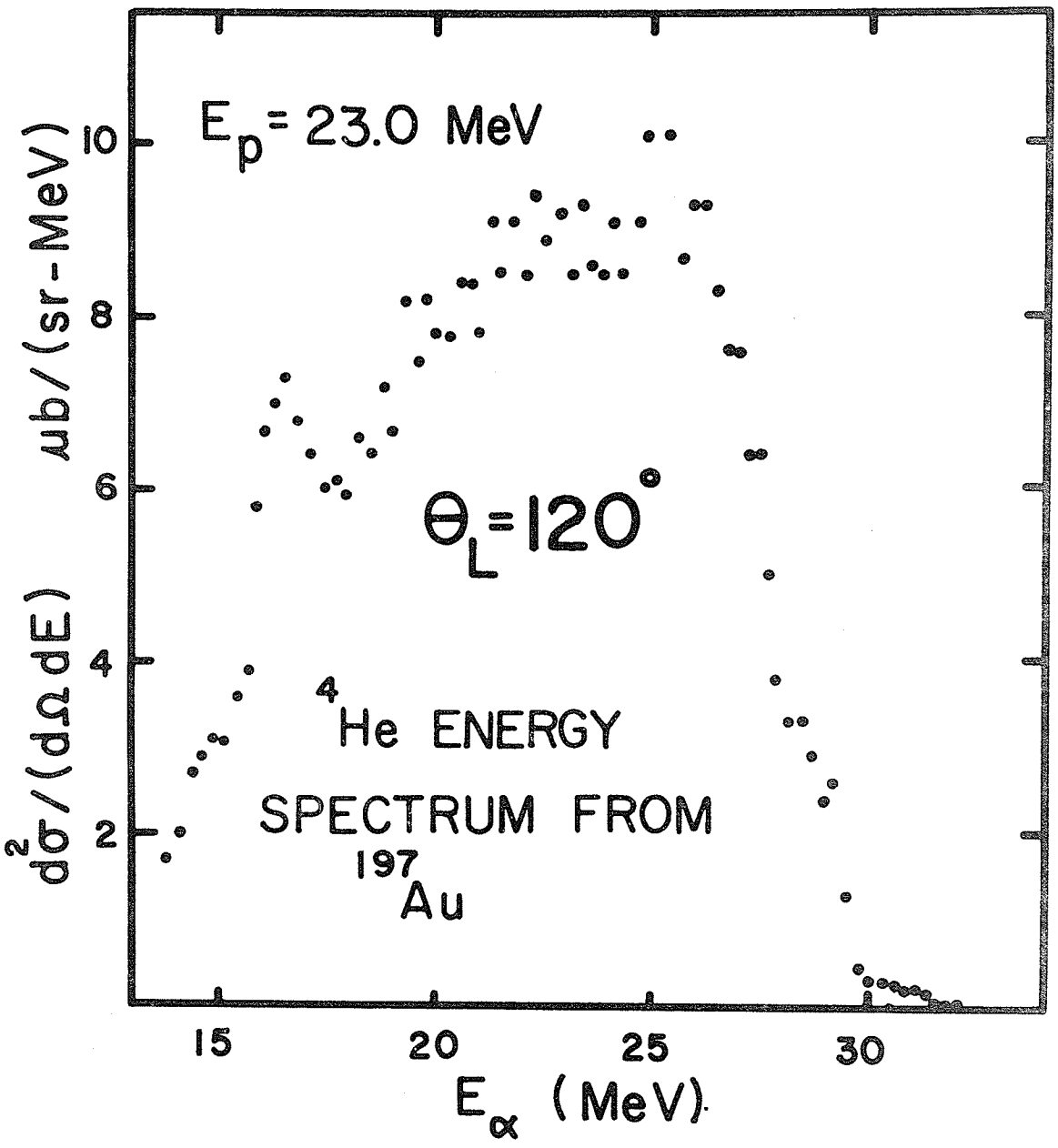
E_p = 23.0 MeV
θ_L = 120°
^{4}He ENERGY SPECTRUM FROM ^{197}Au
$d^2\sigma/(d\Omega dE)$ μb/(sr-MeV)
2
4
6
8
10
15
20
25
30
E_α (MeV)

Figure 2.15

Alpha particle spectrum from ^{197}Au

bombarded with 23.0 MeV protons

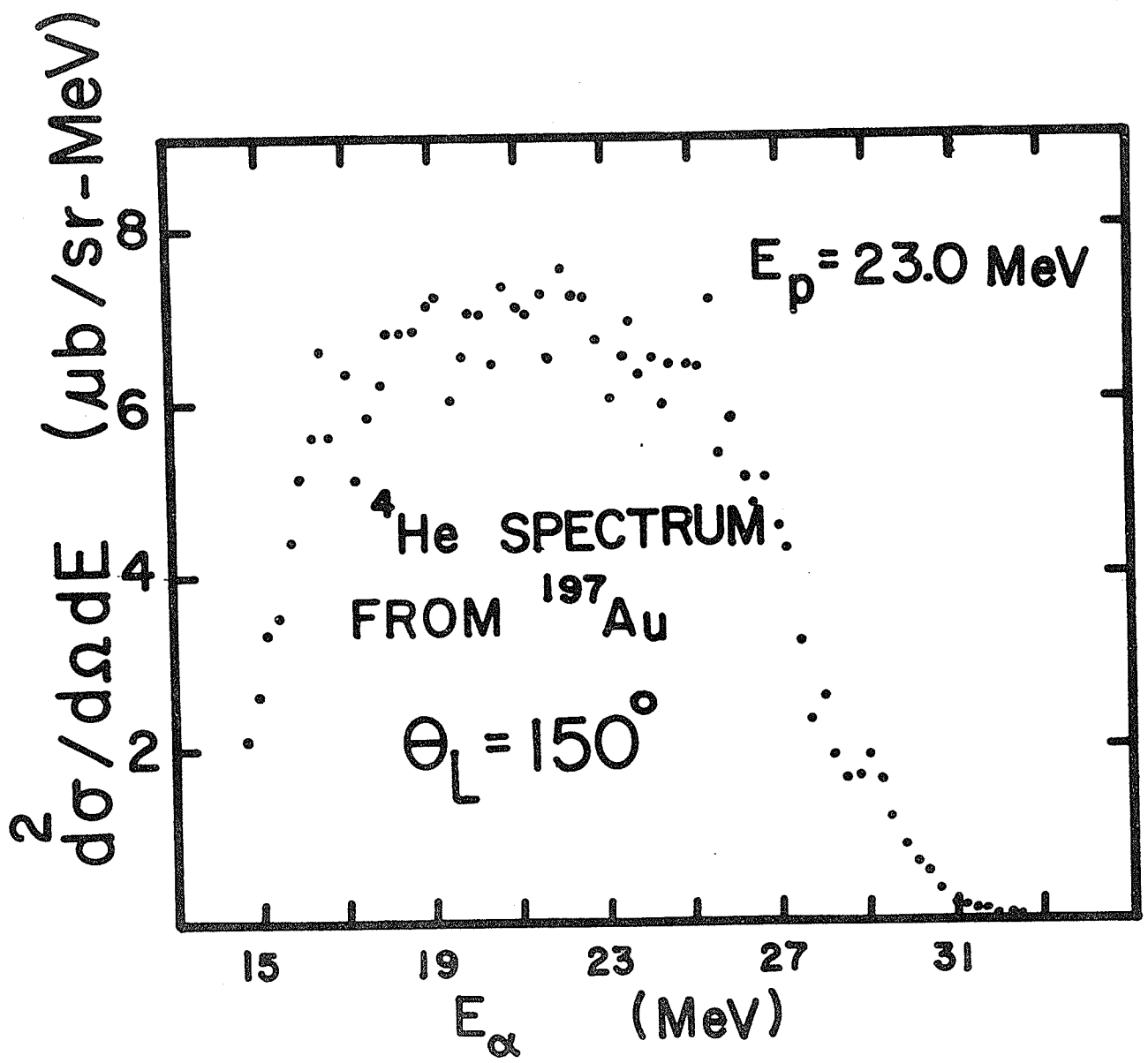
E_p = 23.0 MeV
^{4}He SPECTRUM
FROM ^{197}Au
θ_L = 150°
$\frac{d^2\sigma}{d\Omega dE}$ (μb/sr-MeV)
2
4
6
8
15
19
23
27
31
E_α (MeV)

Figure 2.16

Alpha particle yield from ^{197}Au bombarded with protons of various energies.

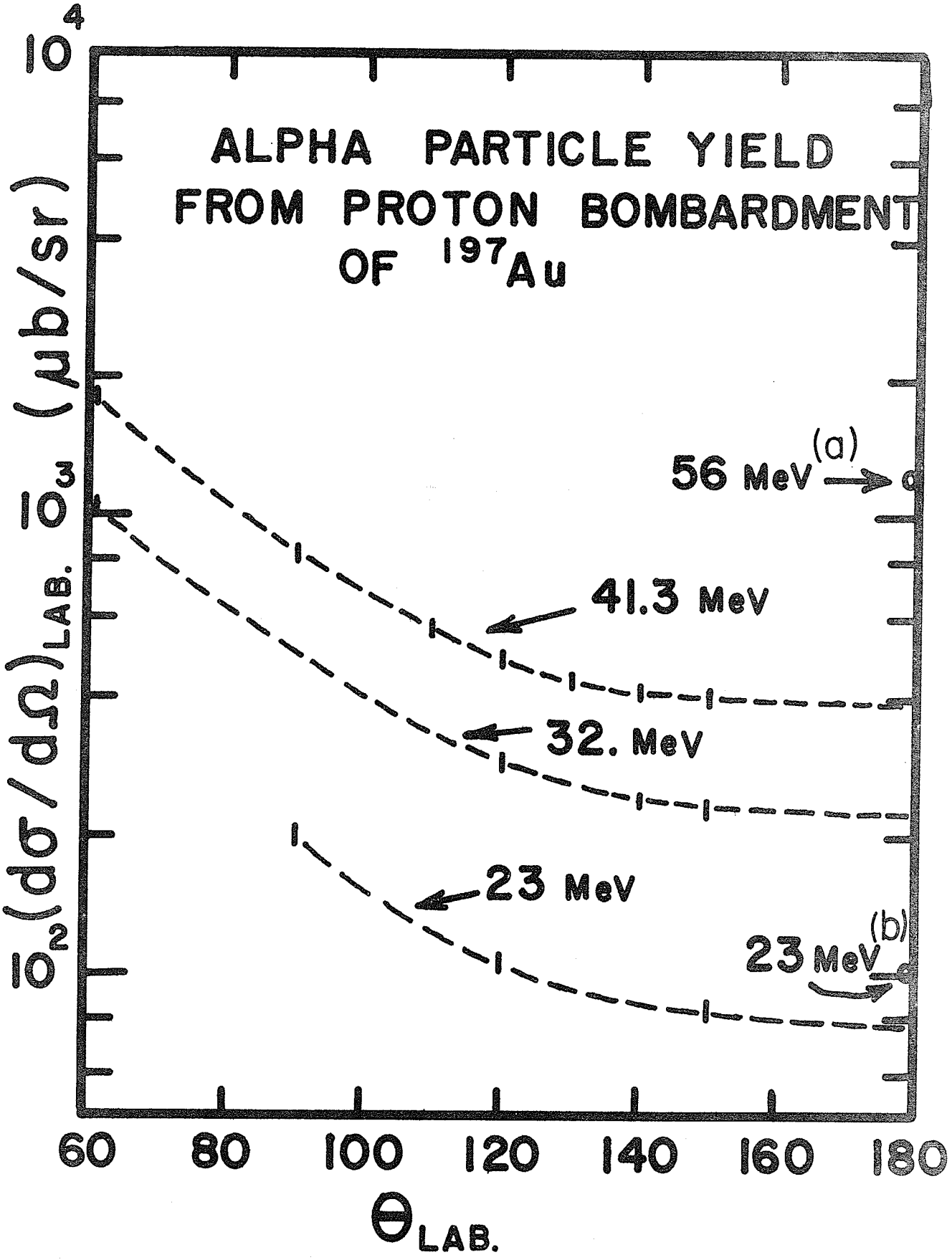
ALPHA PARTICLE YIELD
FROM PROTON BOMBARDMENT
OF ^{197}Au
10^4
10^3
10^2
$(d\sigma/d\Omega)_{LAB.}$ ($\mu b/sr$)
56 MeV (a)
41.3 MeV
32. MeV
23 MeV
23 MeV (b)
60
80
100
120
140
160
180
$\theta_{LAB.}$

Figure 2.17

Energy Level Diagrams for the residual Nuclei ^{20}Ne, ^{24}Mg, ^{55}Co, ^{56}Fe.

ENERGY LEVEL DIAGRAMS

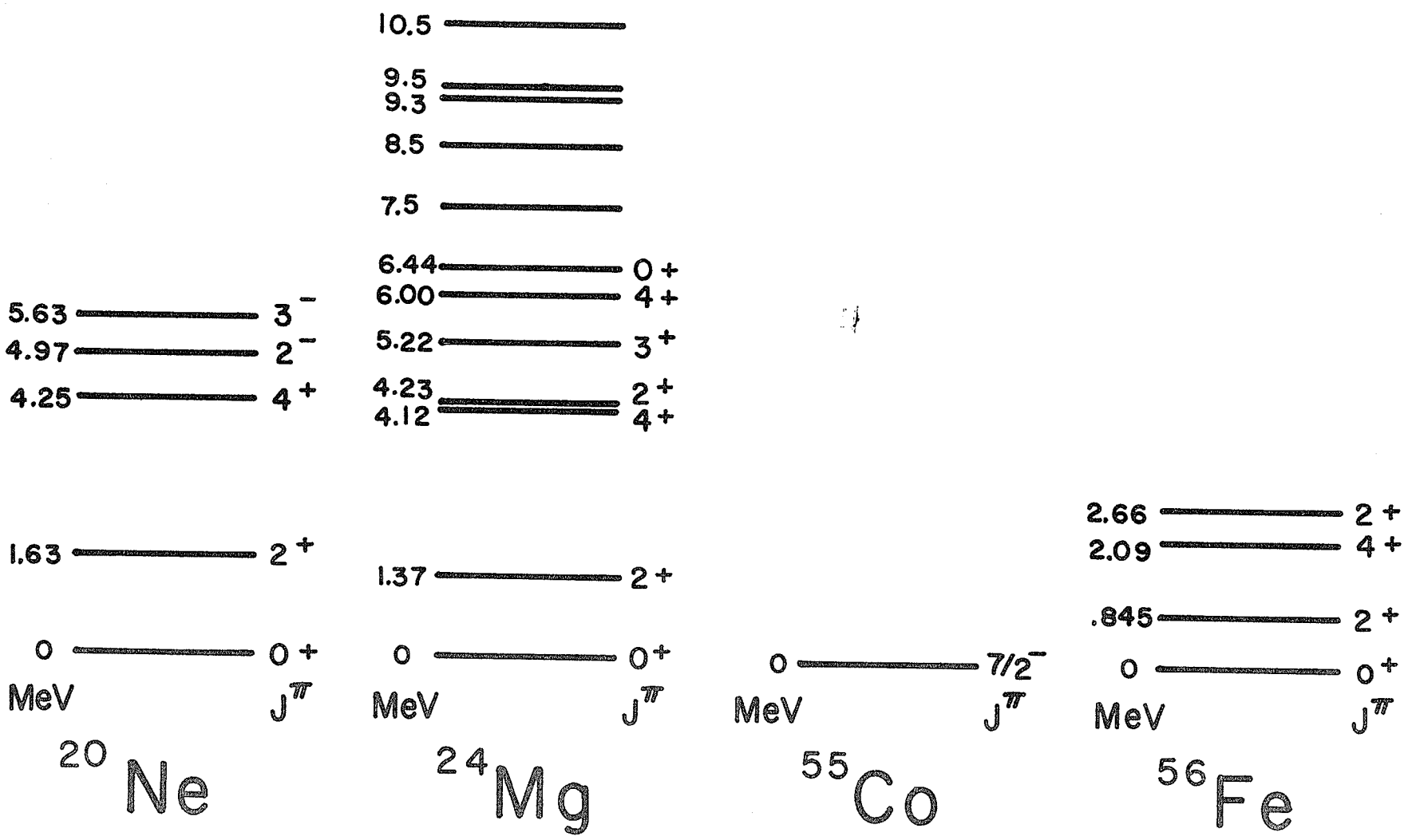

CHAPTER III

THEORETICAL CONSIDERATIONS

A. Statistical Model

1. Introduction

For a number of years various authors[11-20] have attempted to explain the continuum part of the energy spectrum of particles resulting from the bombardment of various nuclei. Nearly all analyses have been done in terms of the "evaporation" model based on the assumption of the formation of a compound nucleus. A comprehensive survey of the compound statistical features of nuclear reactions was given in the review article by Bodansky[37]. In all cases, the formation of a compound nucleus in a well defined state, in which the incident particle shares its energy among all the nucleons of the target nucleus, has been treated as independent of its disintegration. The assumption of this independence was based on the "random phase approximation". That is, it was assumed that at the excitation energy of the compound nucleus there are many energy levels of all types and since the incident beam or the level widths were broad compared to the energy level spacing, many levels of the compound nucleus were excited. The wave functions of these levels were assumed to have random phases so that when phase averages were performed the interference terms vanished. The result of this was that for the absorption of nucleons having an energy range of the order 10-50 MeV the

angular distribution would be isotropic[22]. The model used for the calculation of the energy spacing was usually based on the so-called "Fermi-gas" model[24,31,35] in which it was assumed, among other things, that there was a set of independent particles confined to a potential well. For the purposes of estimating the density of levels the Fermi-gas model, although a poor representation of the nucleus, should be adequate since the residual interactions (inter-nucleon forces) do neither create nor destroy energy levels (that is the number of states remain the same)[24,38].

2. The Formalism

Lang[35], Ericson[24] and Newton[38] have shown that the level density W for the "Fermi-gas" model has the form,

$$\omega(U) = \text{const.}\ a^{-1/4}\ (U+t)^{-5/4}\ \exp[2\sqrt{aU}\,]$$ where a is the level density parameter, which on the assumption that we have equidistant spacing in the energy levels of the Fermi-gas can be explicitely shown[24] to be

$$a = 2\left(\frac{\pi}{3}\right)^{4/3} \frac{m\, r_o^2}{\hbar^2} A$$ where m is the nucleon mass, r_o its radius and A the atomic weight of the nucleus for which we want $\omega(U)$. Also $U = E - \delta$ represents the excitation energy minus the pairing energy δ[30].

Thomas[36] has shown that the angular momentum dependence of the level density, under the assumption that the nuclear moment of inertia is infinite (see Appendix 3.A), introduces a factor of $\tau^{-3/2}$ into the expression for the

level density, where τ is the "nuclear temperature" defined by

$$\frac{1}{\tau} = \frac{d \ln\omega(U)}{d U} = \left(\frac{a}{U}\right)^{1/2} - \frac{5}{4}\,\frac{1}{(U + t)} \qquad (3\text{-}1)$$

where t, given by the relationship $U = at^2 - t$, yields

$$t = \frac{.5}{a}\left(1 + \sqrt{1+4aU}\right) \qquad (3\text{-}2)$$

Consider now the reaction of the form (Figure 3.1)

$$X + a \longrightarrow C \rightarrow Y + b.$$

Then, according to the statistical model [31,34,35] and following the notation of BUTTNER [32] the differential energy cross-section

$$\sigma(a,b)\, dE_b = \sigma_a(E_a)\, \frac{\Gamma_b\, dE_b}{\sum_{b'} \Gamma_{b'}}$$

where

$$\Gamma_b(E_b)dE_b = \frac{g_b\, k_b^2(E_b)}{2\pi^2}\, \sigma_b(E_b)\, \frac{\omega_Y(E^b_{max} - E_b)}{\omega_C(E_a + S_{aC})}\, dE_b$$

and

$$\sum_{b'} \Gamma_{b'} = \sum_{b'} \int_{E_{b'}=0}^{E^{b'}_{max}} \frac{g_{b'}\, k^2_{b'}(E_{b'})}{2\pi^2}\, \sigma_{b'}(E_{b'})\, \frac{\omega_Y(E^{b'}_{max} - E_{b'})}{\omega_C(E_a + S_{aC})}\, dE_{b'}$$

where σ_a is the compound cross section for the reaction $X + a \rightarrow C$, while $\sigma_i(E_i)$ are the inverse reaction cross sections, that is, the cross-sections for the formation of C, with an excitation $E_a + S_{aC}$, resulting from the bombardment of Y, having an excitation $E^i_{max} - E_i$ by a particle i. The summation extends over all possible decay modes of the compound nucleus C.

Figure 3.1

Schematic of single particle emission process.

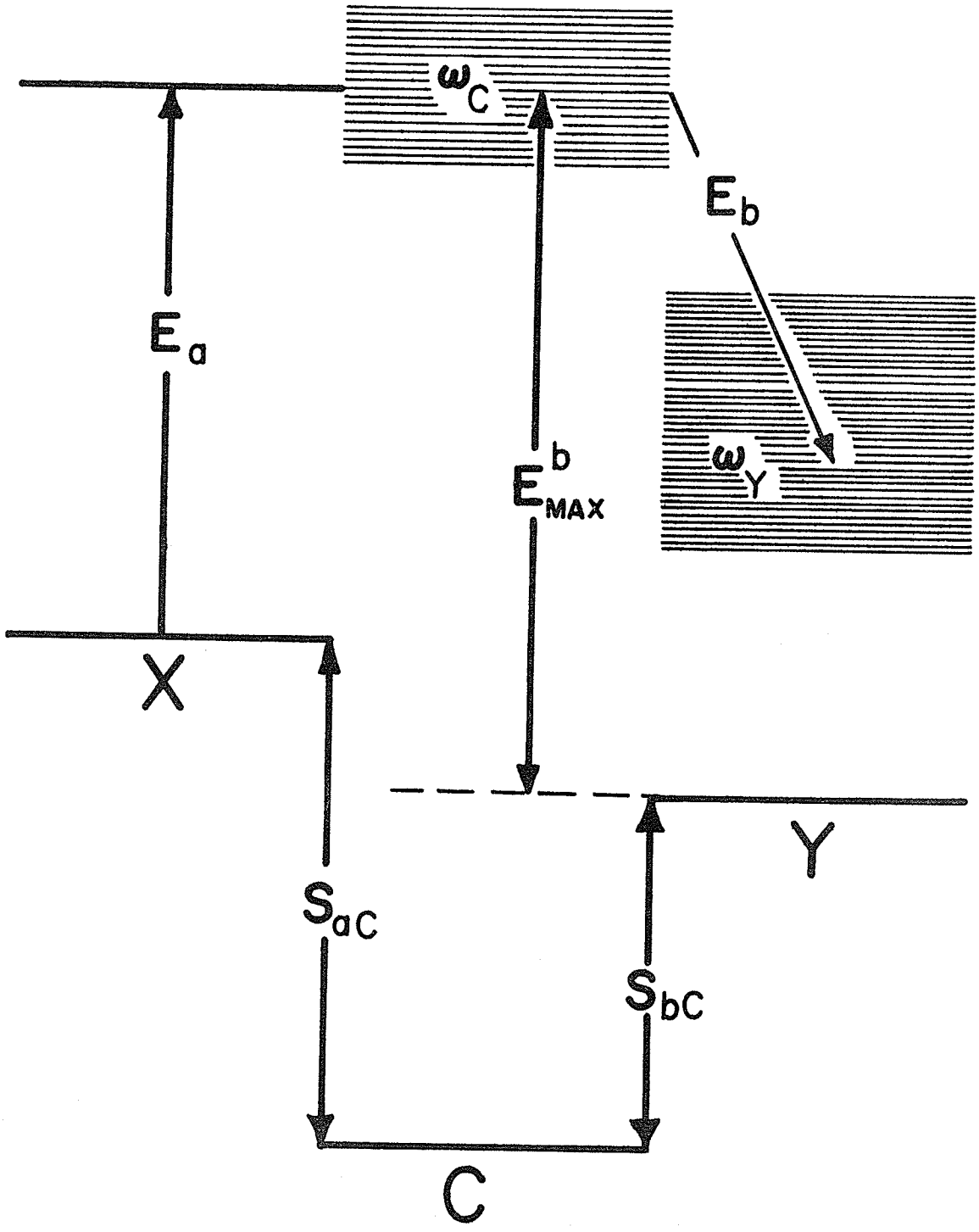
ω_C
E_b
E_a
E^b_{MAX}
ω_Y
X
Y
S_{aC}
S_{bC}
C

Also $g_i\, k_i^2\,(E_i) = (2s_i+1)\, \frac{2\, m_i\, E_i}{\hbar^2}$ where s_i is the spin of i, m_i is its mass and E_i its energy.

Physically Γ_b, can be thought of as a "level width", related to the mean lifetime T of the compound nucleus C by

$$\sum_{b'} \Gamma_{b'} = \frac{\hbar}{T}$$

Hence we think of $\sum_{b'} \Gamma_{b'}$ as the "total width" while a specific decay rate $\Gamma_{b'}$ is denoted as a "partial width" for the decay into channel b'. Thus $\frac{\Gamma_b}{\sum_{b'} \Gamma_{b'}}$ is thought of as a "branching ratio" which determines what fraction of the compound nucleus decays into the specific channel b. Basically the differential energy spectra (of the products b) are determined by phase space factors, inverse reaction cross-sections, the level densities of the nuclei involved and the probability of forming the compound nucleus C.

Up to now we have assumed that the ejection of a single particle b was sufficient to "cool" the compound nucleus so that no more particles of the type b could be again ejected from the residual mucleus. It is this aspect which we specifically want to explore in this work. That is, we are interested in the degree to which multiple-particle emission contributes to the particle spectrum.

Rather simplified calculations [21,34,39] have been performed previously. In addition several authors [11,23] have calculated the cross sections of multiple-particle emission by Monte-Carlo calculations. A few analytic

calculations[13,25,40] of the differential energy spectra of the resulting multiple-emission products have been made but nearly all calculations were performed with extremely simplified formulae for the level densities.

In order to study the multiple emission of particles having small branching ratios (such as alphas and deuterons) we choose the analytical approach since Monte-Carlo routines become impractical when the "yield" is so low that the necessary statistics cannot be obtained in a reasonable computational time on present day computors.

The basis for our theoretical calculations lies in the work of BUTTNER[32] et al. They calculated the cross sections for the emission of two particles using reasonable value for the level densities (except that they neglected to include the factor $\tau^{-3/2}$). We have expanded their formalism in order to calculate the differential energy spectra and our excitation energies being higher, we have included the effect of the third particle (shower) as well. Thus our calculations will be valid up to the threshold of the fourth particle emission.

Figure 3.2 illustrates the multiple-particle emission process. The first particle energy differential cross-section is given by

$$\sigma(a;b)\,dE_b = \sigma_a(E_a)\;\frac{\Gamma_b(E_b)\,dE_b}{\sum_{b'}\Gamma_{b'}(E_{b'})} \qquad (3.16)$$

The second particle energy differential cross-section is

$$\sigma(a;b,c)\,dE'_c = \sigma_a(E_a) \int_{E_b=0}^{E^{bc}_{max}-E'_c} \frac{\Gamma_b(E_b)\,dE_b\;\Gamma_c(E'_c)\,dE'_c}{\sum_{b'} \Gamma_{b'}(E_{b'}) \sum_{c'} \Gamma_{c'}(E'_{c'})} \qquad (3.17)$$

while the third particle energy differential cross-section is

$$\sigma(a;b,c,d)\,dE''_d = \sigma_a(E_a) \int_{E_b=0}^{E^{bcd}_{max}-E''_d} \int_{E'_c=0}^{E^{bcd}_{max}-E''_d-E_b} \frac{\Gamma_b(E_b)\,dE_b\,\Gamma_c(E'_c)\,dE'_c\;\Gamma_d(E''_d)\,dE''_d}{\sum_{b'} \Gamma_{b'}(E_{b'}) \sum_{c'} \Gamma_{c'}(E'_{c'}) \sum_{d'} \Gamma_{d'}(E''_{d'})} \qquad (3.18)$$

where

$$\Gamma_b(E_b)\,dE_b = \frac{g_b k_b^2}{2\pi^2}\,\sigma_b(E_b)\,\frac{\omega_Y(E^b_{max}-E_b)}{\omega_C}\,dE_b$$

$$\Gamma_c(E'_c)\,dE'_c = \frac{g_c k_c^2}{2\pi^2}\,\sigma_c(E'_c)\,\frac{\omega_Z(E^{bc}_{max}-E_b-E'_c)}{\omega_Y(E^b_{max}-E_b)}\,dE'_c$$

$$\Gamma_d(E''_d)\,dE''_d = \frac{g_d k_d^2}{2\pi^2}\,\sigma_d(E''_d)\,\frac{\omega_W(E^{bcd}_{max}-E_b-E'_c-E''_d)}{\omega_Z(E^{bc}_{max}-E_b-E'_c)}\,dE''_d$$

$$\sum_{b'} \Gamma_{b'}(E_{b'}) = \sum_{b'} \int_{E_{b'}=0}^{E^{b'}_{max}} \frac{g_{b'} k_{b'}^2}{2\pi^2}\,\sigma_{b'}(E_{b'})\,\frac{\omega_Y(E^{b'}_{max}-E_{b'})}{\omega_C}\,dE_{b'}$$

and similarly for $\sum_{c'} \Gamma_{c'}(E'_{c'})$ and $\sum_{d'} \Gamma_{d'}(E''_{d'})$

Hence for example after cancelling factors common to both numerator and denominator, we have

Figure 3.2

Schematic of multiple-particle emission process.

DECAY OF COMPOUND NUCLEUS

$$\sigma(a;x)_{obs.} = \sigma(a;x) + \sum_{b'} \sigma(a;b'x) + \sum_{b'} \sum_{c'} \sigma(a;b'c'x)$$

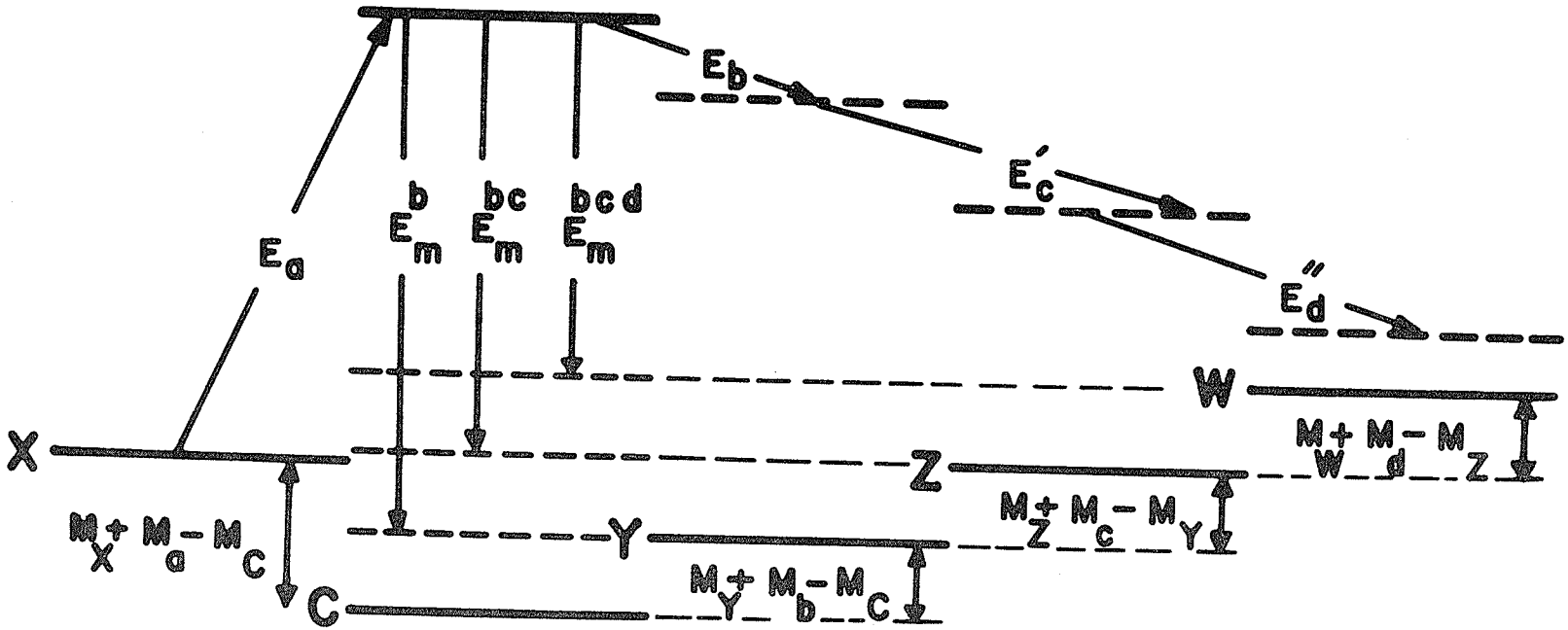

$$\sigma(a;b,c,d)\,dE_d'' = \frac{\sigma_a(E_a)}{\sum_{b'} \int_{E_{b'}=0}^{E_{max}^{b'}} g_{b'} k_{b'}^2 \sigma_{b'}(E_{b'}) \omega_Y(E_{max}^{b'} - E_{b'})\,dE_{b'}} \int_{E_b=0}^{E_{max}^{bcd} - E_d''} \left[\frac{g_b k_b^2 \sigma_b(E_b)\, \omega_Y(E_{max}^{b} - E_b)}{\sum_{c'} \int_{E_{c'}=0}^{E_{max}^{c'b} - E_b} g_{c'} k_{c'}^2 \sigma_{c'}(E_{c'}') \omega_Z(E_{max}^{bc'} - E_b - E_{c'}')\,dE_{c'}'} \right.$$

$$\left. \times \int_{E_c'=0}^{E_{max}^{bcd} - E_d'' - E_b} \frac{g_c k_c^2 \sigma_c(E_c') \omega_Z(E_{max}^{bc} - E_b - E_c')\, g_d k_d^2 \sigma_d(E_d'') \omega_W(E_{max}^{bcd} - E_b - E_c' - E_d'')\,dE_b\,dE_c'}{\sum_{d'} \int_{E_{d'}''=0}^{E_{max}^{bcd'} - E_b - E_c'} g_{d'} k_{d'}^2 \sigma_{d'}(E_{d'}'') \omega_W(E_{max}^{bcd'} - E_b - E_c' - E_{d'}'')\,dE_{d'}''} \right] dE_d'' \qquad (3.19)$$

In the above $\sigma_i(E_i)_{i \neq a}$ are the inverse reaction cross sections. One of the basic difficulties in the application of the evaporation model is the lack of precise knowledge of the cross-section for forming the original compound nucleus by bombarding the excited residual nucleus with particle i of energy E_i. These cross-sections cannot be experimentally obtained since we know of no way to "prepare" the nuclei to be bombarded. We thus assume that the inverse reaction cross-sections are those given by say, optical model calculations for nuclei in their ground state.

The summation (b', c', d') over the competing events was carried out over neutrons, protons, deuterons and alpha particles. Although our formalism can take account of the competition from He^3, tritons and gamma emission, these were ignored since they are known to be small in comparison to the other particles in the energy range (20-60 MeV) of interest. Competition from gamma emission

becomes important only if we are below or just near the threshold for particle emission.

A computer code[26] programmed to evaluate Equation 3.16-3.18 calculates $\sigma_{inverse}(E_i)$ by suitable evaluation of polynomials which were, by a previous computer code, fitted to the data of other works. For $\sigma_{inverse}$(neutrons) we used the values given by DOSTROVSKY[23]. For $\sigma_{inverse}$ (alphas) we used the tabulations of Huizenga and Igo[27,28], while for $\sigma_{inverse}$ (deuterons) and $\sigma_{inverse}$ (protons) we used the tabulations given by Shapiro[29].

The level density used had the form:

$$\omega(U) = \text{const.}\ a^{-1/4}\ (U+t)^{-5/4}\ \tau^{-3/2}\ \exp\left[2\sqrt{aU}\right]$$

where the excitation energy U, corrected by the pairing energy according to the tabulations given by CAMERON[30], was obtained from experimental nuclear mass values[41]. The pairing energies for the even-even (residual) nuclei are about twice those for the odd-even nuclei, while they are zero for the odd-odd nuclei.

The pairing energy was introduced because it was known that even-even nuclei had a <u>smaller</u> level density than did odd-odd nuclei having the same excitation energy and atomic weight. Thus the excitation energy of even-even nuclei are <u>effectively</u> reduced while those for odd-odd nuclei remain the same.

The numerical values for t and τ were obtained from equations 3.2 and 3.1 respectively.

Experimentally one measures the energy spectrum of a certain particle x which results from the bombardment of a heavy nucleus by particle a. In order to make a comparison with the experimental results one must calculate the differential energy yield given by $\sigma(a;x)dE_x$, $\sigma(a; b,x)\ dE_x$, $\sigma(a; b, c,x)\ dE_x$ for a specific value of E_a, a suitable range of E_x (over which the measurement was made) and all possible combinations of intermediate particles b and c. Thus

$$\left[\sigma(a;x)\,dE_x\right]_{TOTAL} = \sigma(a;x)\,dE_x + \sum_b \sigma(a;b,x)\,dE_x + \sum_b \sum_c \sigma(a;b,c,x)\,dE_x$$

The theoretical evaluation of the "total" energy spectrum at 20 points requires approximately 200 minutes of computation on an IBM 360-65 computer. Computational uncertainties, determined by the number of integration steps, usually amount to less than 10%. The computor program and necessary instructions have been written in the form of an internal report[44)]

3.B DWBA THEORETICAL CONSIDERATIONS

The details of the DWBA theory used to fit our experimental results have been sufficiently described elsewhere[2,45,46,47] and will therefore not be repeated here. However it seems worthwhile stating some of the basic assumptions and approximations incorporated in this theory.

We consider the reaction B(b, a) A to be one of pick-up where b = a − x and B = A + x, x being the group of transferred nucleons.

We assumed the reaction was direct, that is, there was good overlap between the wave functions in the incident and exit channels so that the collision may occur with the minimum of rearrangement of the constituent nucleons.

We assume that the elastic scattering is the predominant process and that non-elastic reaction events can be treated as perturbations. The relative motion before and after the reaction is described by distorted waves which include the elastic scattering (calculated in the optical model approximation) - the transition is then simply one between elastic scattering states.

We assume the interaction V_{bx} in the matrix element taken between the internal states of the colliding pairs is central and that b and x are in an s-state of relative motion within a. That is, the cluster of 3 transferred nucleons (for p,α reactions) are assumed to have the internal properties of a triton ($L = 0$, $S = {}^1/_2$, $T = {}^1/_2$) and to originate in the shells having a single radial quantum number n.

The bound triton-core system was treated as a particle moving in a central potential having the same radial dependence form f(r) as the real part of the optical potentials. This bound state is required to have the correct separation energy and for given input values of r_t and a_t the potential depth V_t is adjusted until this condition is satisfied with the correct number of radial nodes (a number which is read into the DWBA code - see Appendix 4A).

Instead of using the often used "zero-range approximation" wherein one assumes a is "emitted" at the point where b is "absorbed" we make the more realistic calculation taking into account finite range effects through the use of the "local energy approximation" with a square well dependence whose radius and depth are those giving the same R.M.S. size for the square well wave function as for the harmonic oscillator wave function. The values one obtained when this was done for (p,α) reactions were

$r_o = 2.78$ fm , $V_o = 40$ MeV for the square well parameters.

We assume the potential for both ingoing and outgoing channels have the form

$$U = -Vf(r) - iW_v f(r') + 4i\, W_d a'' \frac{df(r'')}{dr''}$$ where the first term

is the real part of the Saxon-Wood potential, while the other two are the imaginary volume and surface potentials and where $f(r) = \left(1 + \exp\left\{\frac{r - r_o A^{1/3}}{a}\right\}\right)^{-1}$.

A coulomb potential corresponding to a uniformly charged sphere of radius $r_c A^{1/3}$ is also added.

We neglect spin-orbit coupling and exchange (knock-out) processes.

CHAPTER IV

a. ANALYSIS OF THE $^{27}Al(p,\alpha)^{24}Mg_{G.S.}$ REACTION.

We will now discuss a systematic approach which has been used in the analysis of the (p,α) reactions discussed in this part of the work. In order to extract any meaningful information (such as the experimental spectroscopic factor) from such an analysis one must reduce the number of freely adjustable parometers (ie, parameters whose value can neither be determined theoretically nor extracted from other experimental results) to an absolute minimum.

In view of the uncertainties in the values of parameters involved in spin-orbit interactions it was decided to neglect these from the calculations.

The basic assumptions and approximations of the DWBA code used for this analysis have already been discussed in Chapter III.

The DWBA code requires the determination of the parameter RADNOD, defined as the number of nodes (excluding zero and infinity) in the radial wavefunction for the centre of mass of the transferred (triton) cluster.

A procedure for determining this parameter is given in Appendix 4.a. Now $J_i^{\pi} = 5/2^+$ & $J_f = 0^+$ hence $l_t = 2$ (in agreement with value obtained by a diffraction model fit done by a Minnesota group [5] to their $^{27}Al(p,\alpha)^{24}Mg$ angular distribution). Excluding the zero and infinity the number of nodes in the bound radial wave function of the triton-core system then has a value, assuming the pick-up of three

d 5/2 nucleons, of 2.

Besides the entrance and exit channel optical parameters (determined by optical model fits to the target and residual nuclei by protons and alphas respectively) the only other "free" parameters are those of the bound state system r_t and a_t which are respectively the width and surface thickness of the real Saxon-Woods potential which we adopt for the bound-state triton-core interaction.

However, the optical parameters of an elastic scattered state may well serve as a guide to the value of r_t and a_t in this bound state and we will hence use as a guide the values one obtains by doing the optical model fits to the elastic scattering of tritons (or when not available, that of He^3 which we assume will introduce little error) from the residual nuclei of the (p,α) reaction.

Several authors[50,64,65] have made He^3 elastic scattering fits on Mg near 30 MeV with the following results

$$r_t = 1.07 - 1.15 \text{ fm} \qquad a_t = .69 - .85 \text{ fm}$$

Most of our initial analysis was made using the parameters extracted by GRIFFITHS[65] namely $r_t = 1.069$ fm, $a_t = .85$ fm.

The experimental elastic scattering data from Minnesota[60] for $E_p = 39.8$ MeV was close enough to the 41.3 MeV at which $^{27}Al(p,\alpha)^{24}Mg$ was measured and was used to extract the proton channel optical parameters with the use of an automatic search program[59]. The search routine allows any desired number of the optical parameters to be varied automatically until the agreement between the prediction

of the optical model and the experimental results are optimized according to the χ^2 parameter defined as

$$\chi^2 = \frac{1}{N} \sum_N \left(\frac{\sigma_E(\theta) - \sigma_{Th}(\theta)}{\delta\sigma_E(\theta)} \right)^2 \qquad \text{where}$$

$\sigma_{Th}(\theta)$ is the optical model prediction of the differential cross-section at an angle $\theta_{c.m.}$, $\sigma_E(\theta) \pm \delta\sigma_E(\theta)$ the corresponding experimental value and assigned error and N the number of experimental data points.

The search routine was started from optical parameters previously obtained in other works[51,56,57] except that the spin-orbit parameters were now excluded. Convergence to a good fit was thus quite rapid and the six best solutions are tabulated in Table 4.1. The theoretical fits are shown, together with the experimental differential elastic scattering cross-sections in Figures 4.1-4.6.

Again, through the use of the automatic search program the alpha channel optical parameters were extracted by fitting the elastic scattering data of 50 MeV alpha from ^{24}Mg to $70^\circ_{c.m.}$, extended to $133^\circ_{c.m.}$ by the 43 MeV alpha elastic scattering data at 43 MeV[62]. This data fortunately corresponds closely to the time reversed alpha particle laboratory energy of 48.3 MeV (Appendix 4.b) of the ^{27}Al(p,α)^{24}Mg reaction we measured for E_p= 41.3 MeV.

There exist, however, many sets of parameters, having a wide range of real well potential depths (V_α) which all give more or less equally good fits to the elastic scattering data.

Table 4.1

Tabulation of the optical parameters giving the best χ^2 fits to the elastic scattering of protons from ^{27}Al.

TABLE 4.1

OPTICAL PARAMETERS GIVING BEST FITS TO THE EXPERIMENTAL DATA OF HINTZ[60] --- THE ELASTIC SCATTERING OF 39.8 MeV PROTONS FROM ^{27}Al

FIT	a	b	c	d	e	f
V_o (MeV)	43.07	37.34	42.07	37.38	40.93	49.69
r_o (fm)	1.197	1.197	1.144	1.223	1.152	1.122
a_o (fm)	.6408	.7161	.6818	.6772	.7435	.6081
W_v (MeV)	0.0	7.785	4.570	6.584	9.763	0.0
r_v (fm)		1.400	1.386	1.460	1.485	
a_v (fm)		.6878	.6536	.6361	.5136	
W_s (MeV)	7.141	0.0	2.187	0.850	0.0	7.203
r_s (fm)	1.018		1.386	1.460		1.109
a_s (fm)	.7035		.6536	.6361		.6660
r_c (fm)	1.2	1.2	1.2	1.2	1.2	1.2
χ^2 (arb.)	6.5	9.4	10.8	5.9	7.3	12.7

Figure 4.1

Theoretical fit to the proton elastic scattering from ^{27}Al.

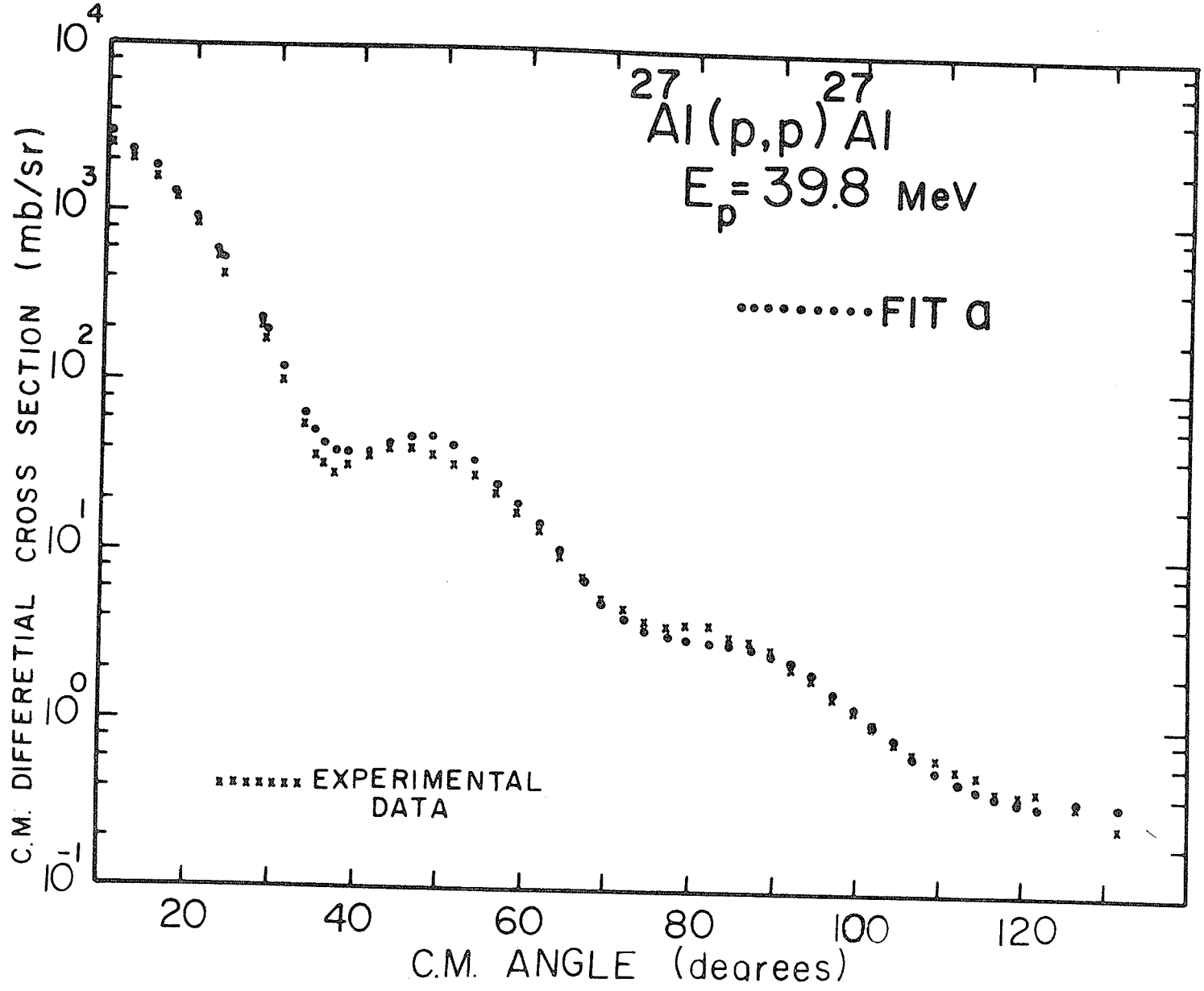
$^{27}Al(p,p)^{27}Al$
E_p= 39.8 MeV
.....FIT a
xxxxxxx EXPERIMENTAL DATA
C.M. DIFFERETIAL CROSS SECTION (mb/sr)
C.M. ANGLE (degrees)
10^4
10^3
10^2
10^1
10^0
10^{-1}
20
40
60
80
100
120

Figure 4.2

Theoretical fit to the proton elastic scattering from ^{27}Al.

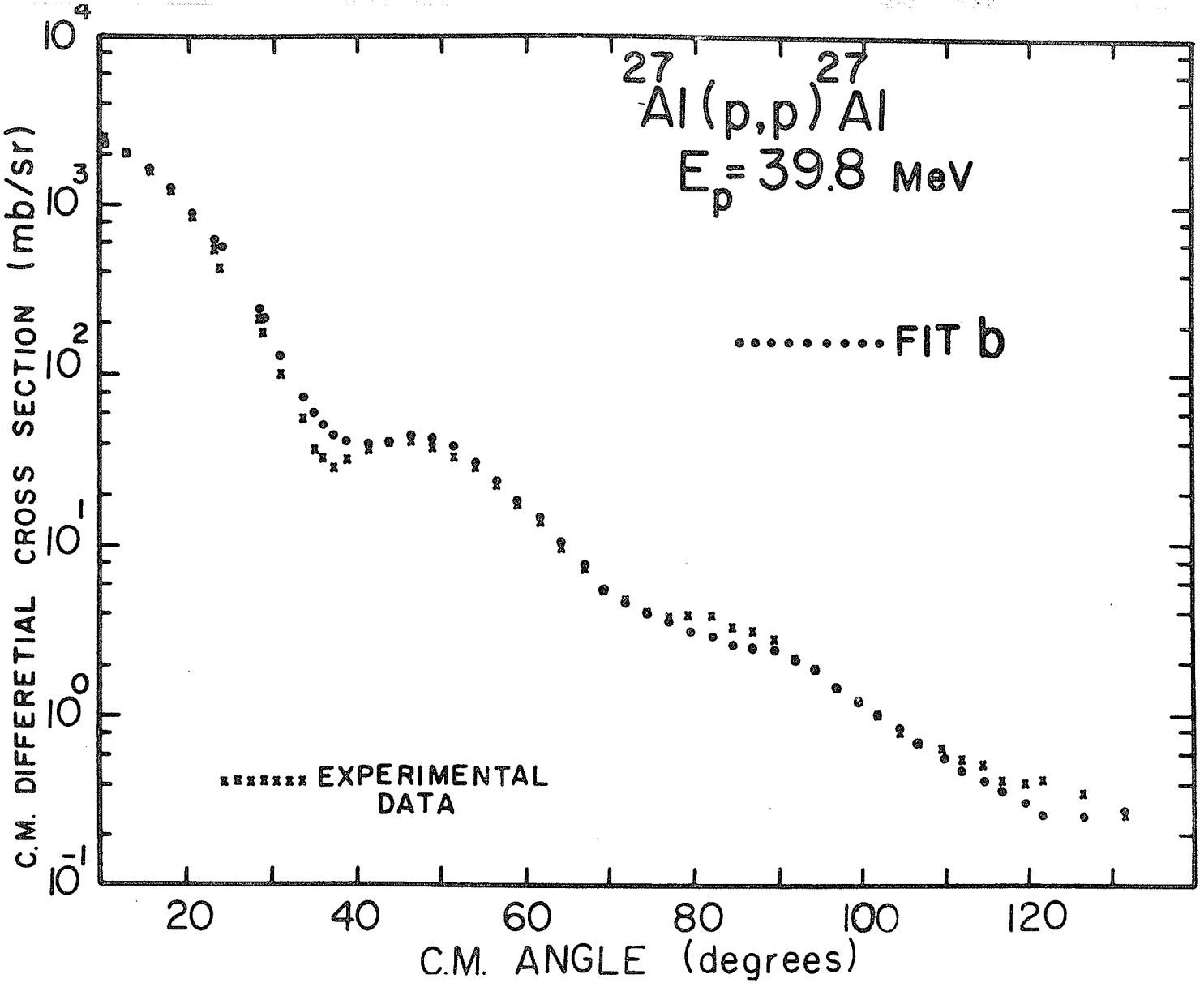
$^{27}Al(p,p)^{27}Al$
E_p= 39.8 MeV
FIT b
EXPERIMENTAL DATA
C.M. DIFFERETIAL CROSS SECTION (mb/sr)
C.M. ANGLE (degrees)
10^4
10^3
10^2
10^1
10^0
10^{-1}
20
40
60
80
100
120

Figure 4.3

Theoretical fit to the proton elastic scattering from ^{27}Al

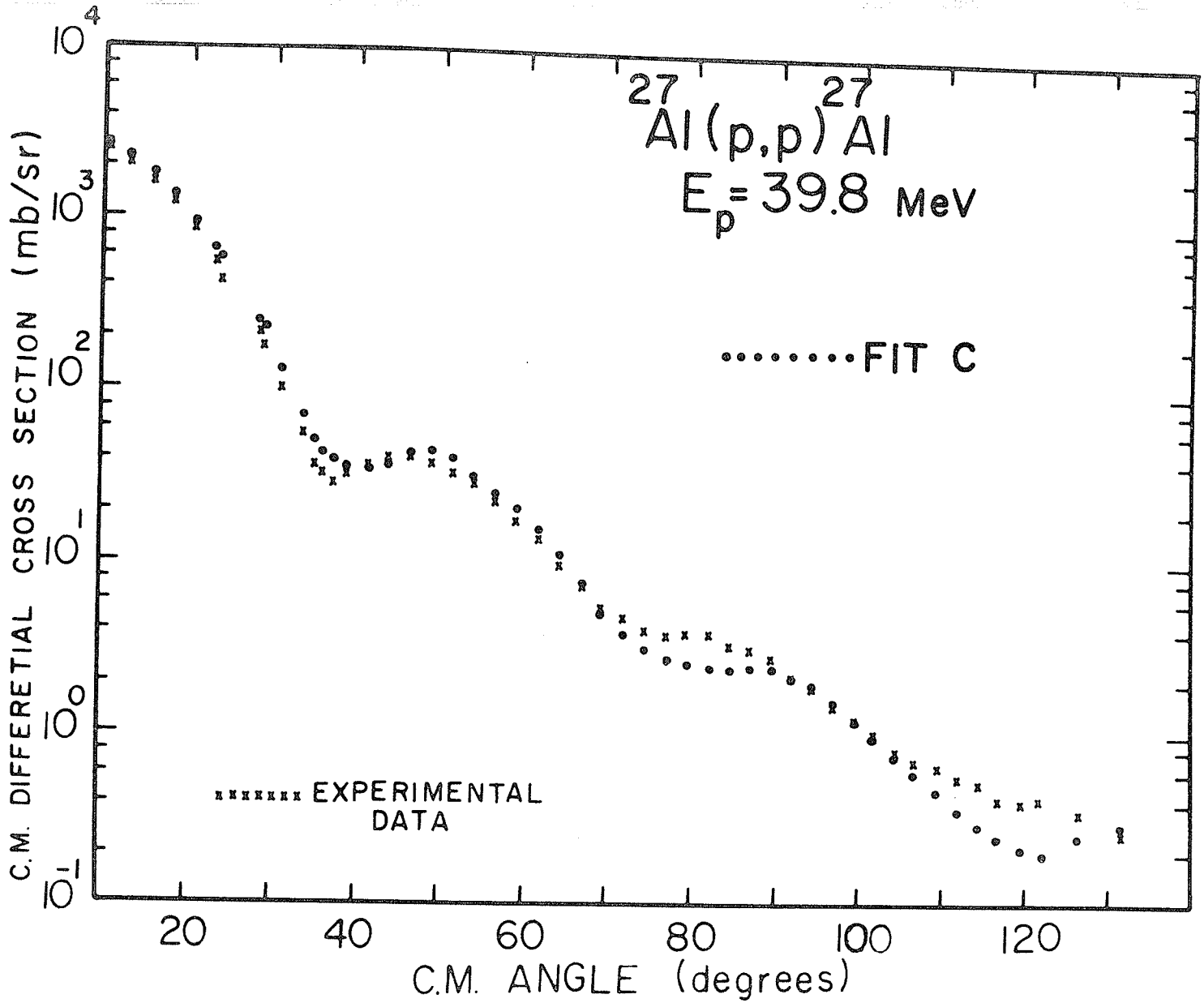
$^{27}Al(p,p)^{27}Al$
E_p=39.8 MeV
.....FIT C
xxxxxxx EXPERIMENTAL DATA
C.M. DIFFERETIAL CROSS SECTION (mb/sr)
C.M. ANGLE (degrees)
10^4
10^3
10^2
10^1
10^0
20
40
60
80
100
120

Figure 4.4

Theoretical fit to the proton elastic scattering from ^{27}Al.

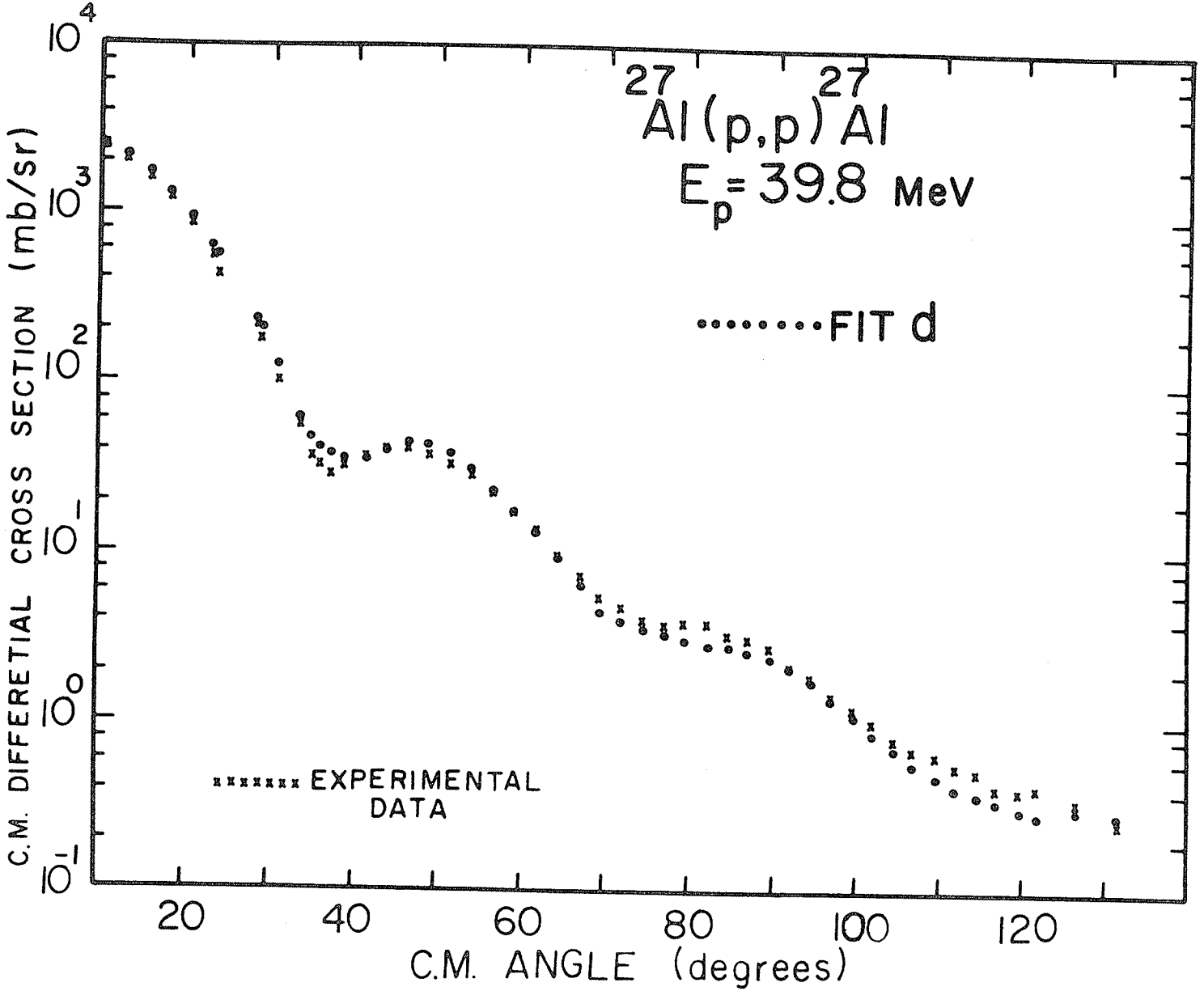
$^{27}Al(p,p)^{27}Al$
$E_p = 39.8$ MeV
.....FIT d
xxxxxxx EXPERIMENTAL DATA
C.M. DIFFERETIAL CROSS SECTION (mb/sr)
C.M. ANGLE (degrees)
10^4
10^3
10^2
10^1
10^0
10^{-1}
20
40
60
80
100
120

Figure 4.5

Theoretical fit to the proton elastic scattering from ^{27}Al.

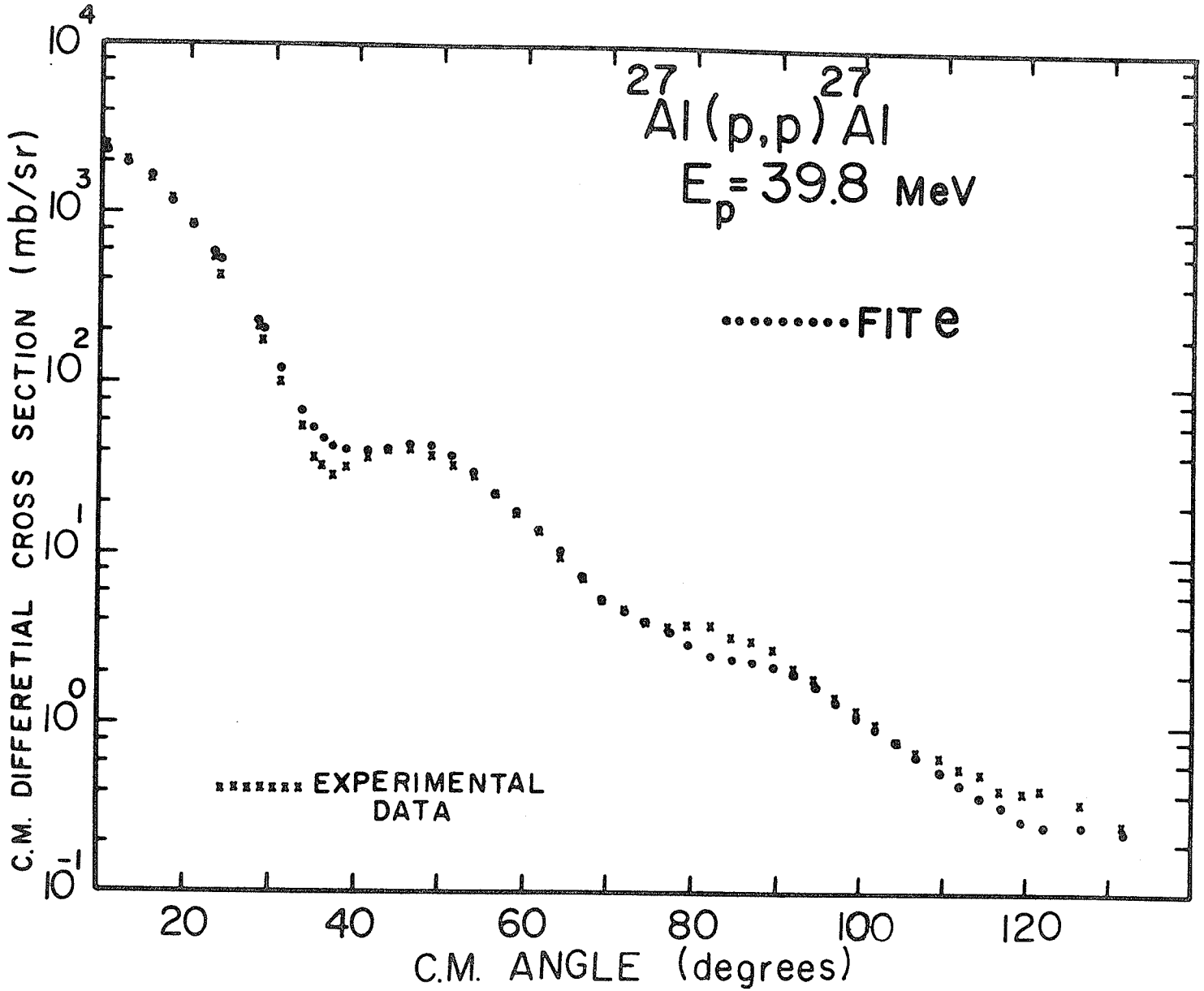
$^{27}Al(p,p)^{27}Al$
$E_p = 39.8$ MeV
FIT e
EXPERIMENTAL DATA
C.M. DIFFERETIAL CROSS SECTION (mb/sr)
C.M. ANGLE (degrees)
10^4
10^3
10^2
10^1
10^0
10^{-1}
20
40
60
80
100
120

Figure 4.6

Theoretical fit to the proton elastic scattering from ^{27}Al.

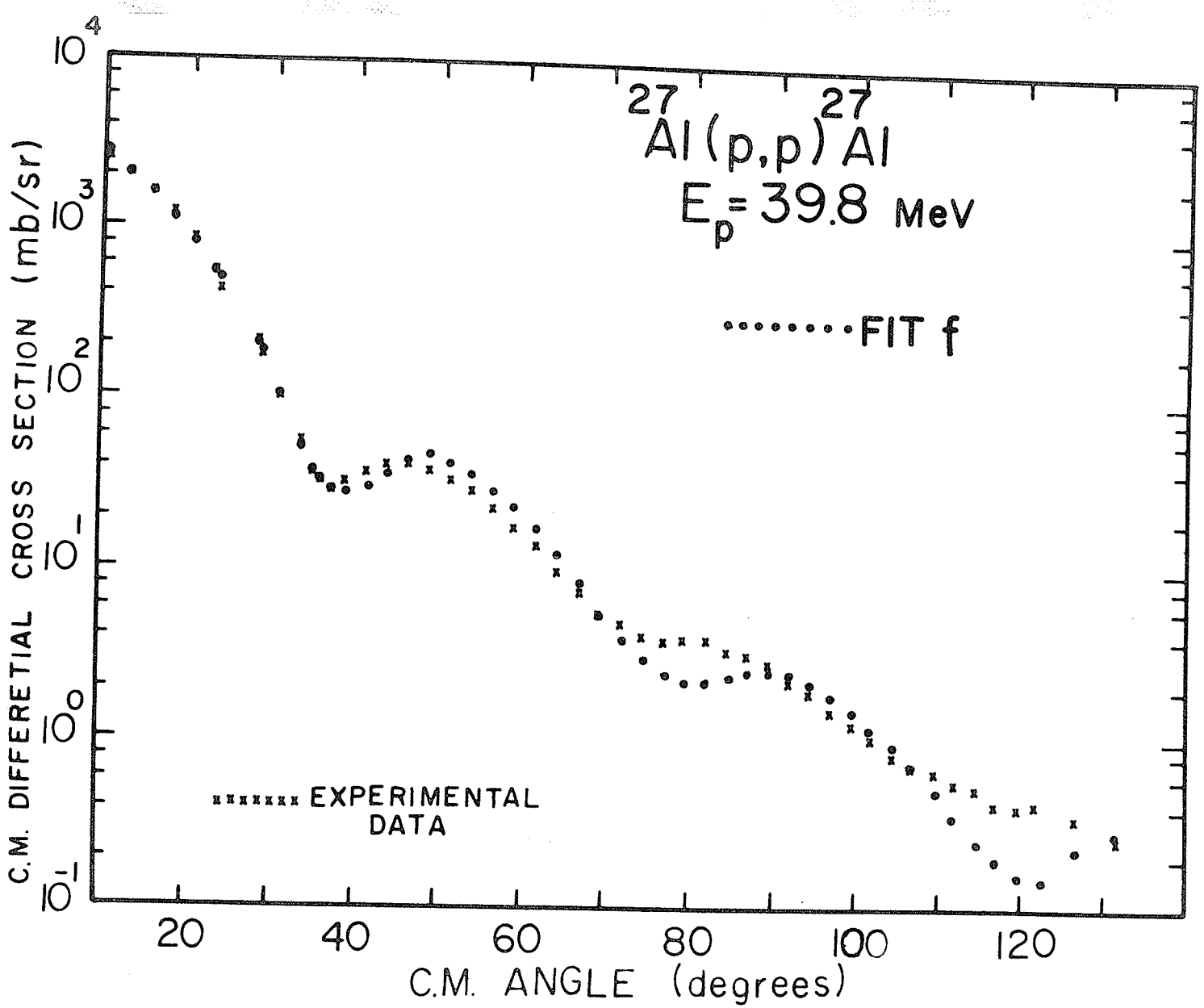
$^{27}Al(p,p)^{27}Al$
$E_p = 39.8$ MeV
FIT f
EXPERIMENTAL DATA
C.M. DIFFERETIAL CROSS SECTION (mb/sr)
C.M. ANGLE (degrees)
10^4
10^3
10^2
10^1
10^0
10^{-1}
20
40
60
80
100
120

These ambiguities are known to occur for composite particles[54] as a result of the wave function inside the nuclear potential containing extra half-waves. In fact, as one can note from the tabulated results, the real well potential depths giving χ^2 minima in the search routine differ by about 60 MeV. This has been previously observed[46].

Theoretically the real well depth for elastic scattering of composite particles, made up of n nucleons, is expected to be approximately n times the depth[52,53] obtained from analysis of single nucleon scattering data. Hence one expects the real well depth of the optical model parameters, giving the best fit to the (p,α) experimental results, to be approximately 200 MeV. Solutions having $V_\alpha \approx 200$ MeV and $V_\alpha \approx 200 \pm 60$ MeV were then used in the theoretical analysis with the hope that since the interior wave function is relatively more important for (p,α) reactions than it is for elastic alpha scattering one might be able to determine which V_α depth is the more valid one to use.

Results of optical model fits to the elastic scattering of alphas from ^{24}Mg are given in Table 4.2 and Figures 4.7-4.12.

In the attempt to fit the ^{27}Al(p,α)^{24}Mg data there are then left as free parameters the triton parameters and the choice of which set of best-fit optical parameters one can use. However we can severly restrict our choice of the proton optical parameters since the DWBA calculations are not very sensitive to them. We thus restrict our

Table 4.2

Tabulation of the optical parameters giving the best χ^2 fits to the elastic scattering of alphas from ^{24}Mg.

TABLE 4.2

OPTICAL PARAMETERS GIVING BEST FITS TO THE EXPERIMENTAL DATA OF BERKELEY[62] --- THE ELASTIC SCATTERING OF 50. MeV ALPHAS FROM ^{24}Mg

FIT	a	b	c	d	e	f
V_o (MeV)	138.11	197.56	262.44	135.83	190.28	253.19
r_o (fm)	1.444	1.406	1.387	1.461	1.430	1.423
a_o (fm)	.5366	.5179	.4982	.5493	.5224	.4918
W_v (MeV)	30.31	33.92	37.60	0.0	0.0	0.0
r_v (fm)	1.440	1.404	1.365			
a_v (fm)	.5721	.5093	.5116			
W_s (MeV)	0.0	0.0	0.0	46.52	59.85	60.11
r_s (fm)				1.363	1.353	1.341
a_s (fm)				.4060	.3737	.3817
r_c (fm)	1.4	1.4	1.4	1.4	1.4	1.4
χ^2 (arb.)	9.6	11.9	14.5	5.8	5.8	15.5

Figure 4.7

Theoretical fit to the alpha elastic scattering from ^{24}Mg.

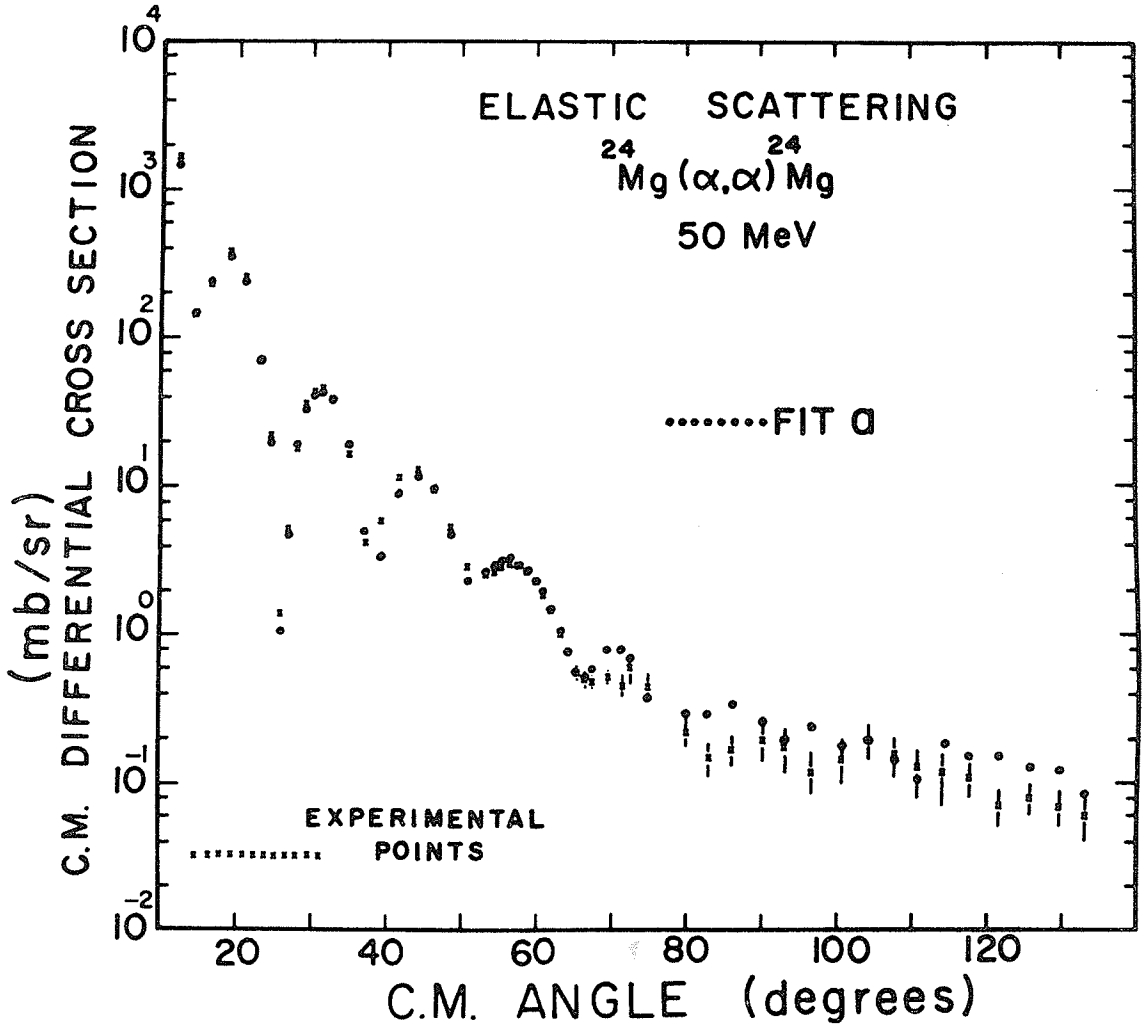
ELASTIC SCATTERING
$^{24}Mg(\alpha,\alpha)^{24}Mg$
50 MeV
FIT a
EXPERIMENTAL POINTS
C.M. DIFFERENTIAL CROSS SECTION (mb/sr)
C.M. ANGLE (degrees)
10^4
10^3
10^2
10^1
10^0
10^{-1}
10^{-2}
20
40
60
80
100
120

Figure 4.8

Theoretical fit to the alpha elastic scattering from ^{24}Mg.

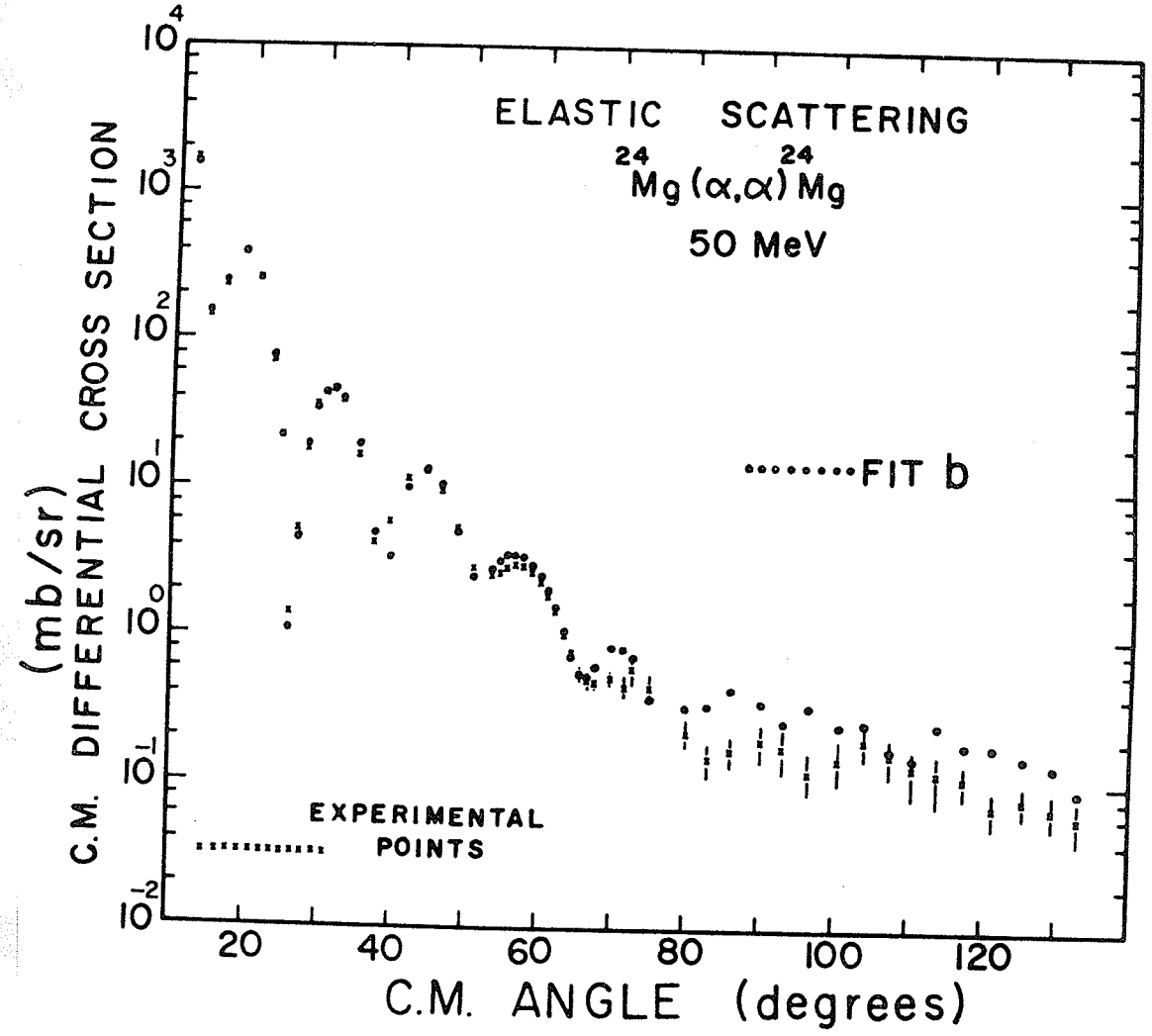
ELASTIC SCATTERING
24 24
Mg (α,α) Mg
50 MeV
FIT b
EXPERIMENTAL POINTS
C.M. DIFFERENTIAL CROSS SECTION (mb/sr)
C.M. ANGLE (degrees)
10^4
10^3
10^2
10^1
10^0
10^-1
10^-2
20
40
60
80
100
120

Figure 4.9

Theoretical fit to the alpha elastic scattering from ^{24}Mg.

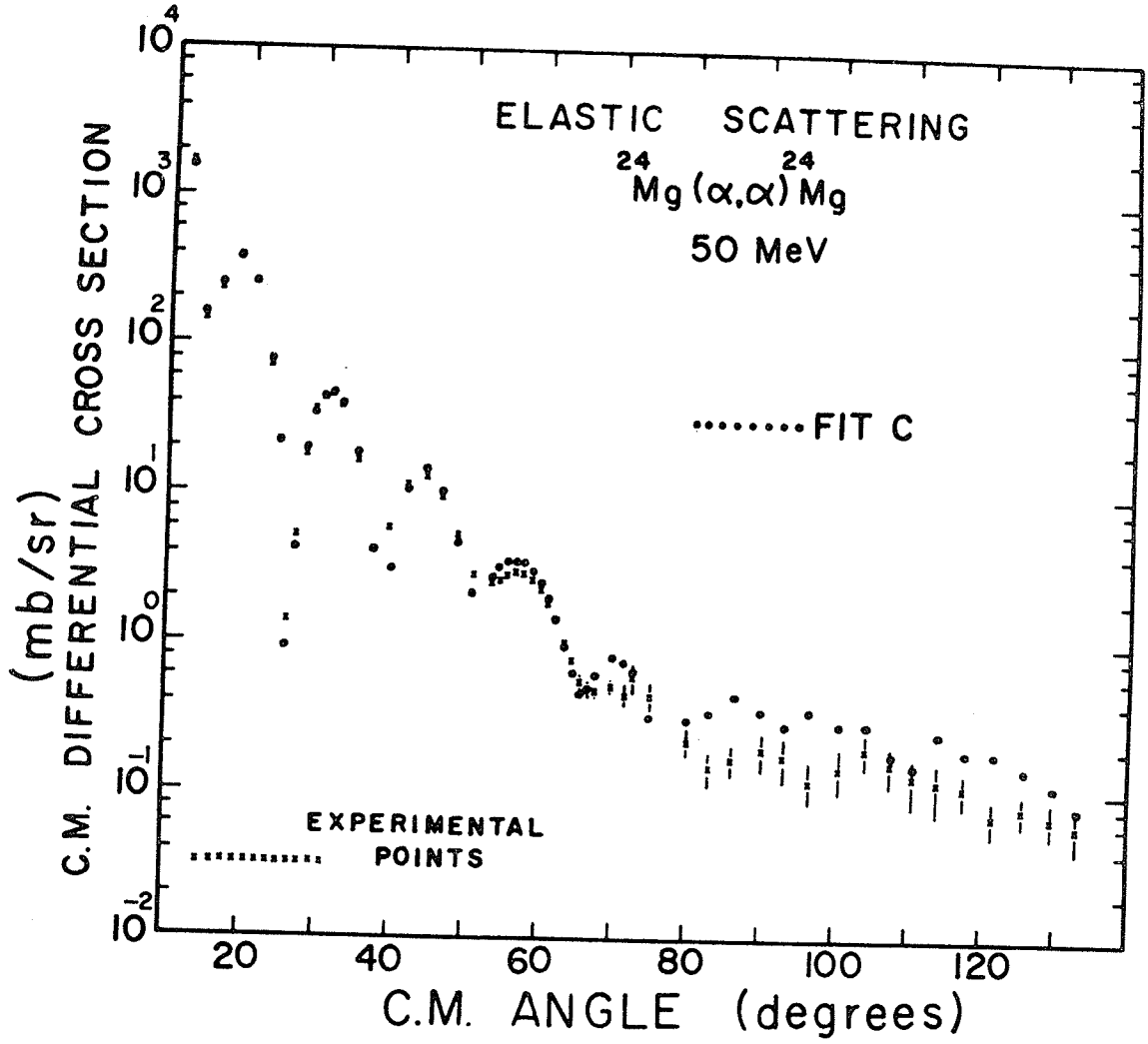
ELASTIC SCATTERING
$^{24}Mg(\alpha,\alpha)^{24}Mg$
50 MeV
FIT C
EXPERIMENTAL POINTS
C.M. DIFFERENTIAL CROSS SECTION (mb/sr)
C.M. ANGLE (degrees)
10^4
10^3
10^2
10^1
10^0
10^{-1}
10^{-2}
20
40
60
80
100
120

Figure 4.10

Theoretical fit to the alpha elastic scattering from ^{24}Mg.

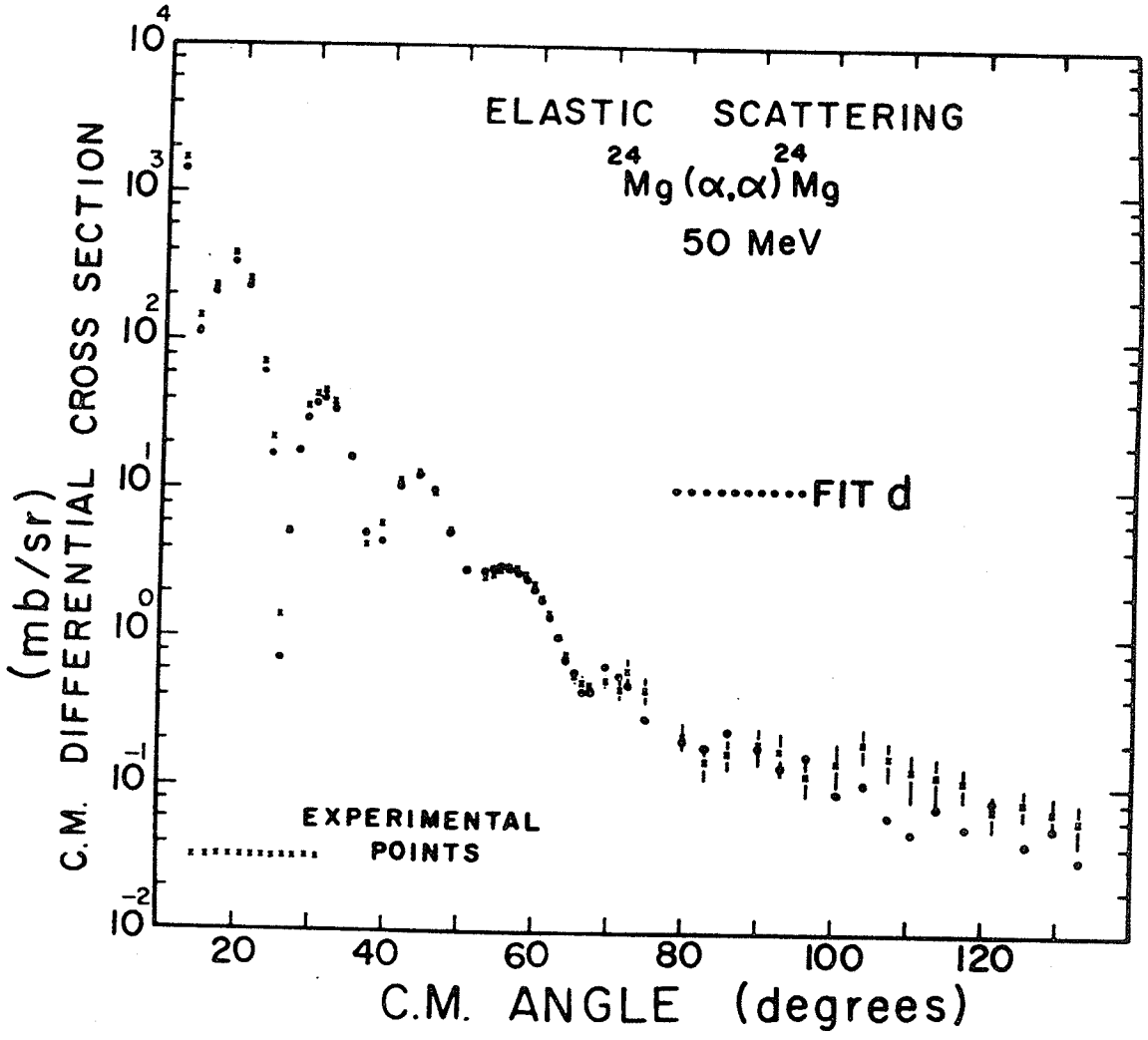
ELASTIC SCATTERING
$^{24}Mg(\alpha,\alpha)^{24}Mg$
50 MeV
FIT d
EXPERIMENTAL POINTS
C.M. DIFFERENTIAL CROSS SECTION (mb/sr)
C.M. ANGLE (degrees)
10^4
10^3
10^2
10^1
10^0
10^{-1}
10^{-2}
20
40
60
80
100
120

Figure 4.11

Theoretical fit to the alpha elastic scattering from ^{24}Mg.

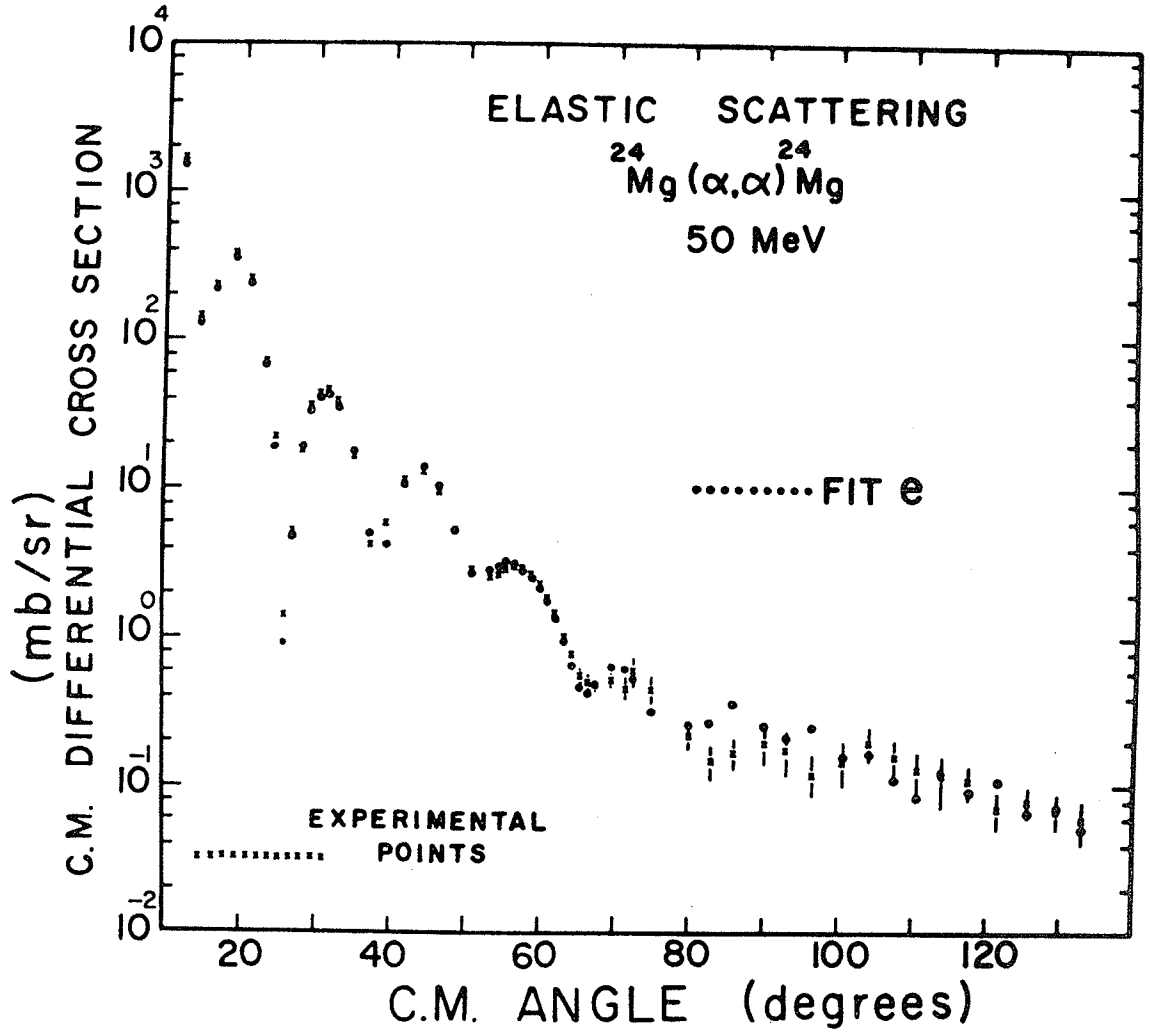
ELASTIC SCATTERING
$^{24}Mg(\alpha,\alpha)^{24}Mg$
50 MeV
FIT e
EXPERIMENTAL POINTS
C.M. DIFFERENTIAL CROSS SECTION (mb/sr)
C.M. ANGLE (degrees)
10^4
10^3
10^2
10^1
10^0
10^{-1}
10^{-2}
20
40
60
80
100
120

Figure 4.12

Theoretical fit to the alpha elastic scattering from ^{24}Mg.

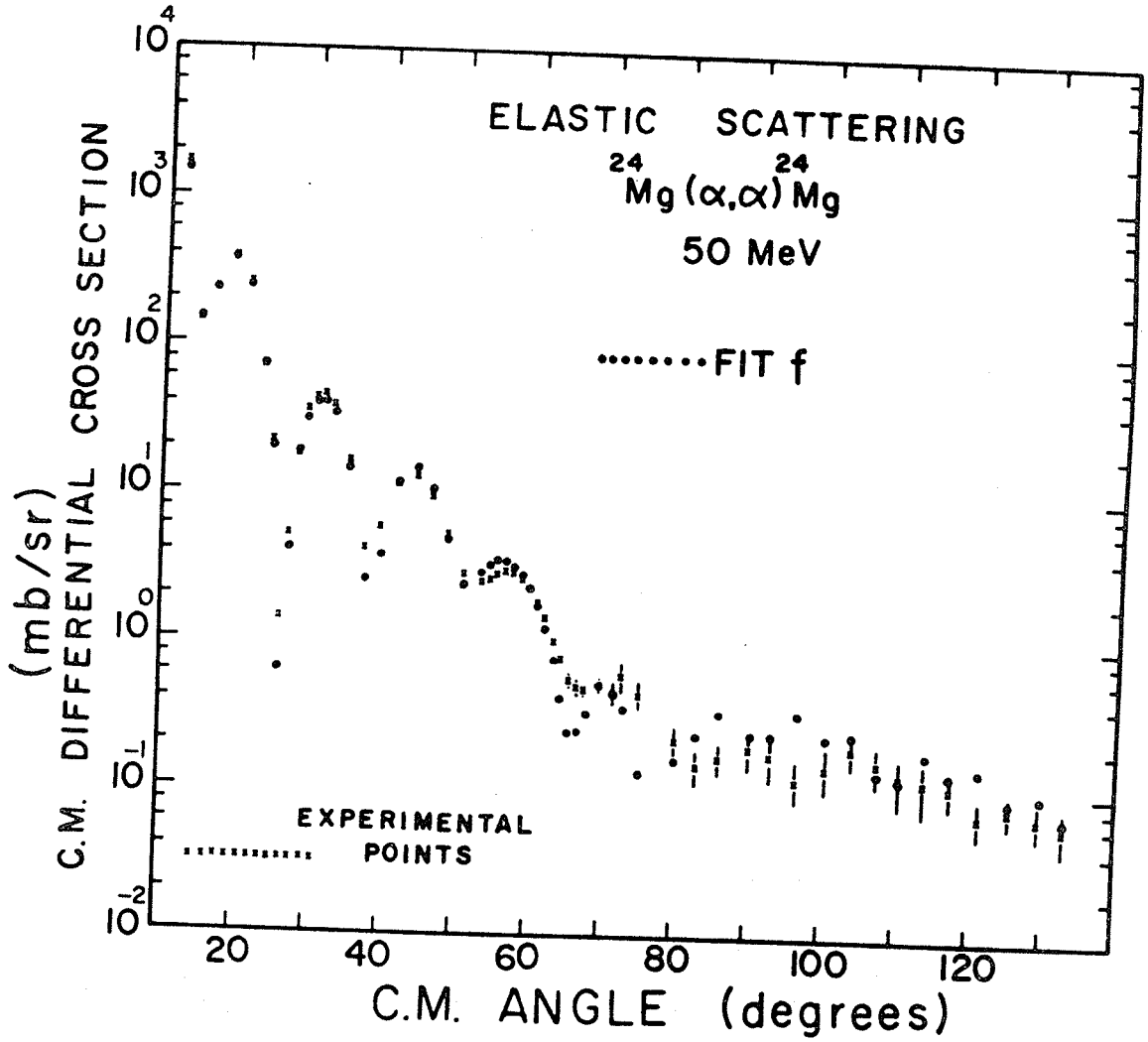
ELASTIC SCATTERING
24 24
Mg (α,α) Mg
50 MeV
FIT f
EXPERIMENTAL POINTS
C.M. DIFFERENTIAL CROSS SECTION (mb/sr)
C.M. ANGLE (degrees)
10^4
10^3
10^2
10^1
10^0
10^-1
10^-2
20
40
60
80
100
120

analysis to the only two natural choices one can make of all the sets of proton optical parameters, namely, one with pure volume absorption ($WD_p=0$), the other with pure surface absorption ($W_p=0$), each of which had the best χ^2 of all the sets of proton optical parameters.

As has been found in DWBA analysis of other (p,α) reactions[46], the calculations are much more sensitive to the alpha channel than for the proton channel optical parameters. This is illustrated for the three real potential well depth for the alpha channel of approximately 140, 200 and 260 MeV in Figure 4.13-4.15 respectively, wherein curves a and c have V_p = 43.07 MeV while curves b & d have V_p = 40.93 MeV. For each of these three Figures we see that we have essentially two sets of nearly overlapping curves. The two sets each have approximately the same V_α but one set has $WD_\alpha = 0$ while the other has $W_\alpha = 0$. This result unfortunately means that we cannot as yet decide on using either $W_\alpha = 0$ or $WD_\alpha = 0$ (since they give such different results) and we must try both cases in combination with any other variation we wish to make, such as those of the bound state parameters, in order to optimize our fit.

In order to find a suitable fit (s) to the experimental data, judged on the basis of shape (not the normalization, since this would be related to the experimental spectroscopic factor which is to be later compared to the theoretical one) we preformed a manual search of both bound state parameters r_t and a_t over a grid of values

Figure 4.13

The effect on the DWBA calculations resulting from using different sets of proton and alpha optical parameters.

	a	b	c	d	
V_p =	43.07	40.93	43.07	40.93	MeV
V_α =	138.11	138.11	135.83	135.83	MeV

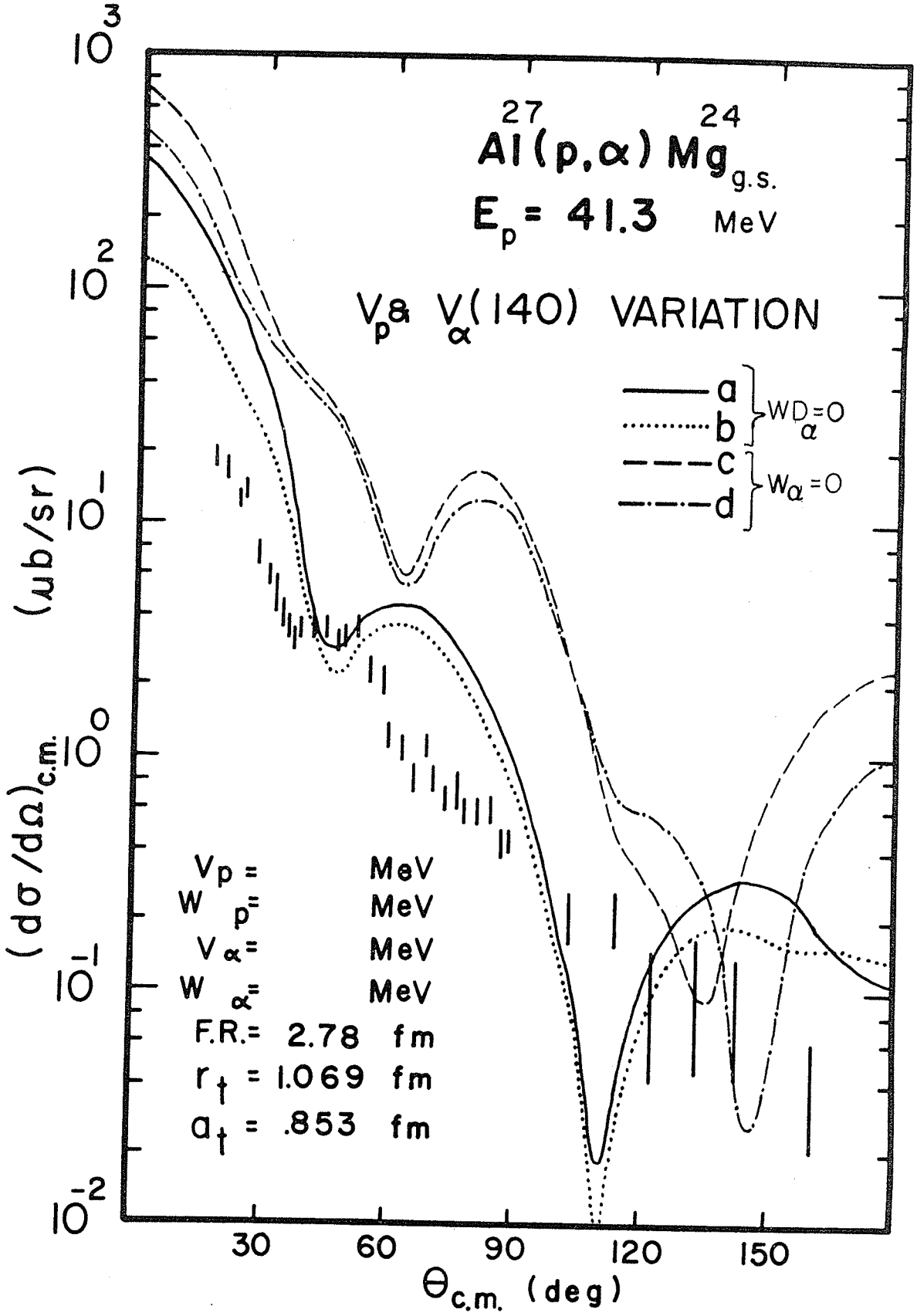
$^{27}Al(p,\alpha)\,^{24}Mg_{g.s.}$
E_p = 41.3 MeV
V_p& V_α(140) VARIATION
a
b
W_α=0
c
d
W_α=0
V_p = MeV
W_p = MeV
V_α = MeV
W_α = MeV
F.R.= 2.78 fm
r_t = 1.069 fm
a_t = .853 fm
$(d\sigma/d\Omega)_{c.m.}$ (μb/sr)
$\theta_{c.m.}$ (deg)
10^3
10^2
10^1
10^0
10^{-1}
10^{-2}
30
60
90
120
150

Figure 4.14

The effect on the DWBA calculations resulting from using different sets of proton and alpha optical parameters.

	a	b	c	d	
V_p =	43.07	40.93	43.07	40.93	MeV
V_α =	197.56	197.56	190.28	190.28	MeV

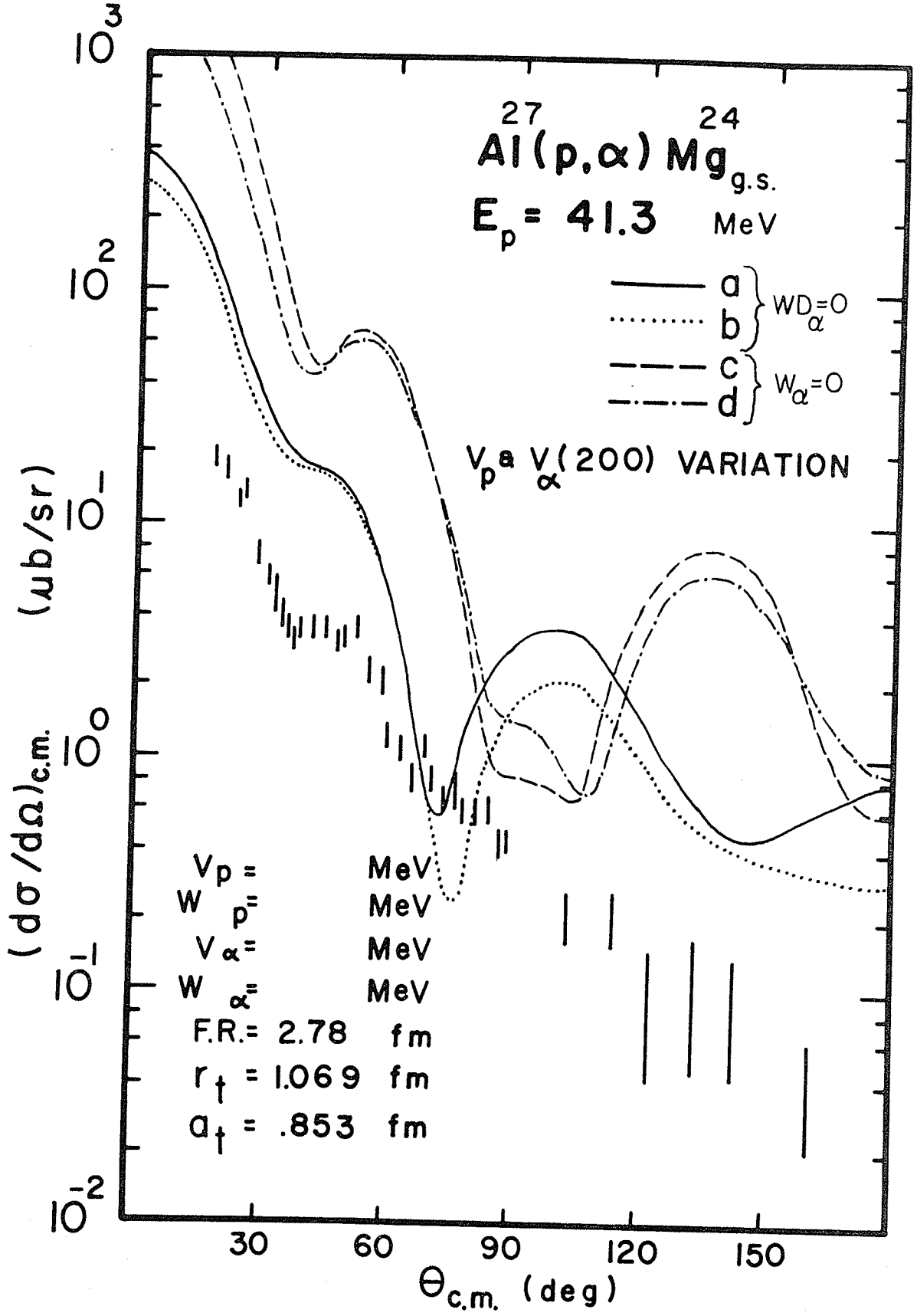
$^{27}Al(p,\alpha)\,^{24}Mg_{g.s.}$
E_p = 41.3 MeV
a
b
WD_α=0
c
d
W_α=0
V_p & V_α(200) VARIATION
V_p = MeV
W_p = MeV
V_α = MeV
W_α = MeV
F.R.= 2.78 fm
r_t = 1.069 fm
a_t = .853 fm
$(d\sigma/d\Omega)_{c.m.}$ (μb/sr)
10^3
10^2
10^1
10^0
10^{-1}
10^{-2}
30
60
90
120
150
$\theta_{c.m.}$ (deg)

Figure 4.15

The effect on the DWBA calculations resulting from the use of different sets of proton and alpha optical parameters.

	a	b	c	d	
V_p =	43.07	40.93	43.07	43.07	Mev
V_α =	253.2	253.2	262.4	262.4	Mev

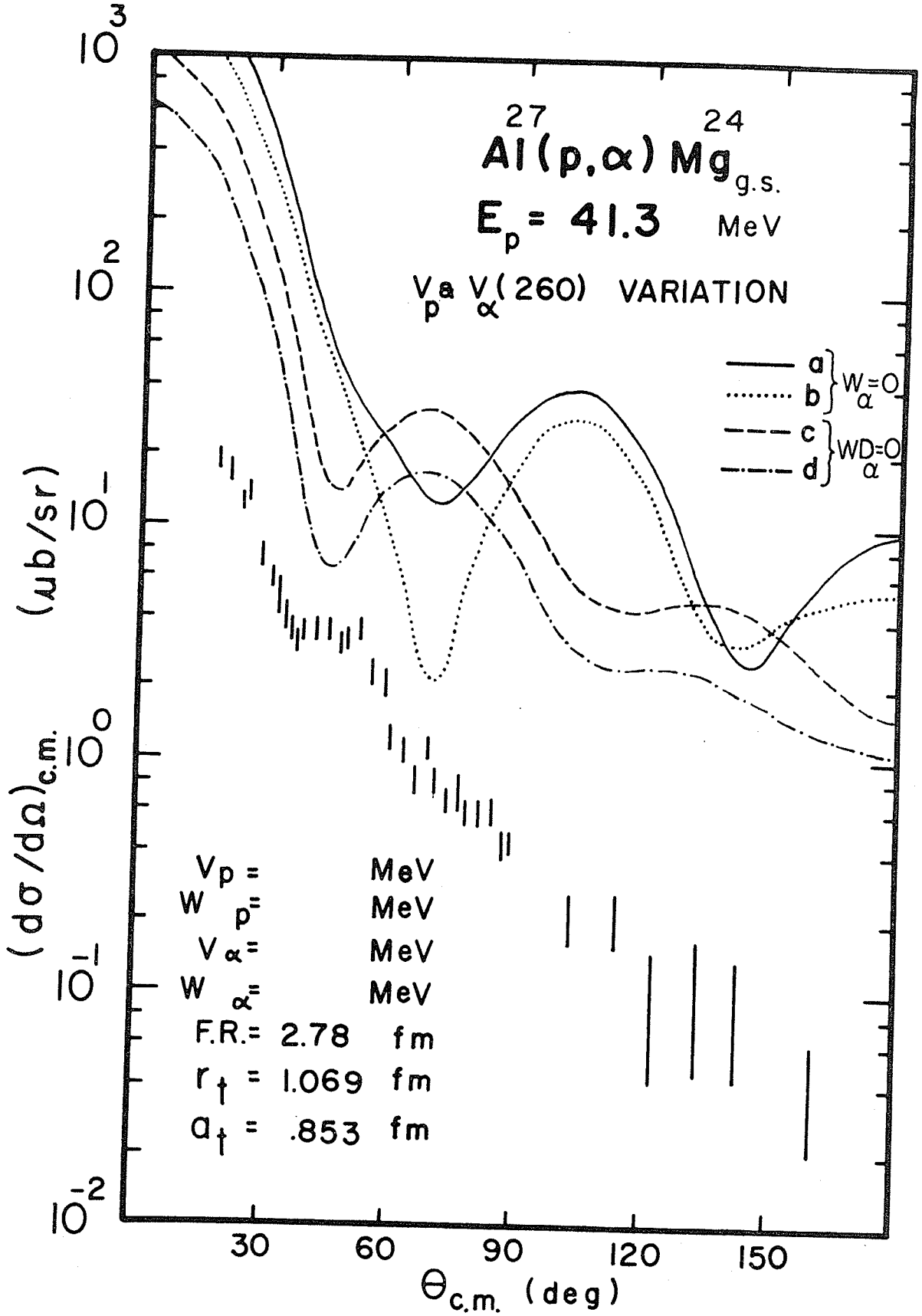
$^{27}Al(p,\alpha)\,^{24}Mg_{g.s.}$
E_p = 41.3 MeV
V_p & V_α (260) VARIATION
a
b
W_α=0
c
d
WD_α=0
V_p = MeV
W_p = MeV
V_α = MeV
W_α = MeV
F.R.= 2.78 fm
r_t = 1.069 fm
a_t = .853 fm
$(d\sigma/d\Omega)_{c.m.}$ (μb/sr)
10^3
10^2
10^1
10^0
10^{-1}
10^{-2}
30
60
90
120
150
$\Theta_{c.m.}$ (deg)

$$r_t = 1.0 - 1.4 \text{ (fm)}$$
$$a_t = .4 - .9$$

for each of the six sets of alpha channel optical parameters in combination with the two sets for the proton channel parameters.

A computor plot and (r_t, a_t) cycling routine which was added to the existing DWBA code [66] greatly facilitated this search.

Little or no systematic trends could be established from the variation of r_t and a_t. In general, however, the peaks and valleys in the theoretical angular distribution moved towards the forward angles with increasing r_t or a_t.

Early in the analysis it was realized that one could not "force" a fit to the experimental results by simple variation of r_t, a_t and the choice of which set of proton optical parameters one used. It became clear that for a good fit one must use a particular set(s) of alpha optical parameters.

Figures 4.16-4.19 illustrate both the relative insensitivity of our choice of the set of proton parameters as well as the failure of r_t and a_t variation to provide a good fit for the case $V_\alpha \approx 200$ MeV, $W_\alpha = 0$.

Figures 4.20-4.23 illustrate variations in the theoretical angular distributions caused by changing r_t and a_t when we had $V_\alpha \approx 140$ MeV, $W_\alpha = 0$ (Figures 4.20-4.21) and when we had $V_\alpha \approx 140$ MeV, $WD_\alpha = 0$ (Figures 4.22-4.23). A good fit could not be obtained for these alpha channel optical parameters.

Figure 4.16

The effect of varying the bound state parameter r_t on the theoretical angular distribution

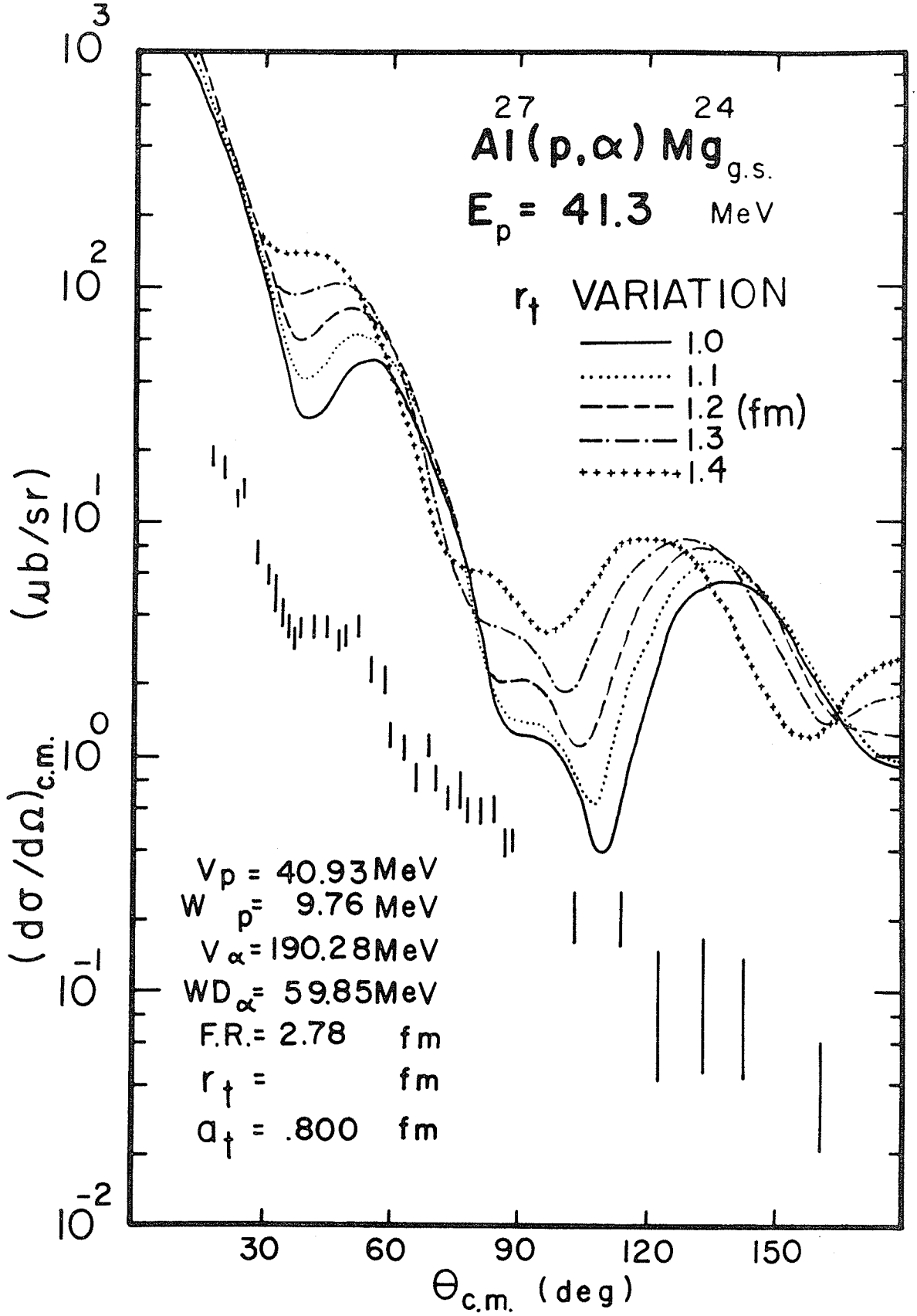
$^{27}Al(p,\alpha)\,^{24}Mg_{g.s.}$
E_p = 41.3 MeV
r_t VARIATION
1.0
1.1
1.2 (fm)
1.3
1.4
Vp = 40.93 MeV
W p= 9.76 MeV
V α = 190.28 MeV
WD α = 59.85 MeV
F.R. = 2.78 fm
r_t = fm
a_t = .800 fm
$(d\sigma/d\Omega)_{c.m.}$ (μb/sr)
10^3
10^2
10^1
10^0
10^{-1}
10^{-2}
30
60
90
120
150
$\Theta_{c.m.}$ (deg)

Figure 4.17

The effect of varying the bound state parameters a_t on the theoretical angular distribution.

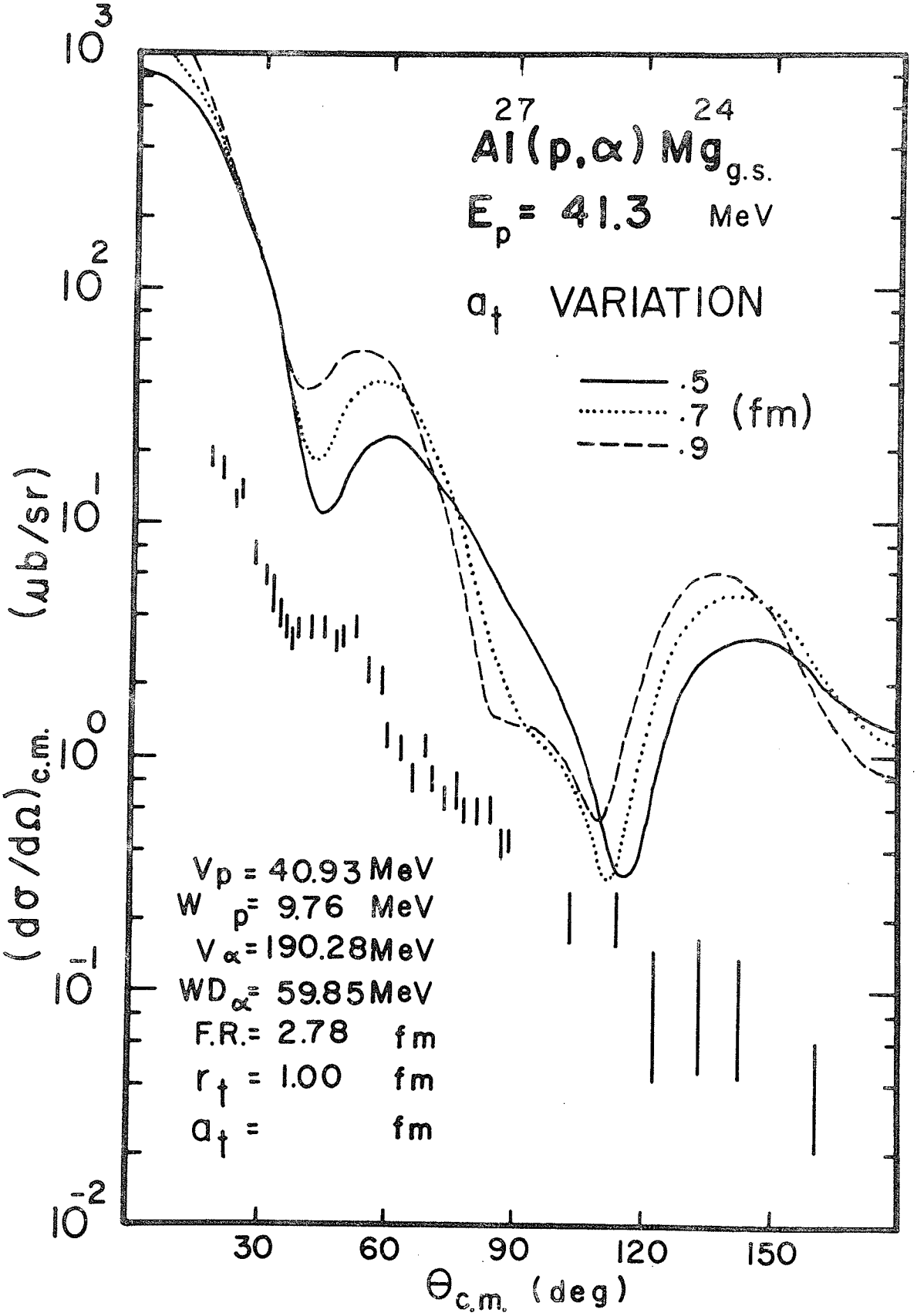
$^{27}Al(p,\alpha)\,^{24}Mg_{g.s.}$
E_p = 41.3 MeV
a_t VARIATION
.5
.7 (fm)
.9
V_p = 40.93 MeV
W_p = 9.76 MeV
V_α = 190.28 MeV
WD_α = 59.85 MeV
F.R. = 2.78 fm
r_t = 1.00 fm
a_t = fm
$(d\sigma/d\Omega)_{c.m.}$ (mb/sr)
$\theta_{c.m.}$ (deg)
10^3
10^2
10^1
10^0
10^{-1}
10^{-2}
30
60
90
120
150

Figure 4.18

The effect of varying the bound state parameters r_t on the theoretical angular distribution

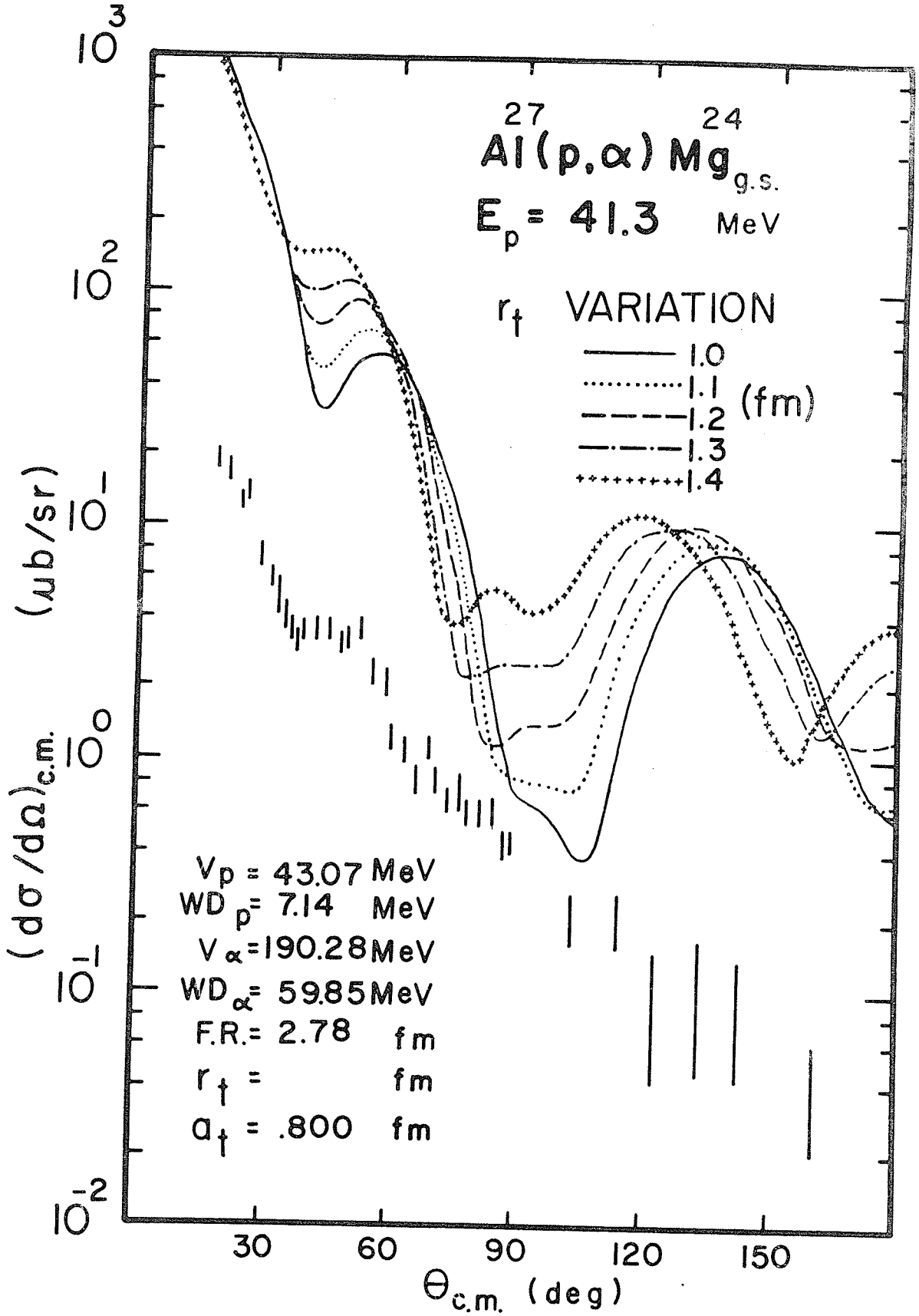
$^{27}Al(p,\alpha)\,^{24}Mg_{g.s.}$
E_p = 41.3 MeV
r_t VARIATION
1.0
1.1 (fm)
1.2
1.3
1.4
V_p = 43.07 MeV
WD_p = 7.14 MeV
V_α = 190.28 MeV
WD_α = 59.85 MeV
F.R. = 2.78 fm
r_t = fm
a_t = .800 fm
$(d\sigma/d\Omega)_{c.m.}$ (μb/sr)
10^3
10^2
10^1
10^0
10^{-1}
10^{-2}
30
60
90
120
150
$\Theta_{c.m.}$ (deg)

Figure 4.19

The effect of varying the bound state parameters a_t on the theoretical angular distribution.

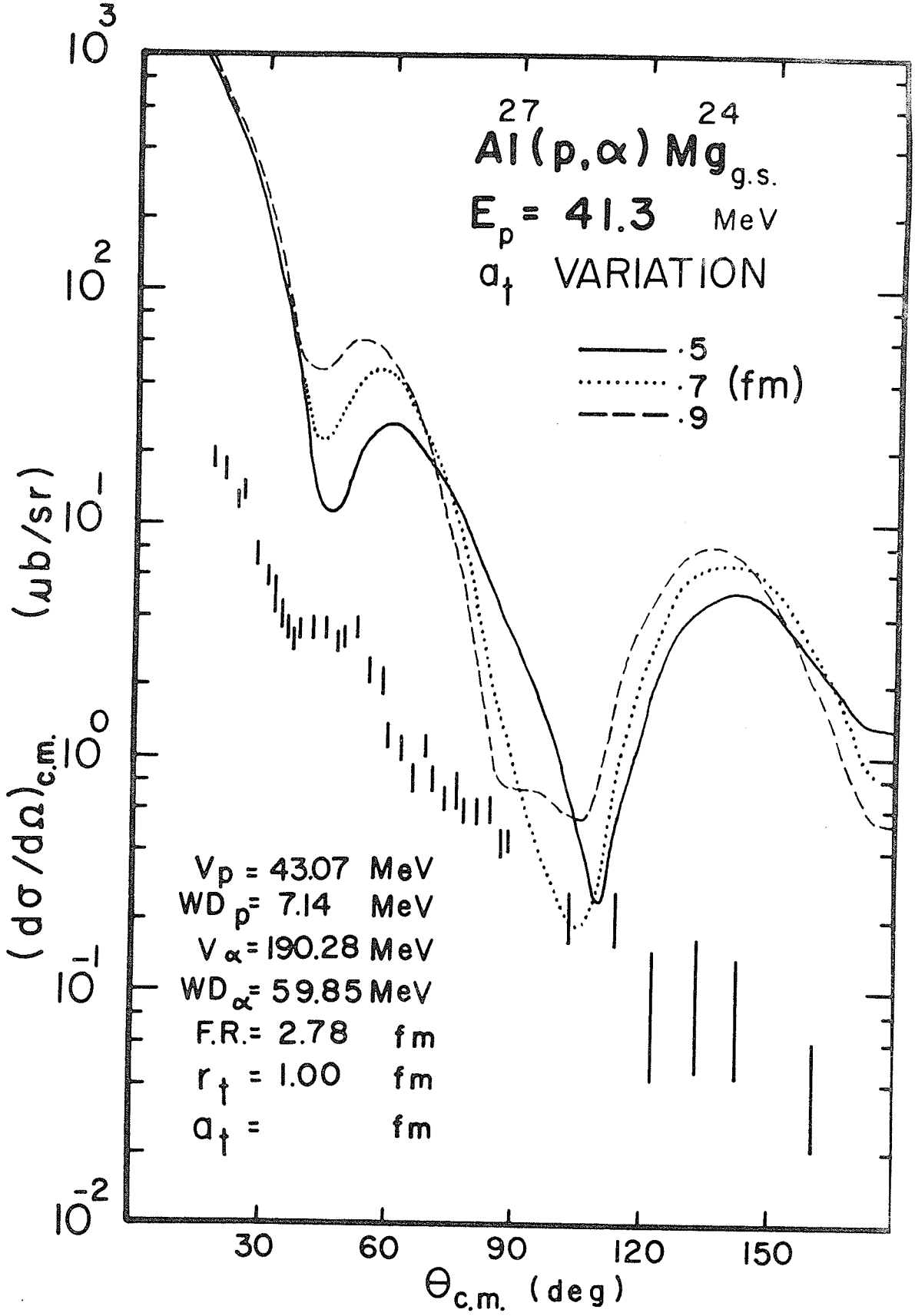
$^{27}Al(p,\alpha)\,^{24}Mg_{g.s.}$
E_p = 41.3 MeV
a_t VARIATION
.5
.7 (fm)
.9
V_p = 43.07 MeV
WD_p = 7.14 MeV
V_α = 190.28 MeV
WD_α = 59.85 MeV
F.R. = 2.78 fm
r_t = 1.00 fm
a_t = fm
$(d\sigma/d\Omega)_{c.m.}$ (μb/sr)
$\theta_{c.m.}$ (deg)
10^3
10^2
10^1
10^0
10^{-1}
10^{-2}
30
60
90
120
150

Figure 4.20

The effect of varying the bound state parameters r_t on the theoretical angular distribution.

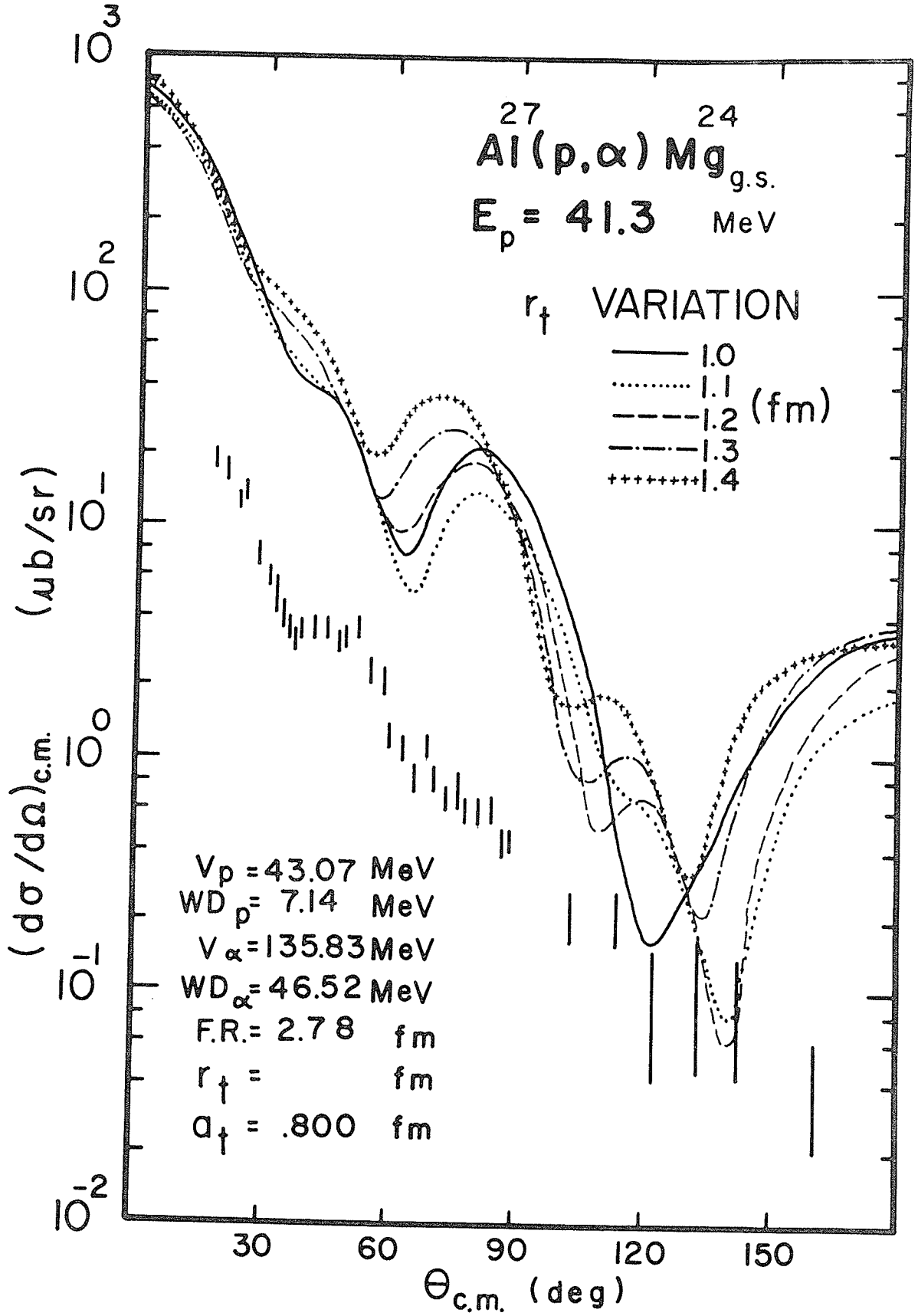
$^{27}Al(p,\alpha)\,^{24}Mg_{g.s.}$
E_p = 41.3 MeV
r_t VARIATION
1.0
1.1
1.2 (fm)
1.3
1.4
V_p = 43.07 MeV
WD_p = 7.14 MeV
V_α = 135.83 MeV
WD_α = 46.52 MeV
F.R. = 2.78 fm
r_t = fm
a_t = .800 fm
$(d\sigma/d\Omega)_{c.m.}$ (mb/sr)
$\Theta_{c.m.}$ (deg)
10^3
10^2
10^1
10^0
10^{-1}
10^{-2}
30
60
90
120
150

Figure 4.21

The effect of varying the bound state parameters a_t on the theoretical angular distribution

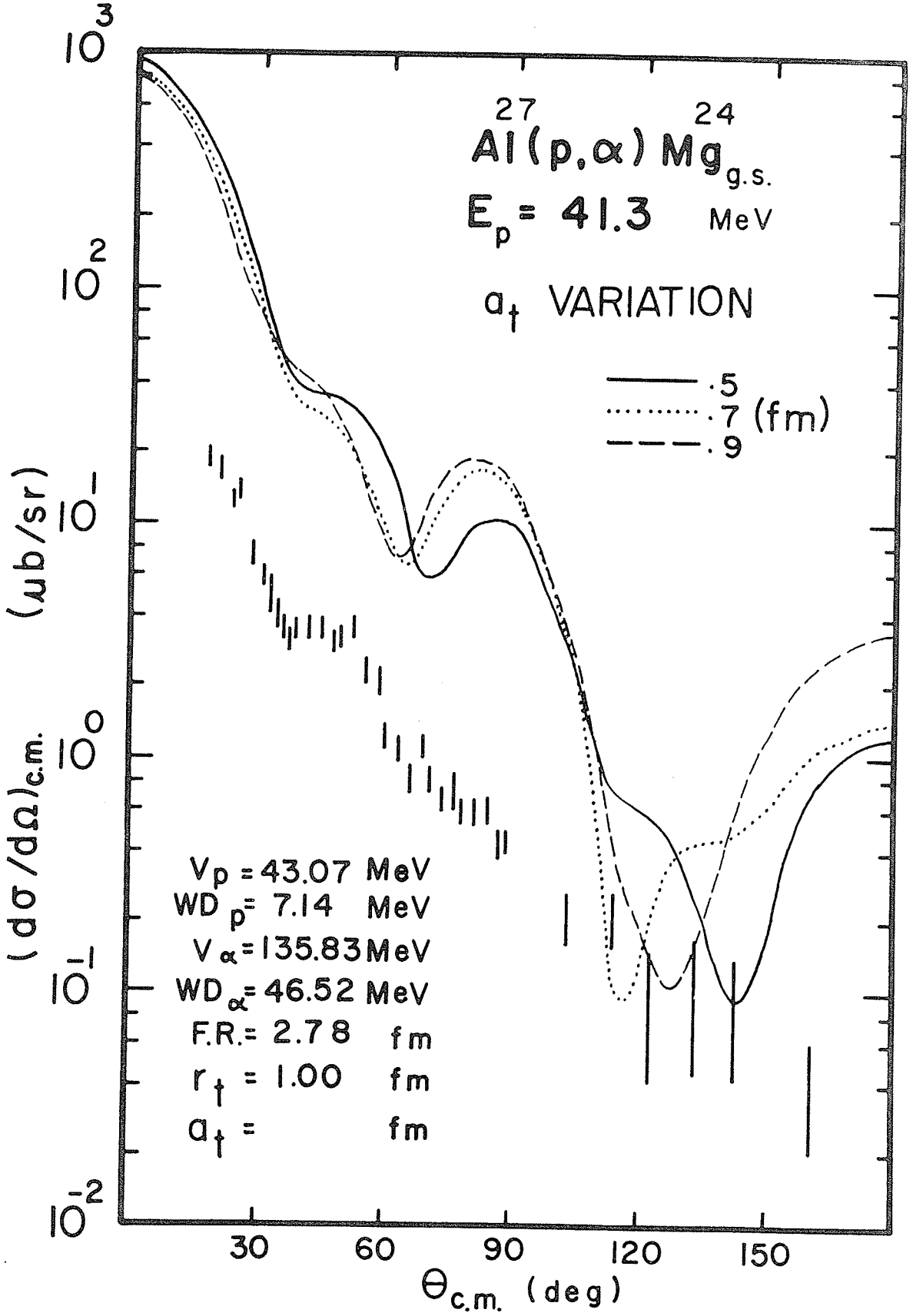
$^{27}Al(p,\alpha)\,^{24}Mg_{g.s.}$
E_p = 41.3 MeV
a_t VARIATION
.5
.7 (fm)
.9
V_p = 43.07 MeV
WD_p = 7.14 MeV
V_α = 135.83 MeV
WD_α = 46.52 MeV
F.R. = 2.78 fm
r_t = 1.00 fm
a_t = fm
$(d\sigma/d\Omega)_{c.m.}$ (μb/sr)
$\theta_{c.m.}$ (deg)
10^3
10^2
10^1
10^0
10^{-1}
10^{-2}
30
60
90
120
150

Figure 4.22

The effect of varying the bound state parameters r_t on the theoretical angular distribution

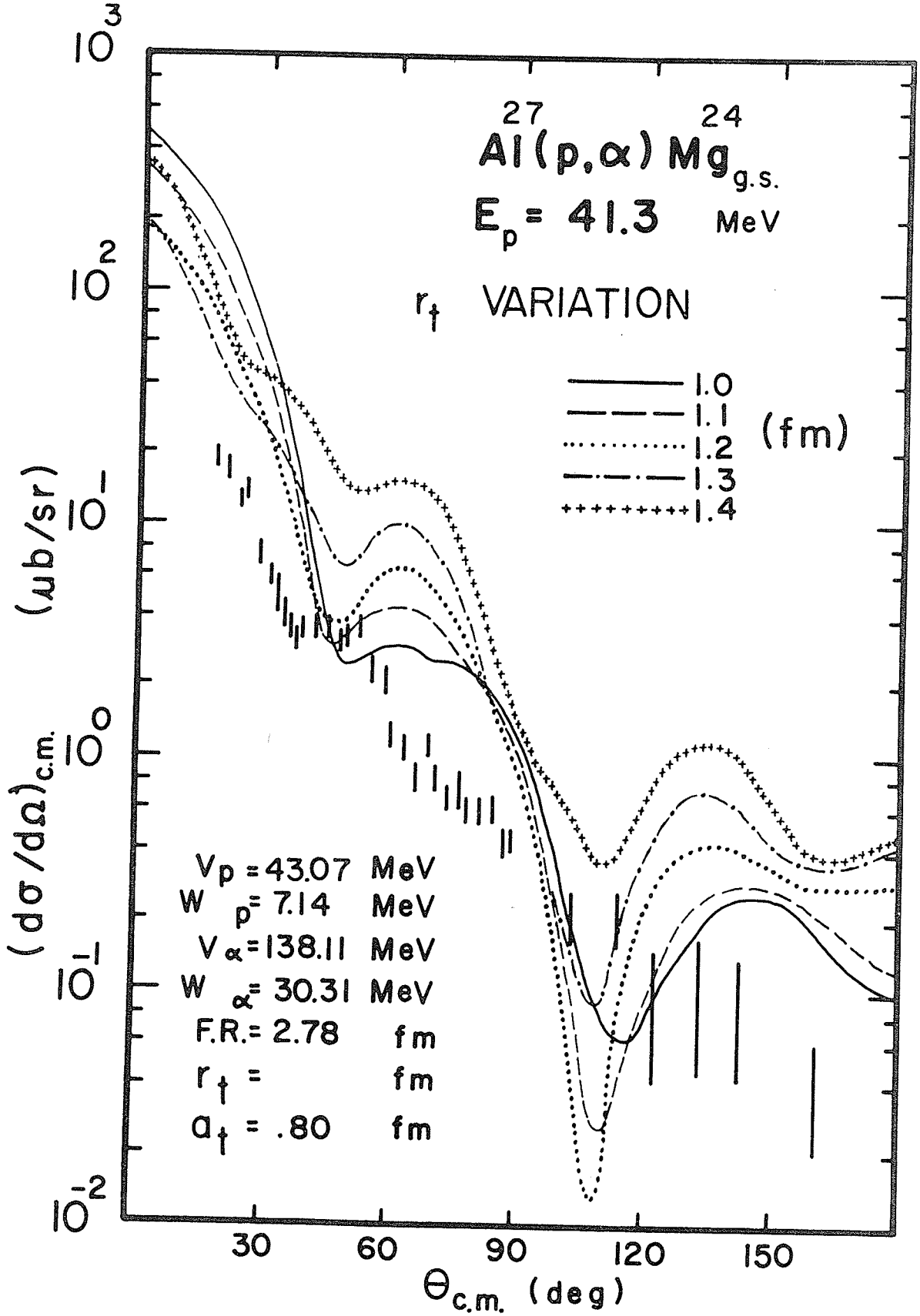
$^{27}Al(p,\alpha)\,^{24}Mg_{g.s.}$
E_p = 41.3 MeV
r_t VARIATION
1.0
1.1
1.2
1.3
1.4
(fm)
V_p = 43.07 MeV
W_p = 7.14 MeV
V_α = 138.11 MeV
W_α = 30.31 MeV
F.R. = 2.78 fm
r_t = fm
a_t = .80 fm
$(d\sigma/d\Omega)_{c.m.}$ (μb/sr)
$\theta_{c.m.}$ (deg)
10^3
10^2
10^1
10^0
10^{-1}
10^{-2}
30
60
90
120
150

Figure 4.23

The effect of varying the bound state parameter a_t on the theoretical angular distribution.

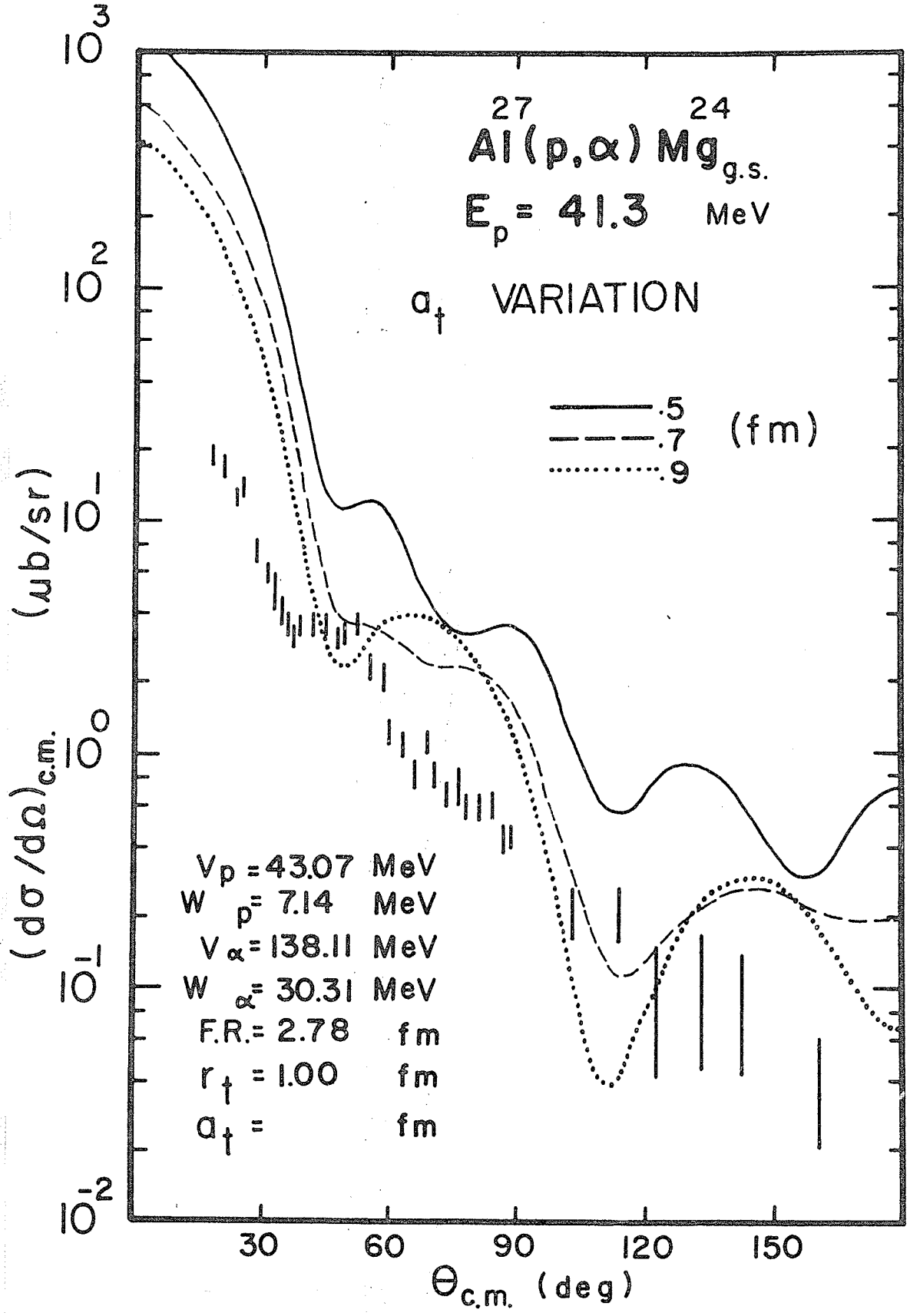
$^{27}Al(p,\alpha)\,^{24}Mg_{g.s.}$
E_p = 41.3 MeV
a_t VARIATION
.5
.7
.9
(fm)
V_p = 43.07 MeV
W_p = 7.14 MeV
V_α = 138.11 MeV
W_α = 30.31 MeV
F.R. = 2.78 fm
r_t = 1.00 fm
a_t = fm
$(d\sigma/d\Omega)_{c.m.}$ (μb/sr)
10^3
10^2
10^1
10^0
10^{-1}
10^{-2}
30
60
90
120
150
$\theta_{c.m.}$ (deg)

Figures 4.24-4.27 illustrate the same thing for $V_\alpha \approx 260$ MeV, $W_\alpha = 0$ and for $V_\alpha \approx 260$ MeV, $WD_\alpha = 0$. However, since the latter case showed some promise of making a suitable fit near $r_t = 1.00$ fm, $a_t = .5$ fm we tried the alternate proton set of optical parameters as well. The result is illustrated in Figures 4.28-4.29 and shows that although the fit is still unsatisfactory it is somewhat better than we had previously obtained.

For the case $V_\alpha \approx 200$ MeV and $WD_\alpha = 0$ we encountered our first satisfactory fit (Figures 4.30-4.31) for $r_t = 1.00$ fm, $a_t = .6$ fm. The alternate set of proton optical parameters improved this fit somewhat (Figures 4.32-4.33).

Now that we had isolated the "correct" set of alpha channel optical parameters we performed a somewhat finer r_t, a_t, grid search. The resultant best fit together with the ones we initially considered are shown in Figure 4.34. The corresponding parameters are tabulated in Table 4.3.

The experimental spectroscopic factor one obtains from fit C is

$$S_{EXP} = \frac{\sigma_{EXP}}{1.93 \quad \sigma_{Th}} = \frac{30 \pm 7}{1.93(228)} = .068 \pm .016$$

where the 1.93 is due to the finite range correction.

It should be remarked that in order to ensure that the above (fit C) was the only acceptable fit one could obtain, we performed an r_t, a_t grid variation over both sets of proton channel optical parameters in combination with all sets of alpha channel optical parameters. No better fit was found.

Figure 4.24

The effect of varying the bound state parameters r_t on the theoretical angular distribution.

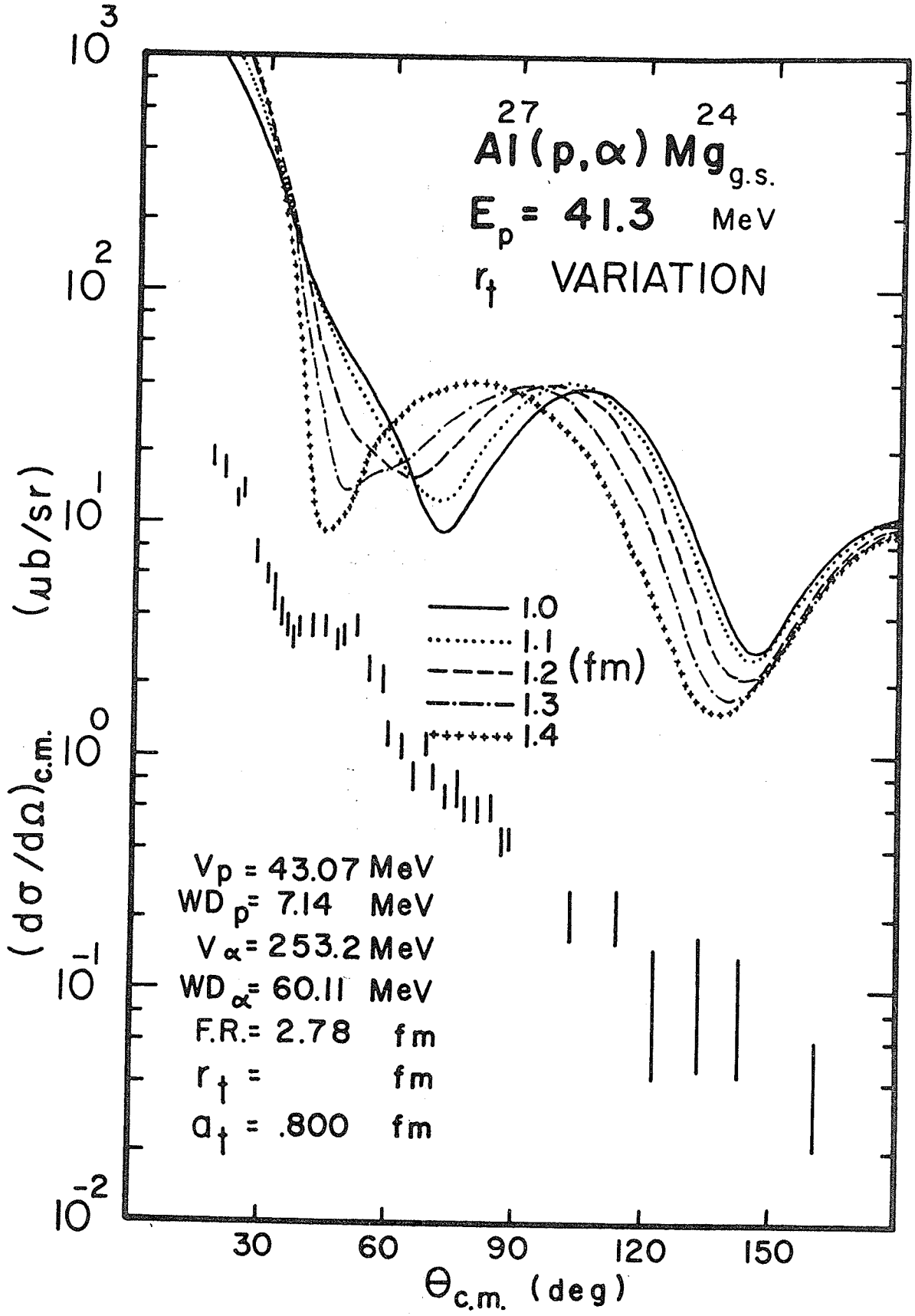
$^{27}Al(p,\alpha)\,^{24}Mg_{g.s.}$
E_p = 41.3 MeV
r_t VARIATION
1.0
1.1
1.2 (fm)
1.3
1.4
V_p = 43.07 MeV
WD_p = 7.14 MeV
V_α = 253.2 MeV
WD_α = 60.11 MeV
F.R. = 2.78 fm
r_t = fm
a_t = .800 fm
$(d\sigma/d\Omega)_{c.m.}$ (μb/sr)
$\theta_{c.m.}$ (deg)
10^3
10^2
10^1
10^0
10^{-1}
10^{-2}
30
60
90
120
150

Figure 4.25

The effect of varying the bound state parameter a_t on the theoretical angular distribution.

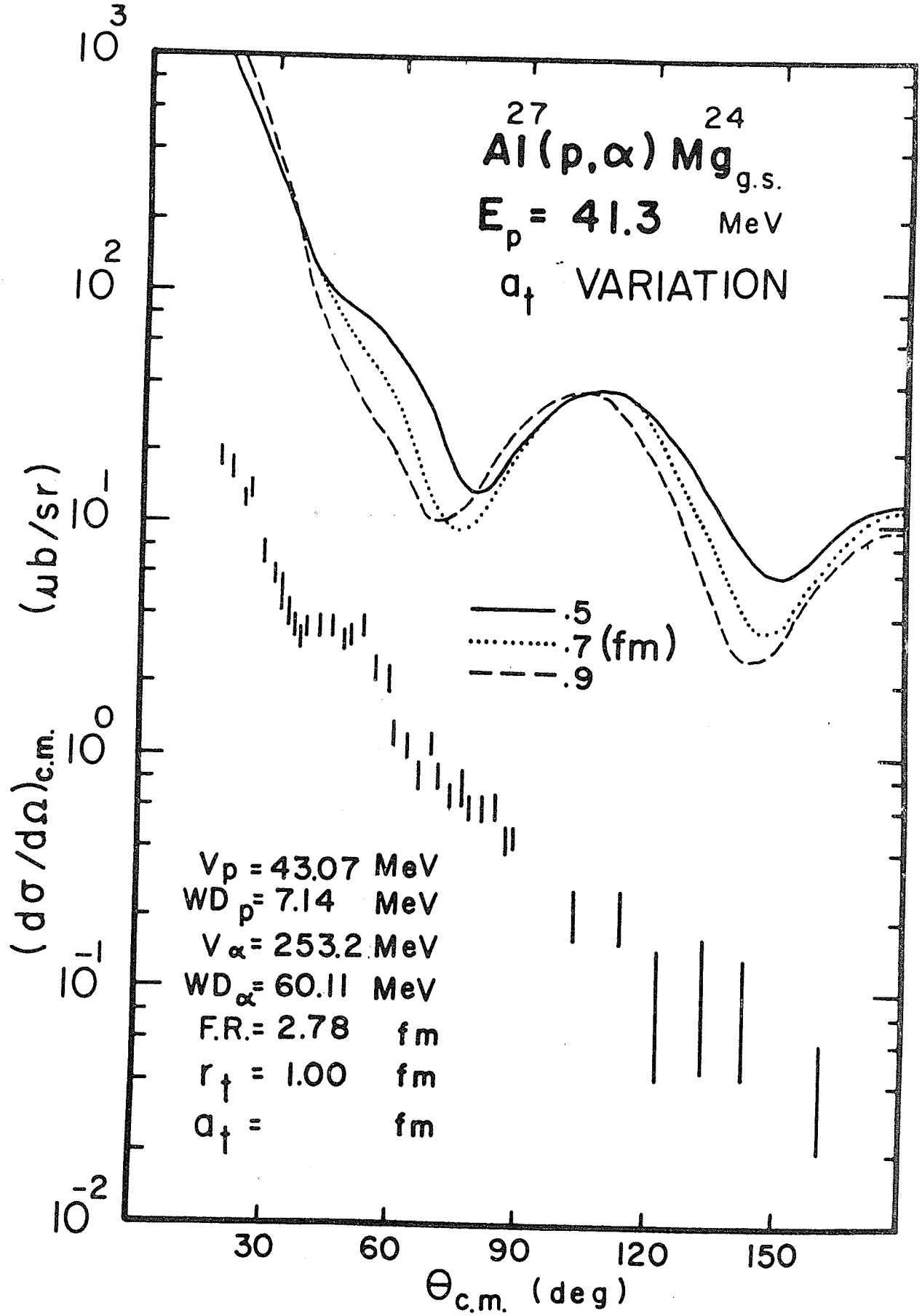
$^{27}Al(p,\alpha)\,^{24}Mg_{g.s.}$
E_p = 41.3 MeV
a_t VARIATION
.5
.7 (fm)
.9
V_p = 43.07 MeV
WD_p = 7.14 MeV
V_α = 253.2 MeV
WD_α = 60.11 MeV
F.R. = 2.78 fm
r_t = 1.00 fm
a_t = fm
$(d\sigma/d\Omega)_{c.m.}$ (μb/sr)
$\theta_{c.m.}$ (deg)
10^3
10^2
10^1
10^0
10^{-1}
10^{-2}
30
60
90
120
150

Figure 4.26

The effect of varying the bound state parameter r_t on the theoretical angular distribution.

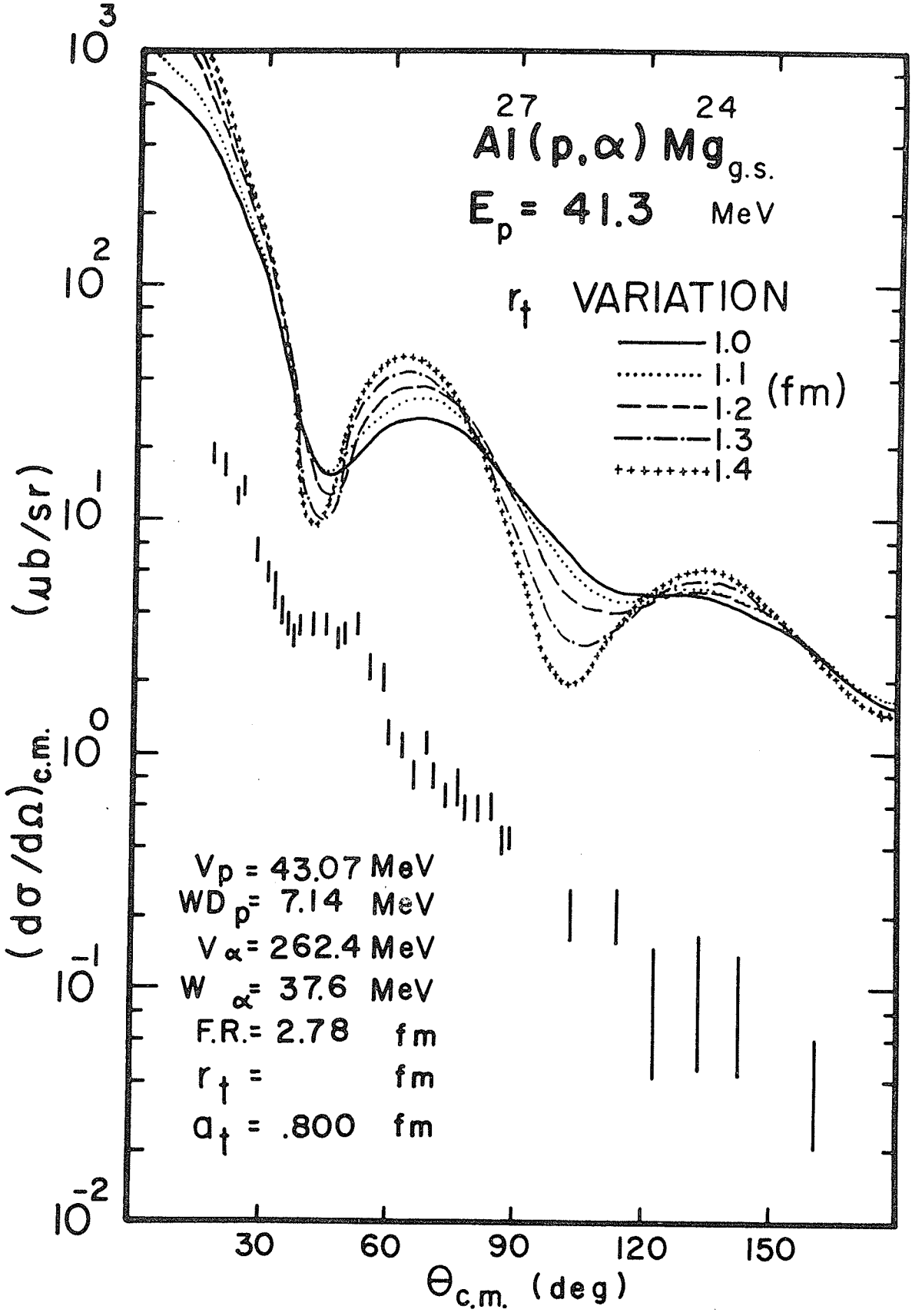
$^{27}Al(p,\alpha)\,^{24}Mg_{g.s.}$
E_p = 41.3 MeV
r_t VARIATION
1.0
1.1
1.2
1.3
1.4
(fm)
V_p = 43.07 MeV
WD_p = 7.14 MeV
V_α = 262.4 MeV
W_α = 37.6 MeV
F.R. = 2.78 fm
r_t = fm
a_t = .800 fm
$(d\sigma/d\Omega)_{c.m.}$ (μb/sr)
10^3
10^2
10^1
10^0
10^{-1}
10^{-2}
30
60
90
120
150
$\Theta_{c.m.}$ (deg)

Figure 4.27

The effect of varying the bound state parameter a_t on the theoretical angular distribution.

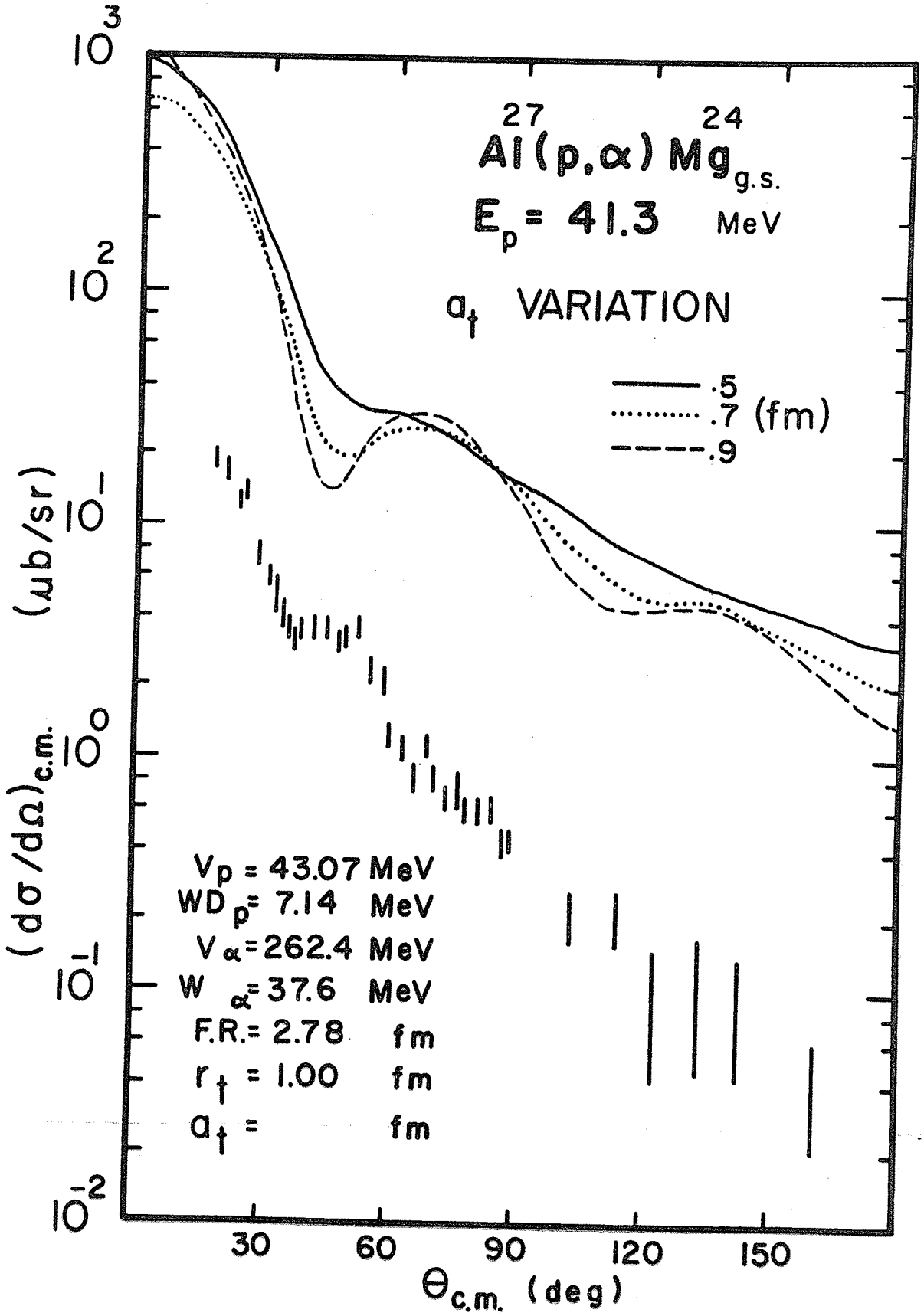
$^{27}Al(p,\alpha)\,^{24}Mg_{g.s.}$
E_p = 41.3 MeV
a_t VARIATION
.5
.7 (fm)
.9
V_p = 43.07 MeV
WD_p = 7.14 MeV
V_α = 262.4 MeV
W_α = 37.6 MeV
F.R. = 2.78 fm
r_t = 1.00 fm
a_t = fm
$(d\sigma/d\Omega)_{c.m.}$ (μb/sr)
$\theta_{c.m.}$ (deg)
10^3
10^2
10^1
10^0
10^{-1}
10^{-2}
30
60
90
120
150

Figure 4.28

The effect of varying the bound state parameter r_t on the theoretical angular distribution.

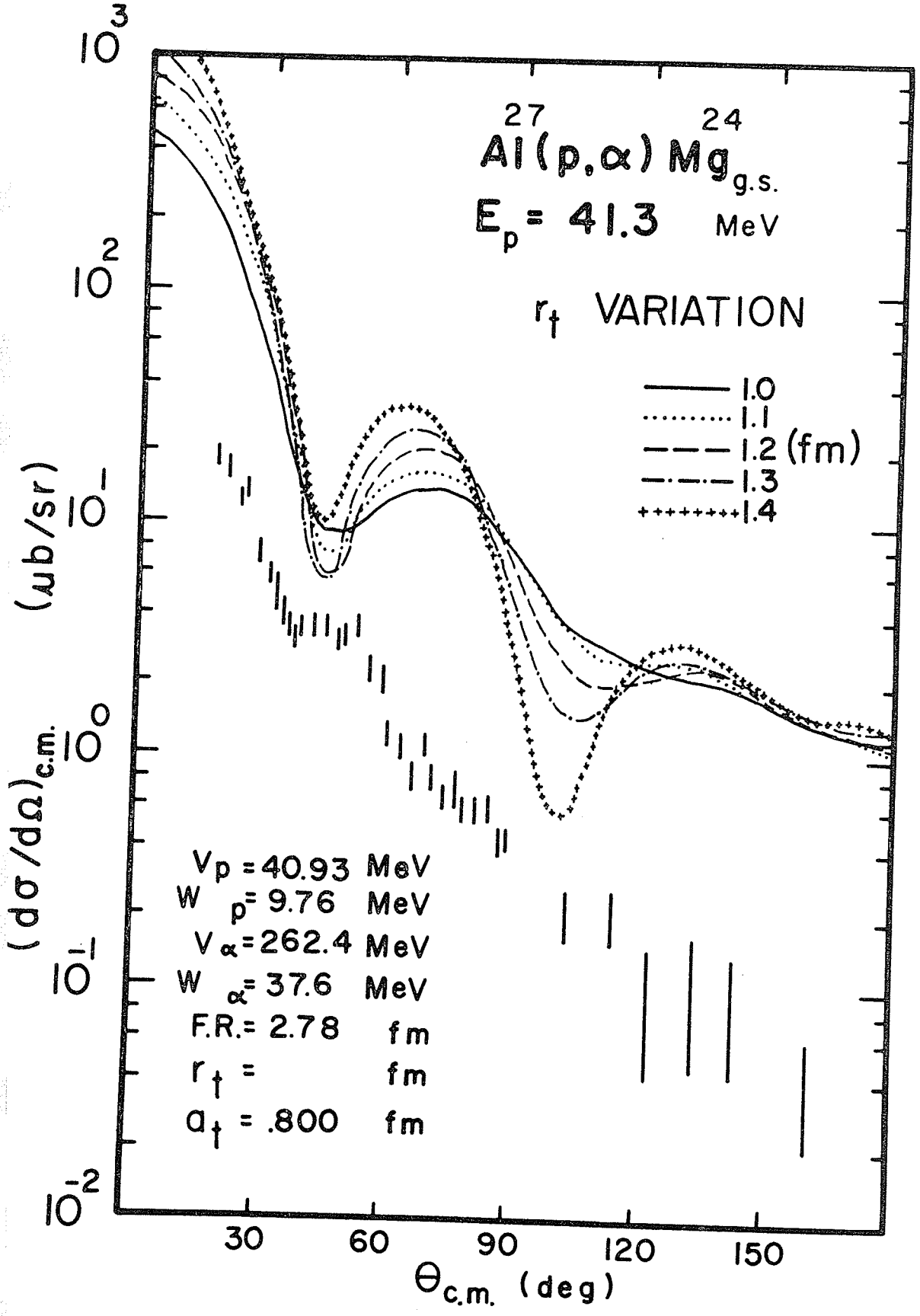
$^{27}Al(p,\alpha)\,^{24}Mg_{g.s.}$
E_p = 41.3 MeV
r_t VARIATION
1.0
1.1
1.2 (fm)
1.3
1.4
V_p = 40.93 MeV
W_p = 9.76 MeV
V_α = 262.4 MeV
W_α = 37.6 MeV
F.R. = 2.78 fm
r_t = fm
a_t = .800 fm
$(d\sigma/d\Omega)_{c.m.}$ (μb/sr)
$\theta_{c.m.}$ (deg)
10^3
10^2
10^1
10^0
10^{-1}
10^{-2}
30
60
90
120
150

Figure 4.29

The effect of varying the bound state parameter a_t on the theoretical angular distribution.

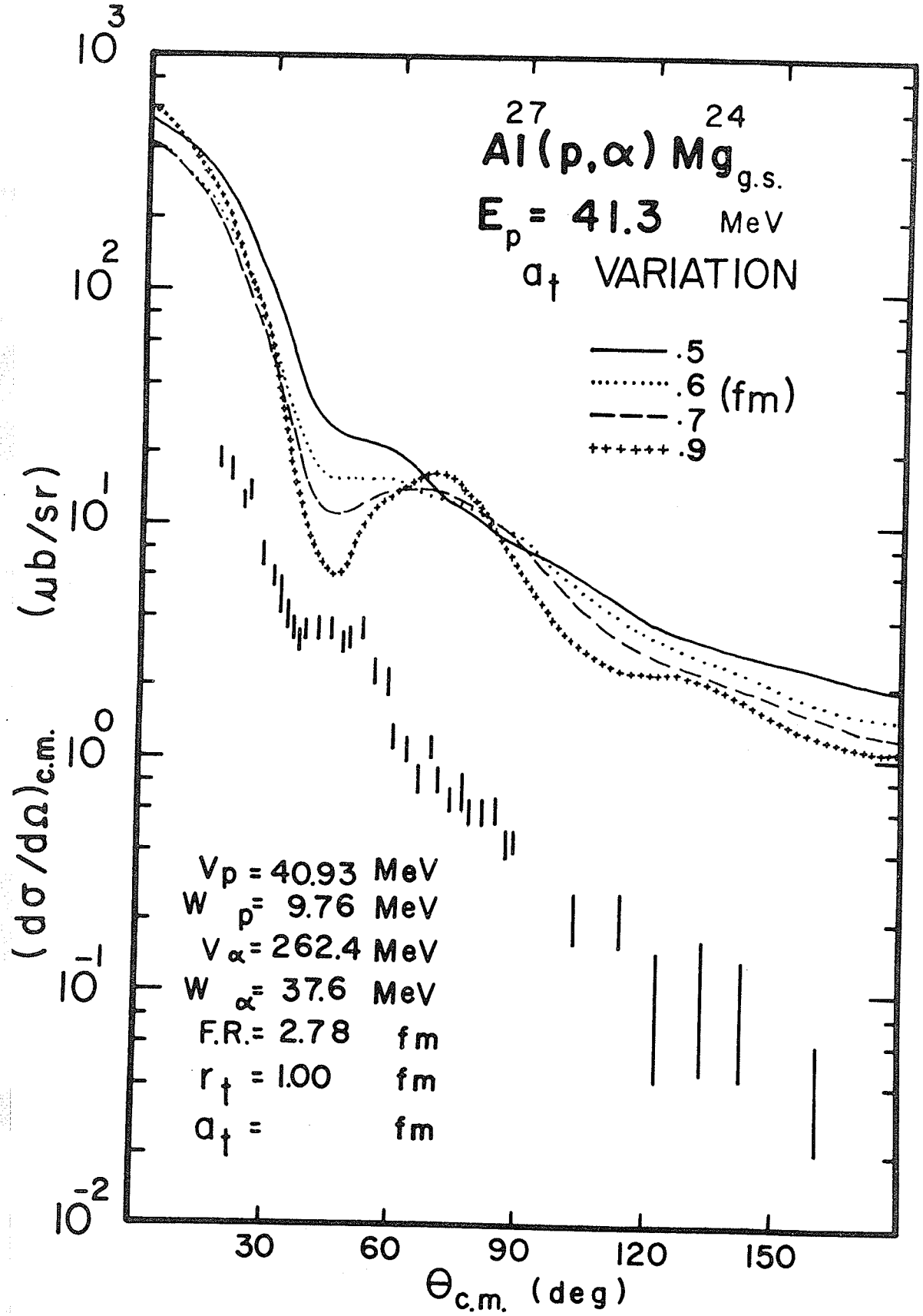
$^{27}Al(p,\alpha)\,^{24}Mg_{g.s.}$
E_p = 41.3 MeV
a_t VARIATION
.5
.6 (fm)
.7
.9
V_p = 40.93 MeV
W_p = 9.76 MeV
V_α = 262.4 MeV
W_α = 37.6 MeV
F.R. = 2.78 fm
r_t = 1.00 fm
a_t = fm
$(d\sigma/d\Omega)_{c.m.}$ (μb/sr)
$\theta_{c.m.}$ (deg)
10^3
10^2
10^1
10^0
10^{-1}
10^{-2}
30
60
90
120
150

Figure 4.30

The effect of varying the bound state parameter r_t on the theoretical angular distribution.

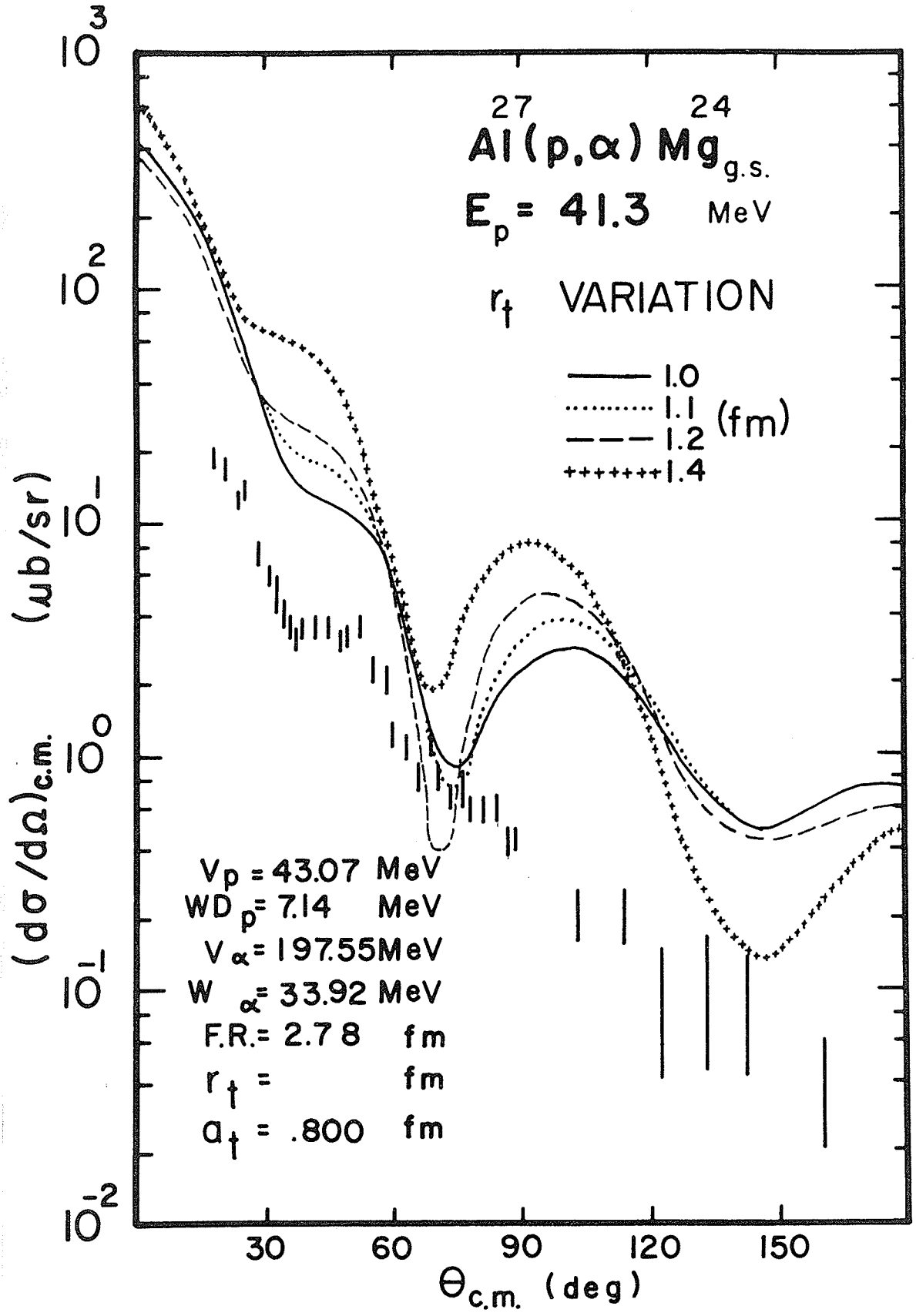
$^{27}Al(p,\alpha)\,^{24}Mg_{g.s.}$
E_p = 41.3 MeV
r_t VARIATION
1.0
1.1
1.2
1.4
(fm)
V_p = 43.07 MeV
WD_p = 7.14 MeV
V_α = 197.55 MeV
W_α = 33.92 MeV
F.R. = 2.78 fm
r_t = fm
a_t = .800 fm
$(d\sigma/d\Omega)_{c.m.}$ (μb/sr)
$\theta_{c.m.}$ (deg)
10^3
10^2
10^1
10^0
10^{-1}
10^{-2}
30
60
90
120
150

Figure 4.31

The effect of varying the bound state parameter a_t on the theoretical angular distribution.

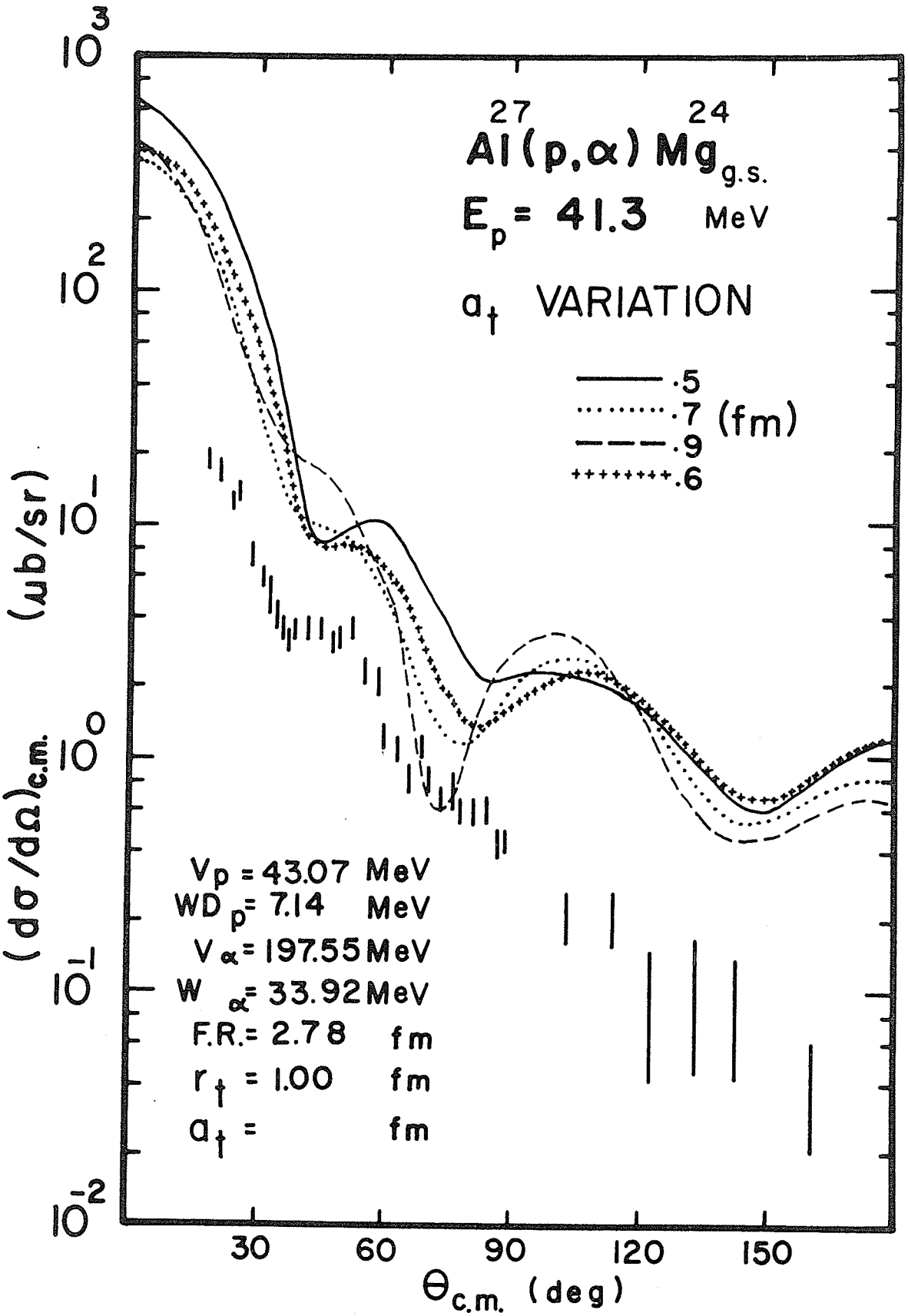
$^{27}Al(p,\alpha)\,^{24}Mg_{g.s.}$
E_p = 41.3 MeV
a_t VARIATION
.5
.7 (fm)
.9
.6
V_p = 43.07 MeV
WD_p = 7.14 MeV
V_α = 197.55 MeV
W_α = 33.92 MeV
F.R. = 2.78 fm
r_t = 1.00 fm
a_t = fm
$(d\sigma/d\Omega)_{c.m.}$ (μb/sr)
$\Theta_{c.m.}$ (deg)
10^3
10^2
10^1
10^0
10^{-1}
10^{-2}
30
60
90
120
150

Figure 4.32

The effect of varying the bound state parameter r_t on the theoretical angular distribution.

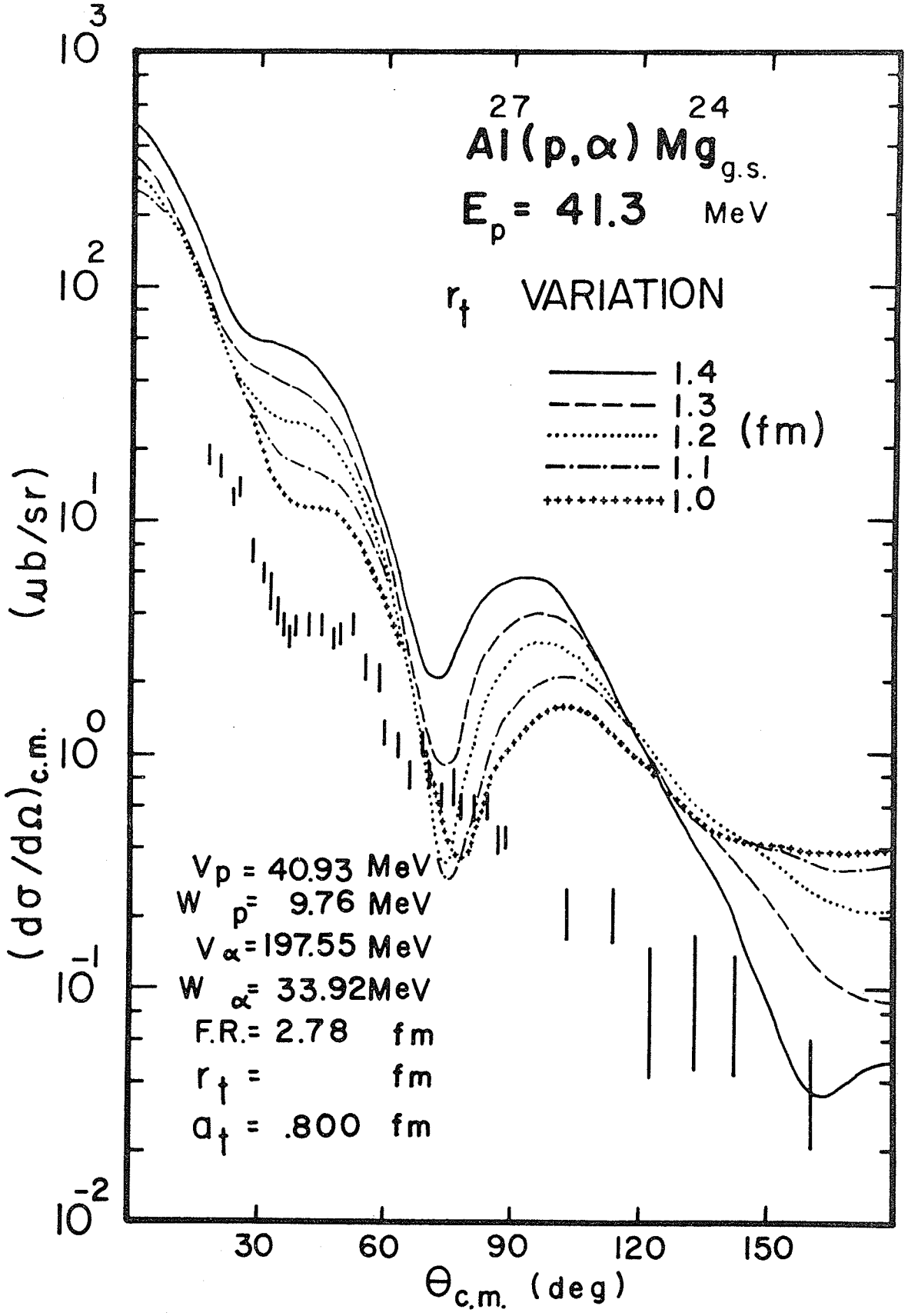
$^{27}Al(p,\alpha)\,^{24}Mg_{g.s.}$
E_p = 41.3 MeV
r_f VARIATION
1.4
1.3
1.2 (fm)
1.1
1.0
V_p = 40.93 MeV
W_p = 9.76 MeV
V_α = 197.55 MeV
W_α = 33.92 MeV
F.R. = 2.78 fm
r_f = fm
a_f = .800 fm
$(d\sigma/d\Omega)_{c.m.}$ (μb/sr)
$\theta_{c.m.}$ (deg)
10^3
10^2
10^1
10^0
10^{-1}
10^{-2}
30
60
90
120
150

Figure 4.33

The effect of varying the bound state parameter a_t on the theoretical angular distribution.

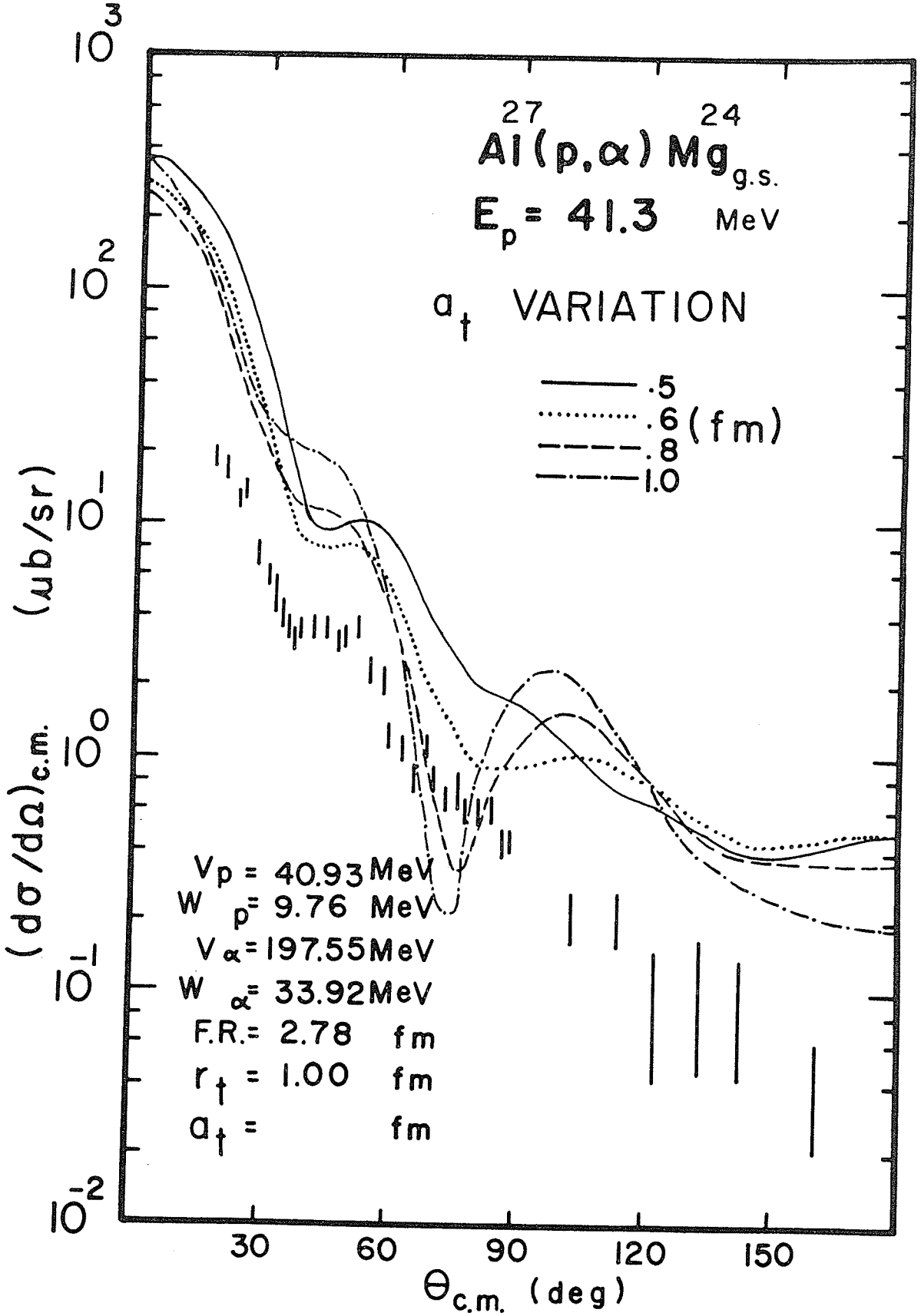
$^{27}Al(p,\alpha)\,^{24}Mg_{g.s.}$
E_p = 41.3 MeV
a_t VARIATION
.5
.6 (fm)
.8
1.0
V_p = 40.93 MeV
W_p = 9.76 MeV
V_α = 197.55 MeV
W_α = 33.92 MeV
F.R. = 2.78 fm
r_t = 1.00 fm
a_t = fm
$(d\sigma/d\Omega)_{c.m.}$ (μb/sr)
$\theta_{c.m.}$ (deg)
10^3
10^2
10^1
10^0
10^{-1}
10^{-2}
30
60
90
120
150

Figure 4.34

Shows the only three fits considered for extracting experimental spectroscopic factor. Fit c represents the best fit.

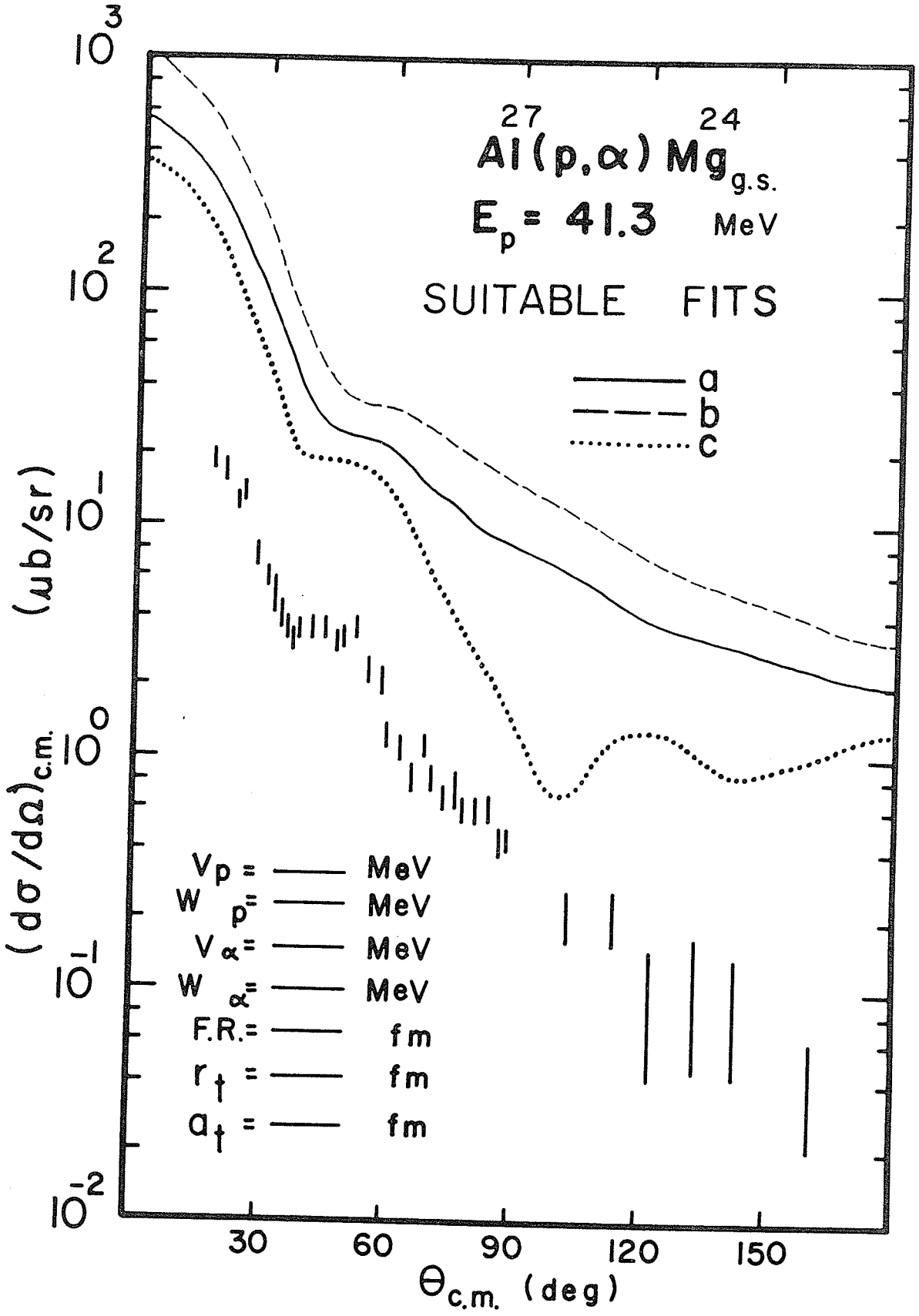
$^{27}Al(p,\alpha)\,^{24}Mg_{g.s.}$
E_p = 41.3 MeV
SUITABLE FITS
a
b
c
V_p = —— MeV
W_p = —— MeV
V_α = —— MeV
W_α = —— MeV
F.R. = —— fm
r_t = —— fm
a_t = —— fm
$(d\sigma/d\Omega)_{c.m.}$ (μb/sr)
10^3
10^2
10^1
10^0
10^{-1}
10^{-2}
30
60
90
120
150
$\theta_{c.m.}$ (deg)

Table 4.3

Tabulation of optical parameters of suitable DWBA fits to the $^{27}Al(p,\alpha)^{24}Mg$ reaction

TABLE 4.3

PARAMETERS OF SUITABLE FITS

	a	b	c *
V_p (MeV) =	40.93	43.07	40.93
W_p (MeV) =	9.76	0.0	9.76
WD_p (MeV) =	0.0	7.14	0.0
V_α (MeV) =	262.44	262.44	197.56
W_α (MeV) =	37.6	37.6	33.9
WD_α (MeV) =	0.0	0.0	0.0
r_t (fm) =	1.00	1.00	1.07
a_t (fm) =	.50	.50	.45
F.R.(fm) =	2.78	2.78	2.78
$\sigma_{TH}(\mu b)$ =	419	772	228
S_{EXP} =	$.036 \pm .009$	$.020 \pm .005$	$.067 \pm .016$
S_{TH} =	.081	.081	.081

* c represents our best fit

The theoretical spectroscopic factor of .081 given in Table 4.3 was obtained[73] by assuming jj coupling and SHM wave functions for the three transferred nucleons. The structure of ^{27}Al was assumed to have the form

$$^{24}Mg \left[(1d_{5/2})^2\right]^{J_n=0}_{\text{SENIORITY=0}} (1d_{5/2})^{J_p=\frac{5}{2}}_{\text{SENIORITY=1}}$$

that is, the three outer nucleons were assumed to occupy Nilsson level #7.† The agreement between the theoretical and experimental spectroscopic factors is extremely satisfactory for the best fit "c" where S = .067 ± .016.

† More appropriately, for the $^{27}Al(p,\alpha)^{24}Mg$ reaction the two transferred neutrons occupy intrinsic states of Nilsson orbit 5, 6 and 7. Expanding the Nilsson model wave functions in terms of the shell model wave functions one finds that orbit 5 is entirely $d^5/2$ and orbit 6 and 7 have $d^5/2$ as their largest component when expressed in spheroidal symmetric co-ordinates.

For the transferred proton, since one can consider the ground state of ^{27}Al as consisting of ^{28}Si in either the 0^+ of the 2^+ state coupled to a $d^5/2$ proton hole, we are led to assume that the odd proton which is removed from ^{27}Al in triton pick-up is mostly in a $d^5/2$ state.

ANALYSIS OF THE $^{23}Na(p,\alpha)^{20}Ne_{g.s.}$ REACTION

Chapter 4 b.

Since for this reaction $J_i^{\pi} = 3/2^+$ and $J_f^{\pi} = 0^+$ we have again $l_t = 2$ with the result that RADNOD (see 4.a and appendix 4.a) is also 2, based on the assumption that the three picked up nucleons came from the d 5/2 shell.

The proton optical parameters were obtained from our optical model fits to the data of the elastic scattering of 49.5 MeV protons[61] from ^{24}Mg. This was done since there was no data available for ^{23}Na. However, since the variation of these parameters from one nucleus to another is slow and smooth and since we already know that the DWBA calculations are relatively insensitive[2,46] to the proton parameters, this approximation should introduce little error into our analysis. The alpha channel optical parameters were extracted by fitting the 50.9 MeV alpha elastic scattering[63] from ^{20}Ne. Both channel energies were fairly close to the desired 45.5 MeV for the proton channel and the time reversed alpha channel energy of 55.1 MeV at which we measured the (p,α) angular distribution.

The fits for the proton channel are tabulated in Table 4.4 and are compared to the experimental elastic scattering results in Figures 4.35-4.41. The starting values for the searches were taken from the following references.

(a), (b) and (c) used references [57,61]

(d) and (e) used reference [55]

Table 4.4

Tabulation of the optical parameters giving the best χ^2 fits to the elastic scattering of protons from ^{24}Mg.

TABLE 4.4

OPTICAL PARAMETERS GIVING BEST FITS TO THE EXPERIMENTAL DATA OF RUSH, BURGE, LEWIS and SMITH[61] --- THE ELASTIC SCATTERING OF 49.5 MeV PROTONS FROM ^{24}Mg

FIT	a	b	c	d	e	f	g
V_0 (MeV)	42.33	39.54	48.70	43.41	35.57	35.51	42.33
r_0 (fm)	1.054	1.055	1.145	1.191	1.138	1.151	1.217
a_0 (fm)	.8022	.7730	.6746	.7267	.7535	.7553	.6420
W_v (MeV)	9.681	8.751	0.0	0.0	7.896	8.280	0.0
r_v (fm)	1.485	1.502			1.386	1.294	
a_v (fm)	.5164	.5428			.6925	.5919	
W_s (MeV)	0.0	0.0	6.470	7.743	0.0	0.0	6.138
r_s (fm)			1.185	1.055			1.240
a_s (fm)			.758	.7243			.6200
r_c (fm)	1.2	1.2	1.2	1.2	1.2	1.2	1.2
χ^2 (arb.)	45.7	62.6	56.5	62.5	47.8	42.2	72.7

Figure 4.35

Theoretical fit to the proton elastic scattering from ^{24}Mg.

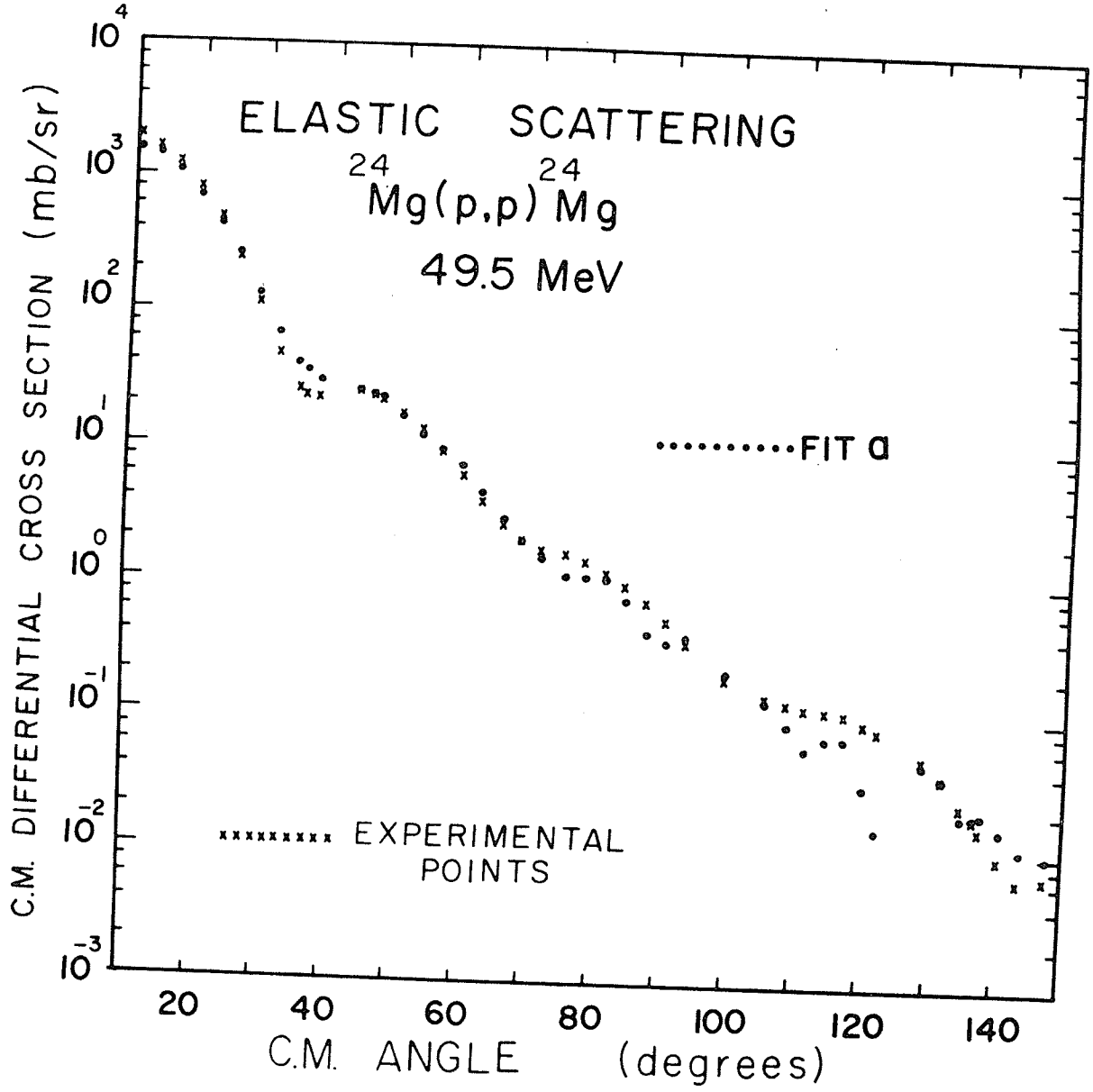
ELASTIC SCATTERING
24 24
Mg(p,p) Mg
49.5 MeV
FIT a
EXPERIMENTAL POINTS
C.M. DIFFERENTIAL CROSS SECTION (mb/sr)
C.M. ANGLE (degrees)
10^4
10^3
10^2
10^1
10^0
10^-1
10^-2
10^-3
20
40
60
80
100
120
140

Figure 4.36

Theoretical fit to the proton elastic scattering from ^{24}Mg.

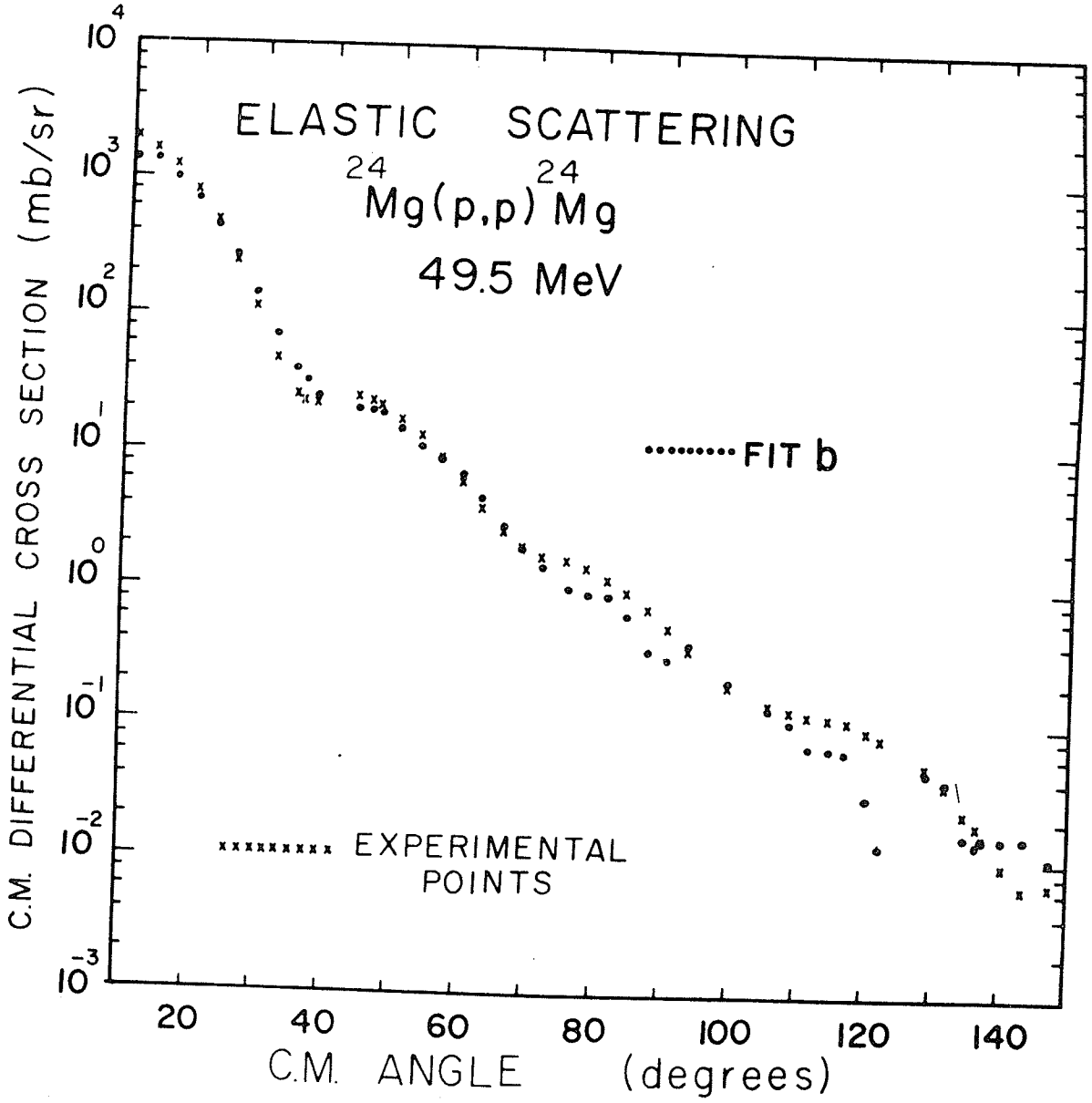
ELASTIC SCATTERING
24 24
Mg(p,p) Mg
49.5 MeV
FIT b
EXPERIMENTAL POINTS
C.M. DIFFERENTIAL CROSS SECTION (mb/sr)
C.M. ANGLE (degrees)
10^4
10^3
10^2
10^1
10^0
10^-1
10^-2
10^-3
20
40
60
80
100
120
140

Figure 4.37

Theoretical fit to the proton elastic scattering from ^{24}Mg.

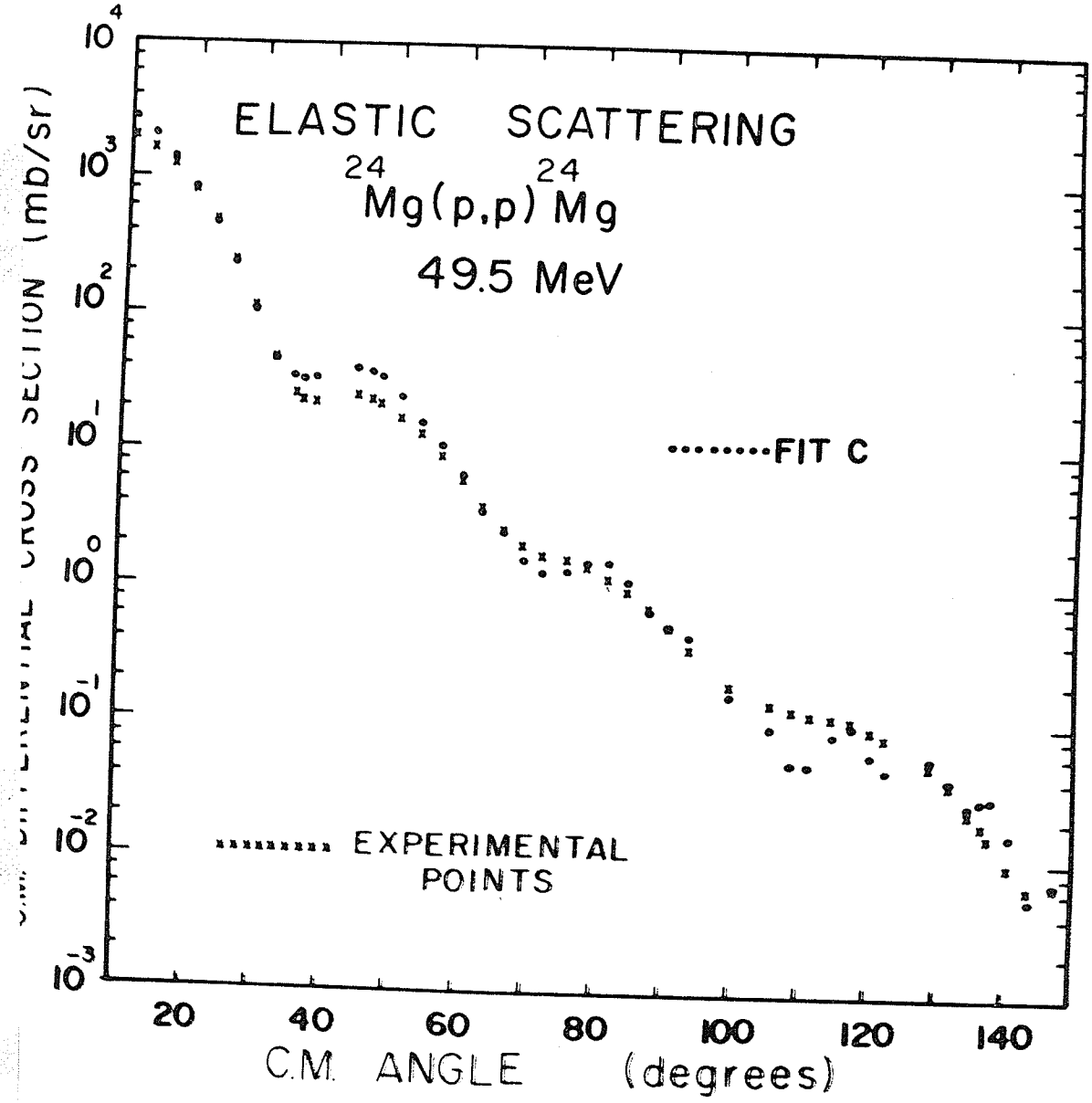
ELASTIC SCATTERING
24 24
Mg(p,p) Mg
49.5 MeV
FIT C
EXPERIMENTAL POINTS
C.M. ANGLE (degrees)
20
40
60
80
100
120
140

Figure 4.38

Theoretical fit to the proton elastic scattering from ^{24}Mg.

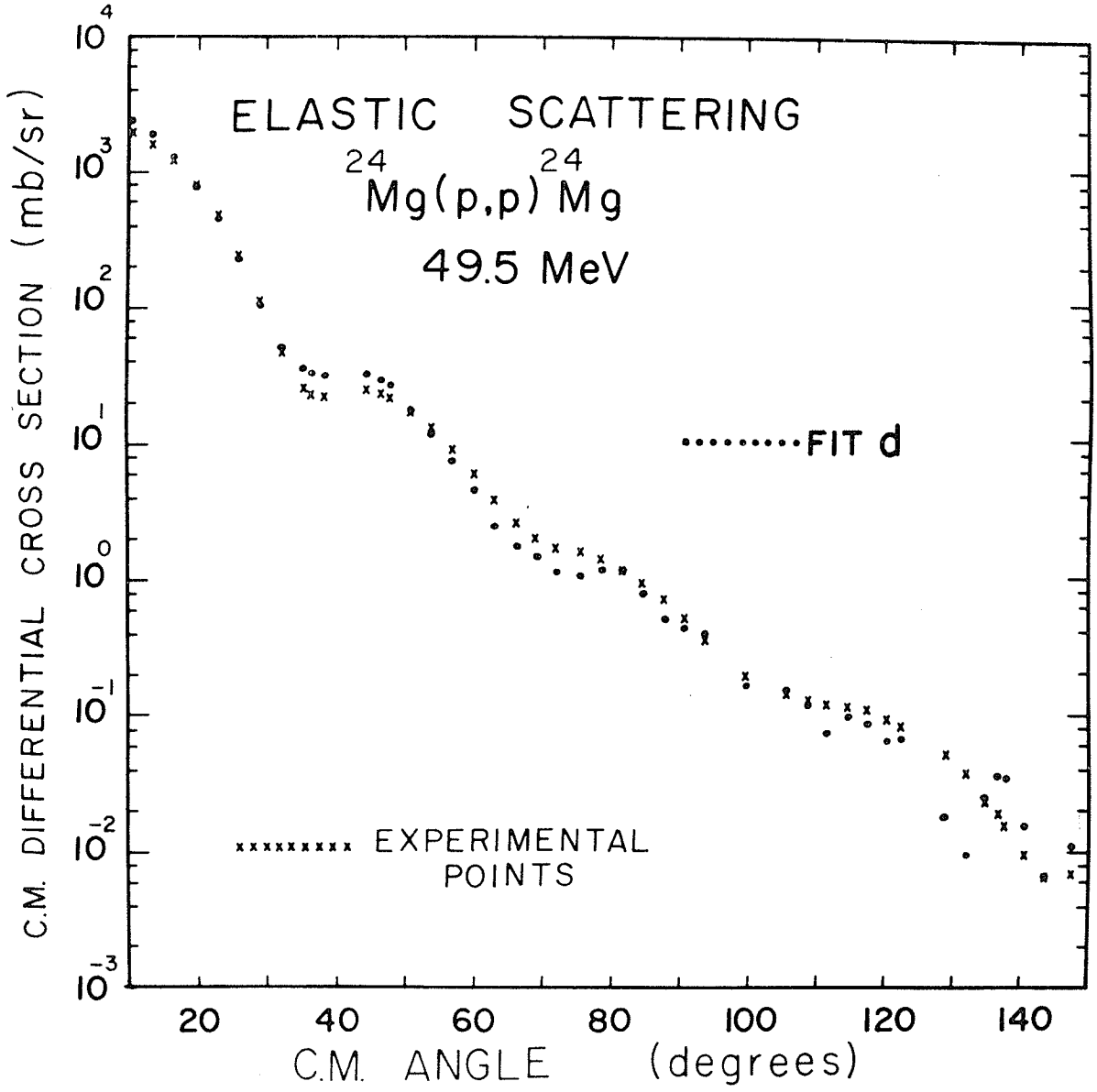
ELASTIC SCATTERING
24 24
Mg(p,p) Mg
49.5 MeV
FIT d
EXPERIMENTAL POINTS
C.M. DIFFERENTIAL CROSS SECTION (mb/sr)
C.M. ANGLE (degrees)
10^4
10^3
10^2
10^1
10^0
10^-1
10^-2
10^-3
20
40
60
80
100
120
140

Figure 4.39

Theoretical fit to the proton elastic scattering from ^{24}Mg.

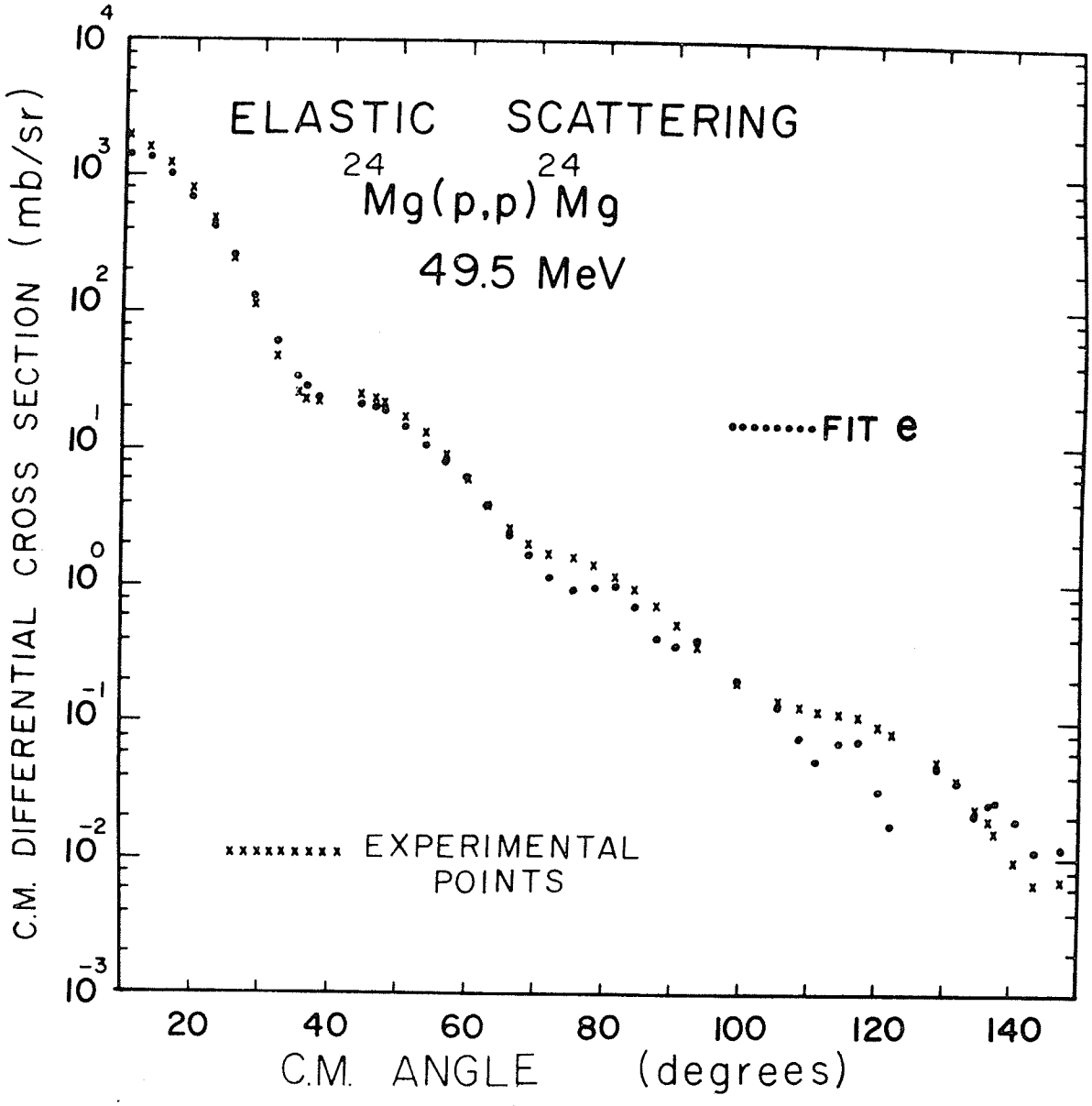
ELASTIC SCATTERING
24 24
Mg(p,p) Mg
49.5 MeV
FIT e
EXPERIMENTAL POINTS
C.M. DIFFERENTIAL CROSS SECTION (mb/sr)
C.M. ANGLE (degrees)
10^4
10^3
10^2
10^1
10^0
10^-1
10^-2
10^-3
20
40
60
80
100
120
140

Figure 4.40

Theoretical fit to the proton elastic scattering from ^{24}Mg.

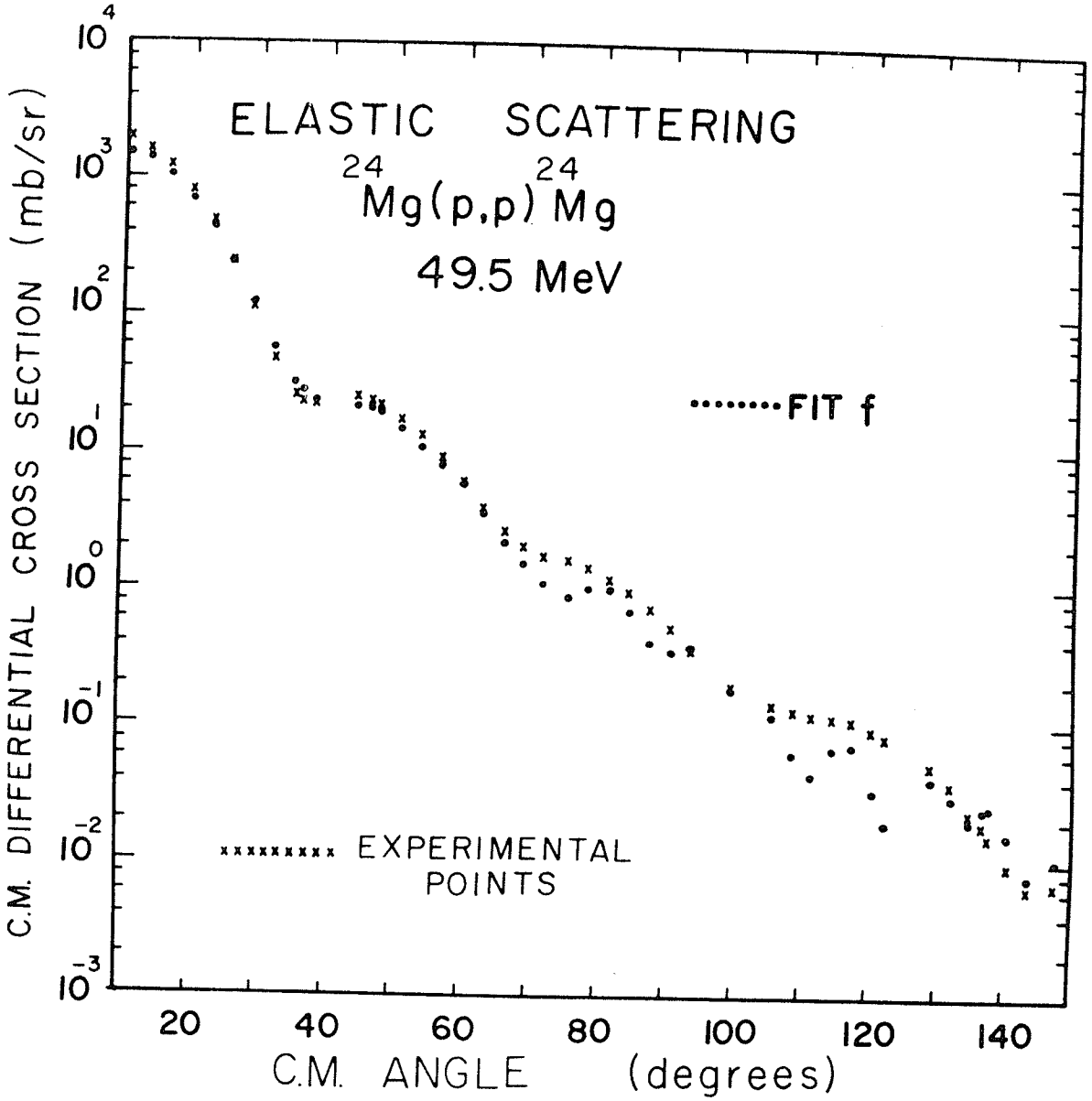
ELASTIC SCATTERING
24 24
Mg(p,p) Mg
49.5 MeV
FIT f
EXPERIMENTAL POINTS
C.M. DIFFERENTIAL CROSS SECTION (mb/sr)
C.M. ANGLE (degrees)
10^4
10^3
10^2
10^1
10^0
10^-1
10^-2
10^-3
20
40
60
80
100
120
140

Figure 4.41

Theoretical fit to the proton elastic scattering from ^{24}Mg

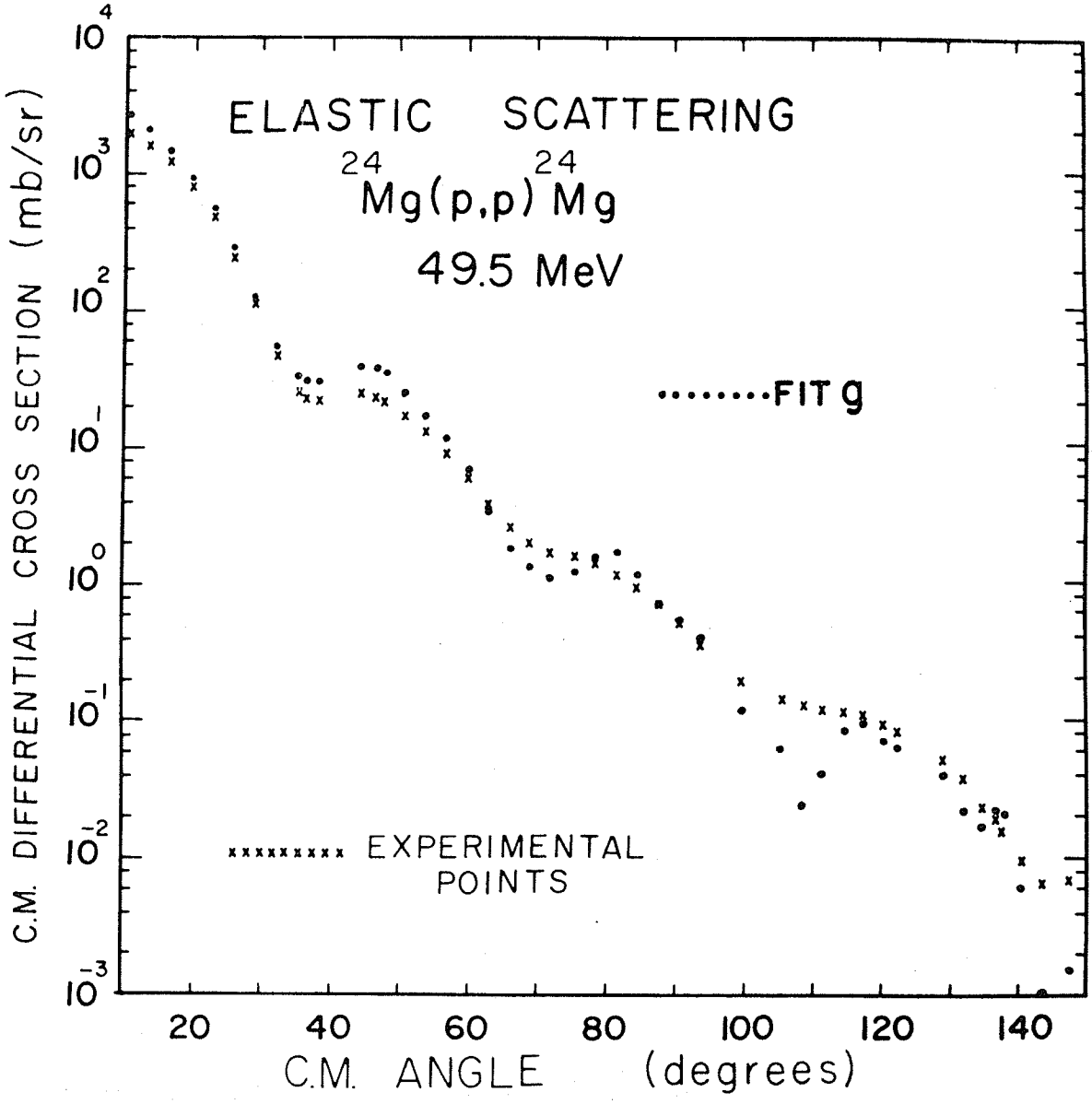
ELASTIC SCATTERING
24 24
Mg(p,p) Mg
49.5 MeV
FIT g
EXPERIMENTAL POINTS
C.M. DIFFERENTIAL CROSS SECTION (mb/sr)
C.M. ANGLE (degrees)
10^4
10^3
10^2
10^1
10^0
10^-1
10^-2
10^-3
20
40
60
80
100
120
140

The values for searches (f) and (g) were taken from reasonable guesses for V, W and WD using the "average" optical parameters listed in reference [67]

The extraction of the alpha optical parameters was initiated by using the parameters corresponding to the best fits to $^{24}Mg(\alpha,\alpha)^{24}Mg$ (see Chapter 4.a) and to those of $O^{16}(\alpha,\alpha)^{16}O$ (reference 2).

The theoretical alpha elastic scattering fits to the experimental data are shown in Figures 4.42-4.47 along with the corresponding tabulated optical parameters in Table 4.5 as was observed in our analysis of ^{27}Al the various solutions of the optical model fits had depths of the real well optical potential grouped about 140, 200 and 260 MeV.

The DWBA fit routine proceeded as follows. We performed a DWBA calculation for all combinations of all the sets of proton optical parameters in conjunction with each set of alpha optical parameters while keeping the bound state parameters fixed to r_t = 1.065 fm and a_t = .860 fm. These values of the bound state parameters were interpolations of values extracted by ^{3}He elastic scattering optical model fits to ^{12}C and Mg by Baugh et al [50].

The result was, as was found to be the case for the analysis carried out on ^{27}Al, that only a limited number (three to be exact) of sets of alpha channel optical potentials showed any promise of being able to give a satisfactory fit by varying r_t and a_t. Also, as has been previously noted, the calculations were relatively

Table 4.5

Tabulation of the optical parameters giving the best χ^2 fits to the elastic scattering of alphas from ^{20}Ne.

TABLE 4.5

OPTICAL PARAMETERS GIVING BEST FITS TO THE EXPERIMENTAL DATA OF SPRINGER[63] ---THE ELASTIC SCATTERING OF 50.9 MeV ALPHAS FROM ^{20}Ne

FIT	a	b	c	d	e	f
V_o (MeV)	140.82	139.99	199.92	202.50	265.33	258.05
r_o (fm)	1.518	1.506	1.294	1.472	1.458	1.351
a_o (fm)	.5913	.5784	.6567	.5523	.5268	.5876
W_v (MeV)	0.0	32.48	0.0	31.66	37.74	0.0
r_v (fm)		1.451		1.384	1.366	
a_v (fm)		.5824		.5502	.5099	
W_s (MeV)	46.55	0.0	23.80	0.0	0.0	25.96
r_s (fm)	1.416		1.291			1.341
a_s (fm)	.4689		.6673			.5923
r_c (fm)	1.4	1.4	1.4	1.4	1.4	1.4
χ^2 (arb.)	42.7	83.5	186.4	105.7	108.8	264.7

Figure 4.42

Theoretical fit to the alpha elastic scattering from ^{20}Ne.

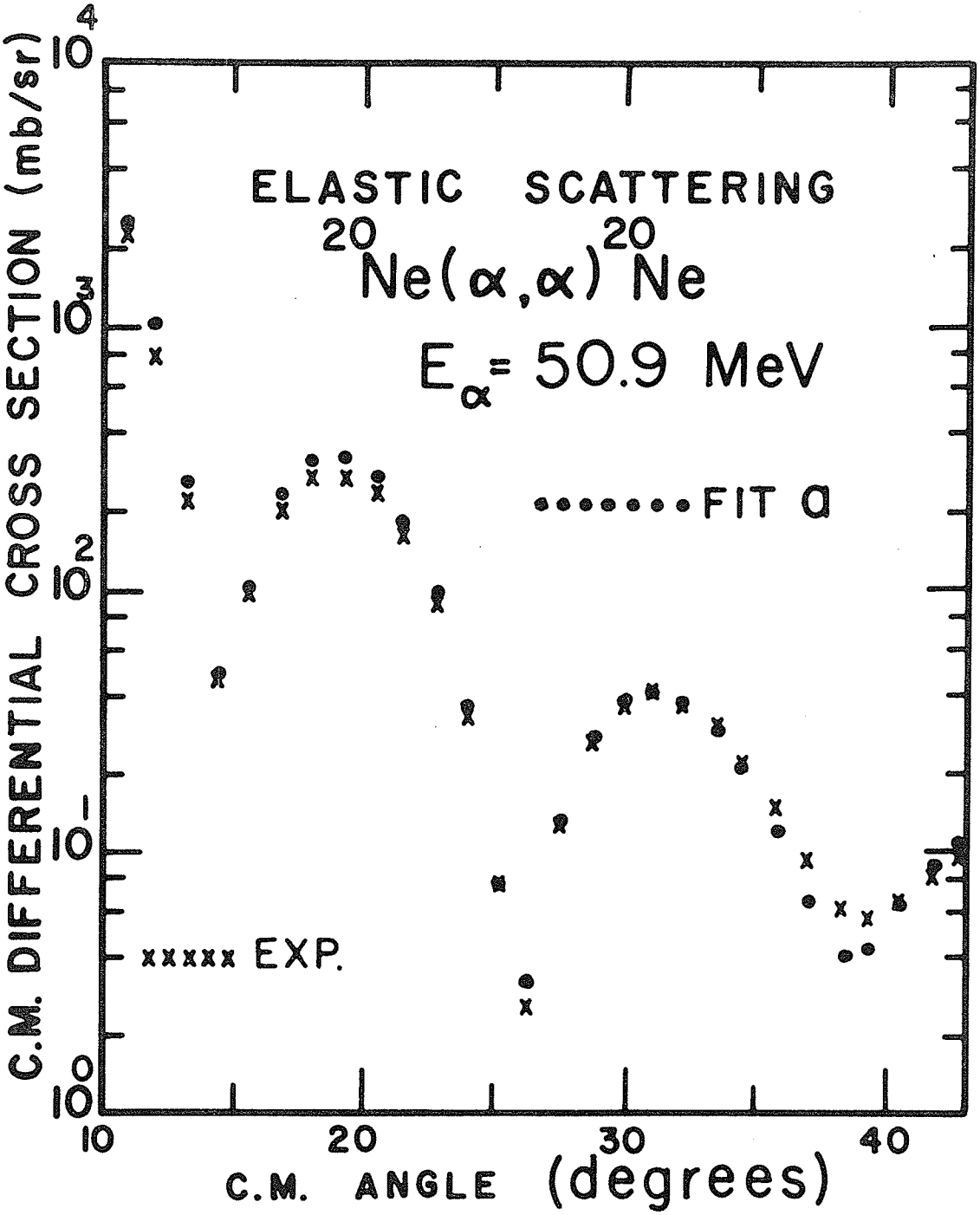
ELASTIC SCATTERING
$^{20}Ne(\alpha,\alpha)^{20}Ne$
E_α = 50.9 MeV
FIT a
EXP.
C.M. DIFFERENTIAL CROSS SECTION (mb/sr)
C.M. ANGLE (degrees)
10^4
10^3
10^2
10
1
10^{-1}
10
20
30
40

Figure 4.43

Theoretical fit to the alpha elastic scattering from ^{20}Ne.

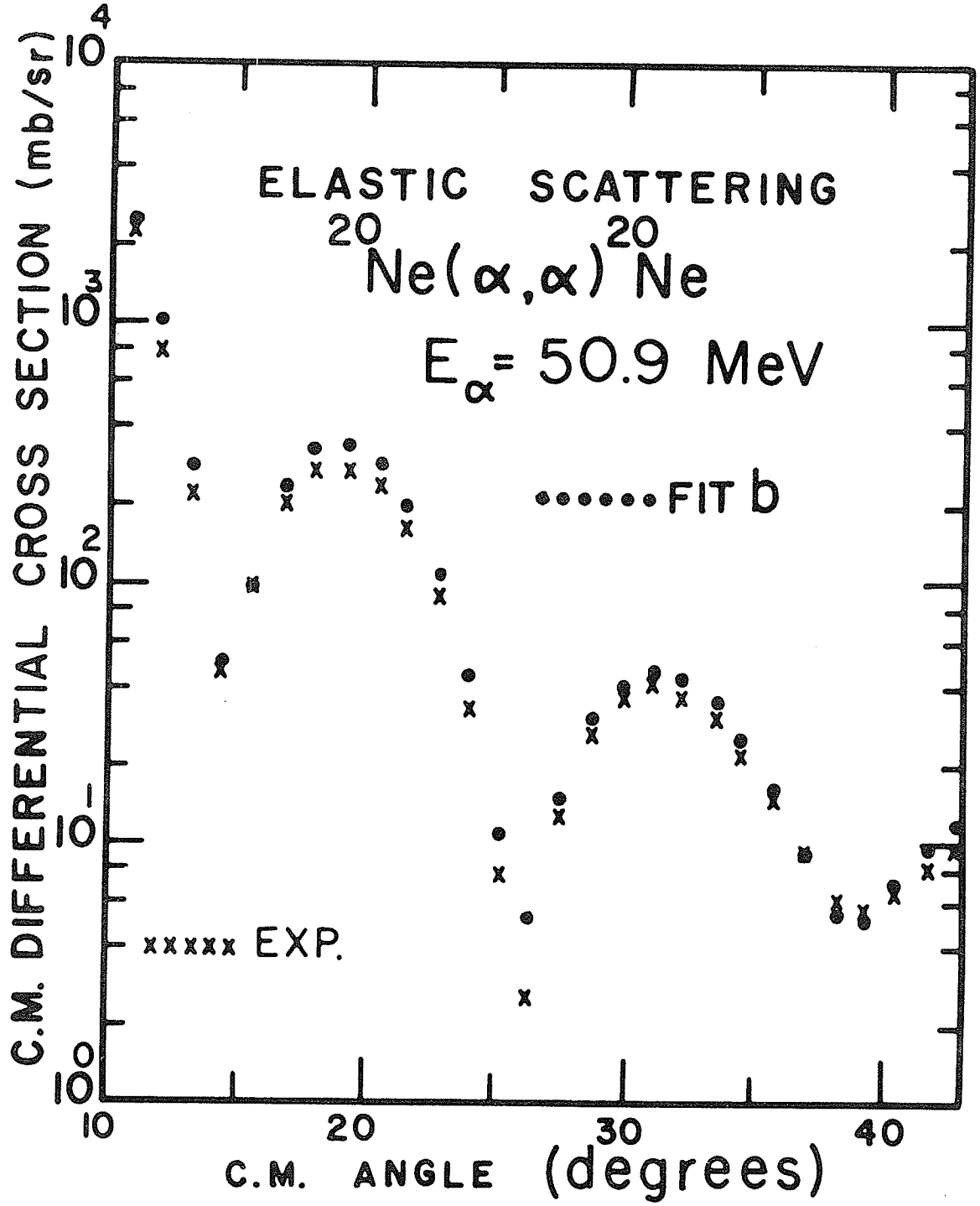
ELASTIC SCATTERING
$^{20}Ne(\alpha,\alpha)^{20}Ne$
E_α = 50.9 MeV
..... FIT b
xxxxx EXP.
C.M. DIFFERENTIAL CROSS SECTION (mb/sr)
10^4
10^3
10^2
10^1
10^0
10
20
30
40
C.M. ANGLE (degrees)

Figure 4.44

Theoretical fit to the alpha elastic scattering from ^{20}Ne.

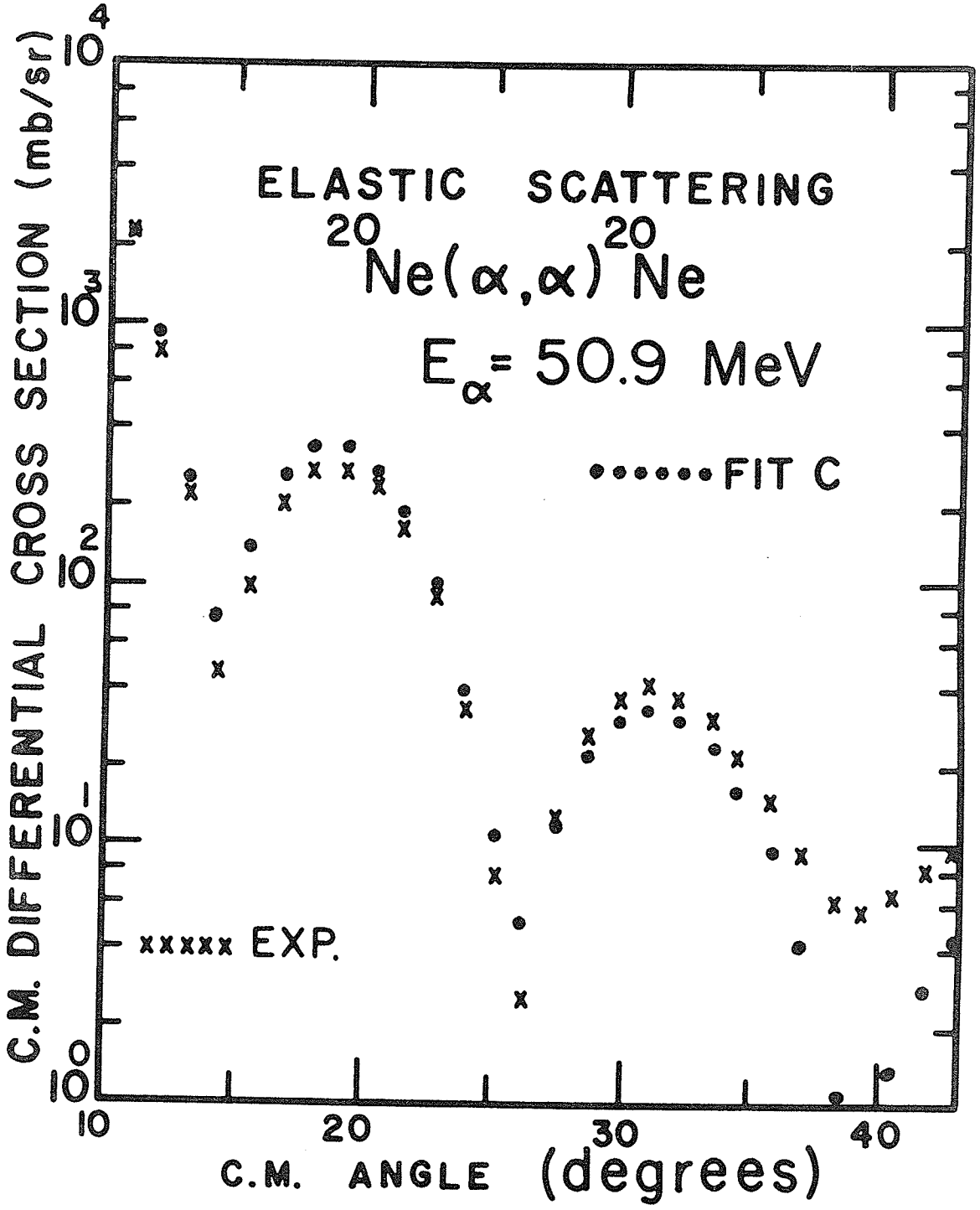
ELASTIC SCATTERING
20Ne(α,α)20Ne
Eα = 50.9 MeV
FIT C
EXP.
C.M. DIFFERENTIAL CROSS SECTION (mb/sr)
C.M. ANGLE (degrees)
10^4
10^3
10^2
10^1
10^0
10
20
30
40

Figure 4.45

Theoretical fit to the alpha elastic scattering from ^{20}Ne.

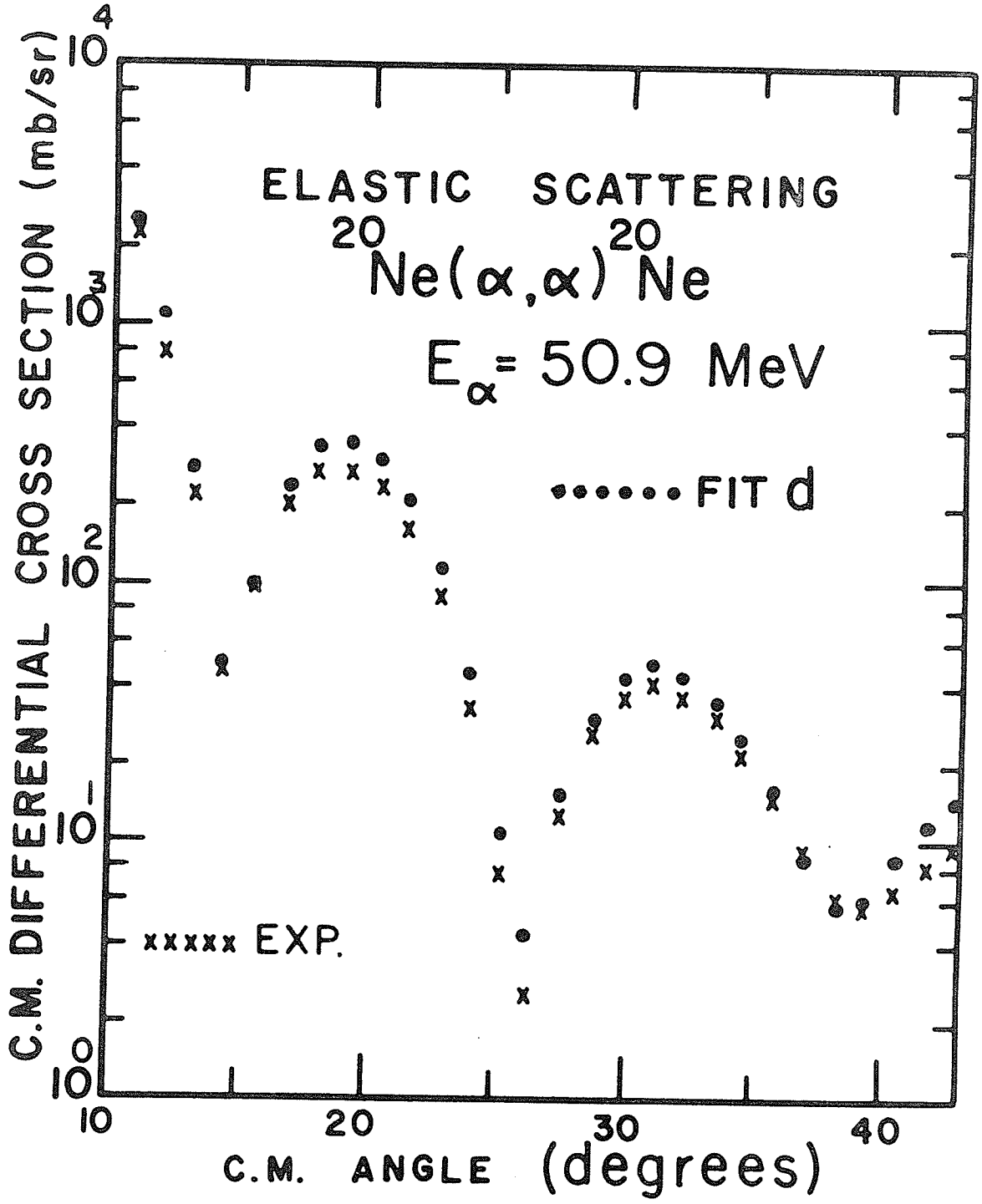
ELASTIC SCATTERING
$^{20}Ne(\alpha,\alpha)^{20}Ne$
E_α = 50.9 MeV
••••• FIT d
xxxxx EXP.
C.M. DIFFERENTIAL CROSS SECTION (mb/sr)
10^4
10^3
10^2
10
1
10^0
10
20
30
40
C.M. ANGLE (degrees)

Figure 4.46

Theoretical fit to the alpha elastic scattering from ^{20}Ne.

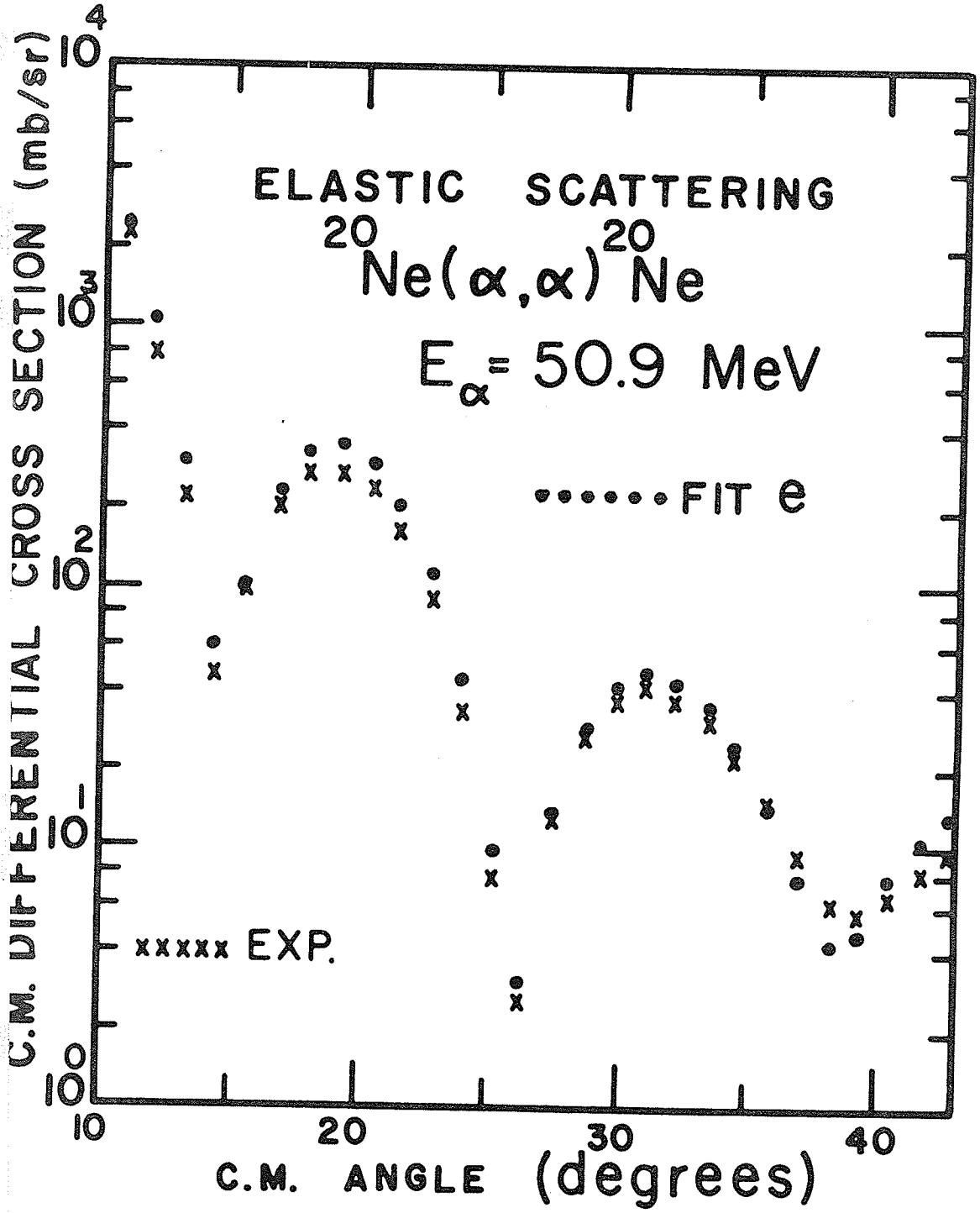
ELASTIC SCATTERING
$^{20}Ne(\alpha,\alpha)^{20}Ne$
E_α = 50.9 MeV
..... FIT e
xxxxx EXP.
C.M. DIFFERENTIAL CROSS SECTION (mb/sr)
10^4
10^3
10^2
10^1
10^0
10
20
30
40
C.M. ANGLE (degrees)

Figure 4.47

Theoretical fit to the alpha elastic scattering from ^{20}Ne.

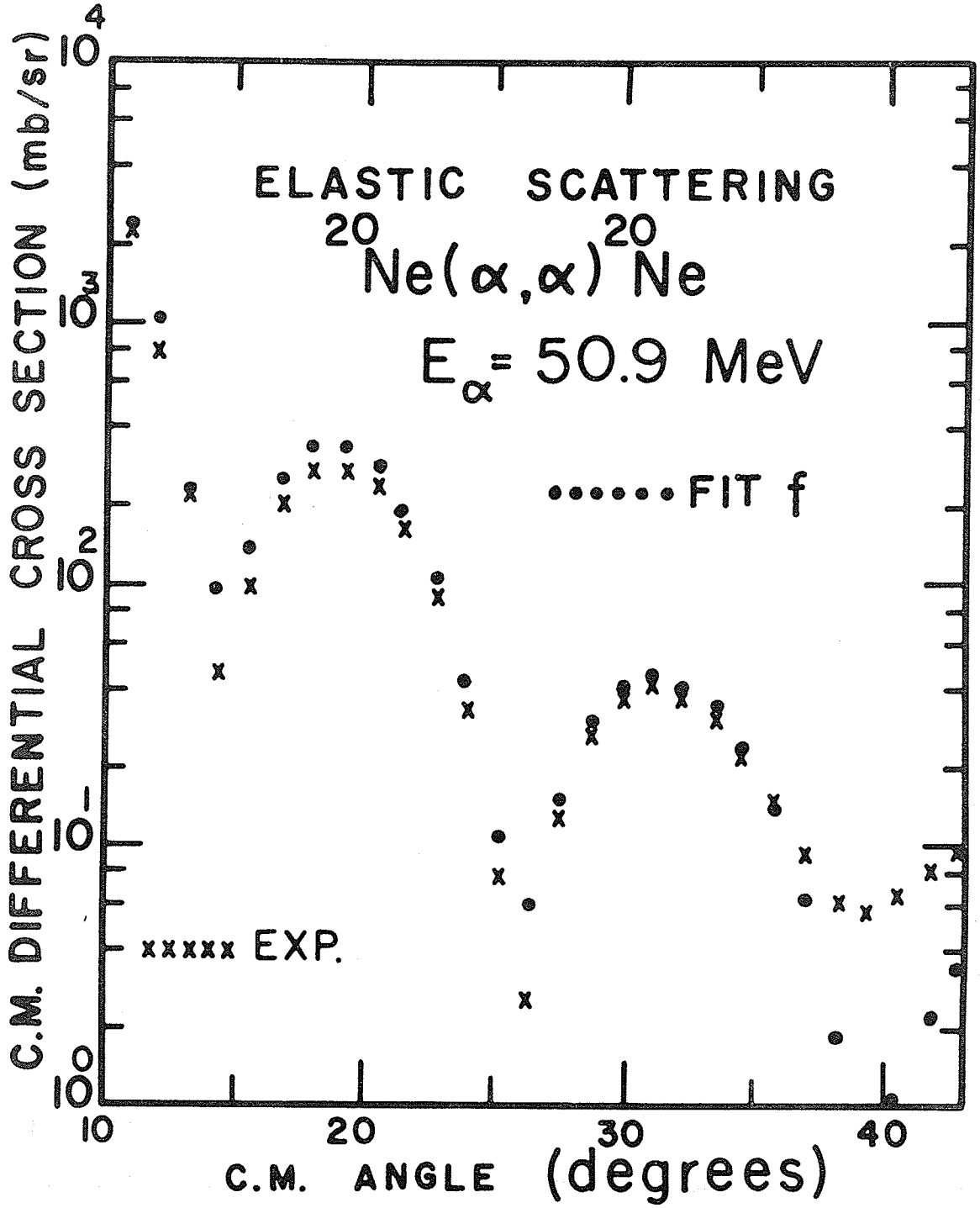
ELASTIC SCATTERING
$^{20}Ne(\alpha,\alpha)^{20}Ne$
E_α = 50.9 MeV
..... FIT f
xxxxx EXP.
C.M. DIFFERENTIAL CROSS SECTION (mb/sr)
10^4
10^3
10^2
10
1
10
20
30
40
C.M. ANGLE (degrees)

insensitive to which set of proton channel optical potentials one used. This is shown in Figure 4.48 where fits a, b, c, and d represent different sets of proton optical parameters.

From now on we conducted the analysis using only two sets of proton optical parameters, one having pure volume absorption ($WD_p = 0$) and the other having pure surface absorption ($W_p = 0$). We also restricted ourself to examining only the sets of alpha channel optical parameters c, d, and e as listed in Table 4.5.

The large differences in the theoretical angular distribution that one obtains for the six sets of alpha channel optical parameters for each set of proton parameters are illustrated in Figures 4.49-4.52 (fits a to f correspond to parameters listed on Table 4.5).

Fits c, d, and e, as already mentioned above, were then examined in more detail by carrying out an r_t, a_t grid search ranging over r_t = 1.0 - 1.4 fm while a_t = .46 - 96 fm.

For the set with $V_\alpha \approx 260$ MeV we obtained an acceptable fit to the experimental results when in addition we used the proton parameters having $WD_p = 0$ (the fit was not nearly as good when we choose proton parameters having $W_p = 0$). This result can be seen in Figures 4.53-4.56 where one should take particular notice of the fit for a_t = .46 shown in Figure 4.56. The agreement is quite good (remembering that the overall normalization is related to the experimental spectroscopic factor) right up to approximately 100° c.m.

Figure 4.48

The effect of different sets of proton parameters on the Theoretical angular distribution.

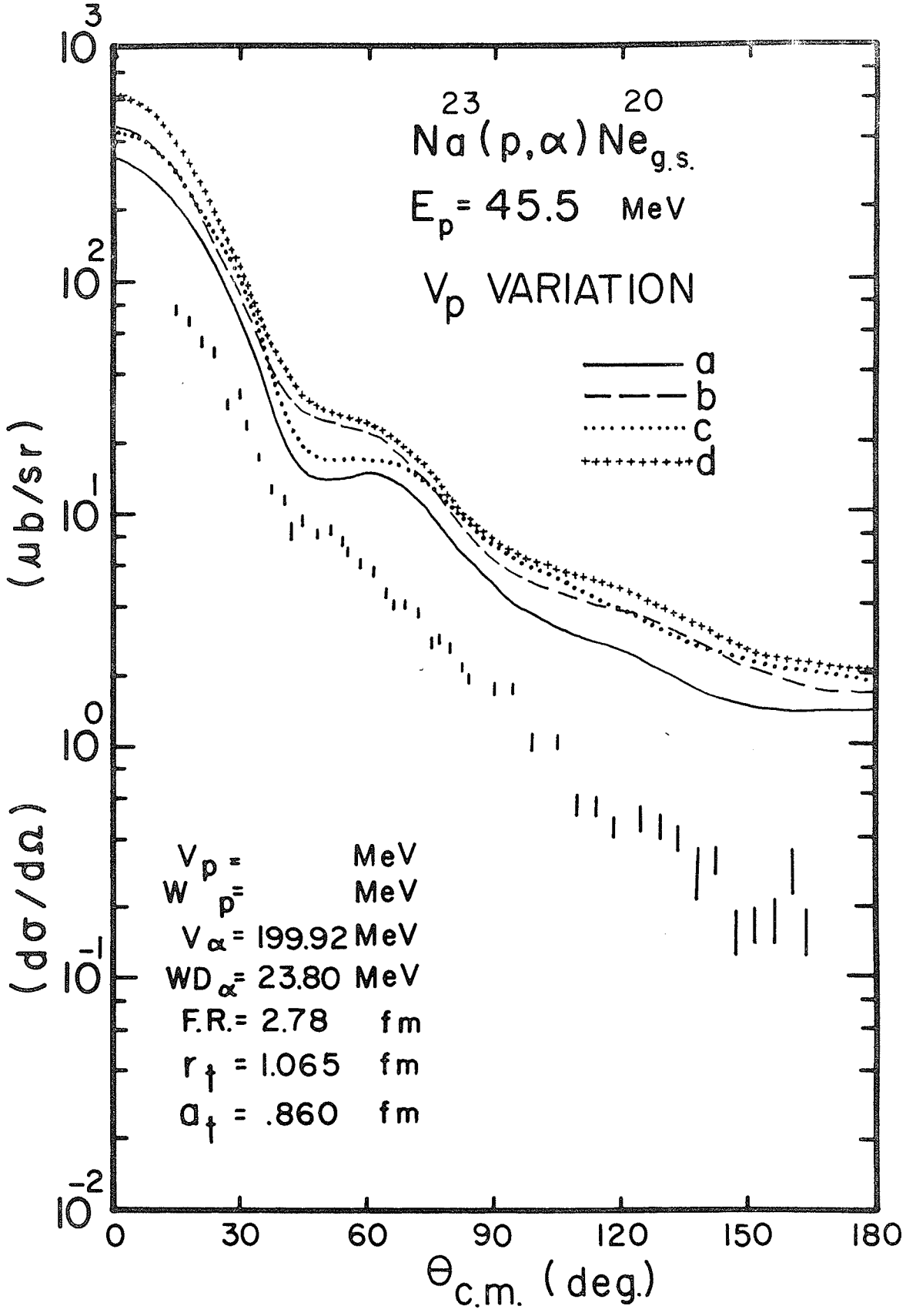
$^{23}Na(p,\alpha)^{20}Ne_{g.s.}$
$E_p = 45.5$ MeV
V_p VARIATION
a
b
c
d
V_p = MeV
W_p = MeV
V_α = 199.92 MeV
WD_α = 23.80 MeV
F.R. = 2.78 fm
r_t = 1.065 fm
a_t = .860 fm
$(d\sigma/d\Omega)$ $(\mu b/sr)$
$\theta_{c.m.}$ (deg.)
10^3
10^2
10^1
10^0
10^{-1}
10^{-2}
0
30
60
90
120
150
180

Figure 4.49

The effect of different sets of alpha parameters on the theoretical angular distribution.

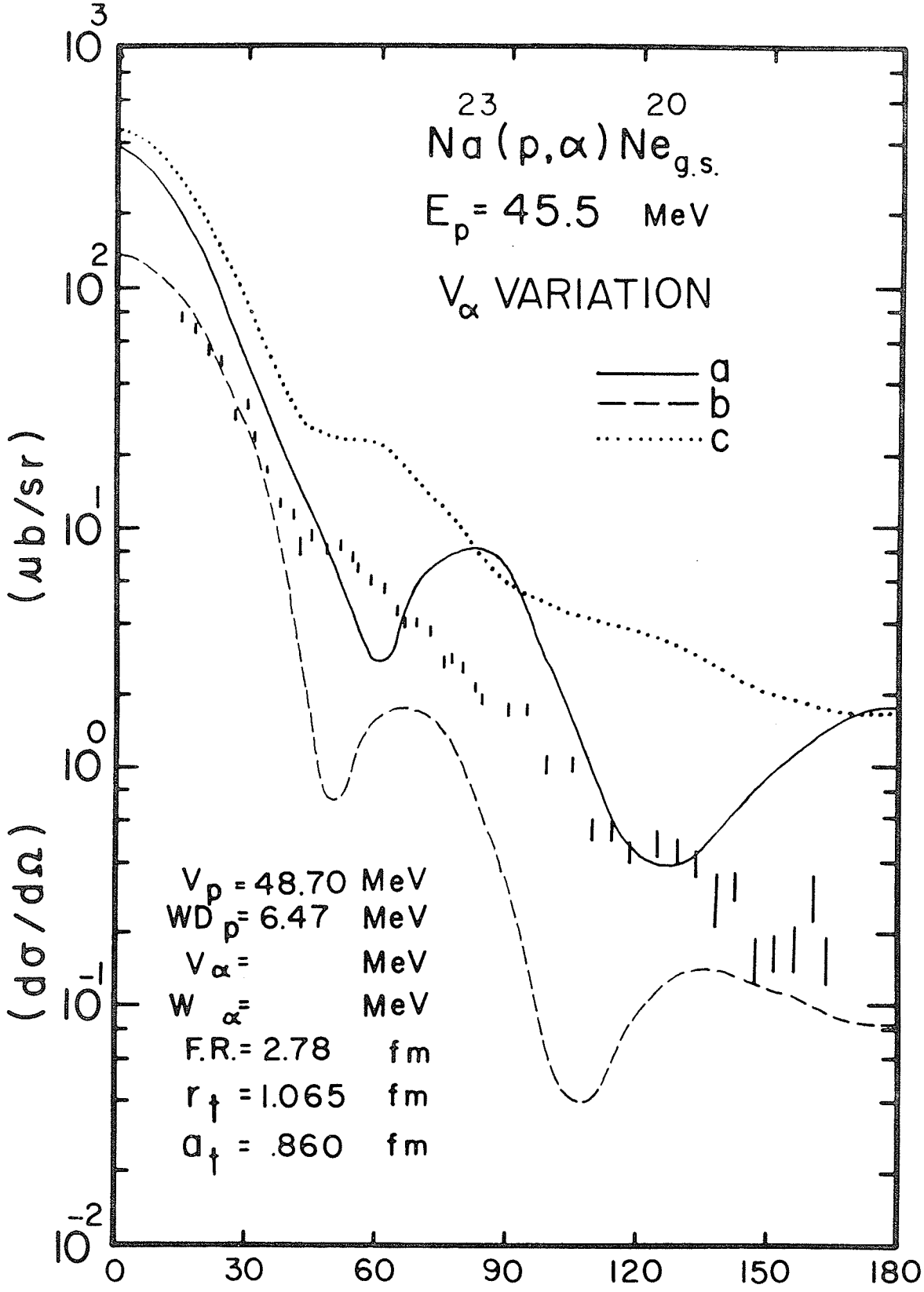
$^{23}Na(p,\alpha)^{20}Ne_{g.s.}$
$E_p = 45.5$ MeV
V_α VARIATION
a
b
c
$V_p = 48.70$ MeV
$WD_p = 6.47$ MeV
$V_\alpha =$ MeV
$W_\alpha =$ MeV
F.R. = 2.78 fm
$r_t = 1.065$ fm
$a_t = .860$ fm
$(d\sigma/d\Omega)$ $(\mu b/sr)$
10^3
10^2
10^1
10^0
10^{-1}
10^{-2}
0
30
60
90
120
150
180

Figure 4.50

The effect of different sets of alpha parameters on the theoretical angular distribution.

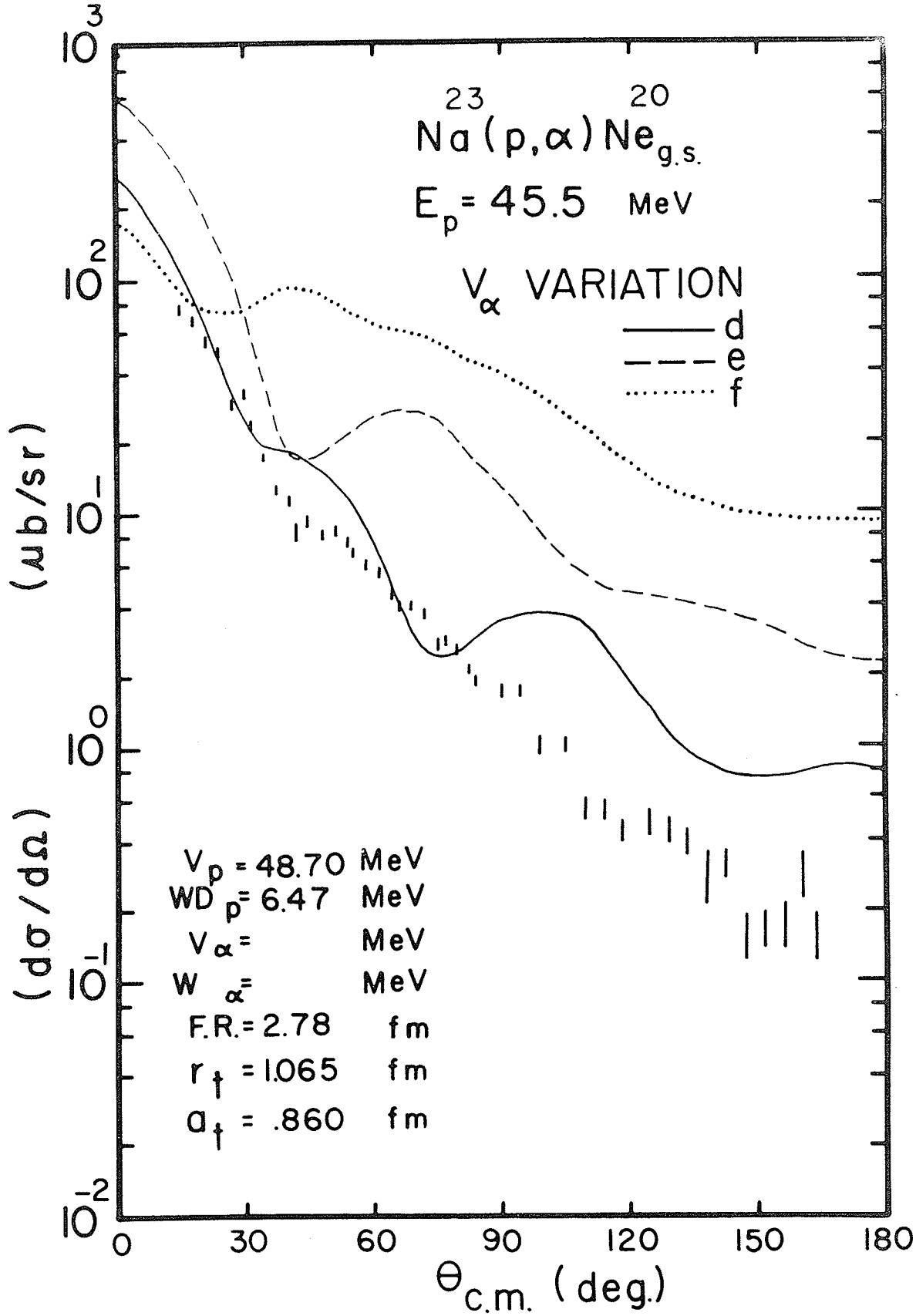
$^{23}Na(p,\alpha)^{20}Ne_{g.s.}$
$E_p = 45.5$ MeV
V_α VARIATION
d
e
f
$V_p = 48.70$ MeV
$WD_p = 6.47$ MeV
$V_\alpha =$ MeV
$W_\alpha =$ MeV
F.R. = 2.78 fm
$r_t = 1.065$ fm
$a_t = .860$ fm
$(d\sigma/d\Omega)$ $(\mu b/sr)$
$\theta_{c.m.}$ (deg.)
10^3
10^2
10^1
10^0
10^{-1}
10^{-2}
0
30
60
90
120
150
180

Figure 4.51

The effect of different sets of alpha parameters on the theoretical angular distribution.

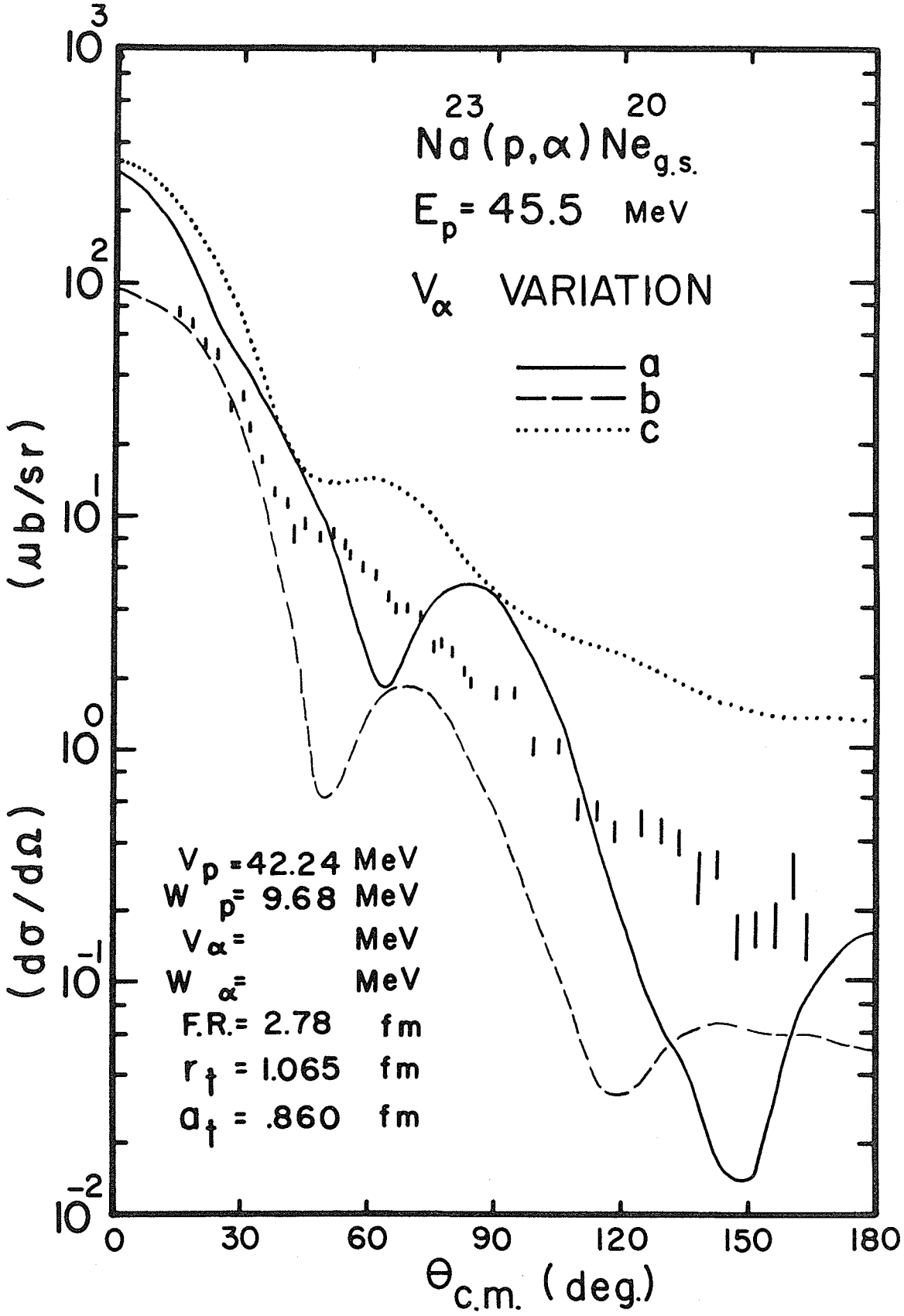
$^{23}Na(p,\alpha)^{20}Ne_{g.s.}$
$E_p = 45.5$ MeV
V_α VARIATION
a
b
c
V_p = 42.24 MeV
W_p = 9.68 MeV
V_α = MeV
W_α = MeV
F.R. = 2.78 fm
r_t = 1.065 fm
a_t = .860 fm
$(d\sigma/d\Omega)$ $(\mu b/sr)$
$\theta_{c.m.}$ (deg.)
10^3
10^2
10^1
10^0
10^{-1}
10^{-2}
0
30
60
90
120
150
180

Figure 4.52

The effect of different sets of alpha parameters on the theoretical angular distribution.

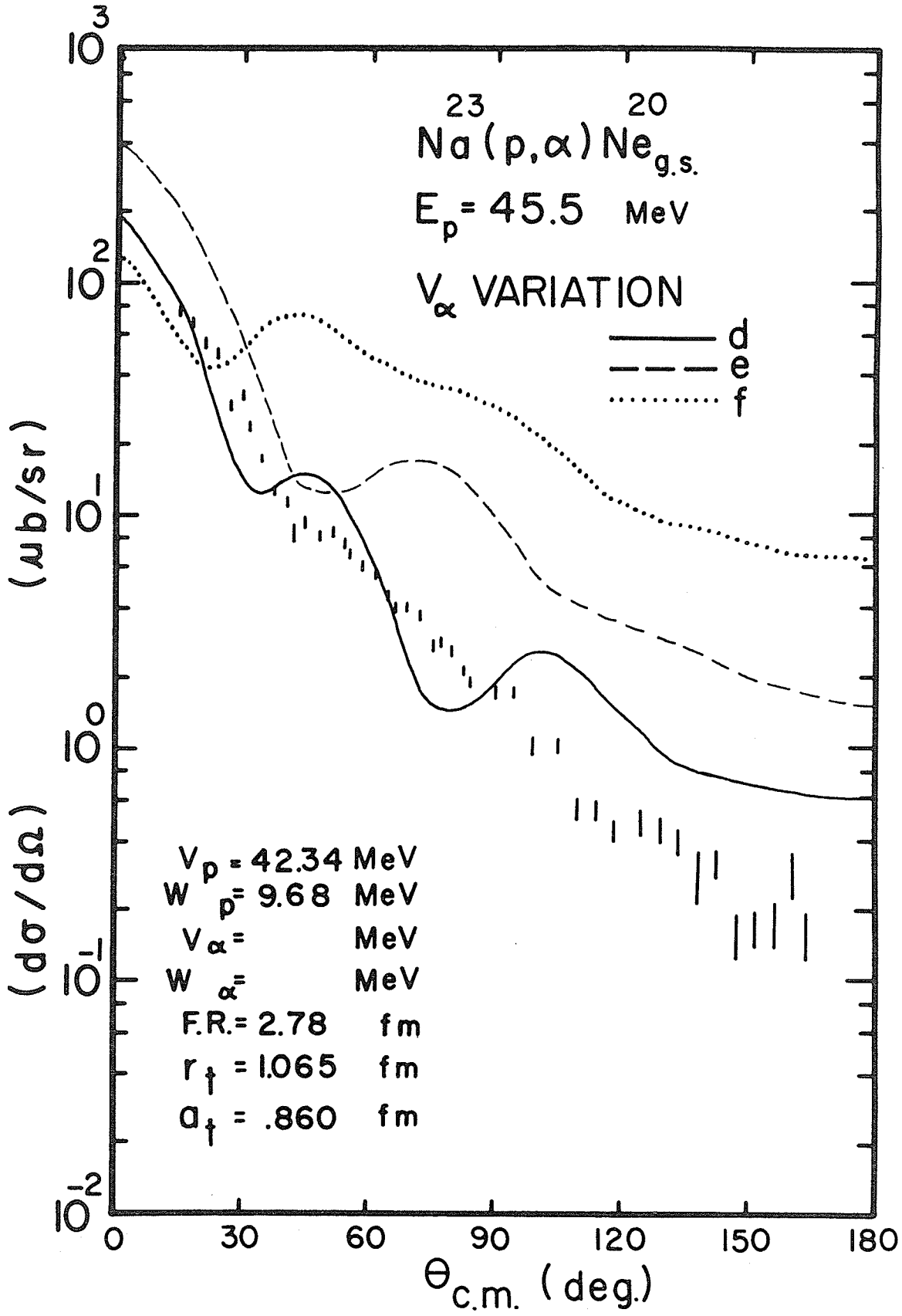
$^{23}Na(p,\alpha)^{20}Ne_{g.s.}$
$E_p = 45.5$ MeV
V_α VARIATION
d
e
f
$V_p = 42.34$ MeV
$W_p = 9.68$ MeV
$V_\alpha =$ MeV
$W_\alpha =$ MeV
F.R. = 2.78 fm
$r_f = 1.065$ fm
$a_f = .860$ fm
$(d\sigma/d\Omega)$ $(\mu b/sr)$
10^3
10^2
10^1
10^0
10^{-1}
10^{-2}
0
30
60
90
120
150
180
$\theta_{c.m.}$ (deg.)

Figure 4.53

The effect of varying the bound state parameter r_t on the theoretical angular distribution.

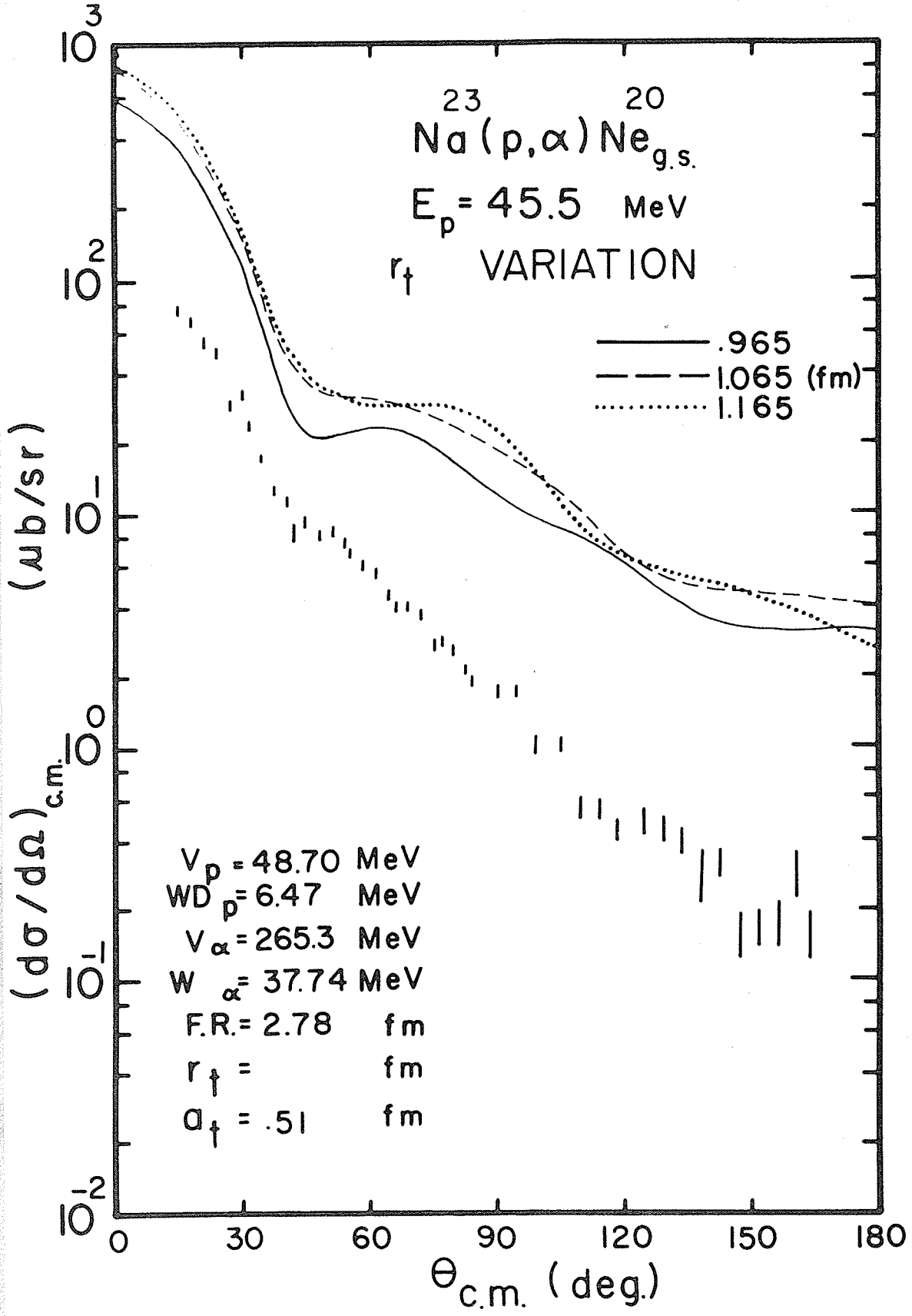
$^{23}Na(p,\alpha)^{20}Ne_{g.s.}$
$E_p = 45.5$ MeV
r_t VARIATION
.965
1.065 (fm)
1.165
$V_p = 48.70$ MeV
$WD_p = 6.47$ MeV
$V_\alpha = 265.3$ MeV
$W_\alpha = 37.74$ MeV
F.R. = 2.78 fm
r_t = fm
a_t = .51 fm
$(d\sigma/d\Omega)_{c.m.}$ (μb/sr)
$\theta_{c.m.}$ (deg.)
10^3
10^2
10^1
10^0
10^{-1}
10^{-2}
0
30
60
90
120
150
180

Figure 4.54

The effect of varying the bound state parameter a_t on the theoretical angular distribution.

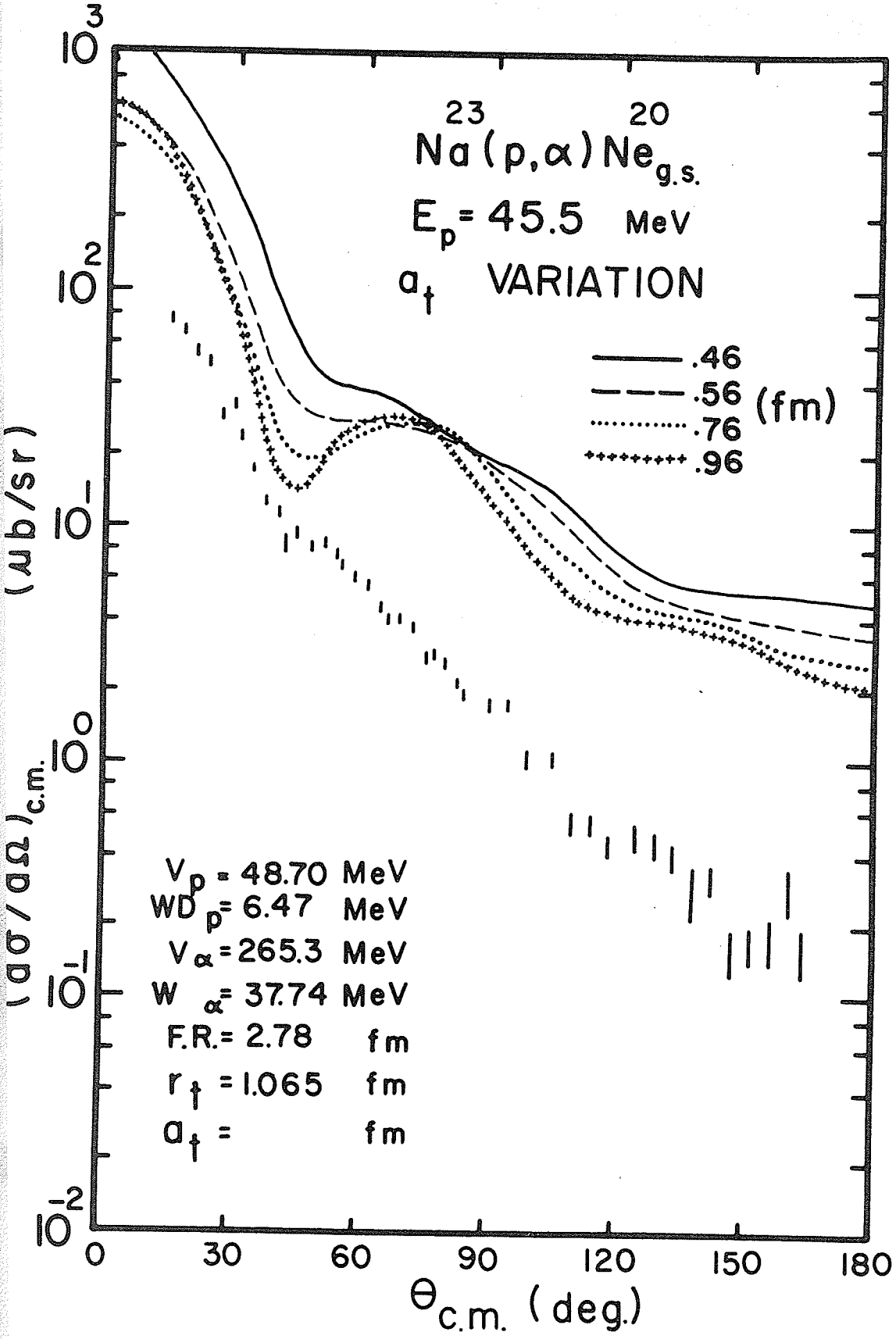
$^{23}Na(p,\alpha)^{20}Ne_{g.s.}$
$E_p = 45.5$ MeV
a_t VARIATION
.46
.56 (fm)
.76
.96
$V_p = 48.70$ MeV
$WD_p = 6.47$ MeV
$V_\alpha = 265.3$ MeV
$W_\alpha = 37.74$ MeV
F.R. = 2.78 fm
$r_t = 1.065$ fm
$a_t =$ fm
$(d\sigma/d\Omega)_{c.m.}$ (μb/sr)
$\theta_{c.m.}$ (deg.)
10^3
10^2
10^1
10^0
10^{-1}
10^{-2}
0
30
60
90
120
150
180

Figure 4.55

The effect of varying the bound state parameter r_t on the theoretical angular distribution.

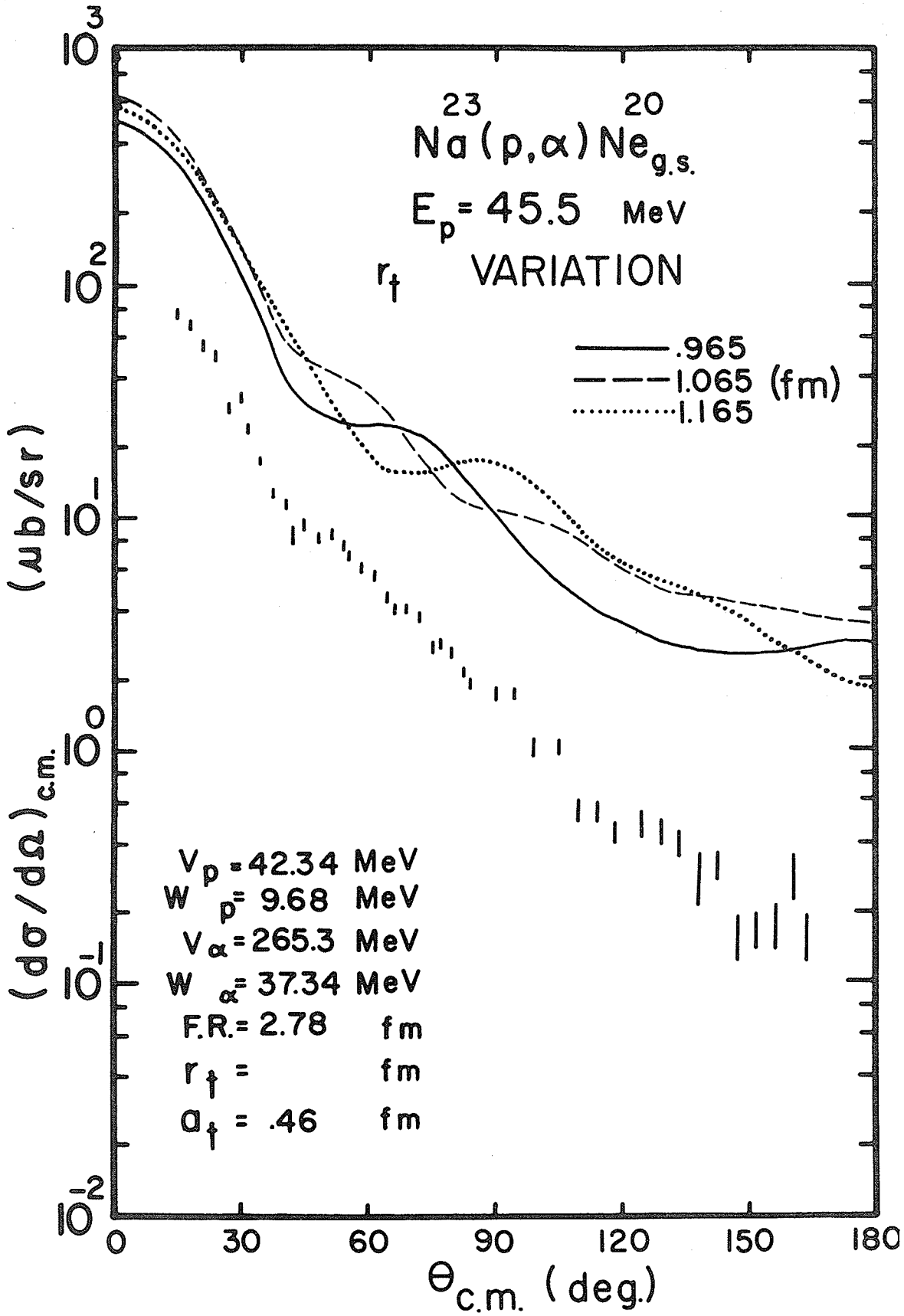
$^{23}Na(p,\alpha)^{20}Ne_{g.s.}$
$E_p = 45.5$ MeV
r_t VARIATION
.965
1.065 (fm)
1.165
$V_p = 42.34$ MeV
$W_p = 9.68$ MeV
$V_\alpha = 265.3$ MeV
$W_\alpha = 37.34$ MeV
F.R. = 2.78 fm
r_t = fm
a_t = .46 fm
$(d\sigma/d\Omega)_{c.m.}$ (μb/sr)
$\theta_{c.m.}$ (deg.)
10^3
10^2
10^1
10^0
10^{-1}
10^{-2}
0
30
60
90
120
150
180

Figure 4.56

The effect of varying the bound state parameter a_t on the theoretical angular distribution.

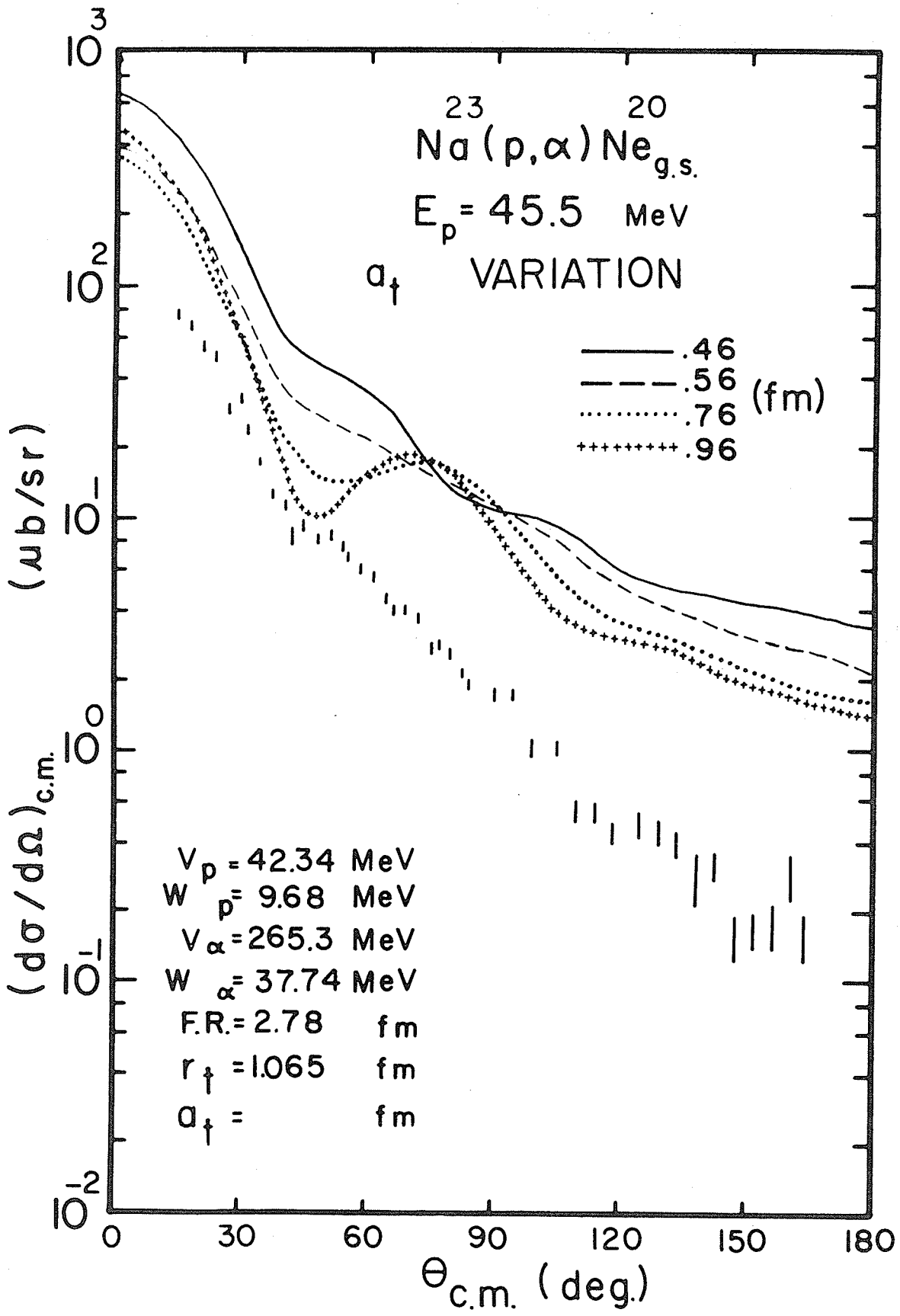
$^{23}Na(p,\alpha)^{20}Ne_{g.s.}$
$E_p = 45.5$ MeV
a_t VARIATION
.46
.56
.76
.96
(fm)
$V_p = 42.34$ MeV
$W_p = 9.68$ MeV
$V_\alpha = 265.3$ MeV
$W_\alpha = 37.74$ MeV
F.R. = 2.78 fm
$r_t = 1.065$ fm
$a_t =$ fm
$(d\sigma/d\Omega)_{c.m.}$ (μb/sr)
$\theta_{c.m.}$ (deg.)
10^3
10^2
10^1
10^0
10^{-1}
10^{-2}
0
30
60
90
120
150
180

The results of a DWBA calculation for $V_\alpha \approx 200$ MeV ($W_\alpha = 0$) for the case where we used the set of proton parameters having $WD_p = 0$ are shown in Figures 4.57 and 4.58. The agreement with the experimental angular distribution near 45° c.m. was found to be unsatisfactory no matter what values of r_t and a_t one used.

For the case $V_\alpha \approx 200$ MeV ($WD_\alpha = 0$) and using the proton set having $W_p = 0$ the fits to the forward angle were quite unsatisfactory. This result is illustrated in Figures 4.59 and 4.60. However, when we choose the alternate proton parameters (those for which $WD_p = 0$) an overall improvement in the fit to the experimental results was observed. This is illustrated in Figures 4.61 and 4.62 where one should take particular note of the fit for $r_t = 1.065$ fm and $a_t = .46$ fm. Except for the extreme forward angles, the fit is quite satisfactory (disregarding, as usual, the overall normalization).

An important observation to make at this point is to note that the parameters which gave the best fit to the analysis of ^{27}Al are almost identical to the ones which gave a good fit for ^{23}Na.

For convenience we list here the corresponding salient parameters.

Figure 4.57

The effect of varying the bound state parameter r_t on the theoretical angular distribution.

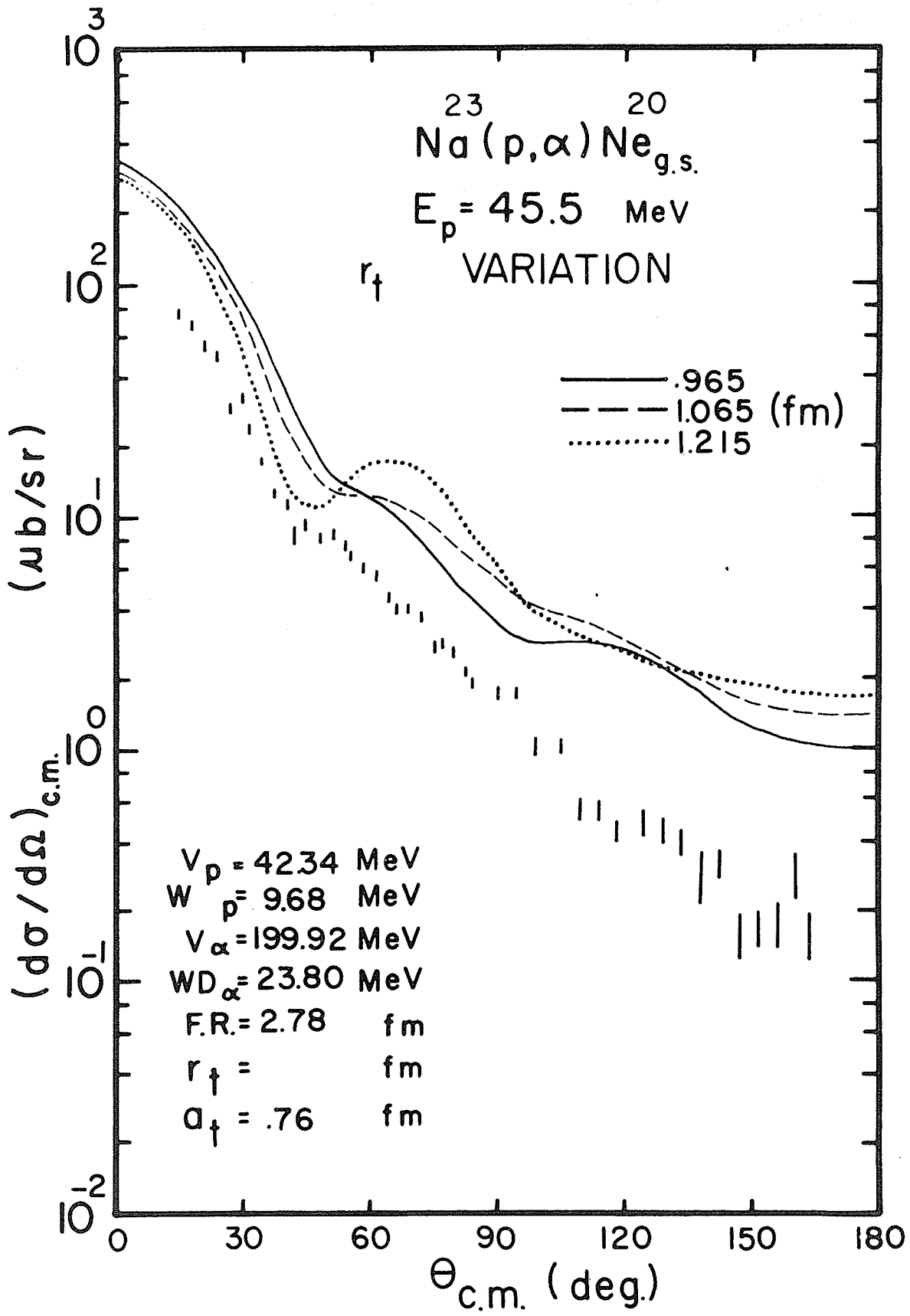
$^{23}Na(p,\alpha)^{20}Ne_{g.s.}$
$E_p = 45.5$ MeV
r_t VARIATION
.965
1.065 (fm)
1.215
$V_p = 42.34$ MeV
$W_p = 9.68$ MeV
$V_\alpha = 199.92$ MeV
$WD_\alpha = 23.80$ MeV
F.R. = 2.78 fm
r_t = fm
a_t = .76 fm
$(d\sigma/d\Omega)_{c.m.}$ (μb/sr)
$\theta_{c.m.}$ (deg.)
10^3
10^2
10^1
10^0
10^{-1}
10^{-2}
0
30
60
90
120
150
180

Figure 4.58

The effect of varying the bound state parameter a_t on the theoretical angular distribution.

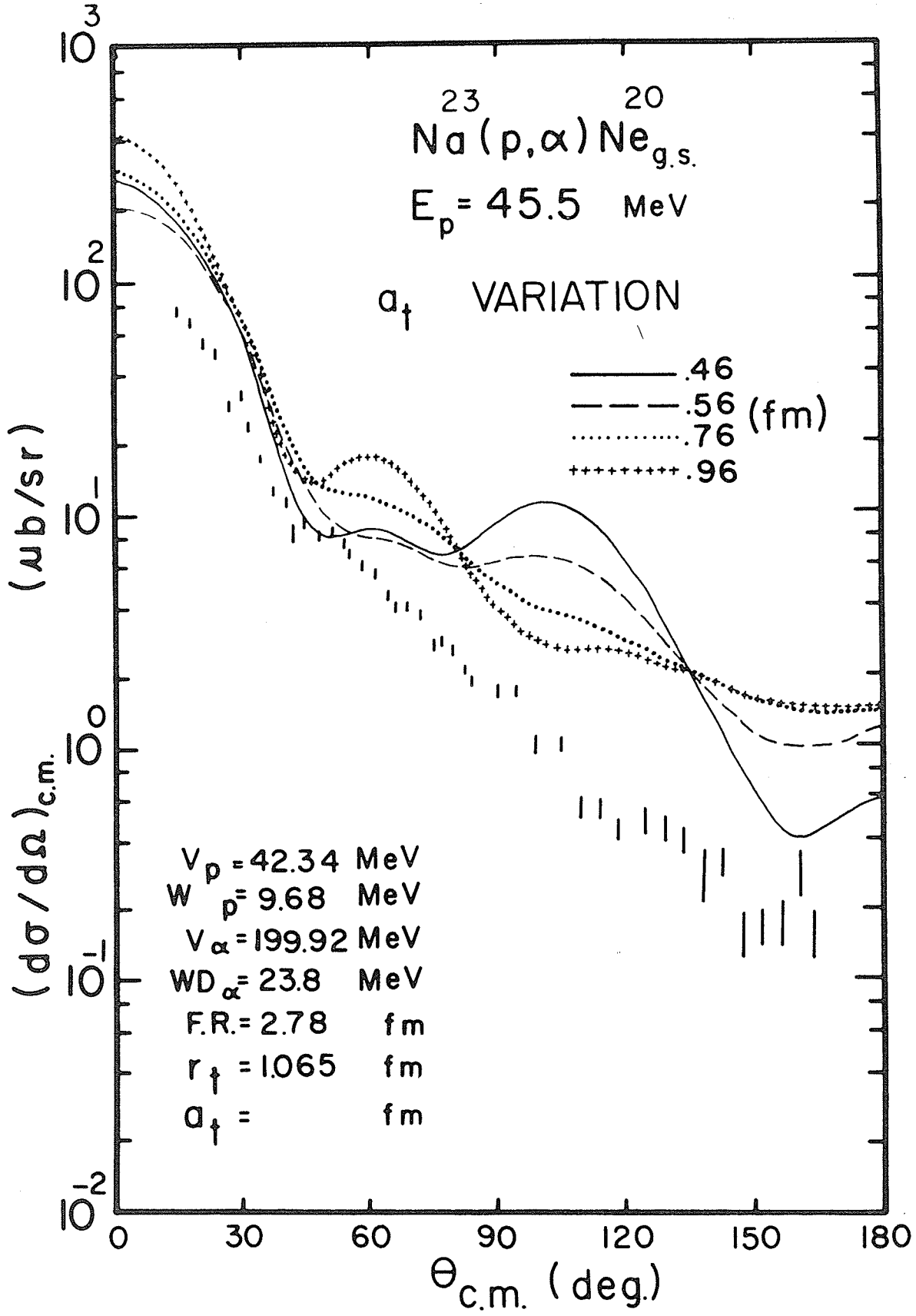
$^{23}Na(p,\alpha)^{20}Ne_{g.s.}$
$E_p = 45.5$ MeV
a_t VARIATION
.46
.56 (fm)
.76
.96
$V_p = 42.34$ MeV
$W_p = 9.68$ MeV
$V_\alpha = 199.92$ MeV
$WD_\alpha = 23.8$ MeV
F.R. = 2.78 fm
$r_t = 1.065$ fm
$a_t =$ fm
$(d\sigma/d\Omega)_{c.m.}$ (μb/sr)
$\theta_{c.m.}$ (deg.)
10^3
10^2
10^1
10^0
10^{-1}
10^{-2}
0
30
60
90
120
150
180

Figure 4.59

The effect of varying the bound state parameter r_t on the theoretical angular distribution.

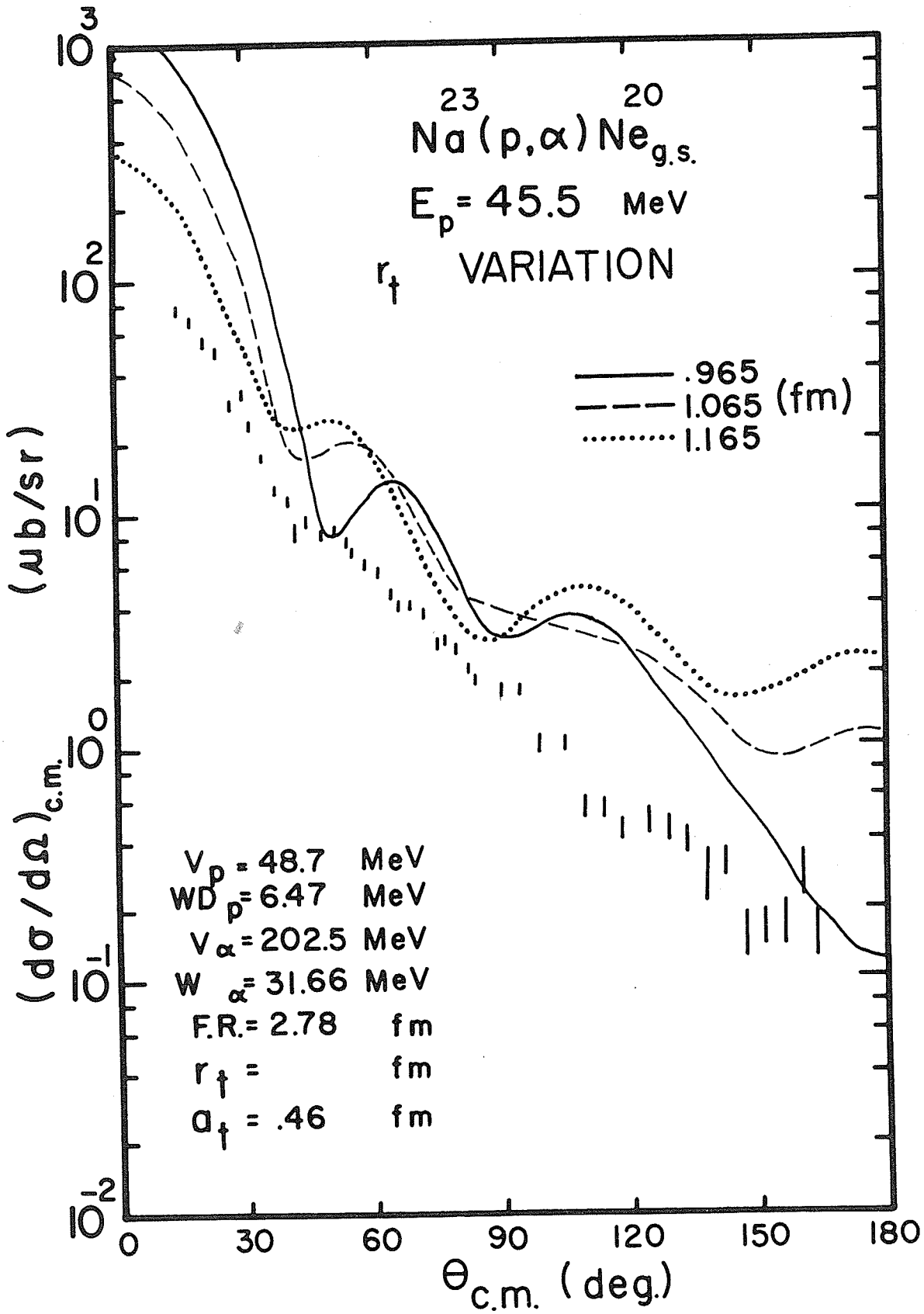
$^{23}Na(p,\alpha)^{20}Ne_{g.s.}$
$E_p = 45.5$ MeV
r_t VARIATION
.965
1.065 (fm)
1.165
$V_p = 48.7$ MeV
$WD_p = 6.47$ MeV
$V_\alpha = 202.5$ MeV
$W_\alpha = 31.66$ MeV
F.R. = 2.78 fm
r_t = fm
a_t = .46 fm
$(d\sigma/d\Omega)_{c.m.}$ (μb/sr)
$\Theta_{c.m.}$ (deg.)
10^3
10^2
10^1
10^0
10^{-1}
10^{-2}
0
30
60
90
120
150
180

Figure 4.60

The effect of varying the bound state parameter a_t on the theoretical angular distribution.

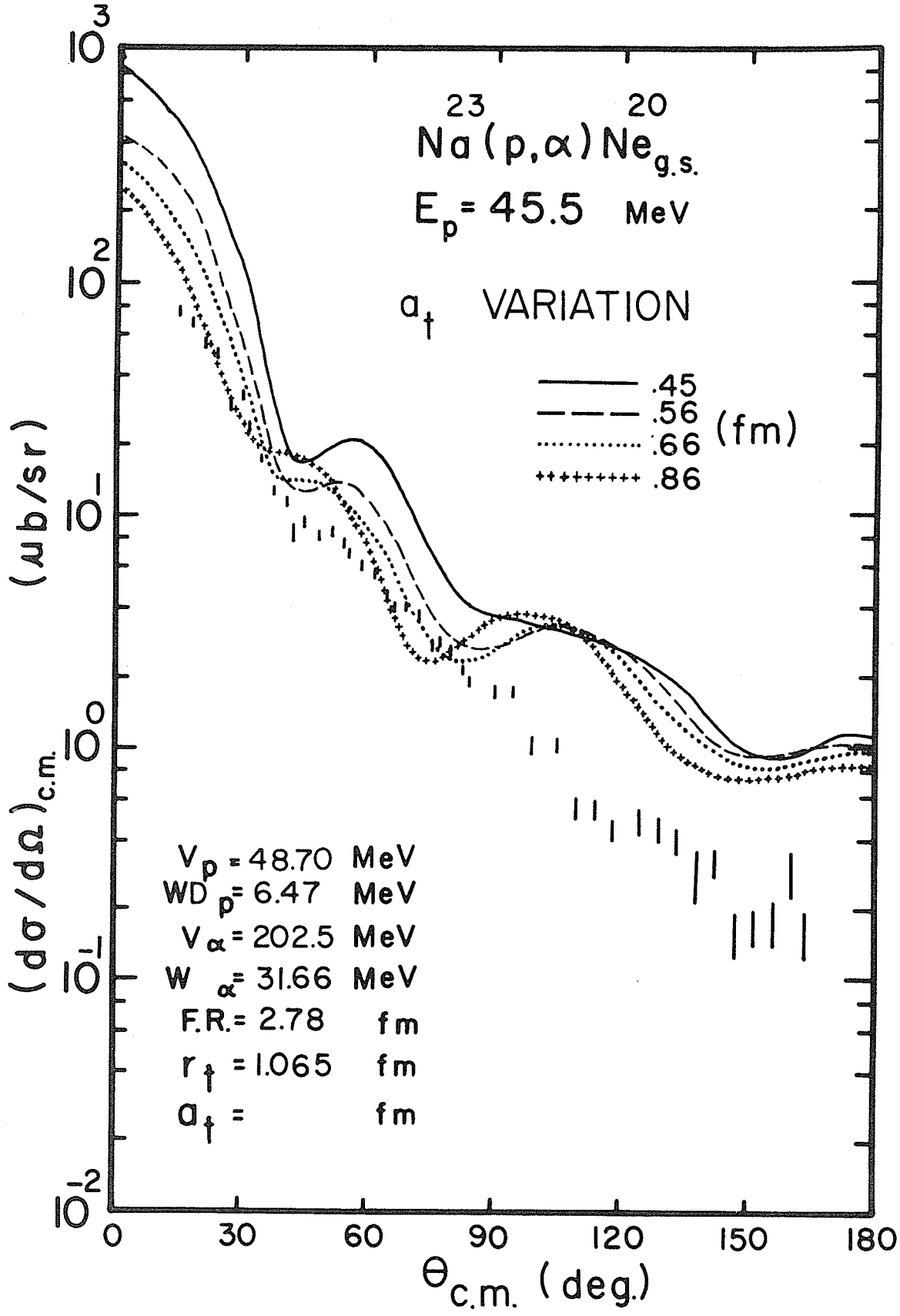
$^{23}Na(p,\alpha)^{20}Ne_{g.s.}$
$E_p = 45.5$ MeV
a_t VARIATION
.45
.56
.66
.86
(fm)
$V_p = 48.70$ MeV
$WD_p = 6.47$ MeV
$V_\alpha = 202.5$ MeV
$W_\alpha = 31.66$ MeV
F.R. = 2.78 fm
$r_t = 1.065$ fm
$a_t =$ fm
$(d\sigma/d\Omega)_{c.m.}$ (μb/sr)
$\theta_{c.m.}$ (deg.)
10^3
10^2
10^1
10^0
10^{-1}
10^{-2}
0
30
60
90
120
150
180

Figure 4.61

The effect of varying the bound state parameter r_t on the theoretical angular distribution.

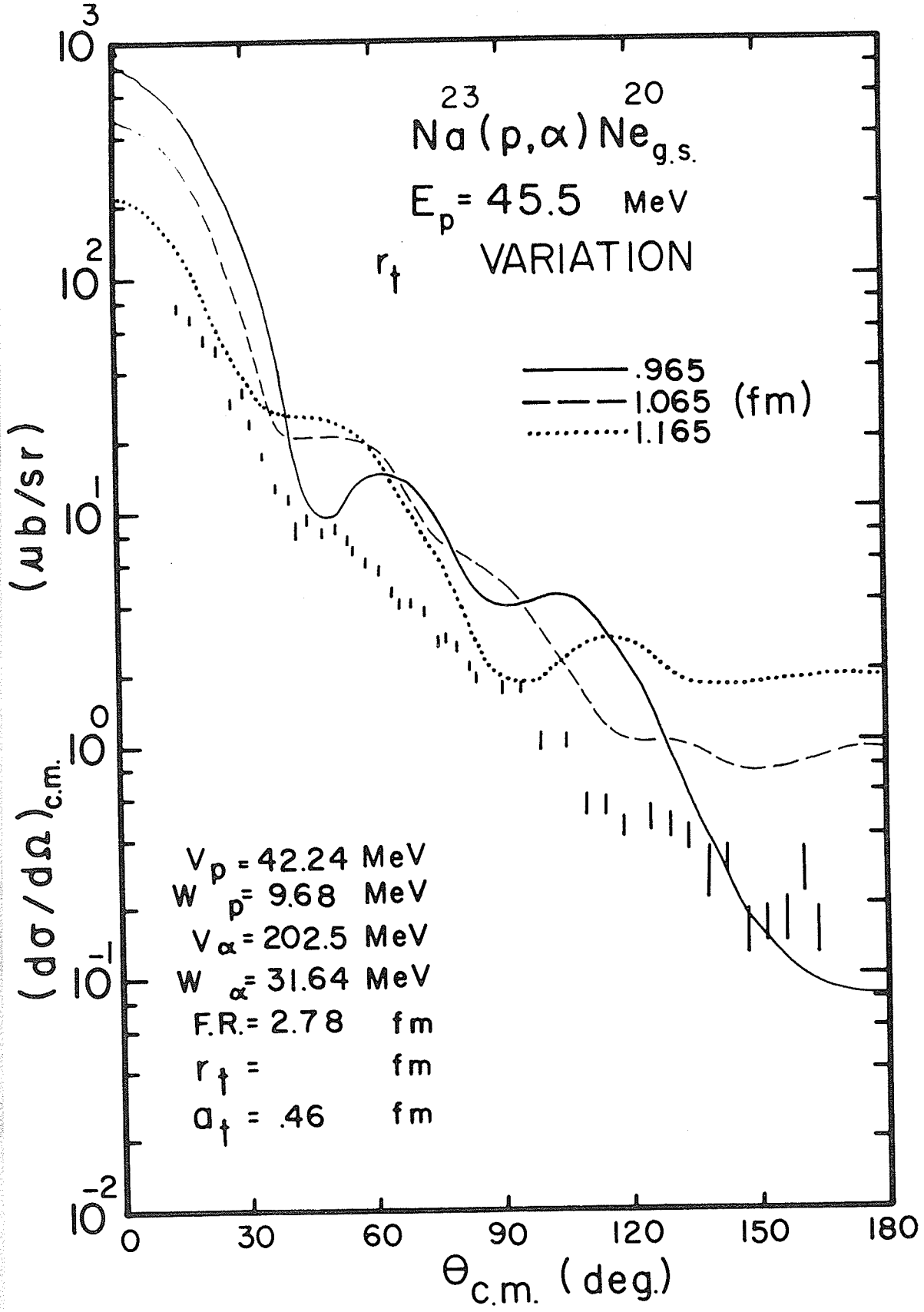
$^{23}Na(p,\alpha)^{20}Ne_{g.s.}$
$E_p = 45.5$ MeV
r_t VARIATION
.965
1.065 (fm)
1.165
$V_p = 42.24$ MeV
$W_p = 9.68$ MeV
$V_\alpha = 202.5$ MeV
$W_\alpha = 31.64$ MeV
F.R. = 2.78 fm
r_t = fm
a_t = .46 fm
$(d\sigma/d\Omega)_{c.m.}$ (μb/sr)
$\theta_{c.m.}$ (deg.)
10^3
10^2
10^1
10^0
10^{-1}
10^{-2}
0
30
60
90
120
150
180

Figure 4.62

The effect of varying the bound state parameter a_t on the theoretical angular distribution.

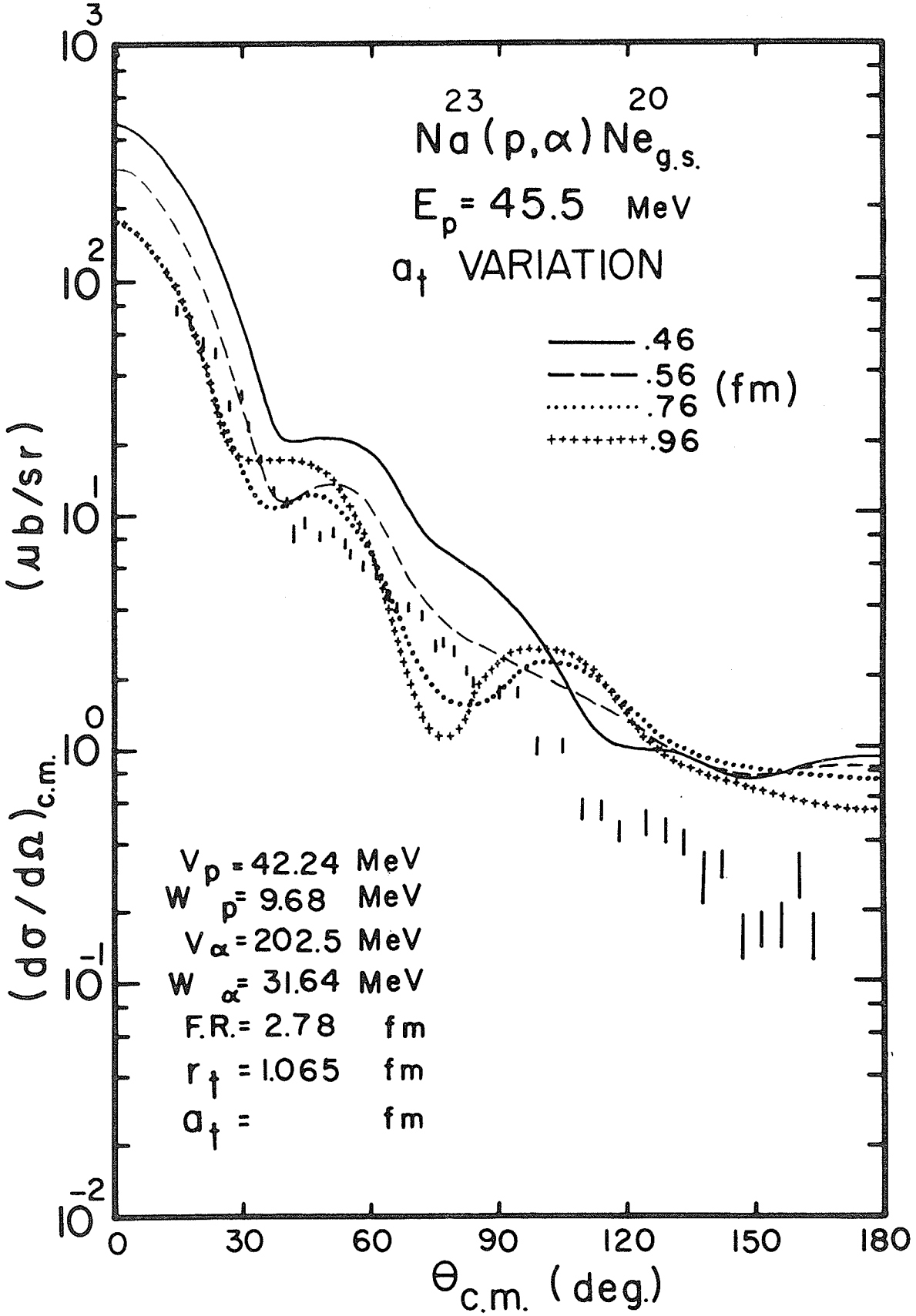
$^{23}Na(p,\alpha)^{20}Ne_{g.s.}$
$E_p = 45.5$ MeV
a_f VARIATION
.46
.56
.76
.96
(fm)
$V_p = 42.24$ MeV
$W_p = 9.68$ MeV
$V_\alpha = 202.5$ MeV
$W_\alpha = 31.64$ MeV
F.R. = 2.78 fm
$r_f = 1.065$ fm
$a_f =$ fm
$(d\sigma/d\Omega)_{c.m.}$ (μb/sr)
$\theta_{c.m.}$ (deg.)
10^3
10^2
10^1
10^0
10^{-1}
10^{-2}
0
30
60
90
120
150
180

		^{27}Al	^{23}Na	
V_p	=	40.93	42.24	MeV
W_p	=	9.76	9.68	MeV
WD_p	=	0.0	0.0	MeV
V_α	=	197.56	202.5	MeV
W_α	=	33.92	31.64	MeV
WD_α	=	0.0	0.0	MeV
r_t	=	1.069	1.065	fm
a_t	=	.45	.46	fm

Notice also that both r_t values are identical to those extracted from the literature of ^{3}He optical model scattering fits to the corresponding residual nuclei.

The last case to be dealt with in the analysis of ^{23}Na is that of $V_\alpha \approx 200$ MeV ($W_\alpha = 0$) where the proton set of parameters is the one having $W_p = 0$. Although the identical case, except then we had $WD_p = 0$, has already been dealt with and found to give unsatisfactory agreement with the experimental results near 45° c.m. we now find the fit has improved to the point where it warrants serious consideration in the extraction of the corresponding experimental spectroscopic factor. (Figures 4.63 and 4.64)

To summarize then, there are three acceptable fits, shown, with their corresponding parameters and experimental spectroscopic factors, in Figure 4.65.

Figure 4.63

The effect of varying the bound state parameter r_t on the theoretical angular distribution.

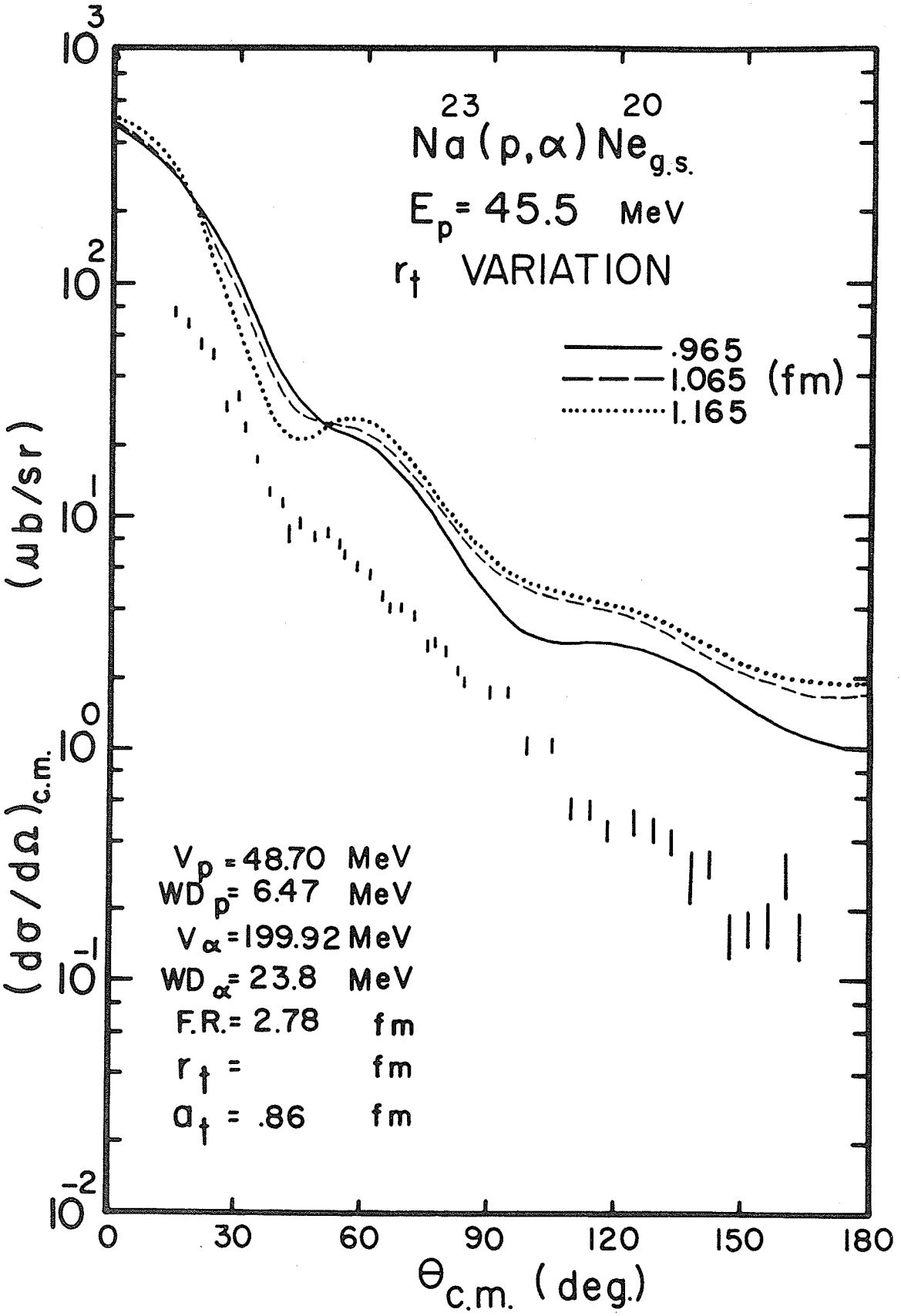
$^{23}Na(p,\alpha)^{20}Ne_{g.s.}$
$E_p = 45.5$ MeV
r_t VARIATION
.965
1.065 (fm)
1.165
$V_p = 48.70$ MeV
$WD_p = 6.47$ MeV
$V_\alpha = 199.92$ MeV
$WD_\alpha = 23.8$ MeV
F.R. = 2.78 fm
r_t = fm
a_t = .86 fm
$(d\sigma/d\Omega)_{c.m.}$ (μb/sr)
$\theta_{c.m.}$ (deg.)
10^3
10^2
10^1
10^0
10^{-1}
10^{-2}
0
30
60
90
120
150
180

Figure 4.64

The effect of varying the bound state parameter a_t on the theoretical angular distribution.

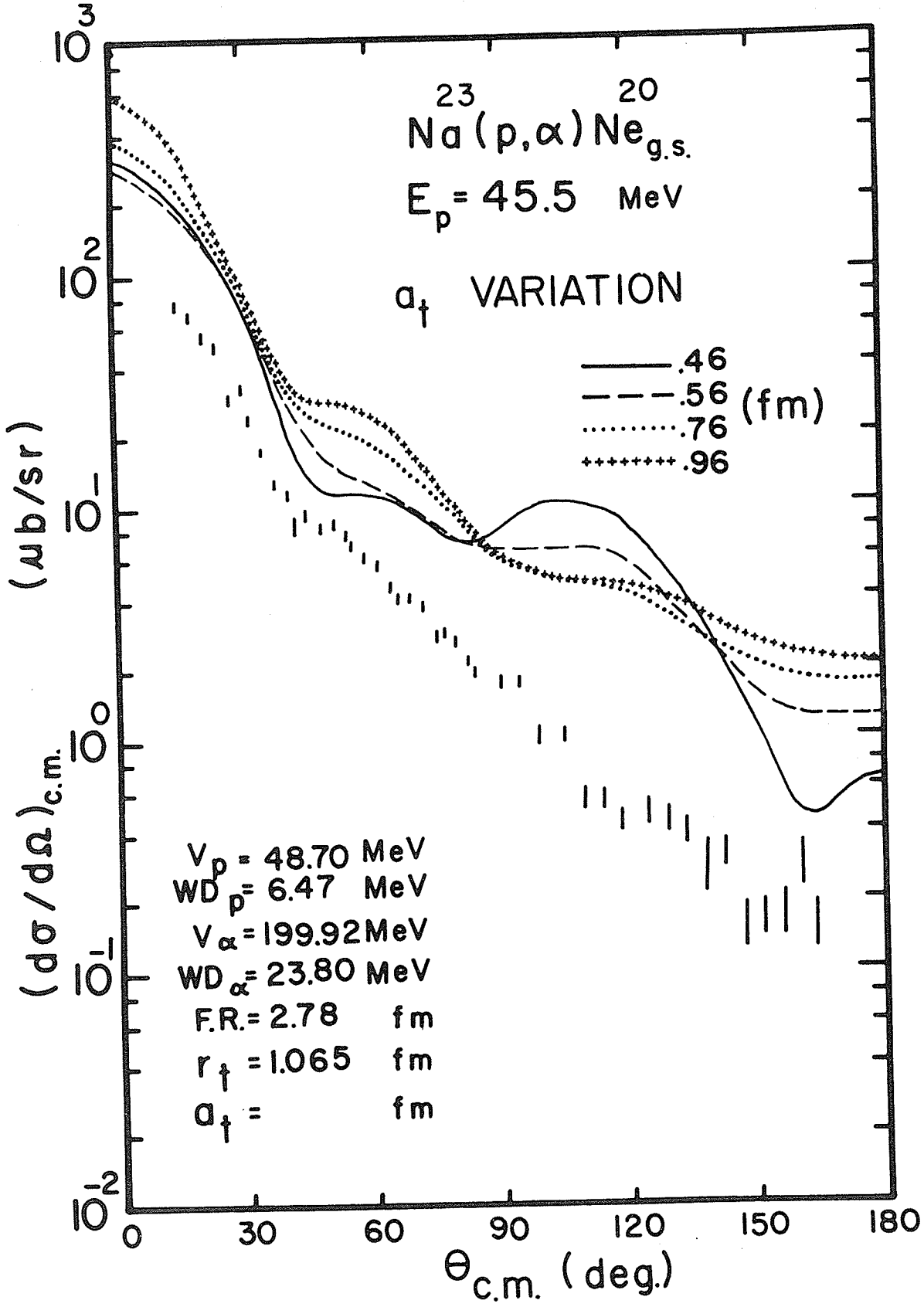
$^{23}Na(p,\alpha)^{20}Ne_{g.s.}$
$E_p = 45.5$ MeV
a_t VARIATION
.46
.56 (fm)
.76
.96
V_p = 48.70 MeV
WD_p = 6.47 MeV
V_α = 199.92 MeV
WD_α = 23.80 MeV
F.R. = 2.78 fm
r_t = 1.065 fm
a_t = fm
$(d\sigma/d\Omega)_{c.m.}$ (μb/sr)
$\theta_{c.m.}$ (deg.)
10^3
10^2
10^1
10^0
10^{-1}
10^{-2}
0
30
60
90
120
150
180

Figure 4.65

Shows the three fits considered for the extraction of the Experimental spectroscopic factor.

Fit c represents the best fit.

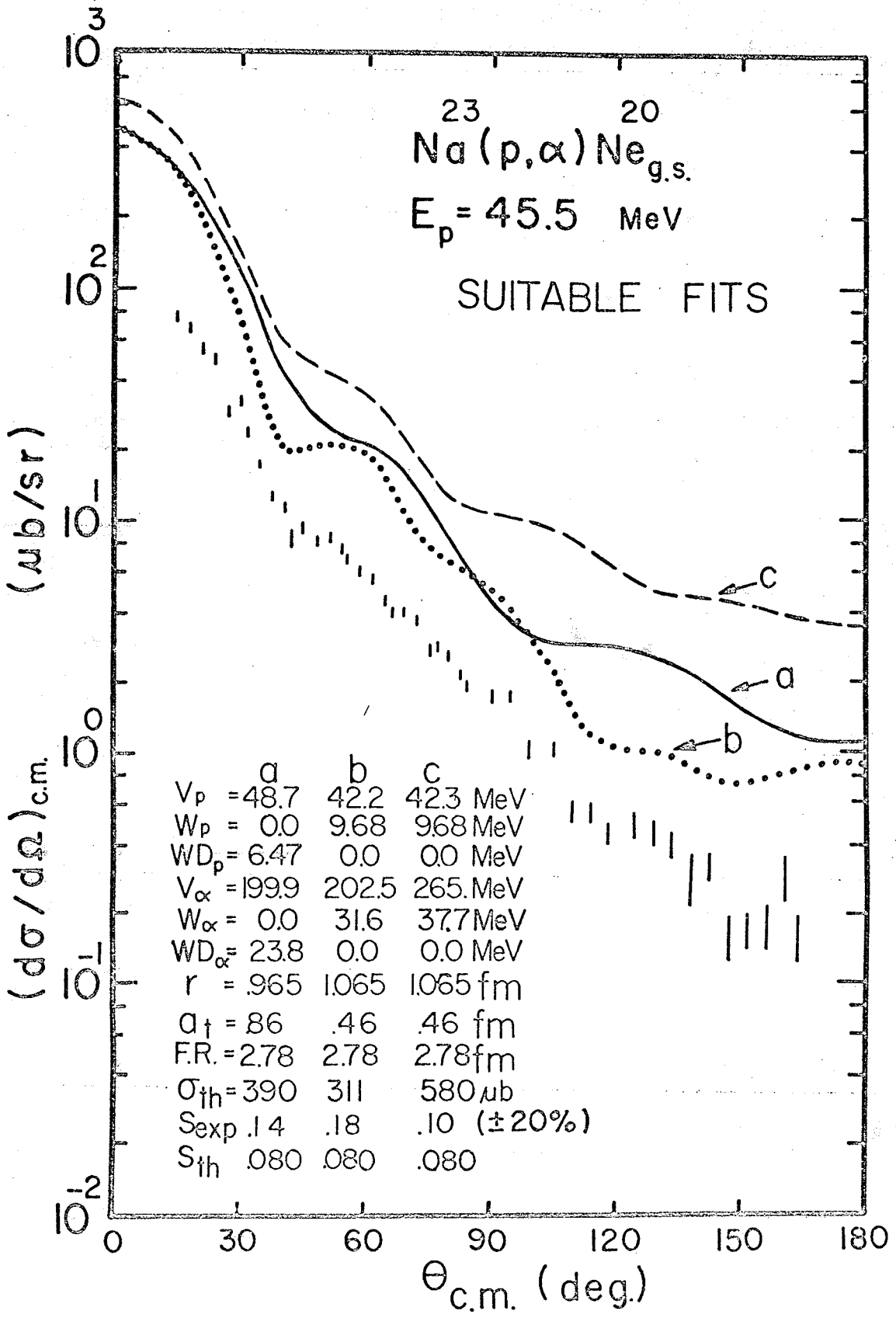
$^{23}Na(p,\alpha)^{20}Ne_{g.s.}$
$E_p = 45.5$ MeV
SUITABLE FITS
$(d\sigma/d\Omega)_{c.m.}$ (μb/sr)
$\theta_{c.m.}$ (deg.)
a
b
c
a b c
V_p =48.7 42.2 42.3 MeV
W_p = 0.0 9.68 9.68 MeV
WD_p= 6.47 0.0 0.0 MeV
V_α =199.9 202.5 265. MeV
W_α = 0.0 31.6 37.7 MeV
WD_α= 23.8 0.0 0.0 MeV
r = .965 1.065 1.065 fm
a_t = .86 .46 .46 fm
F.R. =2.78 2.78 2.78 fm
σ_{th}=390 311 580 μb
Sexp .14 .18 .10 (±20%)
S_{th} .080 .080 .080

The theoretical spectroscopic factor of .080 was calculated[73] assuming jj coupling and SHM wave functions for the three transferred nucleons. The structure of ^{23}Na was assumed to have the form

$$^{20}\text{Ne core} + \left[(1d_{\frac{5}{2}})^2\right]^{J_n=0}_{\text{SENIORITY}=0} + \text{proton in Nilsson orbit 7 } (3/2^+) \quad *$$

The agreement between the theoretical spectroscopic factor (.080) and the experimental spectroscopic factor for our best fit to the ^{23}Na(p,α)^{20}Ne$_{gs}$ angular distribution (.10±.02) in good agreement.

* As was the case for ^{27}Al (page 111), the expansion of the Nilsson model orbit 7, in terms of shell model wave functions, has as its largest component the d5/2 state.

C Analysis of ^{58}Ni (p,α) $^{55}Co_{g.s.}$

Since $J_i^\pi = 0^+$ and $J_f^\pi = {}^7/_2^-$ we have, on the assumption that the (p,α) reaction proceeds via the pick-up of two $p^3/_2$ and one $f^7/_2$ nucleon, that $l_t = 3$ and RADNOD = 3 (see Appendix 4.a).

As usual we used as a guide for the bound state parameters the values extracted from optical model fits to the elastic scattering of a 3-nucleon cluster from the residual nucleus. In this case we used the values $a_t = .909$ fm and $r_t = 1.059$ fm given by Baugh et al[50] for ^3He elastic scattering from ^{56}Fe.

Proton Channel Optical Parameters

Optical model fits to the elastic scattering data of 40 MeV protons on ^{58}Ni by Blumberg et al[48] was used to extract the proton optical parameters. Using as starting values the parameters given by Fricke and Satchler[51], except that we dropped the spin parameters, we obtained the fits tabulated in Table 4.6 and shown in Figures 4.66 - 4.70. Fits c and d are the result of searches initiated by the use of the "average" parameters given in reference 51.

Alpha Channel Optical Parameters

The laboratory alpha particle energy of the inverse reaction giving the required center of mass energy is 42.1 MeV (see Appendix 4.b). Since data

TABLE 4.6

Tabulation of the sets of optical model parameters giving the best fits to the experimental elastic scattering of 40 MeV protons from ^{58}Ni.

TABLE 4.6

OPTICAL PARAMETERS GIVING BEST FITS TO THE EXPERIMENTAL DATA OF BLUMBERG *et al*[48]) --- THE ELASTIC SCATTERING OF 40 MeV PROTONS FROM ^{58}Ni

FIT	a	b	c	d	e
V_o (MeV)	38.94	45.64	44.79	40.89	43.34
r_o (fm)	1.231	1.178	1.175	1.197	1.203
a_o (fm)	.7537	.7467	.7193	.7898	.7242
W_v (MeV)	11.10	—	—	11.69	2.28
r_v (fm)	1.384	—	—	1.367	1.089
a_v (fm)	.2511	—	—	.6832	.5691
W_s (MeV)	—	11.34	8.72	—	8.89
r_s (fm)	—	1.030	1.044	—	1.089
a_s (fm)	—	.6238	.7155	—	.5691
r_c (fm)	1.2	1.2	1.2	1.2	1.2
χ^2 (arb.)	5.45	9.66	7.82	4.37	8.74

FIGURE 4.66

Optical Model fit to the 40 MeV proton elastic scattering from ^{58}Ni.

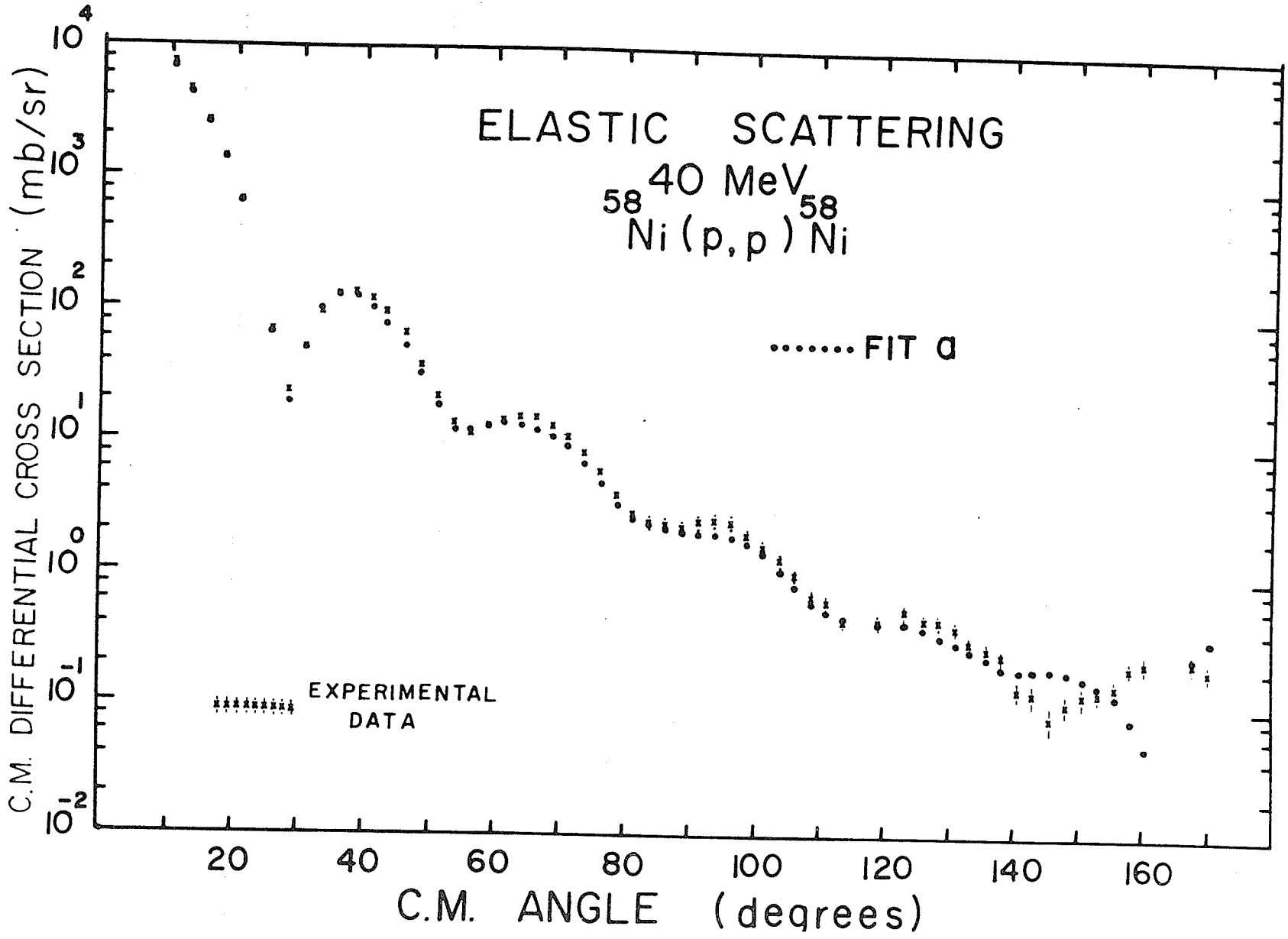
ELASTIC SCATTERING
40 MeV
58Ni(p,p)58Ni
FIT a
EXPERIMENTAL DATA
C.M. DIFFERENTIAL CROSS SECTION (mb/sr)
C.M. ANGLE (degrees)
10^4
10^3
10^2
10^1
10^0
10^-1
10^-2
20
40
60
80
100
120
140
160

FIGURE 4.67

Optical Model fit to the 40 MeV proton elastic scattering from ^{58}Ni.

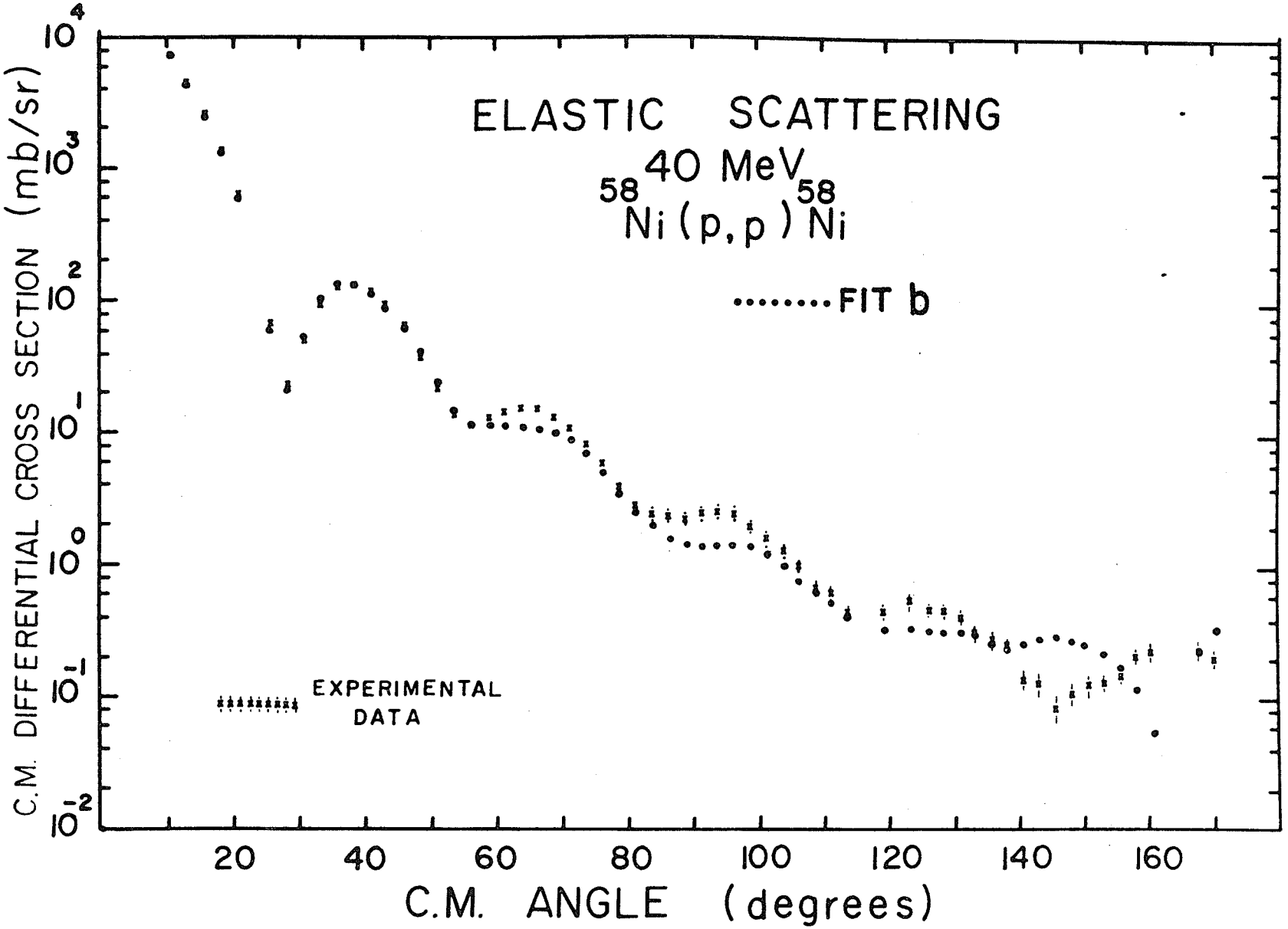
ELASTIC SCATTERING
40 MeV
58Ni(p,p)58Ni
.....FIT b
EXPERIMENTAL DATA
C.M. DIFFERENTIAL CROSS SECTION (mb/sr)
C.M. ANGLE (degrees)
10^4
10^3
10^2
10^1
10^0
10^-1
10^-2
20
40
60
80
100
120
140
160

FIGURE 4.68

Optical Model fit to the 40 MeV proton elastic scattering from ^{58}Ni.

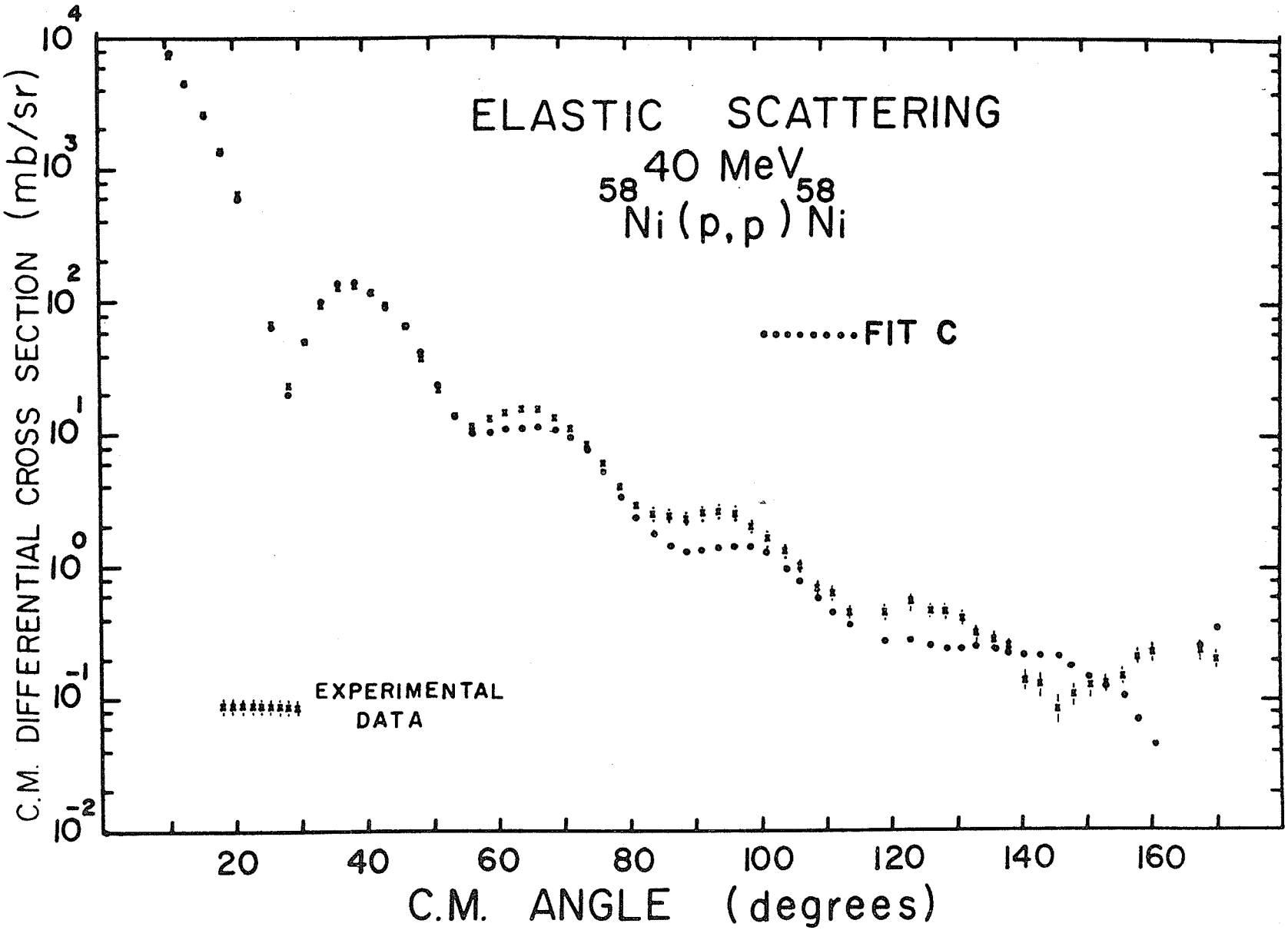
ELASTIC SCATTERING
40 MeV
58Ni(p,p)58Ni
FIT C
EXPERIMENTAL DATA
C.M. DIFFERENTIAL CROSS SECTION (mb/sr)
C.M. ANGLE (degrees)
10^4
10^3
10^2
10^1
10^0
10^-1
10^-2
20
40
60
80
100
120
140
160

FIGURE 4.69

Optical Model fit to the 40 MeV proton elastic scattering from ^{58}Ni.

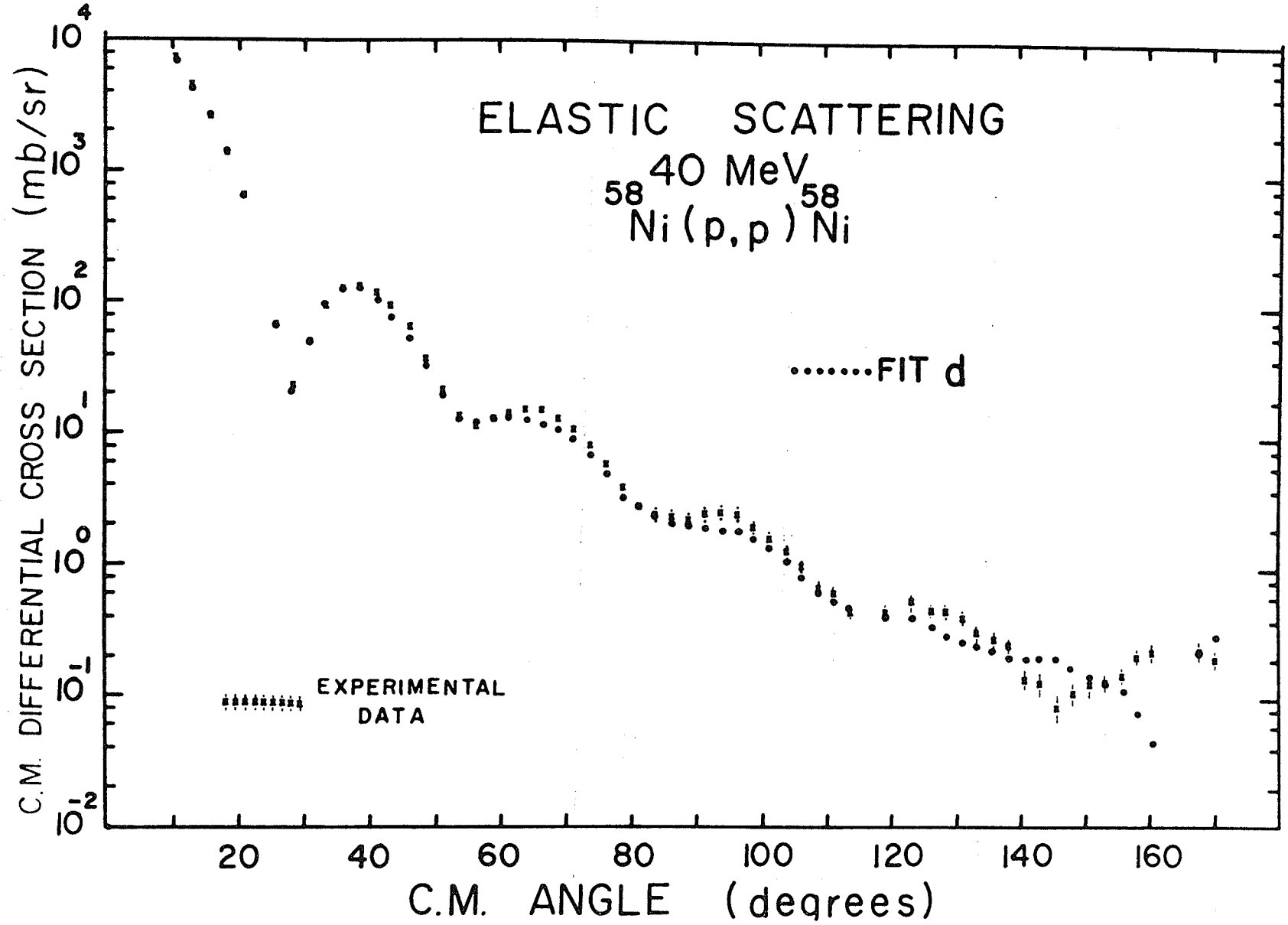
ELASTIC SCATTERING
40 MeV
58Ni(p,p)58Ni
.....FIT d
EXPERIMENTAL DATA
C.M. DIFFERENTIAL CROSS SECTION (mb/sr)
C.M. ANGLE (degrees)
10^4
10^3
10^2
10^1
10^0
10^-1
10^-2
20
40
60
80
100
120
140
160

FIGURE 4.70

Optical Model fit to the 40 MeV proton elastic scattering from ^{58}Ni.

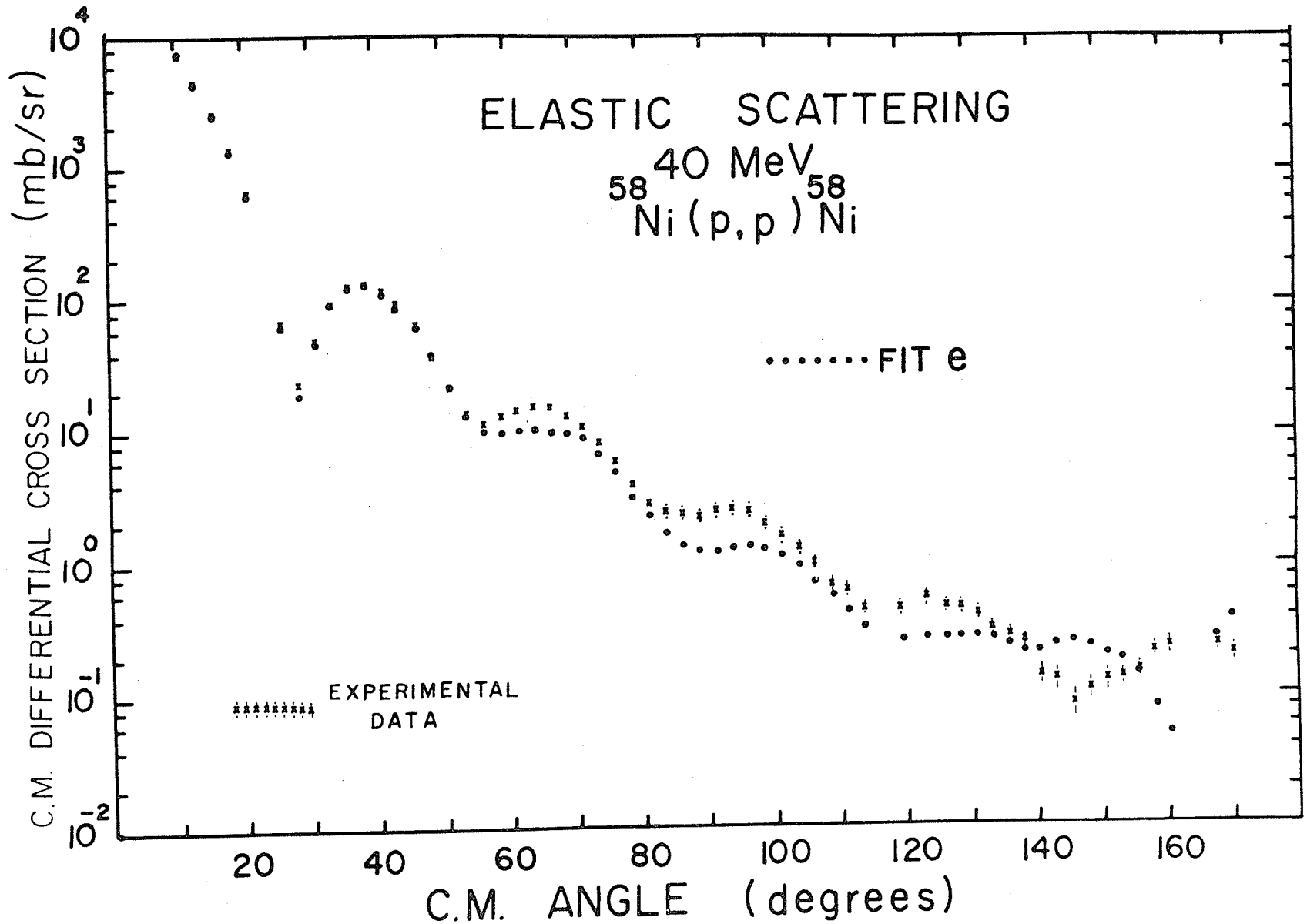
ELASTIC SCATTERING
40 MeV
58Ni(p,p)58Ni
FIT e
EXPERIMENTAL DATA
C.M. DIFFERENTIAL CROSS SECTION (mb/sr)
C.M. ANGLE (degrees)
10^4
10^3
10^2
10^1
10^0
10^-1
10^-2
20
40
60
80
100
120
140
160

was not available for the elastic scattering of alphas from ^{55}Co we used the elastic scattering data on ^{56}Fe for E_α = 44 MeV [49].

A series of searches, initiated at various depths for the real optical potential well (V_α) yielded solutions which grouped about $V_\alpha \simeq 140$, 200 and 260 MeV. Of these many fits we chose two or more from each group (at least one with $WD_\alpha = 0$ and one with $W_\alpha = 0$) which had the better χ^2's. The resultant 9 chosen fits are tabulated in Table 4.7 and shown in Figures 4.71 - 4.79.

DWBA Analysis

As usual, the resultant DWBA calculations were not nearly as sensitive to which set of proton optical parameters was used as they were to which set of alpha optical parameters were used. This effect is shown in Figures 4.80 and 4.81 - 4.82.

A two dimensional manual search, using the bound state parameters r_t and a_t, for each of the five proton sets in combination with each of the nine alpha sets is typifide in Figures 4.83 - 4.84 and resulted in a clear indication which sets of alpha parameters gave the better fits. These were the sets having V_α = 140.39 and V_α = 137.75 MeV (both have pure surface absorption terms).

Figures 4.85 - 4.93 indicate the various fits obtained for two sets of proton parameters, "a" having $WD_p = 0$ and "b" having $W_p = 0$. The corresponding proton parameters are listed in Table 4.6. The various fits

TABLE 4.7

Tabulation of the sets of optical model parameters giving the best fits to the experimental elastic scattering of 44 MeV alphas from ^{56}Fe.

TABLE 4.7

OPTICAL PARAMETERS GIVING BEST FITS
TO THE EXPERIMENTAL DATA OF SACLAY[49]
— THE ELASTIC SCATTERING OF 44 MeV ALPHAS FROM ^{56}Fe

FIT	a	b	c	d	e	f	g	h	j
V_o (MeV)	199.76	246.52	213.94	260.03	140.39	137.75	186.63	148.68	200.6
r_o (fm)	1.4369	1.4256	1.373	1.403	1.396	1.381	1.395	1.420	1.414
a_o (fm)	.5325	.5063	.5707	.5196	.6135	.6310	.5680	.5767	.5402
W_V (MeV)	0.0	0.0	39.6	38.21	0.0	0.0	34.19	30.63	33.83
r_V (fm)	-	-	1.3803	1.369	-	-	1.391	1.424	1.402
a_V (fm)	-	-	.5686	.5006	-	-	.5610	.5744	.5149
W_D (MeV)	61.31	60.73	0.0	0.0	43.72	51.15	0.0	0.0	0.0
r_D (fm)	1.363	1.348	-	-	1.210	1.104	-	-	-
a_D (fm)	.3986	.3984	-	-	.5593	.6280	-	-	-
r_c (fm)	1.4	1.4	1.4	1.4	1.4	1.4	1.4	1.4	1.4
χ^2 (arb.)	14.9	23.6	9.2	15.5	8.0	7.4	8.9	8.5	11.8

FIGURE 4.71

Optical Model fit to the 44 MeV alpha elastic scattering from ^{56}Fe.

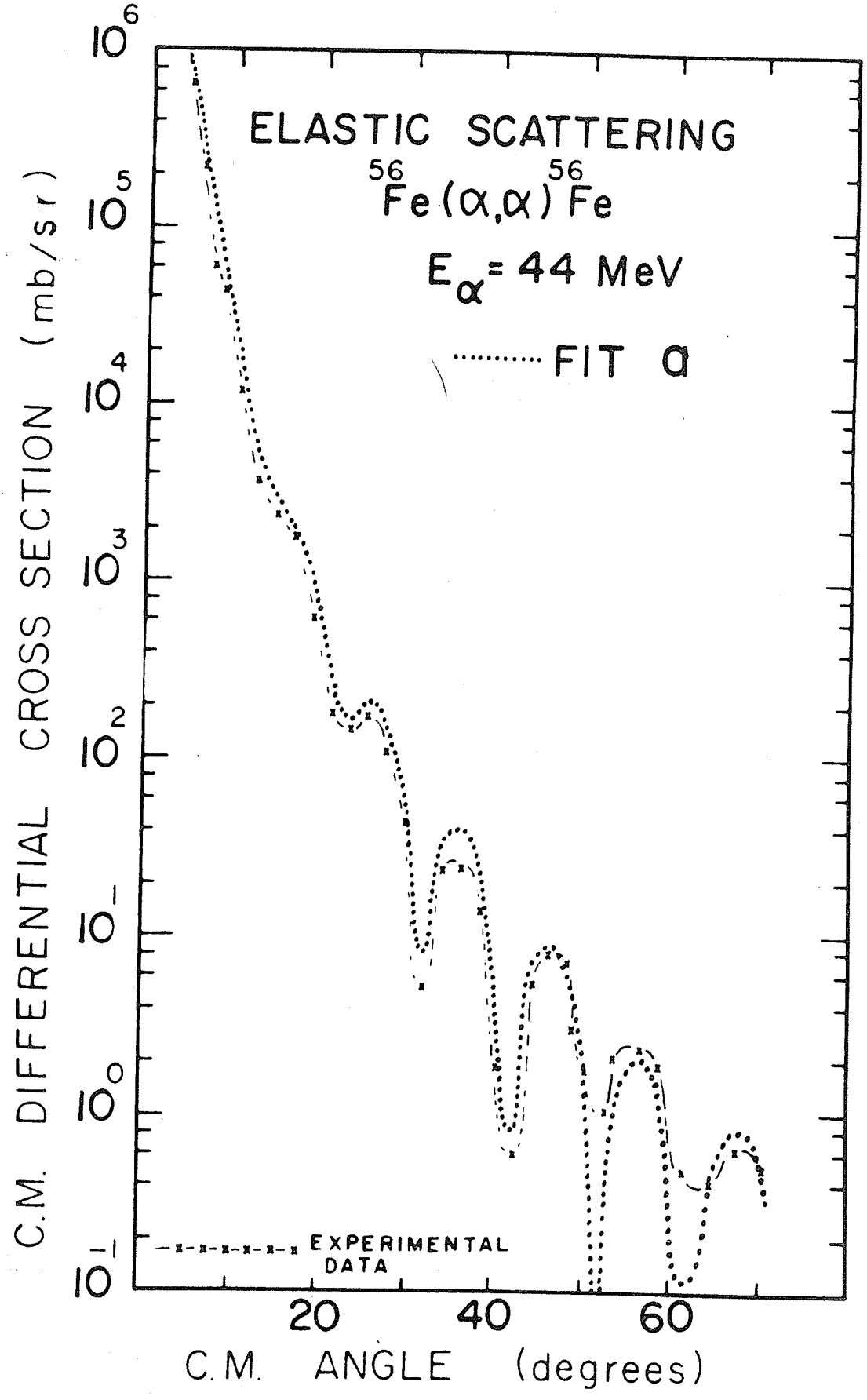
ELASTIC SCATTERING
56 56
Fe(α,α) Fe
Eα = 44 MeV
FIT a
EXPERIMENTAL DATA
C.M. DIFFERENTIAL CROSS SECTION (mb/sr)
C.M. ANGLE (degrees)
10^6
10^5
10^4
10^3
10^2
10^0
20
40
60

FIGURE 4.72

Optical Model fit to the 44 MeV alpha elastic scattering from ^{56}Fe.

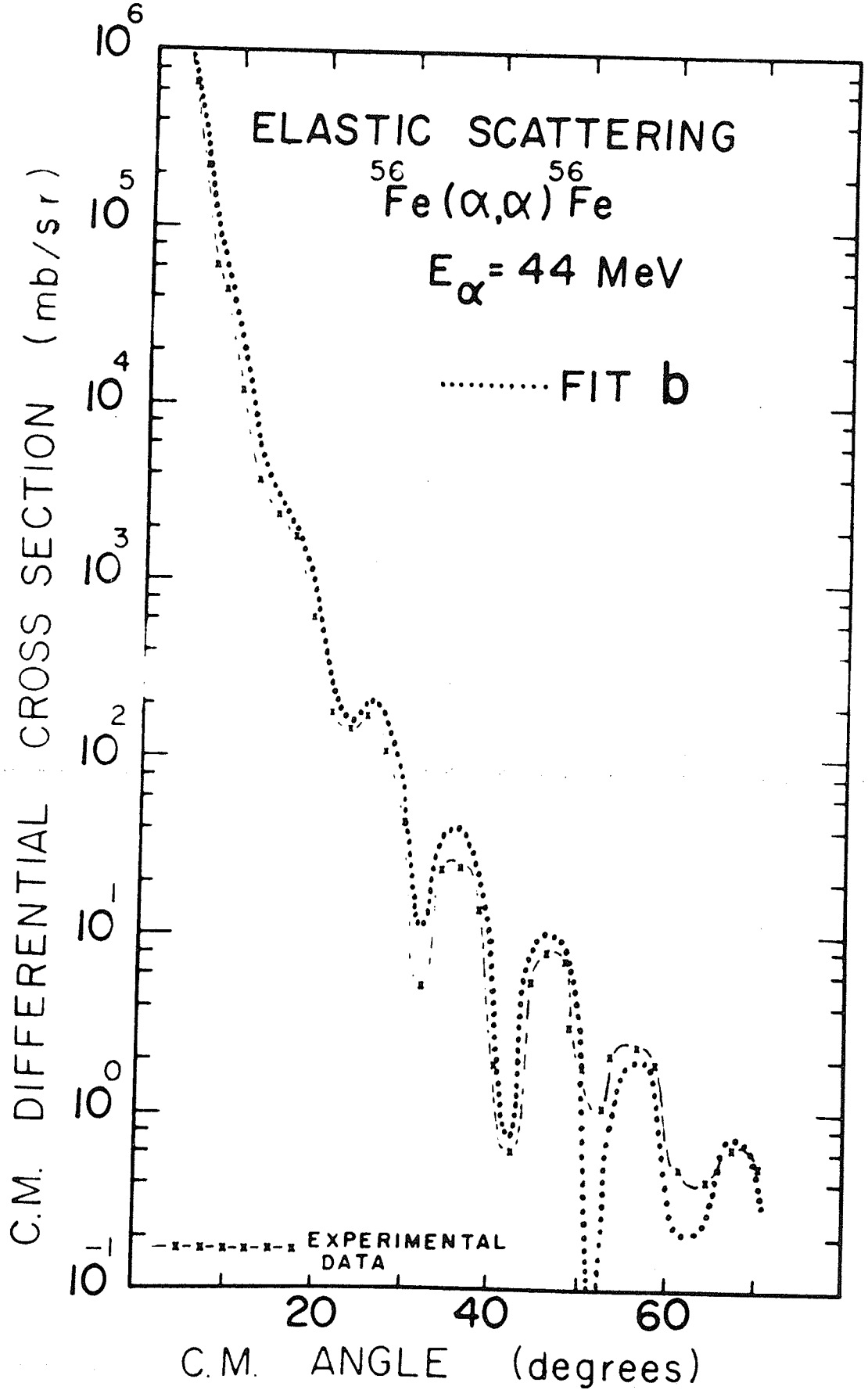
ELASTIC SCATTERING
$^{56}Fe(\alpha,\alpha)^{56}Fe$
E_α = 44 MeV
FIT b
EXPERIMENTAL DATA
C.M. DIFFERENTIAL CROSS SECTION (mb/sr)
C.M. ANGLE (degrees)
10^6
10^5
10^4
10^3
10^2
10^1
10^0
20
40
60

FIGURE 4.73

Optical Model fit to the 44 MeV alpha elastic scattering from ^{56}Fe.

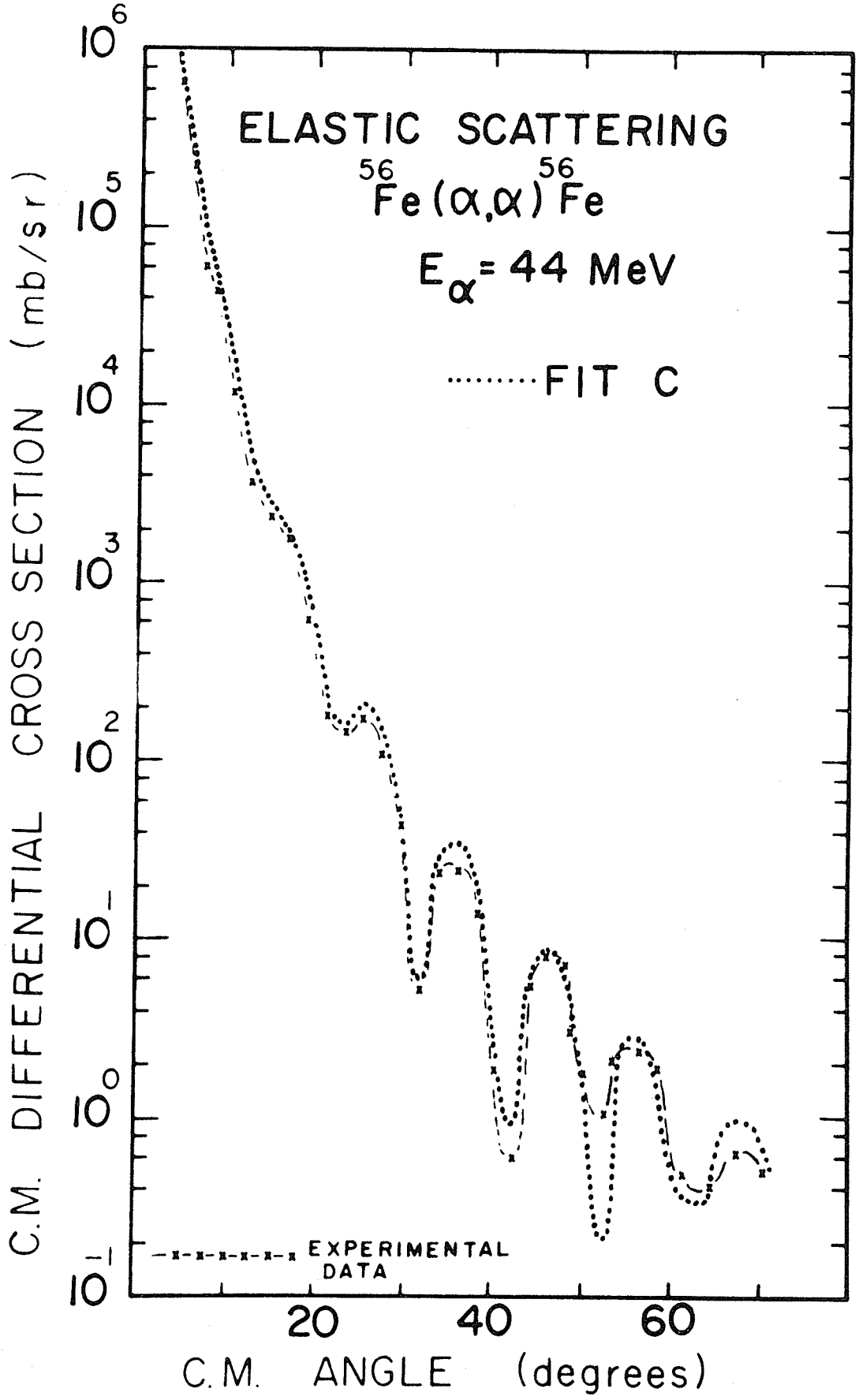
ELASTIC SCATTERING
$^{56}Fe(\alpha,\alpha)^{56}Fe$
E_α = 44 MeV
FIT C
EXPERIMENTAL DATA
C.M. DIFFERENTIAL CROSS SECTION (mb/sr)
C.M. ANGLE (degrees)
10^6
10^5
10^4
10^3
10^2
10_-
10^0
10^{-1}
20
40
60

FIGURE 4.74

Optical Model fit to the 44 MeV alpha elastic scattering from ^{56}Fe

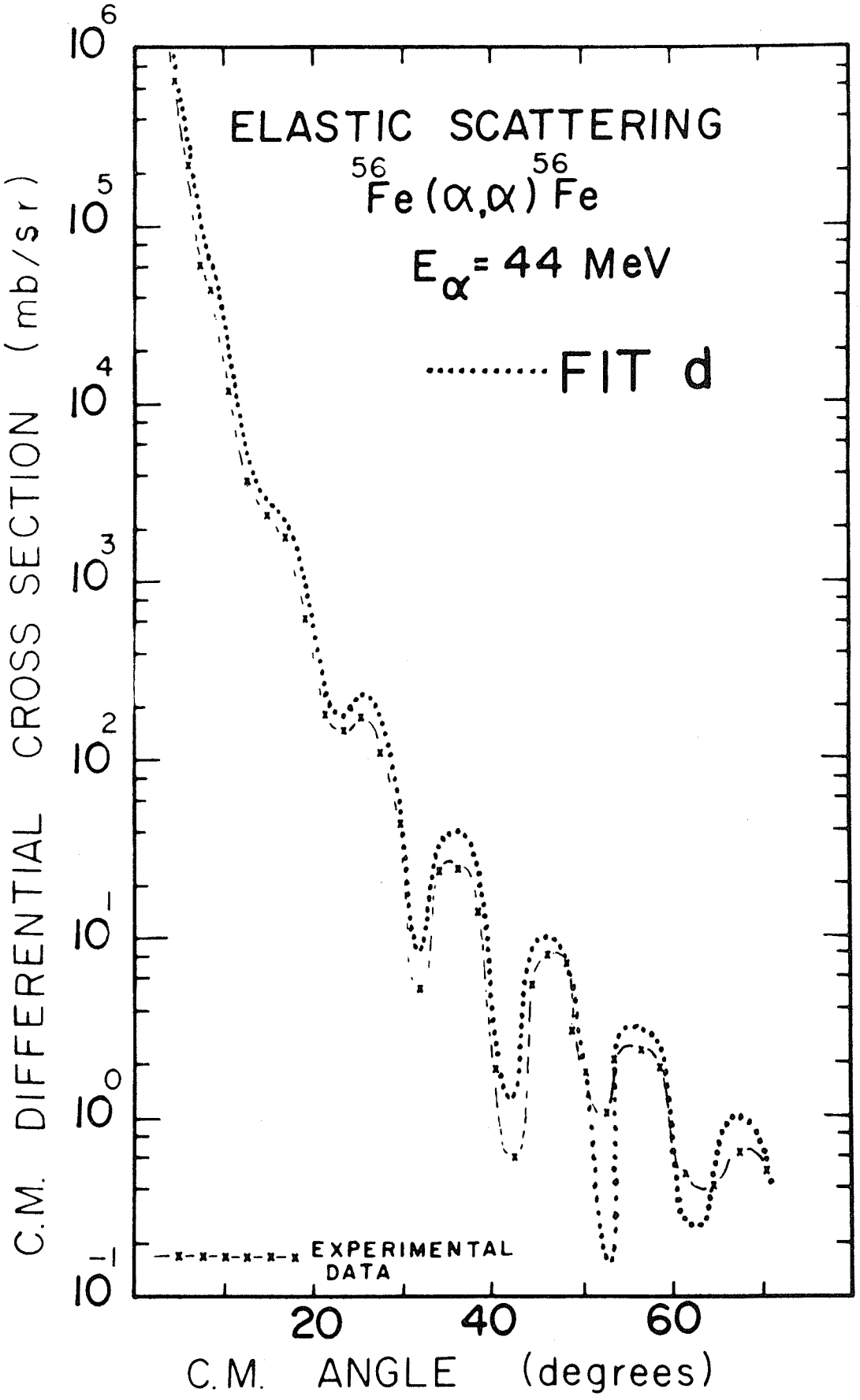
ELASTIC SCATTERING
$^{56}Fe(\alpha,\alpha)^{56}Fe$
E_α = 44 MeV
FIT d
EXPERIMENTAL DATA
C.M. DIFFERENTIAL CROSS SECTION (mb/sr)
C.M. ANGLE (degrees)
10^6
10^5
10^4
10^3
10^2
10^1
10^0
10^{-1}
20
40
60

FIGURE 4.75

Optical Model fit to the 44 MeV alpha elastic scattering from ^{56}Fe

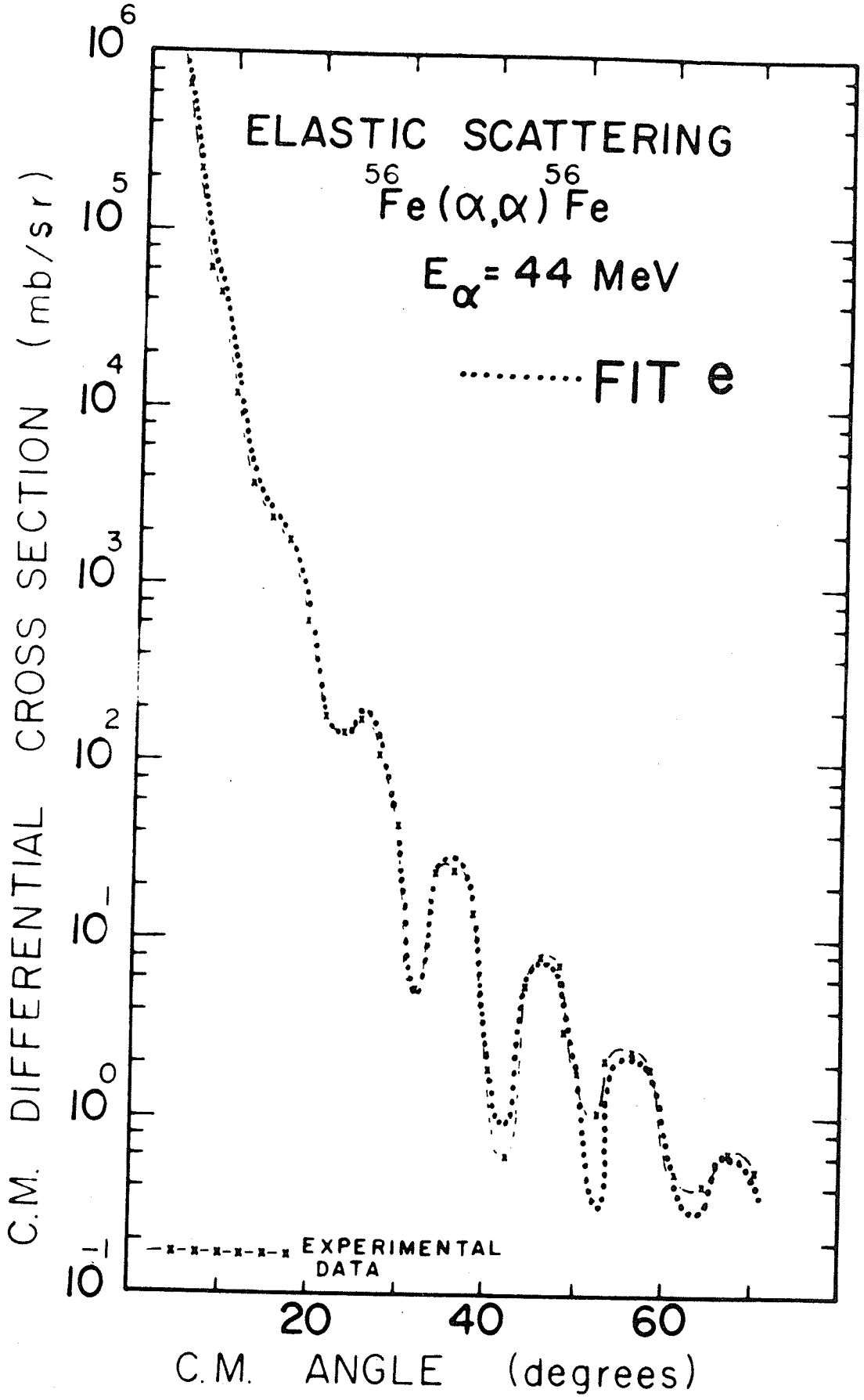
ELASTIC SCATTERING
$^{56}Fe(\alpha,\alpha)^{56}Fe$
E_α = 44 MeV
FIT e
EXPERIMENTAL DATA
C.M. DIFFERENTIAL CROSS SECTION (mb/sr)
C.M. ANGLE (degrees)
10^6
10^5
10^4
10^3
10^2
10^1
10^0
20
40
60

FIGURE 4.76

Optical Model fit to the 44 MeV alpha elastic scattering from ^{56}Fe

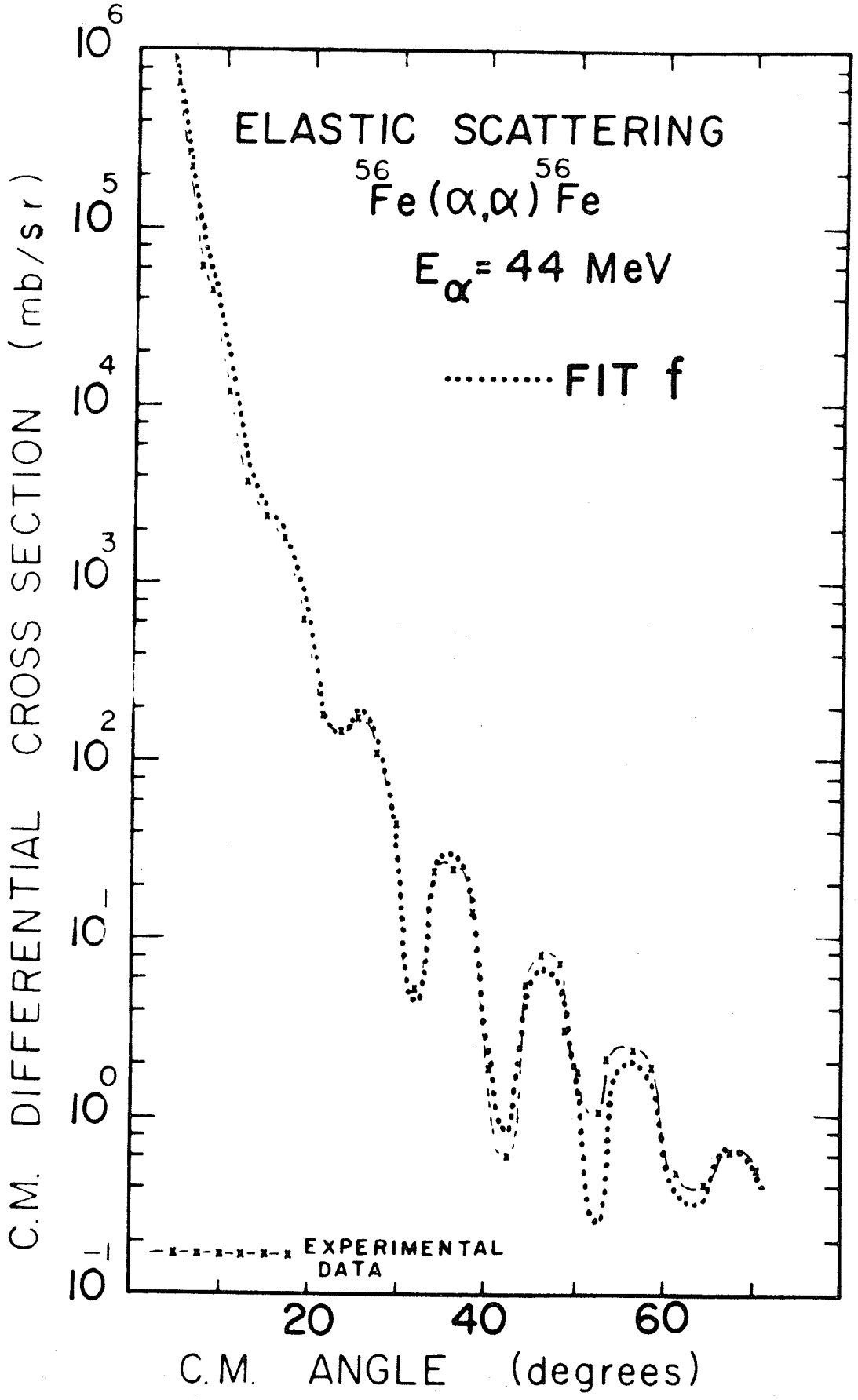
ELASTIC SCATTERING
56Fe(α,α)56Fe
Eα = 44 MeV
FIT f
EXPERIMENTAL DATA
C.M. DIFFERENTIAL CROSS SECTION (mb/sr)
C.M. ANGLE (degrees)
10^6
10^5
10^4
10^3
10^2
10^1
10^0
20
40
60

FIGURE 4.77

Optical Model fit to the 44 MeV alpha elastic scattering from ^{56}Fe

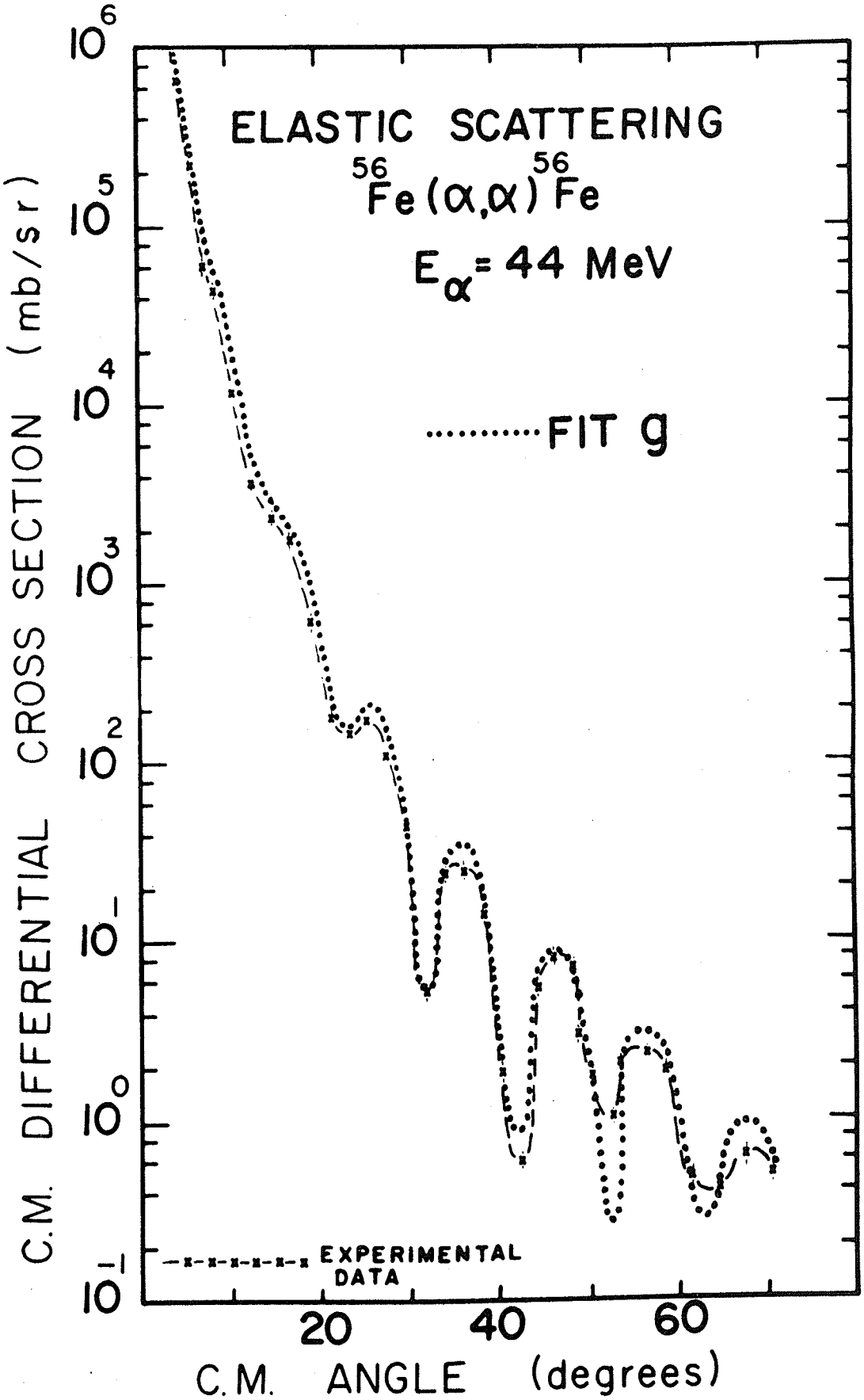
ELASTIC SCATTERING
$^{56}Fe(\alpha,\alpha)^{56}Fe$
E_α = 44 MeV
FIT g
EXPERIMENTAL DATA
C.M. DIFFERENTIAL CROSS SECTION (mb/sr)
C.M. ANGLE (degrees)
10^6
10^5
10^4
10^3
10^2
10^1
10^0
20
40
60

FIGURE 4.78

Optical Model fit to the 44 MeV alpha elastic scattering from ^{56}Fe

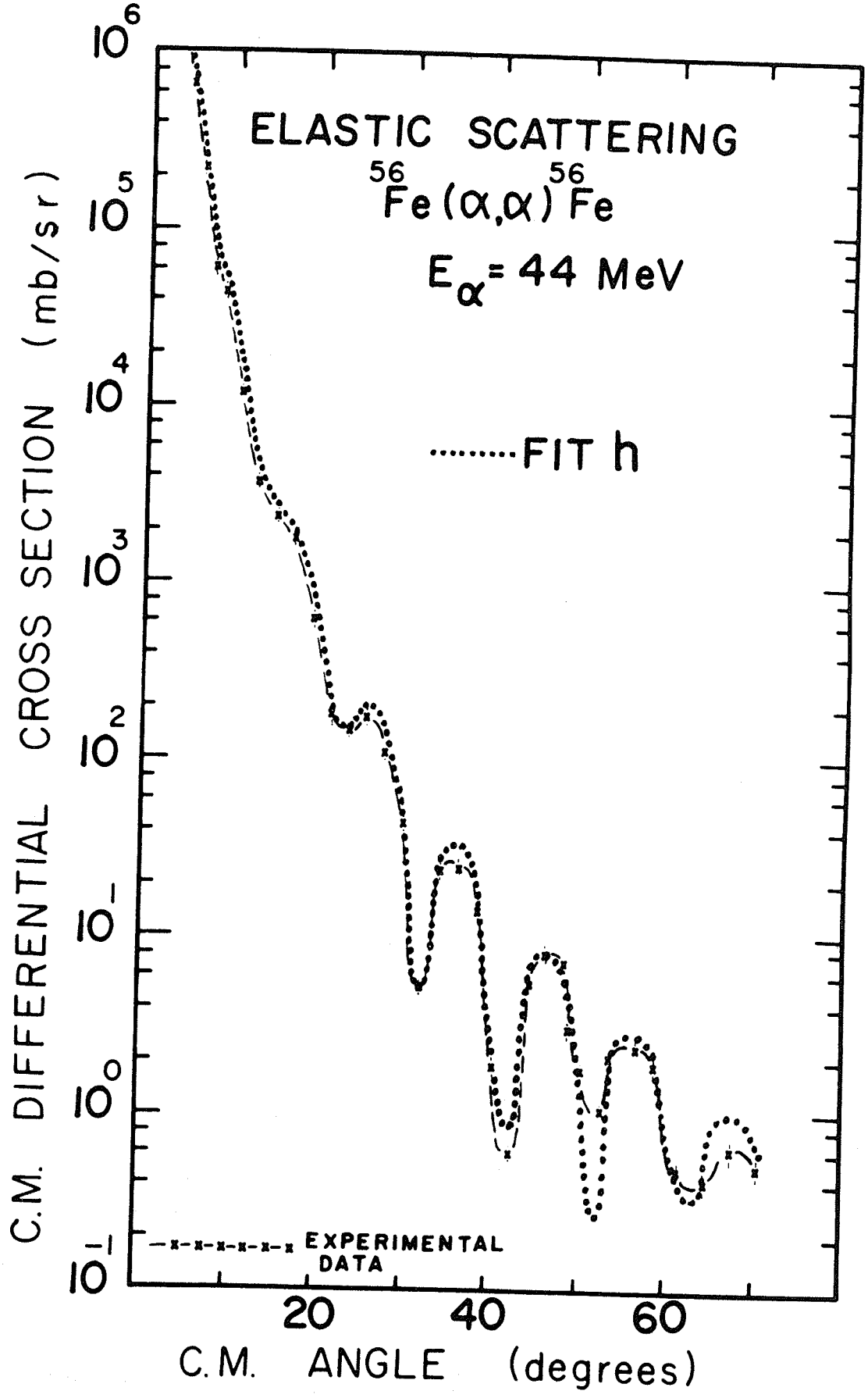
ELASTIC SCATTERING
$^{56}Fe(\alpha,\alpha)^{56}Fe$
E_α = 44 MeV
.....FIT h
EXPERIMENTAL DATA
C.M. DIFFERENTIAL CROSS SECTION (mb/sr)
10^6
10^5
10^4
10^3
10^2
10^1
10^0
10^{-1}
20
40
60
C.M. ANGLE (degrees)

FIGURE 4.79

Optical Model fit to the 44 MeV alpha elastic scattering from ^{56}Fe

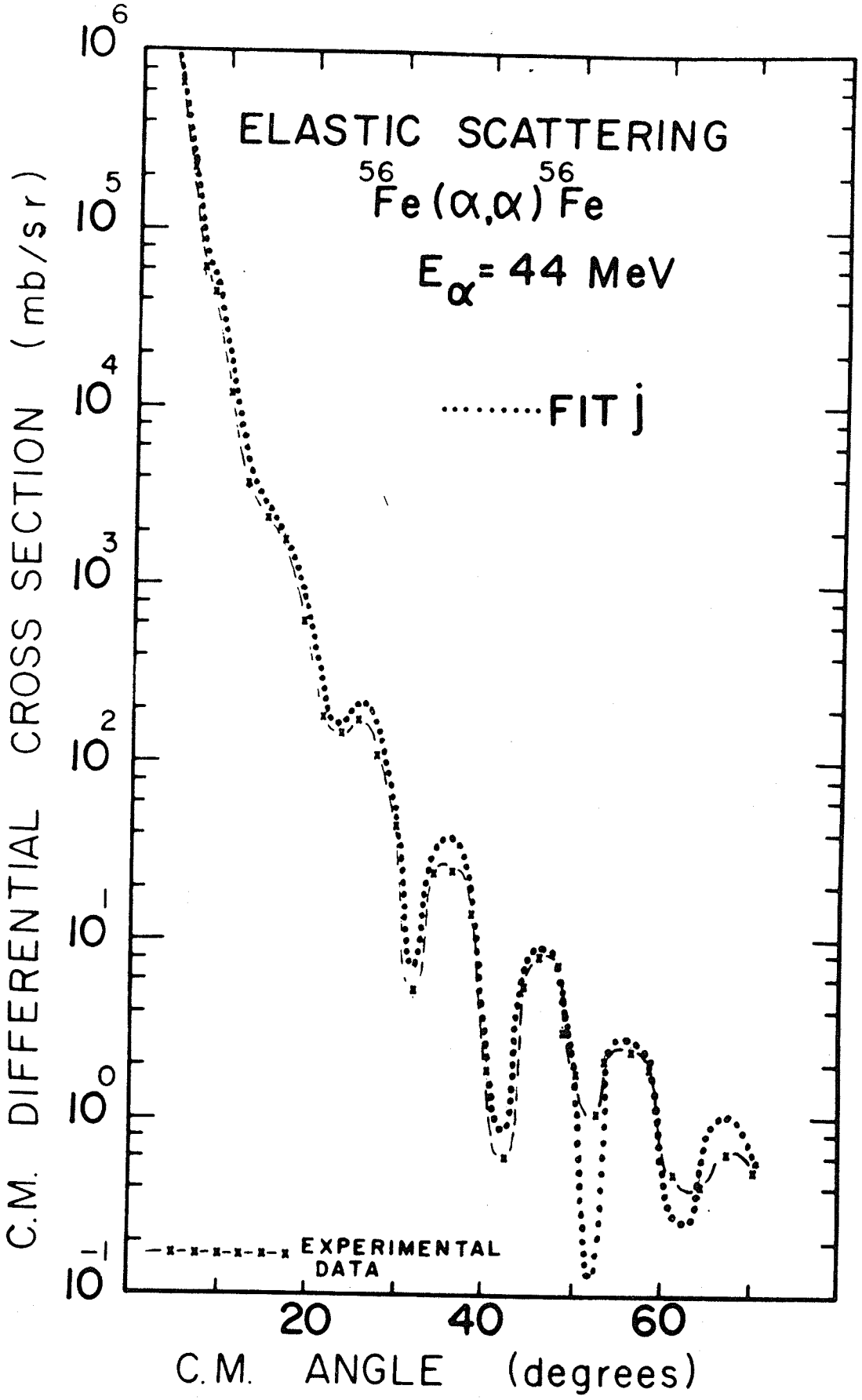
ELASTIC SCATTERING
$^{56}Fe(\alpha,\alpha)^{56}Fe$
E_α = 44 MeV
.....FIT j
EXPERIMENTAL DATA
C.M. DIFFERENTIAL CROSS SECTION (mb/sr)
C.M. ANGLE (degrees)
10^6
10^5
10^4
10^3
10^2
10^1
10^0
10^{-1}
20
40
60

FIGURE 4.80

DWBA calculations for the various sets of proton optical parameters

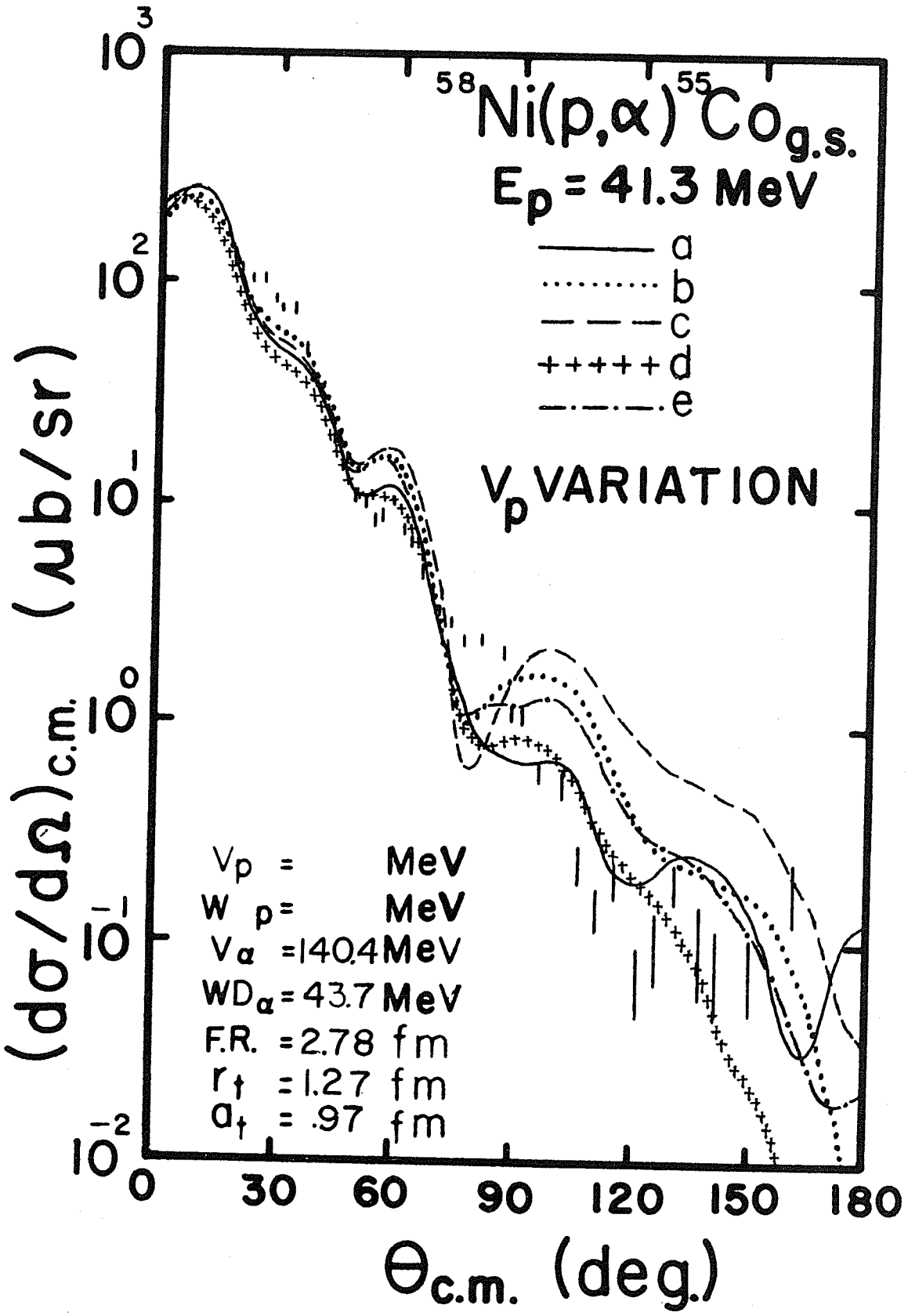
$^{58}Ni(p,\alpha)^{55}Co_{g.s.}$
E_p = 41.3 MeV
a
b
c
d
e
V_p VARIATION
V_p = MeV
W p = MeV
V_α = 140.4 MeV
WD_α = 43.7 MeV
F.R. = 2.78 fm
r_t = 1.27 fm
a_t = .97 fm
$(d\sigma/d\Omega)_{c.m.}$ (μb/sr)
$\theta_{c.m.}$ (deg.)
10^3
10^2
10^1
10^0
10^{-1}
10^{-2}
0
30
60
90
120
150
180

FIGURE 4.81

DWBA calculations for the various sets of alpha optical parameters

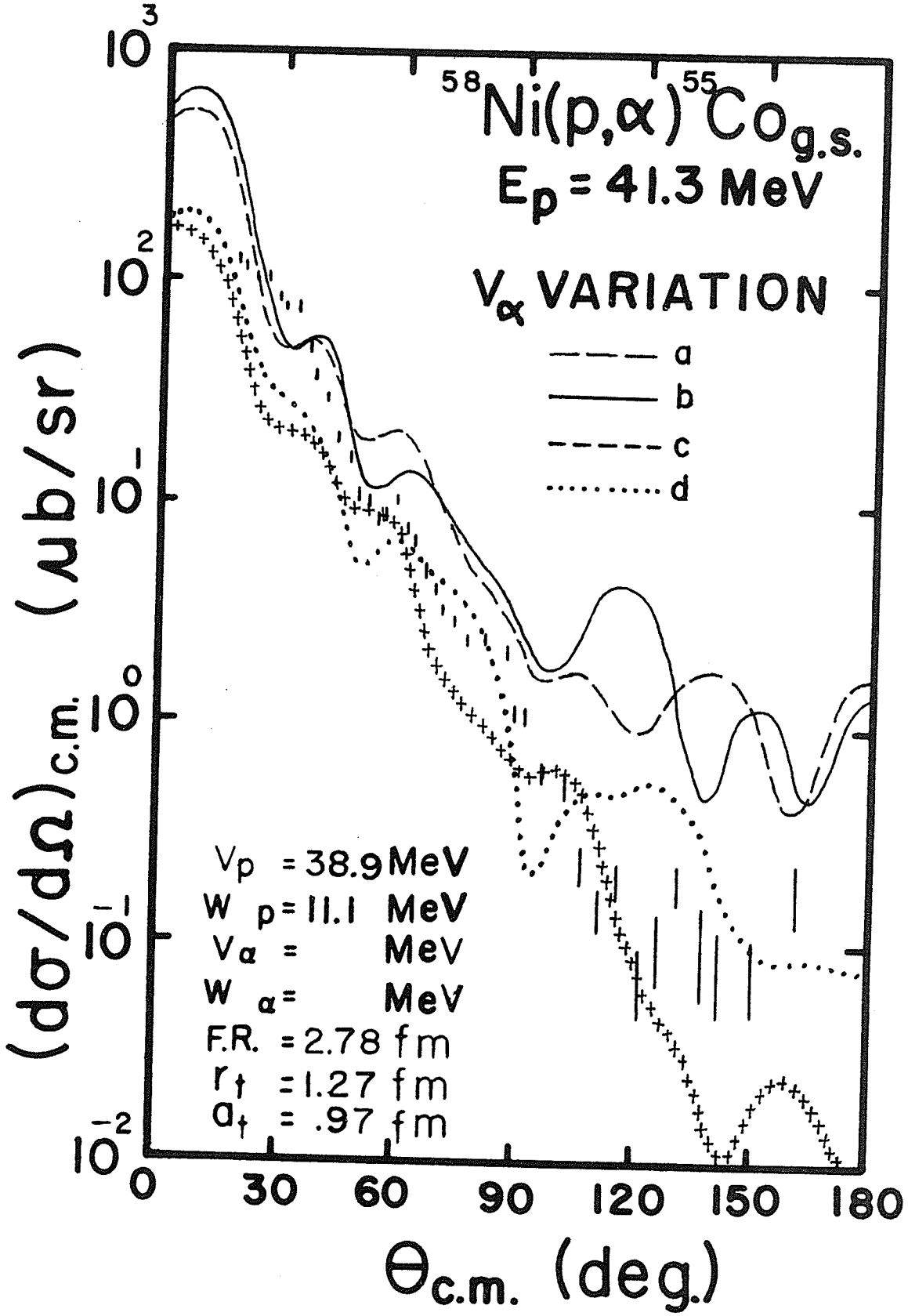
$^{58}Ni(p,\alpha)^{55}Co_{g.s.}$
$E_p = 41.3$ MeV
V_α VARIATION
a
b
c
d
V_p = 38.9 MeV
W p = 11.1 MeV
V_α = MeV
W $_\alpha$ = MeV
F.R. = 2.78 fm
r_t = 1.27 fm
a_t = .97 fm
$(d\sigma/d\Omega)_{c.m.}$ (μb/sr)
$\theta_{c.m.}$ (deg.)
10^3
10^2
10^1
10^0
10^{-1}
10^{-2}
0
30
60
90
120
150
180

FIGURE 4.82

DWBA calculations for the various sets of alpha optical parameters

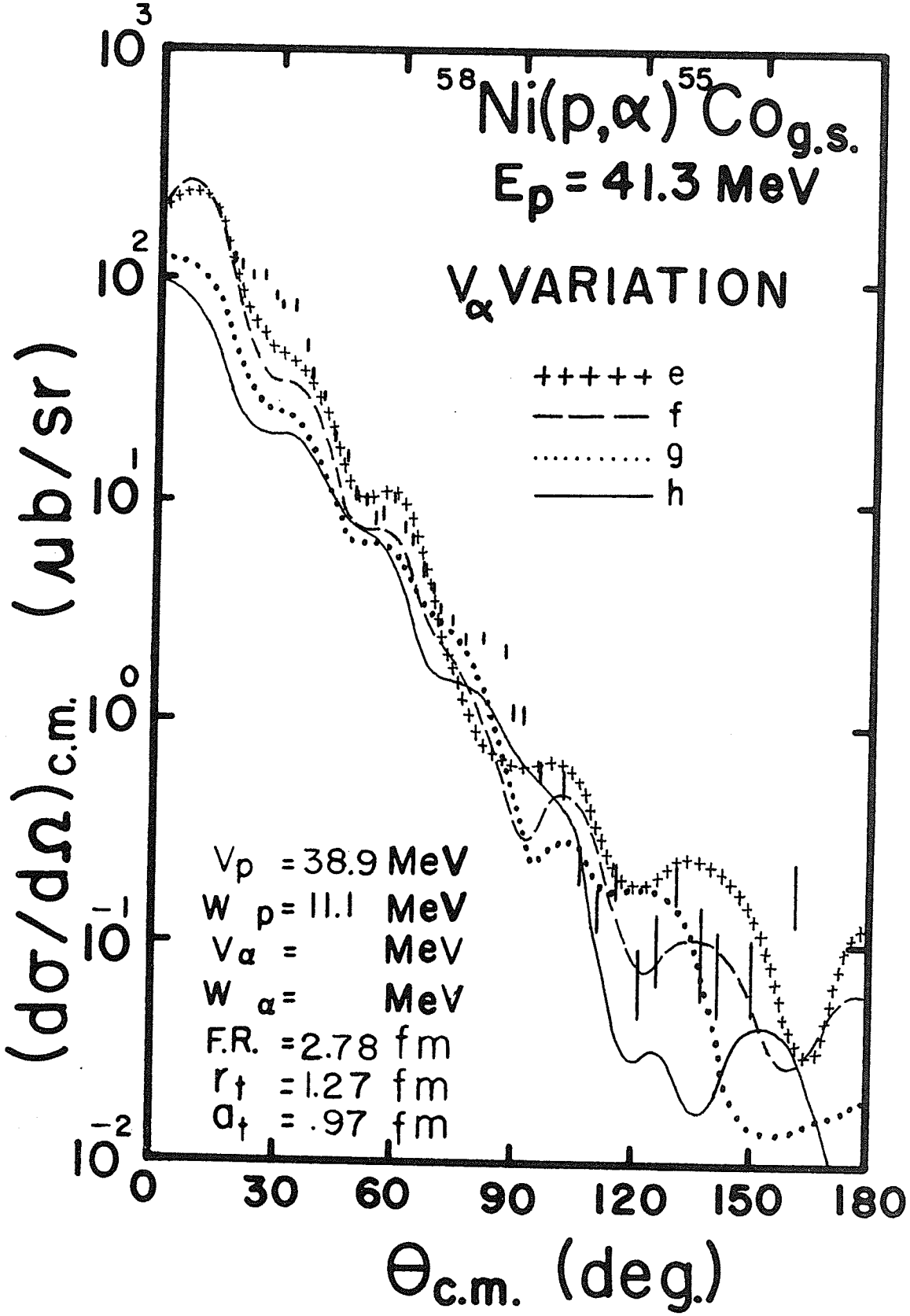
$^{58}Ni(p,\alpha)^{55}Co_{g.s.}$
$E_p = 41.3$ MeV
V_α VARIATION
+++++ e
— — — f
..... g
——— h
V_p = 38.9 MeV
W_p = 11.1 MeV
V_α = MeV
W_α = MeV
F.R. = 2.78 fm
r_t = 1.27 fm
a_t = .97 fm
$(d\sigma/d\Omega)_{c.m.}$ (μb/sr)
$\theta_{c.m.}$ (deg.)
10^3
10^2
10^1
10^0
10^{-1}
10^{-2}
0
30
60
90
120
150
180

FIGURE 4.83

Typical Variation of the DWBA calculations with the bound state parameter r_t

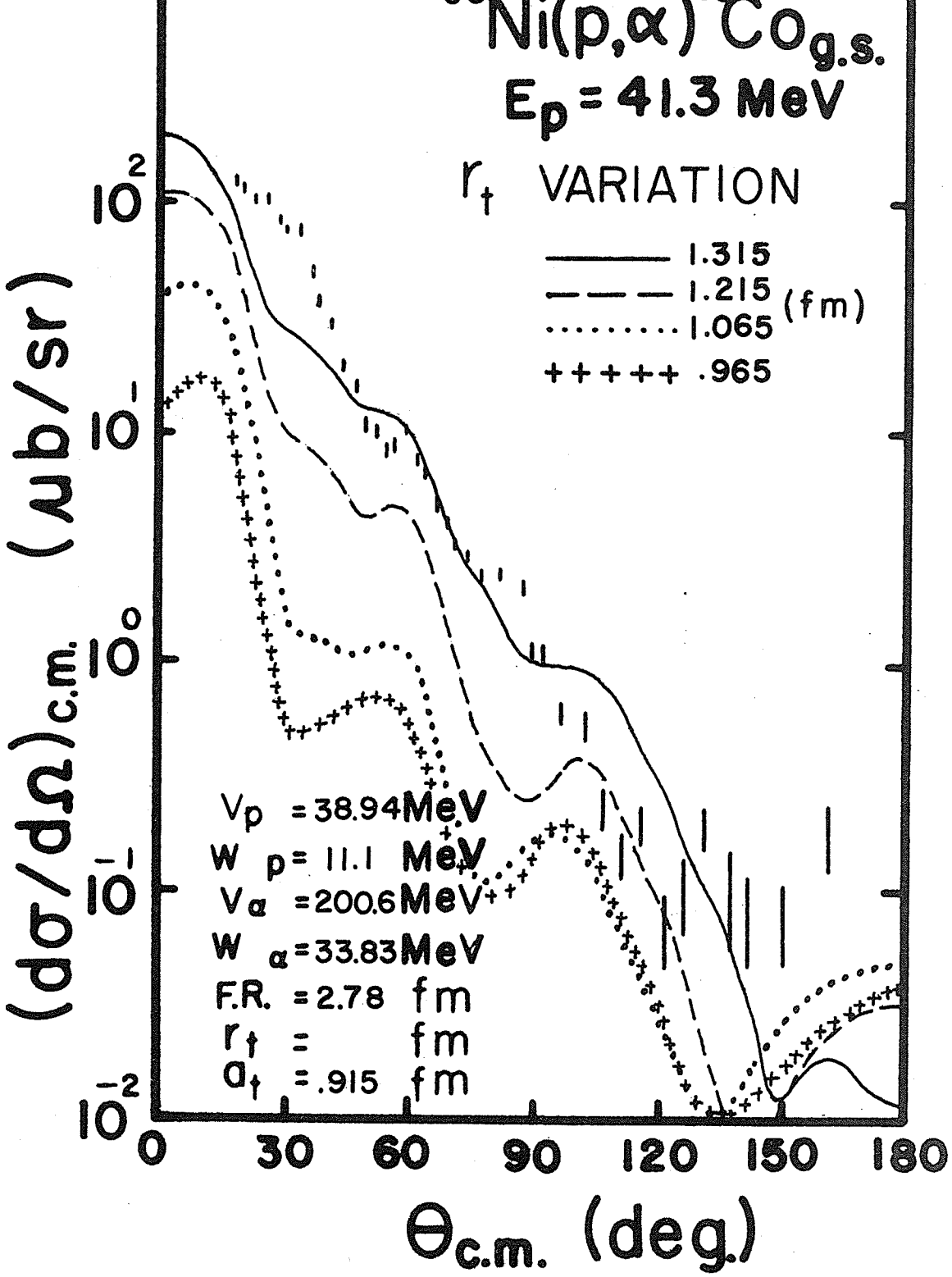
$^{58}Ni(p,\alpha)^{55}Co_{g.s.}$
$E_p = 41.3$ MeV
r_t VARIATION
1.315
1.215 (fm)
1.065
.965
V_p = 38.94 MeV
W p = 11.1 MeV
V_α = 200.6 MeV
W $_\alpha$ = 33.83 MeV
F.R. = 2.78 fm
r_t = fm
a_t = .915 fm
$(d\sigma/d\Omega)_{c.m.}$ (μb/sr)
$\theta_{c.m.}$ (deg.)
10^3
10^2
10^1
10^0
10^{-1}
10^{-2}
0
30
60
90
120
150
180

FIGURE 4.84

Typical Variation of the DWBA calculations with the bound state parameter a_t.

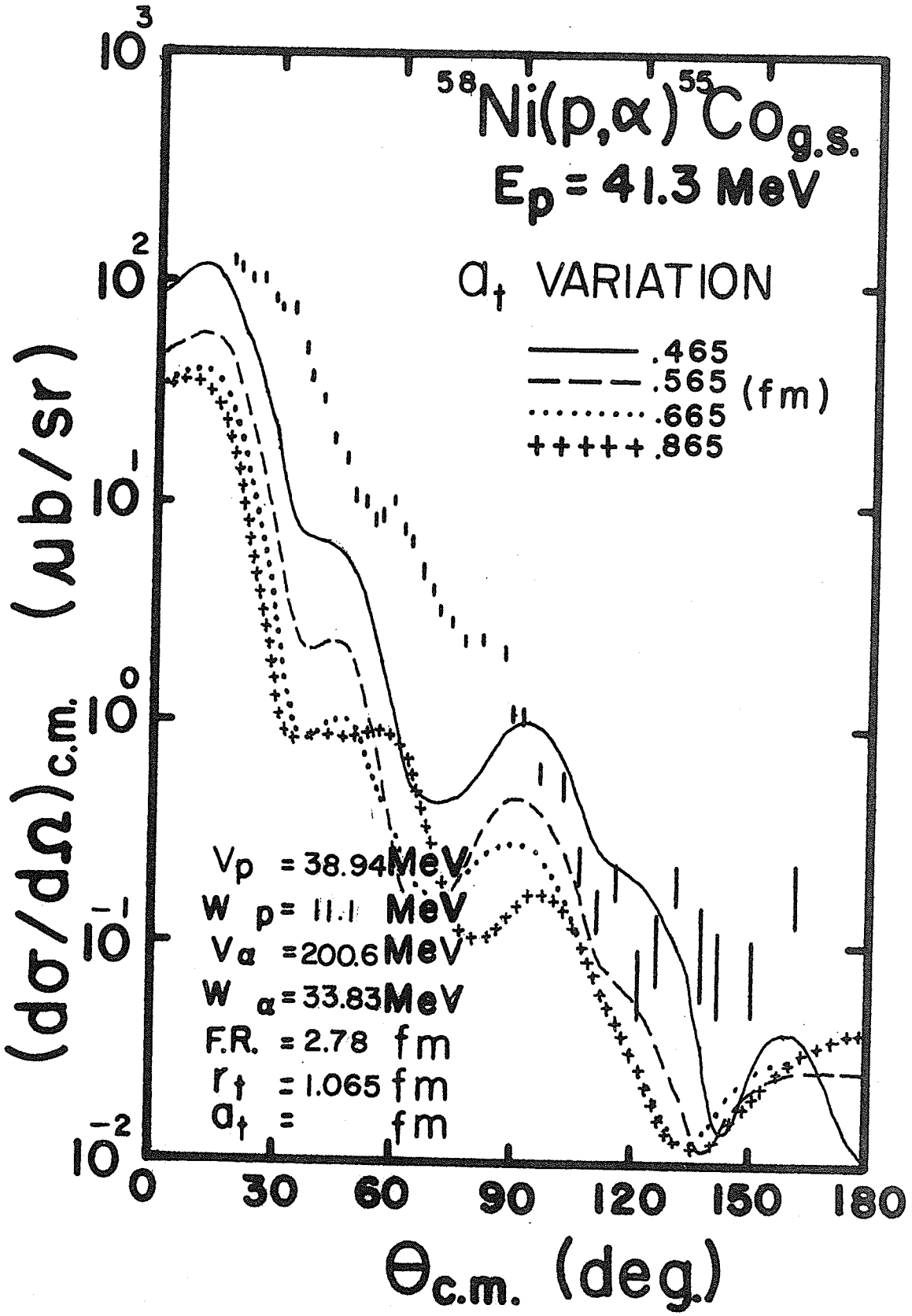
$^{58}Ni(p,\alpha)^{55}Co_{g.s.}$
$E_p = 41.3$ MeV
a_t VARIATION
.465
.565 (fm)
.665
.865
V_p = 38.94 MeV
W_p = 11.1 MeV
V_α = 200.6 MeV
W_α = 33.83 MeV
F.R. = 2.78 fm
r_t = 1.065 fm
a_t = fm
$(d\sigma/d\Omega)_{c.m.}$ (μb/sr)
$\theta_{c.m.}$ (deg.)
10^3
10^2
10^1
10^0
10^{-1}
10^{-2}
0
30
60
90
120
150
180

FIGURE 4.85

Typical DWBA fits to the $^{58}Ni(p,\alpha)\ ^{55}Co_{g.s.}$ reaction for the set of alpha optical parameters "a" listed in Table 4.7

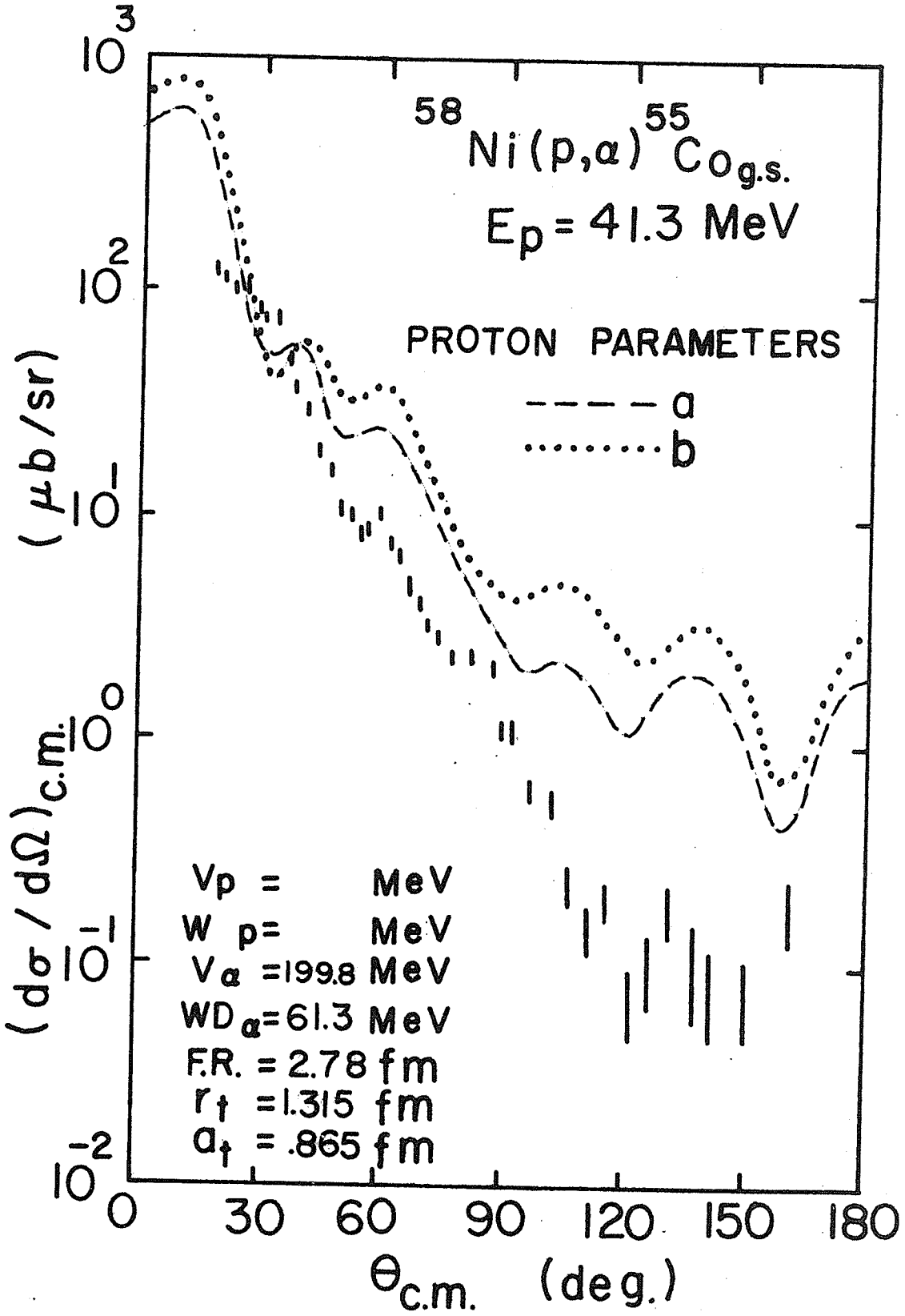
58 Ni(p,α) 55 Co g.s.
Ep = 41.3 MeV
PROTON PARAMETERS
a
b
Vp = MeV
W p= MeV
Vα =199.8 MeV
WDα=61.3 MeV
F.R. = 2.78 fm
rt =1.315 fm
at = .865 fm
(dσ / dΩ)c.m. (μb/sr)
θc.m. (deg.)
10^3
10^2
10^1
10^0
10^-1
10^-2
0
30
60
90
120
150
180

FIGURE 4.86

Typical DWBA fits to the $^{58}Ni(p,\alpha)\ ^{55}Co_{g.s.}$ reaction for the set of alpha optical parameters "b" listed in Table 4.7

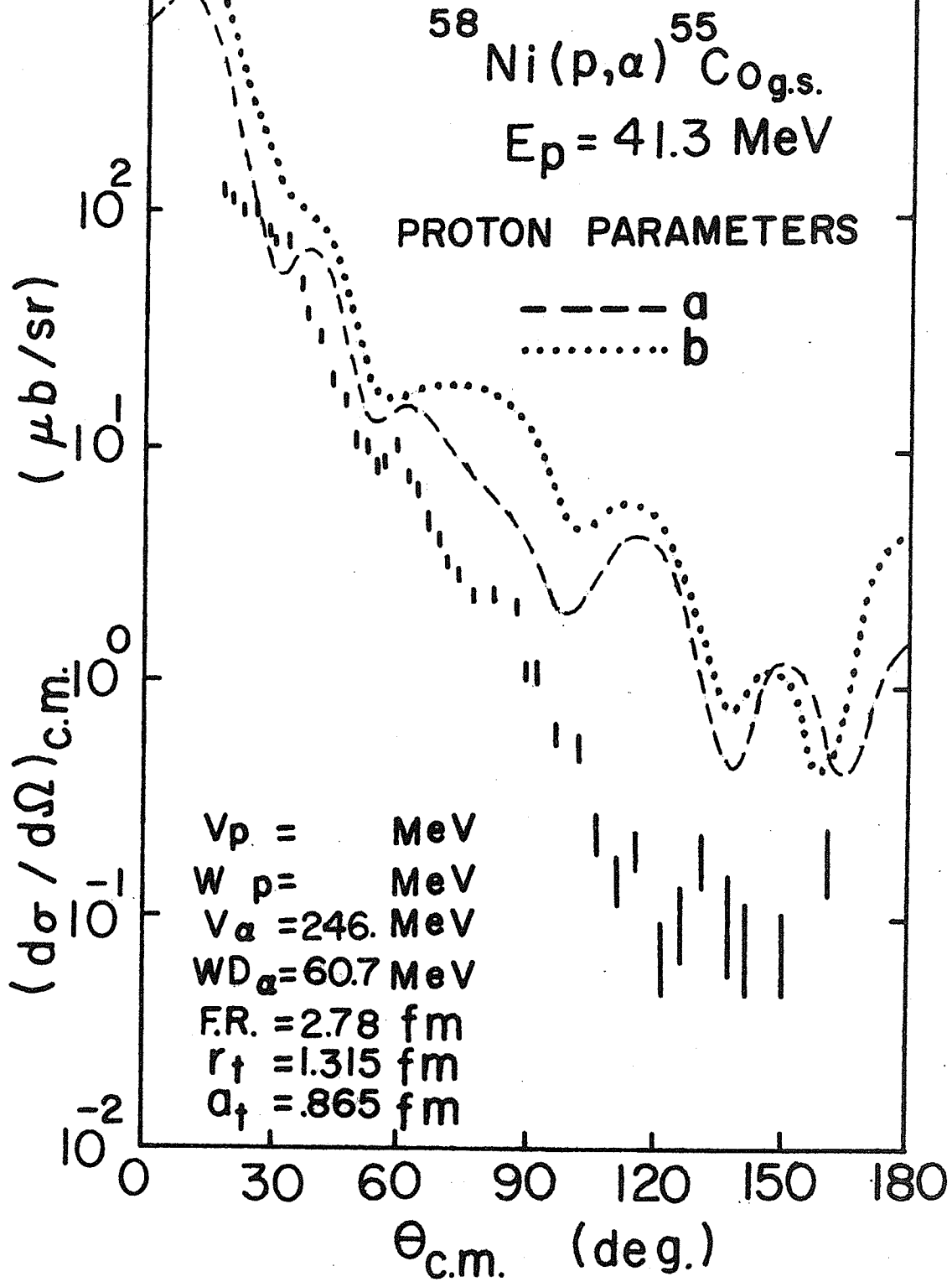
$^{58}Ni(p,\alpha)^{55}Co_{g.s.}$
$E_p = 41.3$ MeV
PROTON PARAMETERS
a
b
$(d\sigma/d\Omega)_{c.m.}$ (μb/sr)
$\theta_{c.m.}$ (deg.)
Vp = MeV
W p= MeV
Vα =246. MeV
WDα=60.7 MeV
F.R. =2.78 fm
r_t =1.315 fm
a_t =.865 fm

FIGURE 4.87

Typical DWBA fits to the $^{58}Ni(p,\alpha)\ ^{55}Co_{g.s.}$ reaction for the set of alpha optical parameters "c" listed in Table 4.7

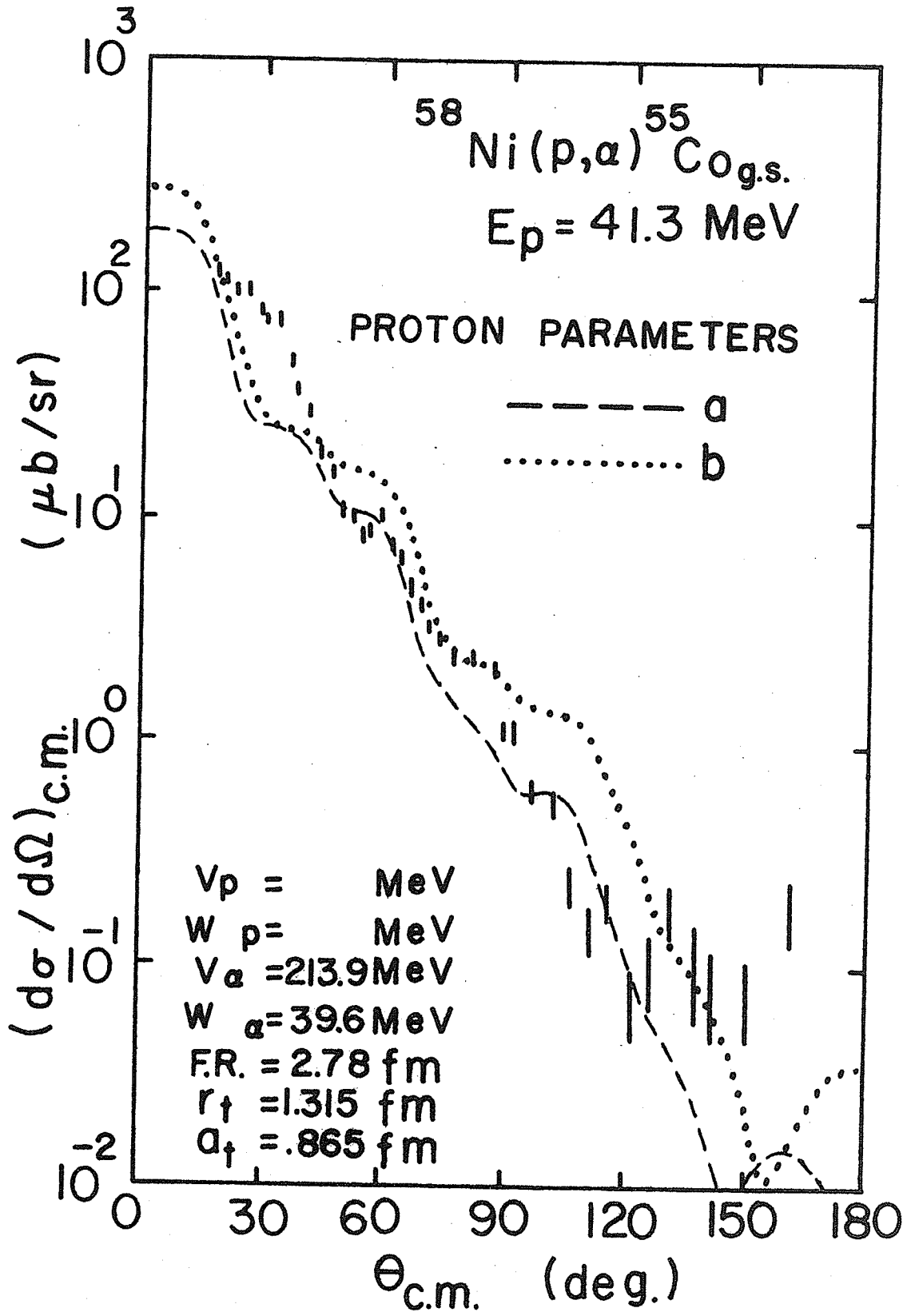
58 Ni(p,α) 55 Co g.s.
Ep = 41.3 MeV
PROTON PARAMETERS
a
b
Vp = MeV
W p= MeV
Vα =213.9 MeV
W α= 39.6 MeV
F.R. = 2.78 fm
rt =1.315 fm
at =.865 fm
(dσ/dΩ)c.m. (μb/sr)
θc.m. (deg.)
10^3
10^2
10^1
10^0
10^-1
10^-2
0
30
60
90
120
150
180

FIGURE 4.88

Typical DWBA fits to the $^{58}Ni(p,\alpha)\ ^{55}Co_{g.s.}$ reaction for the set of alpha optical parameters "d" listed in Table 4.7

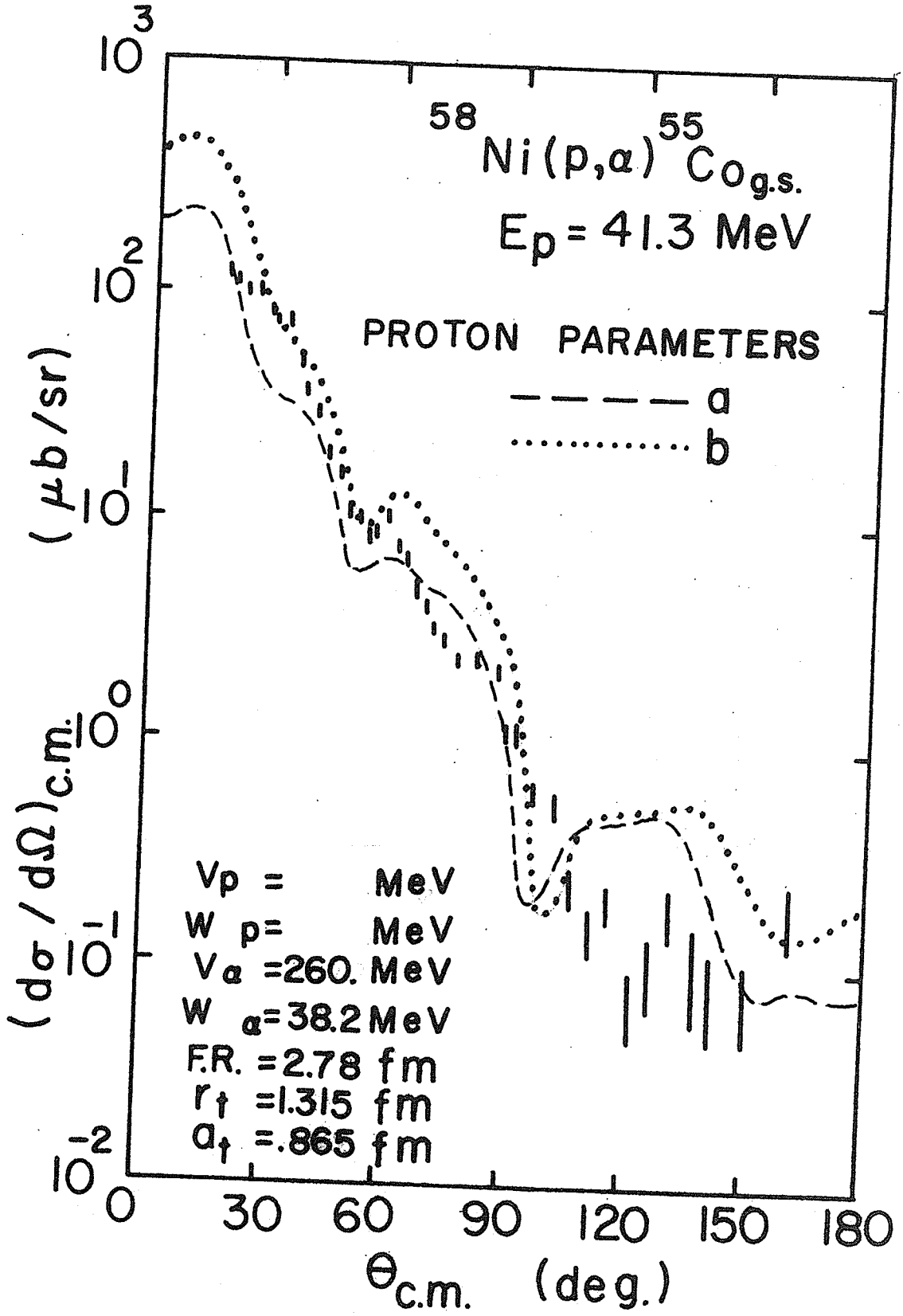
58 Ni(p,α) 55 Co g.s.
Ep = 41.3 MeV
PROTON PARAMETERS
a
b
Vp = MeV
W p= MeV
Vα =260. MeV
W α=38.2 MeV
F.R. =2.78 fm
rt =1.315 fm
at =.865 fm
(dσ/dΩ)c.m. (μb/sr)
θc.m. (deg.)
10^3
10^2
10^1
10^0
10^-1
10^-2
0
30
60
90
120
150
180

FIGURE 4.89

Typical DWBA fits to the $^{58}Ni(p,\alpha)\ ^{55}Co_{g.s.}$ reaction for the set of alpha optical parameters "e" listed in Table 4.7

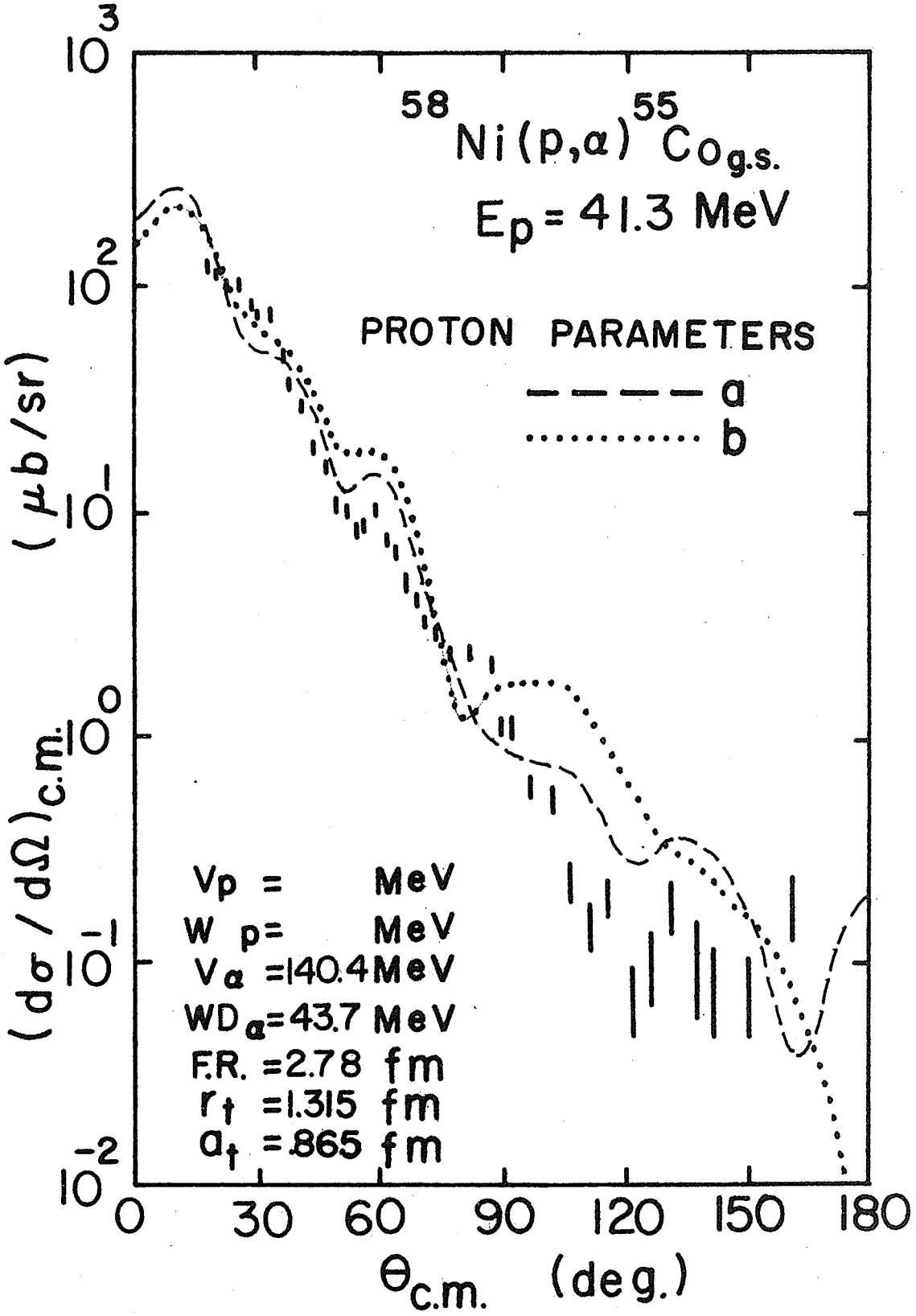
58Ni(p,α)55Co g.s.
Ep = 41.3 MeV
PROTON PARAMETERS
a
b
Vp = MeV
W p= MeV
Vα =140.4 MeV
WDα=43.7 MeV
F.R. =2.78 fm
rt =1.315 fm
at =.865 fm
(dσ/dΩ)c.m. (μb/sr)
θc.m. (deg.)
10^3
10^2
10^1
10^0
10^-1
10^-2
0
30
60
90
120
150
180

FIGURE 4.90

Typical DWBA fits to the $^{58}Ni(p,\alpha)\ ^{55}Co_{g.s.}$ reaction for the set of alpha optical parameters "f" listed in Table 4.7

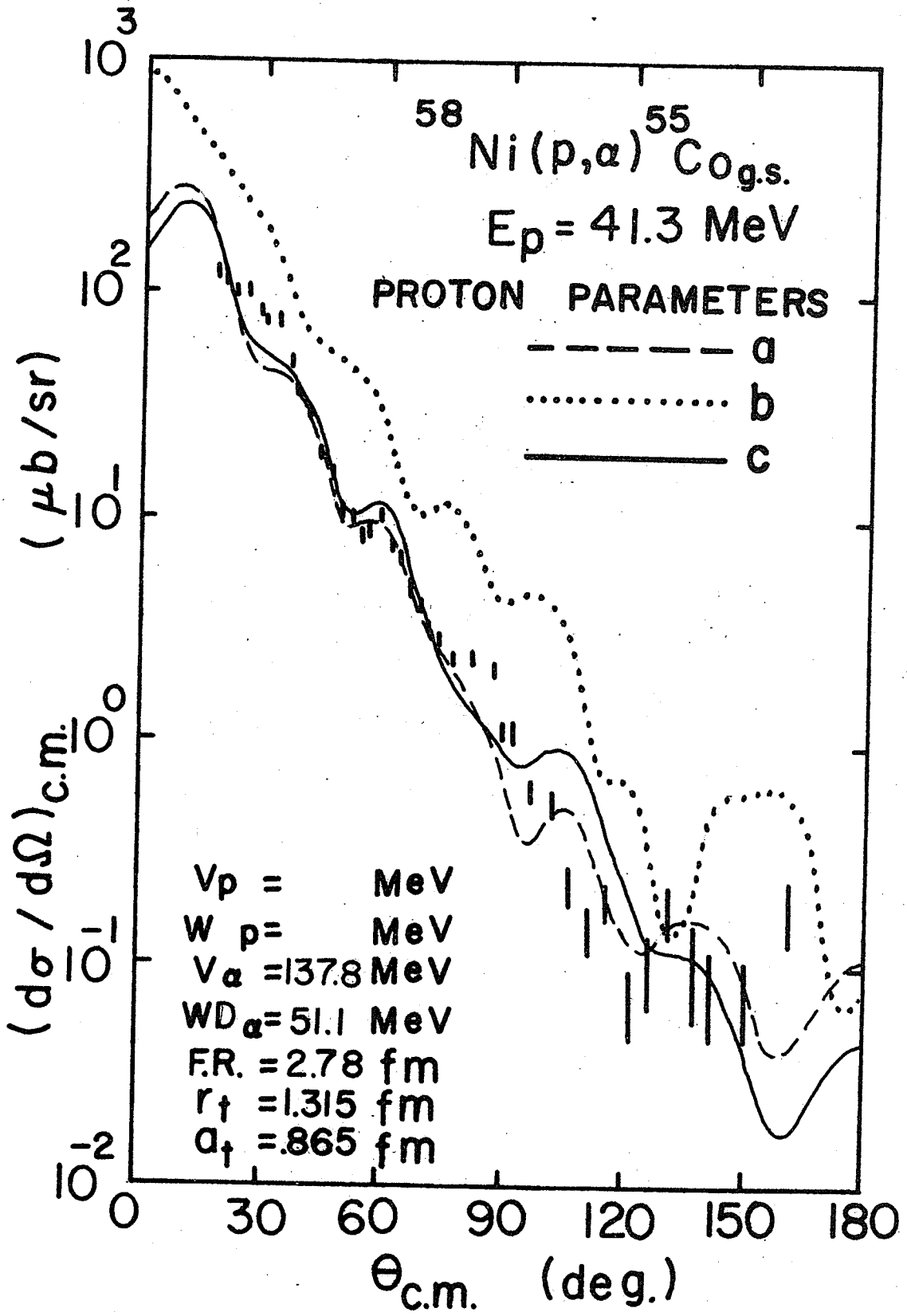
58 Ni(p,α) 55 Co g.s.
Ep = 41.3 MeV
PROTON PARAMETERS
a
b
c
Vp = MeV
W p= MeV
Vα =137.8 MeV
WDα= 51.1 MeV
F.R. =2.78 fm
rt =1.315 fm
at =.865 fm
(dσ/dΩ)c.m. (μb/sr)
θc.m. (deg.)
10^3
10^2
10^1
10^0
10^-1
10^-2
0
30
60
90
120
150
180

FIGURE 4.91

Typical DWBA fits to the $^{58}Ni(p,\alpha)\ ^{55}Co_{g.s.}$ reaction for the set of alpha optical parameters "g" listed in Table 4.7

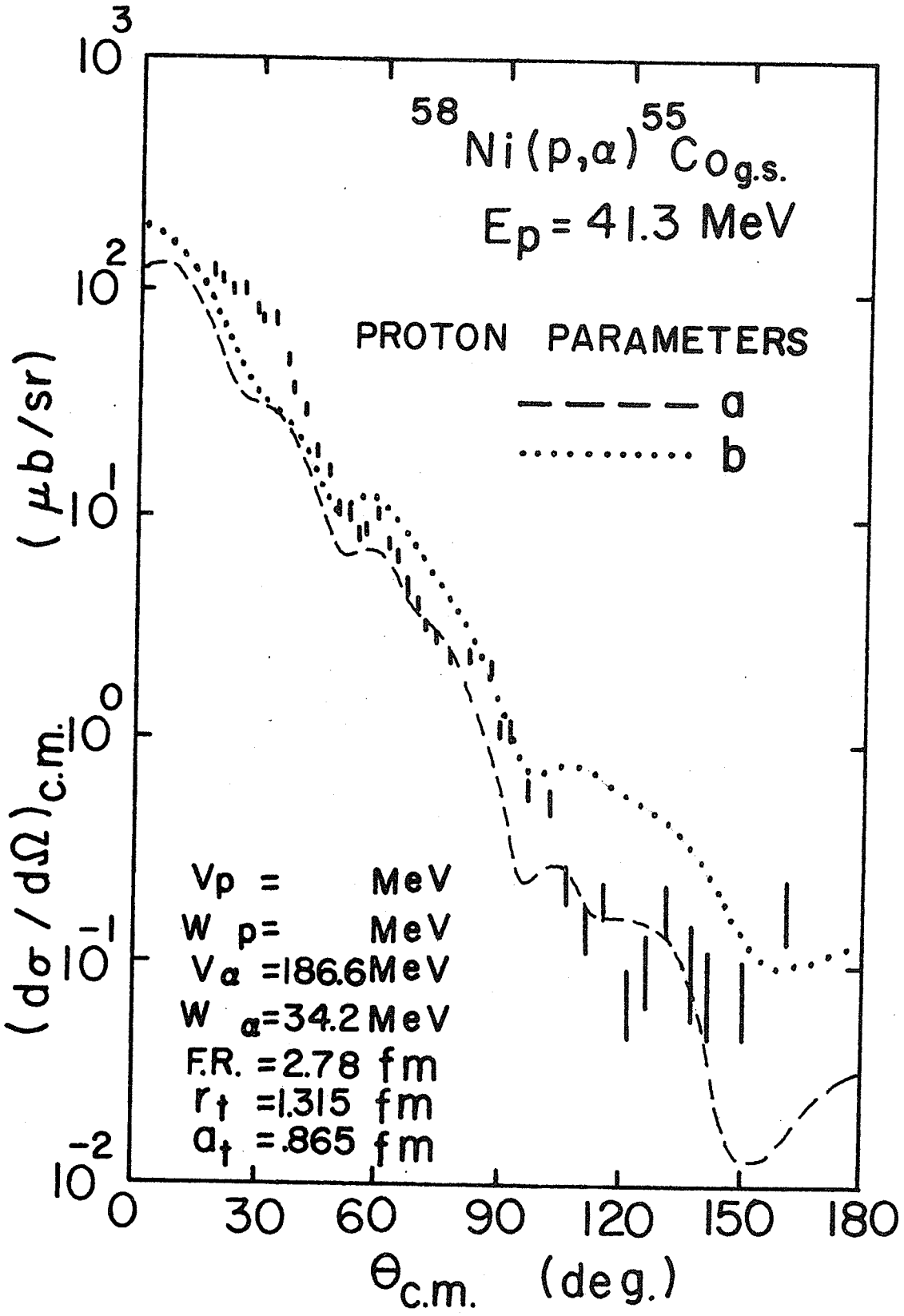
58Ni(p,α)55Co g.s.
Ep = 41.3 MeV
PROTON PARAMETERS
a
b
Vp = MeV
W p= MeV
Vα =186.6MeV
W α=34.2MeV
F.R. =2.78 fm
rt =1.315 fm
at =.865 fm
(dσ/dΩ)c.m. (μb/sr)
θc.m. (deg.)
10^3
10^2
10^1
10^0
10^-1
10^-2
0
30
60
90
120
150
180

FIGURE 4.92

Typical DWBA fits to the $^{58}Ni(p,\alpha)\ ^{55}Co_{g.s.}$ reaction for the set of alpha optical parameters "h" listed in Table 4.7

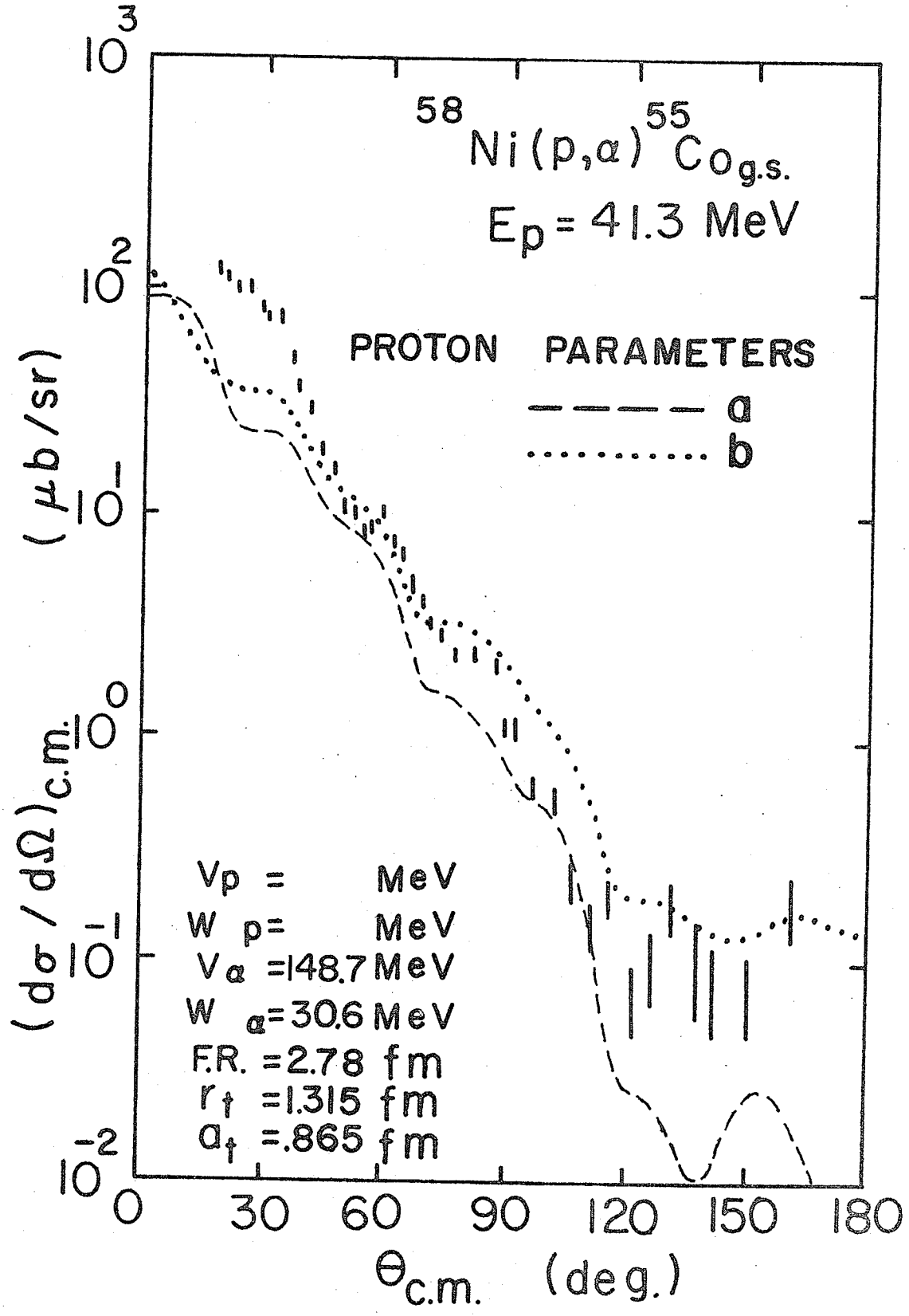
58 Ni(p,α) 55 Co g.s.
Ep = 41.3 MeV
PROTON PARAMETERS
a
b
Vp = MeV
W p= MeV
Vα =148.7 MeV
W α=30.6 MeV
F.R. =2.78 fm
rt =1.315 fm
at =.865 fm
(dσ/dΩ)c.m. (μb/sr)
θc.m. (deg.)
10^3
10^2
10^1
10^0
10^-1
10^-2
0
30
60
90
120
150
180

FIGURE 4.93

Typical DWBA fits to the $^{58}Ni(p,\alpha)\ ^{55}Co_{g.s.}$ reaction for the set of alpha optical parameters "j" listed in Table 4.7

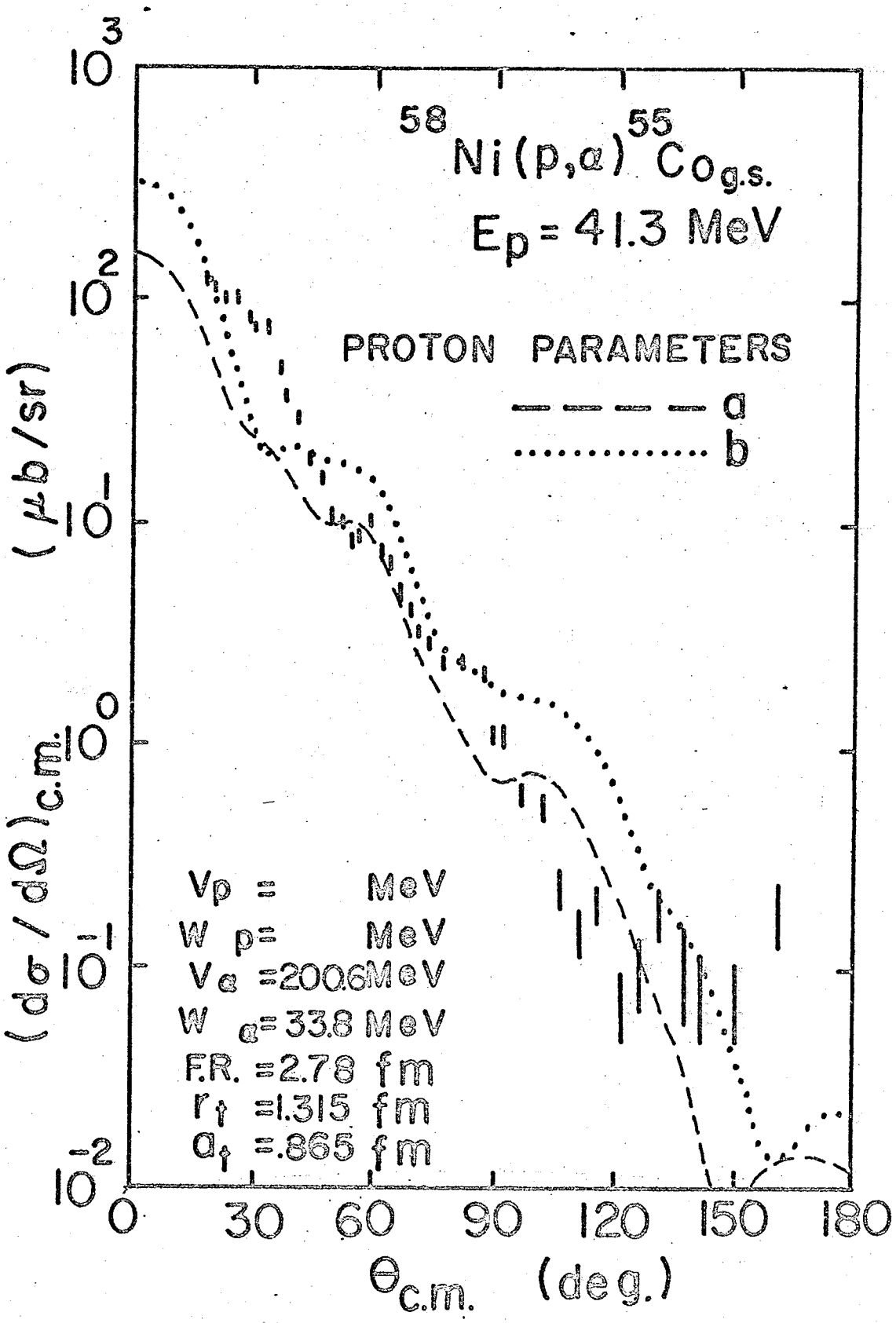
58Ni(p,α)55Co g.s.
Ep = 41.3 MeV
PROTON PARAMETERS
a
b
Vp = MeV
W p= MeV
Vα =200.6MeV
W α= 33.8 MeV
F.R. =2.78 fm
rf =1.315 fm
af =.865 fm
(dσ/dΩ)c.m. (μb/sr)
θc.m. (deg.)
10^3
10^2
10^1
10^0
10^-1
10^-2
0
30
60
90
120
150
180

are typical of the ones obtained for different values of the bound state parameters r_t and a_t. One can readily observe that DWBA fits having the required shape agreement with the experimental data between 20° - 90° can be obtained only for the set of alpha optical parameters having V_α = 137.8 MeV (Figure 4.90). The set having V_α = 140.4 MeV which consists of similar parameters resulted in a somewhat poorer DWBA, as well as elastic scattering, fit.

By somewhat reducing a_t we obtained a highly satisfactory fit for the set of alpha optical parameters having V_α = 137.8 shown in Figure 4.94.

FIGURE 4.94

Best DWBA fit to the $^{58}Ni(p,\alpha)\ ^{55}Co_{g.s.}$ reaction

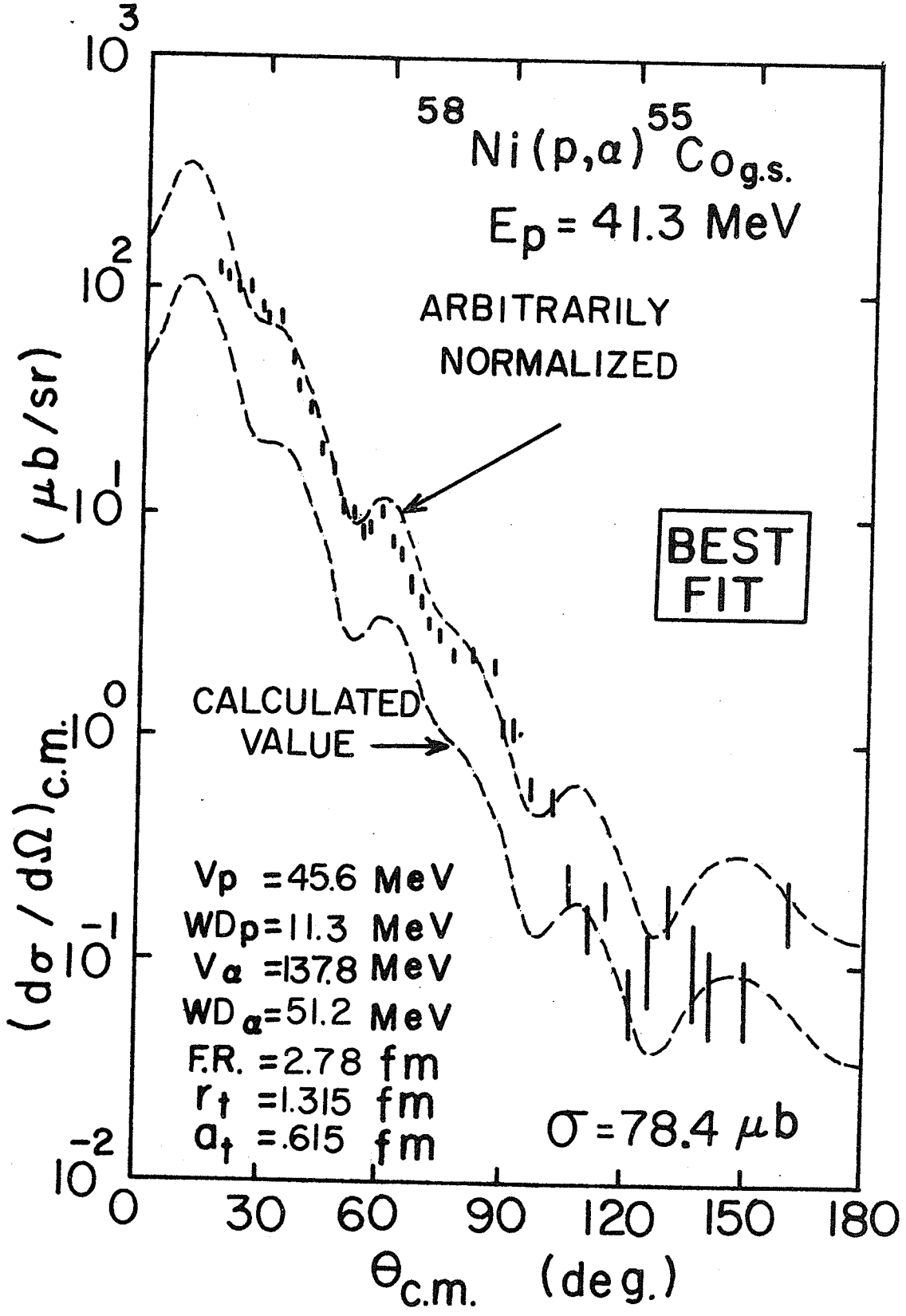
58 Ni(p,α) 55 Co g.s.
Ep = 41.3 MeV
ARBITRARILY NORMALIZED
BEST FIT
CALCULATED VALUE
Vp =45.6 MeV
WDp=11.3 MeV
Vα =137.8 MeV
WDα=51.2 MeV
F.R. =2.78 fm
rt =1.315 fm
at =.615 fm
σ=78.4 μb
(dσ/dΩ)c.m. (μb/sr)
θc.m. (deg.)
10^3
10^2
10^1
10^0
10^-1
10^-2
0
30
60
90
120
150
180

Chapter V

ANALYSIS OF $^{197}Au(p,\alpha)$ REACTION - A STUDY OF THE IMPORTANCE OF MULTIPLE-PARTICLE EMISSION

5.1 Introduction

This chapter consists of a theoretical comparison, based on the statistical model described in Section 3.A, to the experimental (p,α) measurements on ^{197}Au for the four proton energies; 23, 32, 41.3 and 56.3 MeV. We will show that the high energy parts of the experimental energy spectra are inconsistent with the formation of a compound nucleus and must therefore be attributable to direct reaction mechanisms. We will discuss the importance of multiple-particle emission in the theoretical yield for the proton energies of interest.

5.2 Theoretical Evaluation

The necessary inverse reaction compound cross-sections were evaluated as described in Section 3.A. Since the masses of all residual nuclei (resulting from the multiple-particle emission) are approximately in the neighbourhood of 195 and since the inverse reaction cross-sections on these individual nuclei are not sufficiently well known they were all set to the same values. The variation of these inverse cross-sections with energy is shown in Figure 5.1. The inverse cross-sections for neutrons was kept roughly at 2900 mb throughout the entire energy range. The lack of precise knowledge of the inverse cross-sections constituted one of the main uncertainties in the application of the statistical model theory.

FIGURE 5.1

Inverse Reaction Cross Sections for various particles as a function of their incident laboratory energy

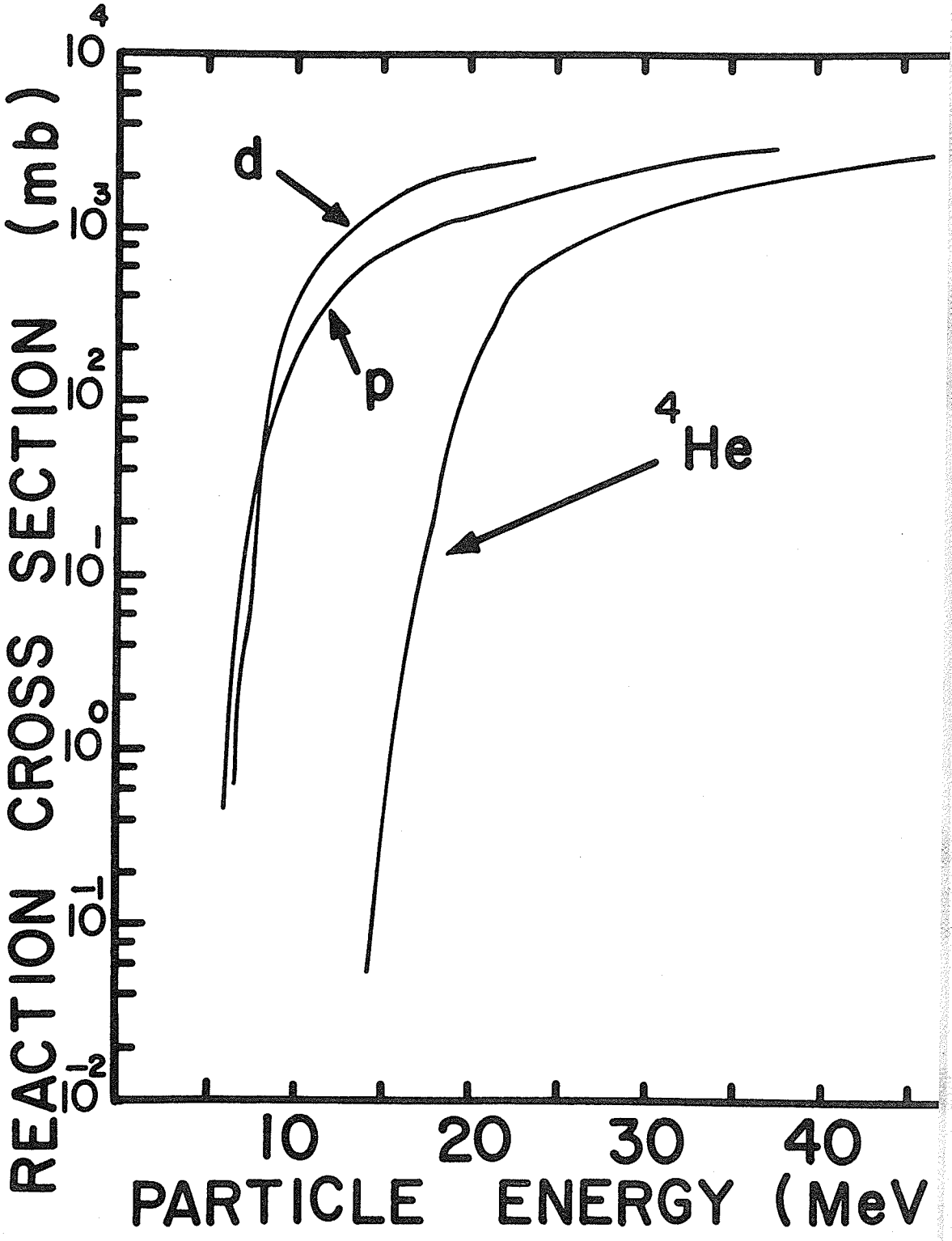
REACTION CROSS SECTION (mb)
10^4
10^3
10^2
10^1
10^0
10^-1
10^-2
d
p
4He
10
20
30
40
PARTICLE ENERGY (MeV

When one takes the alpha energy spectra, from the $^{197}Au(p,\alpha)$ on, observed in the backward angles ($\theta \simeq 150°$) and assumes that these ributable to the statistical nuclear decay mechanism, we obtain (under litional assumption of isotropy) the energy spectra shown in Figure 5.2 four proton energies 23, 32, 41.3 and 56.3 MeV.

Theoretical comparisons to this data were made by varying the lensity parameter α. In one case we used the "NORMAL" values for the energies (those given by CAMERON [30]) while for the other case we pairing energies equal to zero.

The level density parameter α, as determined by other authors in their works [69-72] range from $\frac{A}{8} \rightarrow \frac{A}{10.5}$.

Theoretically, for a fermi-gas model based on equidistant spacings one fermion levels one obtains [24]

$\alpha = 2\left(\frac{\pi}{3}\right)^{4/3} \frac{mr_o^2}{\hbar^2} A$ where m is the nucleon mass, A the atomic mber and r_o the radius parameter of the residual nucleus involved. $A^{1/3}$).

Hence $\alpha = .0512\, r_o^2 A$ where r_o is in fm. For $r_o = 1.4$ fm we have 0.0 MeV^{-1}.

Figure 5.3 shows the typical variation of the partial widths Γ_i various particles (i) formed in the first "shower". As one can readily Γ_i is extremely rapid function of the level density parameter α. ater the initial excitation of the compound nucleus the more rapid is

FIGURE 5.2

Alpha Particle energy spectra from proton bombardment of ^{197}Au as observed for $\theta_L \approx 150°$

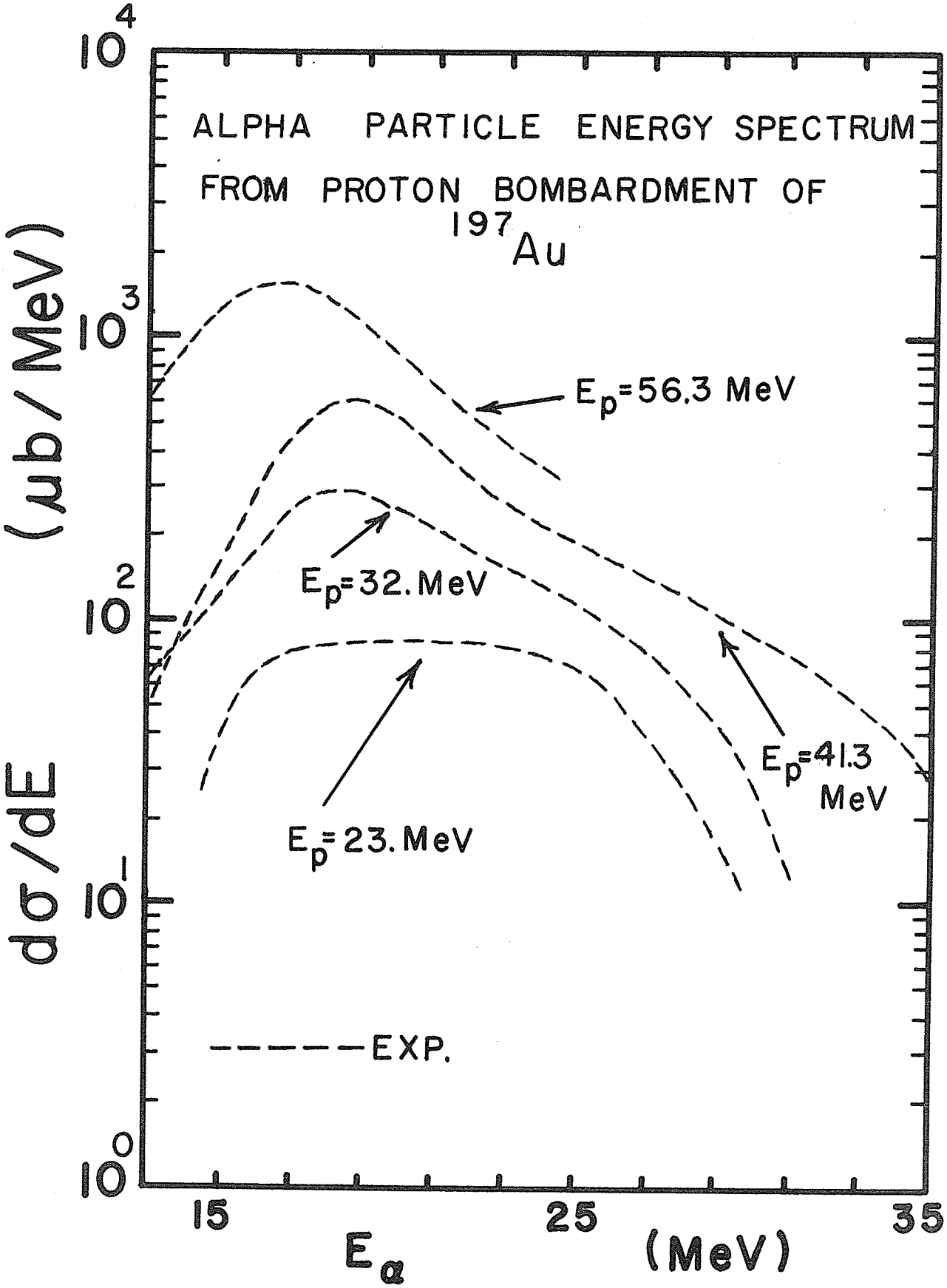
ALPHA PARTICLE ENERGY SPECTRUM
FROM PROTON BOMBARDMENT OF
197 Au
10^4
10^3
10^2
10^1
10^0
(μb / MeV)
dσ/dE
E_p=56.3 MeV
E_p=32. MeV
E_p=41.3 MeV
E_p=23. MeV
-----EXP.
15
25
35
E_α (MeV)

FIGURE 5.3

Variation of first shower partial width

with proton energy Ep and level density parameter α

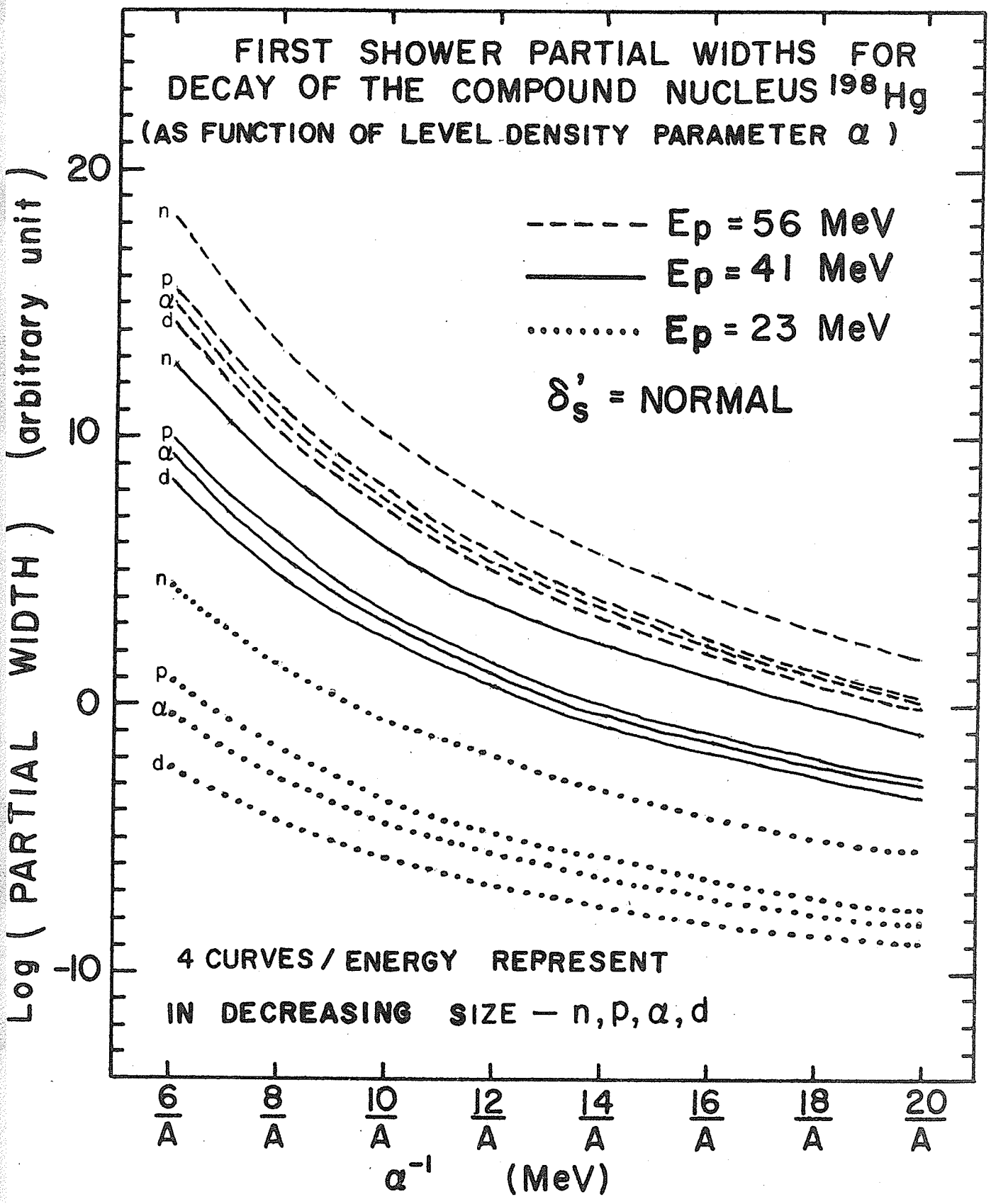
FIRST SHOWER PARTIAL WIDTHS FOR
DECAY OF THE COMPOUND NUCLEUS ^{198}Hg
(AS FUNCTION OF LEVEL DENSITY PARAMETER α)
Ep = 56 MeV
Ep = 41 MeV
Ep = 23 MeV
δ_s' = NORMAL
n
p
α
d
4 CURVES / ENERGY REPRESENT
IN DECREASING SIZE — n, p, α, d
Log (PARTIAL WIDTH) (arbitrary unit)
20
10
0
-10
6/A
8/A
10/A
12/A
14/A
16/A
18/A
20/A
α^{-1} (MeV)

this variation. The variation of the branching ratio $\frac{\Gamma_\alpha}{\Sigma_i \Gamma_i}$ however is not at all so rapid. This can be seen by examination of $\sigma(p,\alpha)$ for the various proton energies in Tables 5.1 - 5.8 as well as by examining the relative displacements of the curves, pertaining to the same Ep, of Figure 5.2.

Qualitatively one can readily judge the importance of multiple-particle emission by simply examining the Q values of the corresponding reactions (Figure 5.4). However, due to the coulomb barrier experienced by the various reaction products, such a tabulation is not too useful. A much more meaningful tabulation can be obtained by subtracting from the Q values of the various reactions the average energy each particle removed from the corresponding compound nucleus (which for each particle will not differ too much, either with excitation energy or the mass A of the residual nuclei which are all ≈ 195). A neutron removes ≈ 2 mev, a proton ≈ 7 mev, a deuteron ≈ 8 mev while an alpha particle removes ≈ 18 mev (These values are≈ Coulomb Barrier + 2T). A tabulation of the resultant "Effective" Q values is thus obtained (see Figure 5.5) showing immediately the relative importance of the various particle contributing to the first, second and third (shower) branching ratios. The excitation energy of ^{198}Hg which results from bombarding ^{197}Au with protons is ≈ Ep + 7.1 MeV. Thus, for example, one would expect contributions to α spectra resulting from the $n\alpha$ cascade to become significant only for Ep $\geq$ 30 MeV, while contribution from the $d\alpha$ cascade is not expected to contribute significantly until Ep $\geq$ 40 MeV.

Tables 5.1 - 5.8 give in tabular form the contributions from the first, second and third "showers" (having integrated over the pertinent energy spectra) for the four proton projectile energies of interest for the case where

TABLE 5.1

Tabulation of the various theoretical contributions to the alpha particle yield due to 23 MeV proton bombardment of ^{197}Au

TABLE 5.1

E_p = 23.0 MeV PAIRING ENERGIES: NORMAL

EXP. CROSS SECTION: .96 ± .10 mb

EXTRACTED LEVEL DENSITY PAR$^{M.}$ = A/(14.4±.4)

LEVEL DENSITY PARAMETER →	A/6.0	A/7.0	A/8.0	A/9.0	A/10.	A/11.	A/12.	A/14.	A/16.	A/20.
$\sigma(p,\alpha)$	2.26 (-2)	4.62 (-2)	8.49 (-2)	1.40 (-1)	2.20 (-1)	3.23 (-1)	4.57 (-1)	8.29 (-1)	1.36 (+0)	2.96 (+0)
$\sigma(p,n\alpha)$	5.17 (-4)	1.18 (-3)	2.42 (-3)	4.19 (-3)	7.09 (-3)	1.07 (-2)	1.59 (-2)	3.12 (-2)	5.47 (-2)	1.35 (-1)
$\sigma(p,p\alpha)$	5.80 (-10)	2.53 (-9)	1.08 (-8)	2.25 (-8)	6.65 (-8)	1.07 (-7)	1.98 (-7)	5.45 (-7)	1.18 (-6)	3.22 (-6)
$\sigma(p,d\alpha)$	0.00 (+0)	0.00 (+0)	0.00 (+0)	0.00 (+0)	0.00 (+0)	0.00 (+0)	0.00 (+0)	0.00 (+0)	0.00 (+0)	0.00 (+0)
$\sigma(p,\alpha\alpha)$	1.70 (-10)	7.56 (-10)	3.17 (-9)	7.67 (-9)	1.70 (-8)	4.46 (-8)	9.31 (-8)	3.25 (-7)	9.01 (-7)	4.24 (-6)
$\sigma(p,nn\alpha)$			2.27 (-10)		5.29 (-10)					
$\sum_{x,y} \sigma(p,xy\alpha)$			2.27 (-10)		5.29 (-10)					
σ_{sum}	2.31 (-2)	4.74 (-2)	8.73 (-2)	1.44 (-1)	2.27 (-1)	3.34 (-1)	4.73 (-1)	8.61 (-1)	1.41 (+0)	3.09 (+0)
$\%\sigma_{sum}$ 1st SHWR	97.8	97.5	97.2	97.1	96.9	96.8	96.6	96.4	96.1	95.6
$\%\sigma_{sum}$ 2nd SHWR	2.23	2.50	2.75	2.91	3.13	3.22	3.36	3.63	3.88	4.35
$\%\sigma_{sum}$ 3rd SHWR			0.00		0.00					

NOTATION : $\overset{2.26}{(-2)} \rightarrow 2.26 \times 10^{-2}$ mb

TABLE 5.2

Tabulation of the various theoretical contributions to the alpha particle yield due to 32 MeV proton bombardment of ^{197}Au

TABLE 5.2

E_p = 32.0 MeV PAIRING ENERGIES: NORMAL

EXP. CROSS SECTION: 2.76 ± .37 mb

EXTRACTED LEVEL DENSITY PAR$^{M.}$ = A/(12.0 ± .5)

LEVEL DENSITY PARAMETER →	A/6.0	A/7.0	A/8.0	A/9.0	A/10.	A/11.	A/12.	A/14.	A/16.	A/20.
σ (p,α)	1.58 (-1)	3.05 (-1)	5.30 (-1)	8.36 (-1)	1.25 (+)0	1.77 (+0)	2.41 (+0)	4.07 (+1)	6.25 (+0)	1.22 (+1)
σ (p,nα)	1.90 (-2)	3.95 (-2)	7.48 (-2)	1.22 (-1)	1.96 (-1)	2.83 (-1)	4.02 (-1)	7.28 (-1)	1.19 (+0)	2.56 (+0)
σ (p,pα)	1.44 (-6)	4.83 (-6)	1.36 (-5)	3.06 (-5)	6.50 (-5)	1.21 (-4)	2.13 (-4)	5.61 (-4)	1.25 (-3)	4.38 (-3)
σ (p,dα)	5.68 (-10)	3.62 (-9)	1.84 (-8)	5.91 (-8)	1.84 (-7)	4.71 (-7)	1.12 (-6)	5.02 (-6)	1.76 (-5)	1.29 (-4)
σ (p,αα)	4.10 (-7)	1.48 (-6)	4.59 (-6)	1.07 (-5)	2.45 (-5)	4.71 (-5)	8.72 (-5)	2.50 (-4)	5.97 (-4)	2.35 (-3)
σ (p,nnα)			1.33 (-2)		2.98 (-2)					
$\sum_{x,y} \sigma$ (p,xyα)			1.33 (-2)		2.98 (-2)					
σ_{sum}	1.77 (-1)	3.44 (-1)	6.18 (-1)	9.58 (-1)	1.48 (+0)	2.05 (+0)	2.81 (+0)	4.80 (+0)	7.44 (+0)	1.48 (+1)
%σ_{sum} 1st SHWR	89.2	88.5	85.7	87.3	84.8	86.2	85.7	84.8	84.0	82.6
%σ_{sum} 2nd SHWR	10.8	11.5	12.1	12.7	13.2	13.8	14.3	15.2	16.0	17.4
%σ_{sum} 3rd SHWR			2.2		2.0					

NOTATION : $^{1.58}_{(-1)} \rightarrow 1.58 \times 10^{-1}$ mb

TABLE 5.3

Tabulation of the various theoretical contributions to the alpha particle yield due to 41.3 MeV proton bombardment of ^{197}Au

TABLE 5.3

E_p = 41.3 MeV PAIRING ENERGIES: NORMAL

EXP. CROSS SECTION: 4.90 ± .38 mb

EXTRACTED LEVEL DENSITY PAR^M = A/(9.9±.2)

LEVEL DENSITY PARAMETER →	A/6.0	A/7.0	A/8.0	A/9.0	A/10.	A/11.	A/12.	A/14.	A/16.	A/20.
σ (p,α)	5.81 (-1)	1.05 (+0)	1.61 (+0)	2.57 (+0)	3.55 (+0)	5.01 (+0)	6.59 (+0)	1.05 (+1)	1.51 (+1)	2.72 (+1)
σ (p,nα)	1.49 (-1)	2.87 (-1)	4.55 (-1)	7.82 (-1)	1.09 (+0)	1.65 (+0)	2.24 (+0)	3.75 (+0)	5.51 (+0)	1.07 (+1)
σ (p,pα)	6.85 (-5)	1.90 (-4)	3.65 (-4)	9.27 (-4)	1.54 (-3)	3.06 (-3)	5.03 (-3)	1.18 (-2)	2.27 (-2)	6.96 (-2)
σ (p,dα)	3.22 (-7)	1.48 (-6)	5.51 (-6)	1.53 (-5)	4.21 (-5)	8.68 (-5)	1.79 (-4)	6.35 (-4)	1.93 (-3)	1.14 (-2)
σ (p,αα)	2.24 (-5)	7.18 (-5)	1.56 (-4)	4.37 (-4)	7.75 (-4)	1.70 (-3)	2.99 (-3)	7.83 (-3)	1.60 (-1)	5.69 (-1)
σ (p,nnα)	8.11 (-2)	1.42 (-1)	2.24 (-1)	3.40 (-1)	4.84 (-1)	6.58 (-1)	8.66 (-1)	1.38 (+0)	2.06 (+0)	3.74 (+0)
$\sum_{x,y}$ σ (p,xyα)	8.11 (-2)	1.42 (-1)	2.24 (-1)	3.40 (-1)	4.84 (-1)	6.59 (-1)	8.67 (-1)	1.39 (+0)	2.06 (+0)	3.75 (+0)
σ_{sum}	8.12 (-1)	1.48 (+0)	2.29 (+0)	3.70 (+0)	5.12 (+0)	7.32 (+0)	9.70 (+0)	1.56 (+1)	2.27 (+1)	4.18 (+1)
%σ_{sum} 1st SHWR	71.6	71.0	70.5	69.6	69.3	68.5	67.9	67.0	66.4	65.2
%σ_{sum} 2nd SHWR	18.4	19.4	19.8	21.2	21.3	22.5	23.1	24.2	24.5	25.8
%σ_{sum} 3rd SHWR	10.0	9.6	9.7	9.2	9.4	9.0	8.9	8.8	9.1	9.0

NOTATION: $\overset{5.81}{(-1)} \rightarrow 5.81 \times 10^{-1}$ mb

TABLE 5.4

Tabulation of the various theoretical contributions to the alpha particle yield due to 56.3 MeV proton bombardment of ^{197}Au

TABLE 5.4

E_p = 56.3 MeV PAIRING ENERGIES: NORMAL

EXP. CROSS SECTION: 15.0 ± 1.0 mb

EXTRACTED LEVEL DENSITY PAR$^{M.}$ = A/(9.5± .2)

LEVEL DENSITY PARAMETER →	A/6.0	A/7.0	A/8.0	A/9.0	A/10.	A/11.	A/12.	A/14.	A/16.	A/20.
σ (p,α)	1.80 (+0)	3.09 (+0)	4.68 (+0)	6.98 (+0)	9.42 (+0)	1.27 (+1)	1.61 (+1)	2.42 (+1)	3.35 (+1)	5.50 (+1)
σ (p,nα)	8.04 (-1)	1.45 (+0)	2.21 (+0)	3.53 (+0)	4.77 (+0)	6.76 (+0)	8.80 (+0)	1.37 (+1)	1.96 (+1)	3.35 (+1)
σ (p,pα)	1.22 (-3)	3.14 (-3)	6.27 (-3)	1.33 (-2)	2.23 (-2)	3.89 (-2)	6.03 (-2)	1.27 (-1)	2.33 (-1)	5.96 (-1)
σ (p,dα)	3.10 (-5)	1.22 (-4)	4.15 (-4)	9.64 (-4)	2.38 (-3)	4.37 (-3)	8.09 (-3)	2.29 (-2)	5.32 (-2)	1.95 (-1)
σ (p,αα)	5.20 (-4)	1.54 (-3)	3.35 (-3)	8.12 (-3)	1.43 (-2)	2.77 (-2)	4.58 (-2)	1.07 (-1)	2.14 (-1)	6.24 (-1)
σ (p,nnα)	7.07 (-1)	1.20 (+0)	1.81 (+0)	2.68 (+0)	3.62 (+0)	4.83 (+0)	6.14 (+0)	9.18 (+0)	1.27 (+1)	2.06 (+1)
$\sum_{x,y}$ σ (p,xyα)	7.07 (-1)	1.20 (+0)	1.82 (+0)	2.68 (+0)	3.64 (+0)	4.85 (+0)	6.18 (+0)	9.28 (+0)	1.29 (+1)	2.12 (+1)
σ_{sum}	3.32 (+0)	5.74 (+0)	8.71 (+0)	1.32 (+1)	1.79 (+1)	2.43 (+1)	3.12 (+1)	4.74 (+1)	6.65 (+1)	1.11 (+2)
%σ_{sum} 1st SHWR	54.4	53.8	53.7	52.8	52.8	52.0	51.6	50.9	50.4	49.4
%σ_{sum} 2nd SHWR	24.3	25.3	25.5	26.9	26.8	28.1	28.6	29.5	30.2	31.5
%σ_{sum} 3rd SHWR	21.3	20.9	20.8	20.3	20.4	19.9	19.8	19.6	19.4	19.1

NOTATION: $\overset{1.80}{(+0)} \rightarrow 1.80 \times 10^{+0}$ mb

TABLE 5.5

Tabulation of the various theoretical contributions to the alpha particle yield due to 23.0 MeV proton bombardment of ^{197}Au

TABLE 5.5

E_p = 23.0 MeV PAIRING ENERGIES: ZERO

EXP. CROSS SECTION: .96 ± .10 mb

EXTRACTED LEVEL DENSITY PAR$^{M.}$ = A/10.9±.3

LEVEL DENSITY PARAMETER →	A/6.0	A/7.0	A/8.0	A/9.0	A/10.	A/11.	A/12.	A/14.	A/16.	A/20.
σ (p,α)	9.69 (-2)	1.80 (-1)	3.03 (-1)	4.73 (-1)	7.00 (-1)	9.80 (-1)	1.33 (+0)	2.24 (+0)	3.45 (+0)	6.82 (+0)
σ (p,nα)	4.80 (-4)	1.13 (-3)	2.30 (-3)	4.19 (-3)	7.09 (-3)	1.13 (-2)	1.73 (-2)	3.65 (-2)	6.95 (-2)	1.87 (-1)
σ (p,pα)	2.18 (-8)	1.96 (-7)	1.19 (-6)	5.29 (-6)	1.84 (-5)	5.25 (-5)	1.28 (-4)	5.22 (-4)	1.43 (-3)	4.65 (-3)
σ (p,dα)	0.00 (+0)	0.00 (+0)	0.00 (+0)	0.00 (+0)	0.00 (+0)	0.00 (+0)	0.00 (+0)	0.00 (+0)	0.00 (+0)	0.00 (+0)
σ (p,ααα)	2.57 (-8)	1.74 (-7)	9.27 (-7)	3.82 (-6)	1.26 (-5)	3.45 (-5)	8.11 (-5)	3.08 (-4)	7.95 (-4)	2.50 (-3)
σ (p,nnα)										
$\sum_{x,y}$ σ (p,xyα)										
σ_{sum}	9.73 (-2)	1.81 (-1)	3.05 (-1)	4.77 (-1)	7.04 (-1)	9.92 (-1)	1.35 (+0)	2.28 (+0)	3.51 (+0)	7.01 (+0)
%σ_{sum} 1st SHWR	99.5	99.4	99.2	99.1	99.0	98.8	98.7	98.3	98.0	97.2
%σ_{sum} 2nd SHWR	.50	.63	.76	.88	1.01	1.15	1.30	1.65	2.04	2.78
%σ_{sum} 3rd SHWR										

NOTATION: $9.69_{(-2)} \rightarrow 9.69 \times 10^{-2}$ mb

TABLE 5.6

Tabulation of the various theoretical contributions to the alpha particle yield due to 32.0 MeV proton bombardment of ^{197}Au

TABLE 5.6

E_p = 32.0 MeV PAIRING ENERGIES: ZERO

EXP. CROSS SECTION: 2.76 ± .37 mb

EXTRACTED LEVEL DENSITY PAR$^{M.}$ = A/(9.3±.3)

LEVEL DENSITY PARAMETER →	A/6.0	A/7.0	A/8.0	A/9.0	A/10.	A/11.	A/12.	A/14.	A/16.	A/20.
$\sigma(p,\alpha)$	5.03 (-1)	8.93 (-1)	1.44 (+0)	2.16 (+0)	3.07 (+0)	4.18 (+0)	5.49 (+0)	8.72 (+0)	1.28 (+1)	2.30 (+1)
$\sigma(p,n\alpha)$	1.57 (-2)	3.35 (-2)	6.27 (-2)	1.07 (-1)	1.70 (-1)	2.54 (-1)	3.63 (-1)	6.69 (-1)	1.10 (+0)	2.42 (+0)
$\sigma(p,p\alpha)$	4.58 (-6)	1.42 (-5)	3.61 (-5)	8.00 (-5)	1.60 (-4)	2.92 (-4)	5.03 (-4)	1.27 (-3)	2.76 (-3)	9.07 (-3)
$\sigma(p,d\alpha)$	1.05 (-10)	7.45 (-10)	3.69 (-9)	1.41 (-8)	4.43 (-8)	1.20 (-7)	2.86 (-7)	1.24 (-6)	4.01 (-6)	2.26 (-5)
$\sigma(p,\alpha\alpha)$	5.64 (-6)	1.74 (-5)	4.49 (-5)	1.02 (-4)	2.15 (-4)	4.34 (-4)	8.67 (-4)	3.48 (-3)	1.32 (-2)	1.20 (-1)
$\sigma(p,nn\alpha)$	4.03 (-2)	6.64 (-2)	1.01 (-1)	1.44 (-1)	1.96 (-1)	2.58 (-1)	3.29 (-1)	4.98 (-1)	7.00 (-1)	1.15 (+0)
$\sum_{x,y} \sigma(p,xy\alpha)$	4.03 (-2)	6.64 (-2)	1.01 (-1)	1.44 (-1)	1.96 (-1)	2.58 (-1)	3.29 (-1)	4.98 (-1)	7.00 (-1)	1.16 (+0)
σ_{sum}	5.59 (-1)	9.92 (-1)	1.60 (+0)	2.41 (+0)	3.44 (+0)	4.70 (+0)	6.19 (+0)	9.89 (+0)	1.46 (+1)	2.67 (+1)
%σ_{sum} 1st SHWR	90.0	89.9	89.8	89.6	89.4	89.1	88.8	88.3	87.6	86.6
%σ_{sum} 2nd SHWR	2.8	3.4	3.9	4.4	4.9	5.4	5.9	6.7	7.6	9.1
%σ_{sum} 3rd SHWR	7.2	6.7	6.3	6.0	5.7	5.5	5.3	5.0	4.8	4.3

NOTATION: $\overset{5.03}{(-1)} \rightarrow 5.03 \times 10^{-1}$ mb

TABLE 5.7

Tabulation of the various theoretical contributions to the alpha particle yield due to 41.3 MeV proton bombardment of ^{197}Au

TABLE 5.7

E_p = 41.3 MeV PAIRING ENERGIES: ZERO

EXP. CROSS SECTION: 4.90 ± .38 mb

EXTRACTED LEVEL DENSITY PAR$^{M.}$ = A/(8.0±.2)

LEVEL DENSITY PARAMETER →	A/6.0	A/7.0	A/8.0	A/9.0	A/10.	A/11.	A/12.	A/14.	A/16.	A/20.
$\sigma(p,\alpha)$	1.39 (+0)	2.39 (+0)	3.72 (+0)	5.42 (+0)	7.49 (+0)	9.93 (+0)	1.26 (+1)	1.93 (+1)	2.72 (+1)	4.58 (+1)
$\sigma(p,n\alpha)$	1.04 (-1)	2.08 (-1)	3.69 (-1)	6.00 (-1)	9.10 (-1)	1.31 (+0)	1.80 (+0)	3.10 (+0)	4.82 (+0)	9.51 (+0)
$\sigma(p,p\alpha)$	1.10 (-4)	3.14 (-4)	7.49 (-4)	1.56 (-3)	2.95 (-3)	5.14 (-3)	8.40 (-3)	1.93 (-2)	3.85 (-2)	1.16 (-1)
$\sigma(p,d\alpha)$	7.17 (-8)	3.89 (-7)	1.56 (-6)	5.01 (-6)	1.36 (-5)	3.26 (-5)	7.03 (-5)	2.61 (-4)	7.81 (-4)	4.93 (-3)
$\sigma(p,\alpha\alpha)$	1.18 (-4)	3.52 (-4)	8.78 (-4)	1.91 (-3)	3.75 (-3)	6.76 (-3)	1.14 (-2)	2.79 (-2)	5.85 (-2)	1.94 (-1)
$\sigma(p,nn\alpha)$	3.57 (-1)	5.85 (-1)	8.85 (-1)	1.26 (+0)	1.71 (+0)	2.24 (+0)	2.84 (+0)	4.27 (+0)	6.01 (+0)	1.08 (+1)
$\sum_{x,y} \sigma(p,xy\alpha)$	3.57 (-1)	5.85 (-1)	8.85 (-1)	1.26 (+0)	1.71 (+0)	2.24 (+0)	2.84 (+0)	4.27 (+0)	6.02 (+0)	1.09 (+1)
σ_{sum}	1.85 (+0)	3.18 (+0)	4.98 (+0)	7.28 (+0)	1.01 (+1)	1.35 (+1)	1.74 (+1)	2.67 (+1)	3.81 (+1)	6.65 (+1)
$\%\sigma_{sum}$ 1st SHWR	75.1	75.0	74.7	74.4	74.0	73.6	73.2	72.8	71.3	68.8
$\%\sigma_{sum}$ 2nd SHWR	5.6	6.6	7.5	8.3	9.1	9.8	10.5	11.8	12.9	14.8
$\%\sigma_{sum}$ 3rd SHWR	19.3	18.4	17.8	17.3	16.9	16.6	16.3	15.4	15.8	16.4

NOTATION: $\overset{1.39}{(+0)}$ = 1.39 X 10^0 mb.

TABLE 5.8

Tabulation of the various theoretical contributions to the alpha particle yield due to 56.3 MeV proton bombardment of ^{197}Au

TABLE 5.8

E_p = 56.3 MeV PAIRING ENERGIES: ZERO

EXP. CROSS SECTION: 15.0 ± 1.0 mb

EXTRACTED LEVEL DENSITY $PAR^{M.} = A/(7.8 \pm .2)$

LEVEL DENSITY PARAMETER →	A/6.0	A/7.0	A/8.0	A/9.0	A/10.	A/11.	A/12.	A/14.	A/16.	A/20.
$\sigma(p,\alpha)$	3.96 (+0)	6.40 (+0)	9.51 (+0)	1.33 (+1)	1.76 (+1)	2.26 (+1)	2.80 (+1)	4.02 (+1)	5.39 (+1)	8.37 (+1)
$\sigma(p,n\alpha)$	6.25 (-1)	1.15 (+0)	1.90 (+0)	2.89 (+0)	4.15 (+0)	5.66 (+0)	7.44 (+0)	1.17 (+1)	1.70 (+1)	2.96 (+1)
$\sigma(p,p\alpha)$	2.22 (-3)	5.47 (-3)	1.16 (-2)	2.18 (-2)	3.77 (-2)	6.07 (-2)	9.24 (-2)	1.88 (-1)	3.36 (-1)	8.21 (-1)
$\sigma(p,d\alpha)$	9.47 (-6)	4.06 (-5)	1.34 (-4)	3.66 (-4)	8.63 (-4)	1.82 (-3)	3.50 (-3)	1.05 (-2)	2.57 (-2)	1.01 (-1)
$\sigma(p,\alpha\alpha)$	2.30 (-3)	6.17 (-3)	1.40 (-2)	2.79 (-2)	5.05 (-2)	8.49 (-2)	1.34 (-1)	2.91 (-1)	5.46 (-1)	1.44 (+0)
$\sigma(p,nn\alpha)$	2.15 (+0)	3.38 (+0)	4.93 (+0)	6.77 (+0)	8.90 (+0)	1.13 (+1)	1.39 (+1)	1.97 (+1)	2.60 (+1)	3.96 (+1)
$\sum_{x,y} \sigma(p,xy\alpha)$	2.15 (+0)	3.38 (+0)	4.93 (+0)	6.78 (+0)	8.91 (+0)	1.13 (+1)	1.39 (+1)	1.97 (+1)	2.62 (+1)	4.01 (+1)
σ_{sum}	6.74 (+0)	1.09 (+1)	1.64 (+1)	2.30 (+1)	3.08 (+1)	3.97 (+1)	4.96 (+1)	7.22 (+1)	9.79 (+1)	1.56 (+2)
$\%\sigma_{sum}$ 1st SHWR	58.8	58.5	58.2	57.7	57.4	56.9	56.5	55.8	54.9	53.7
$\%\sigma_{sum}$ 2nd SHWR	9.3	10.6	11.8	12.8	13.7	14.6	15.4	16.9	18.3	20.5
$\%\sigma_{sum}$ 3rd SHWR	31.9	30.9	30.0	29.5	28.9	28.5	28.1	27.3	26.8	25.8

NOTATION : $3.96_{(+0)} \rightarrow 3.96 \times 10^0$ mb

FIGURE 5.4

Q values for the emission of various particles from ^{198}Hg

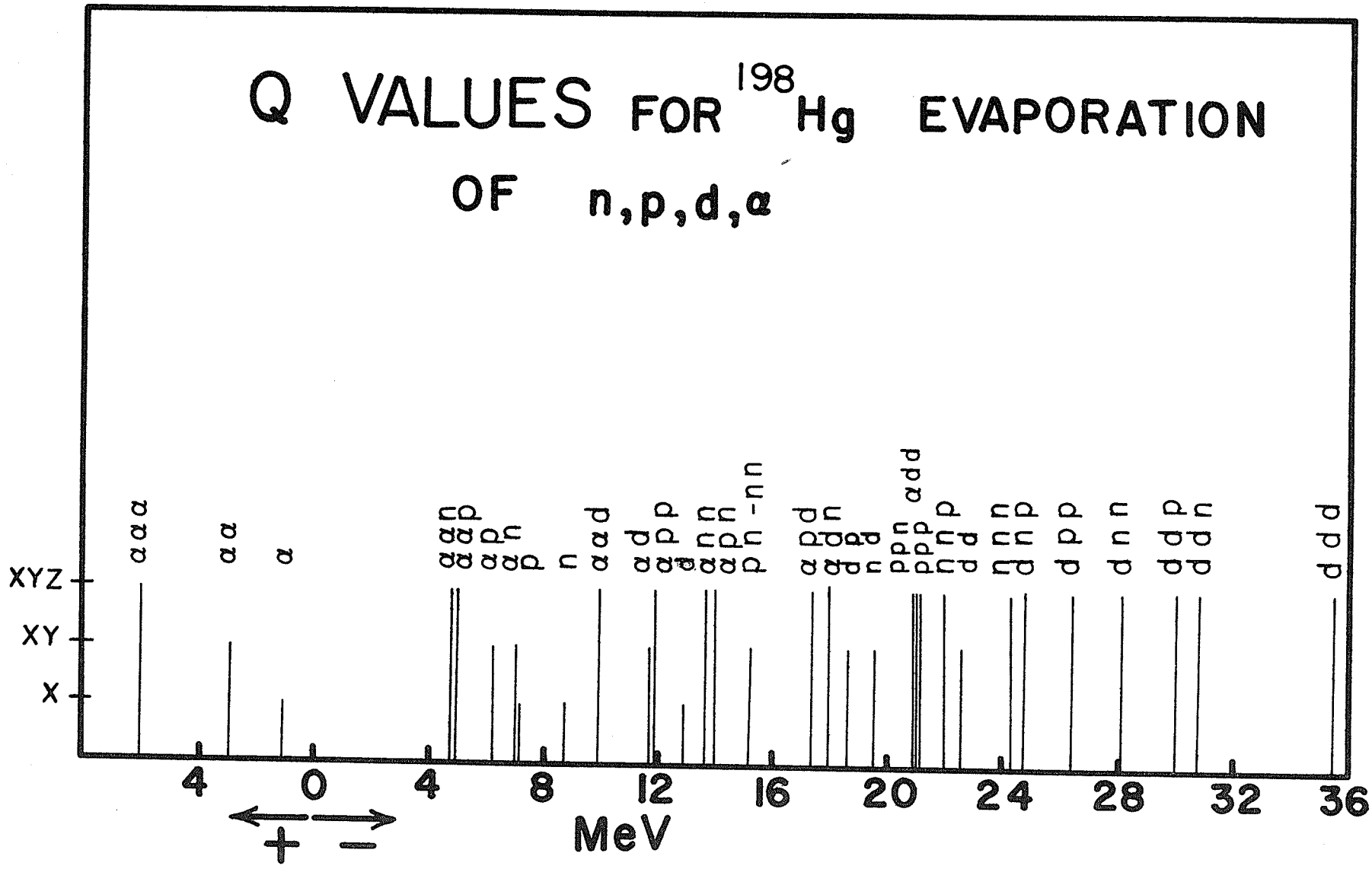
Q VALUES FOR 198Hg EVAPORATION
OF n,p,d,α
XYZ
XY
X
4
0
4
8
12
16
20
24
28
32
36
MeV
+
−

FIGURE 5.5

"Effective" Q values for the

emission of various particles from ^{198}Hg

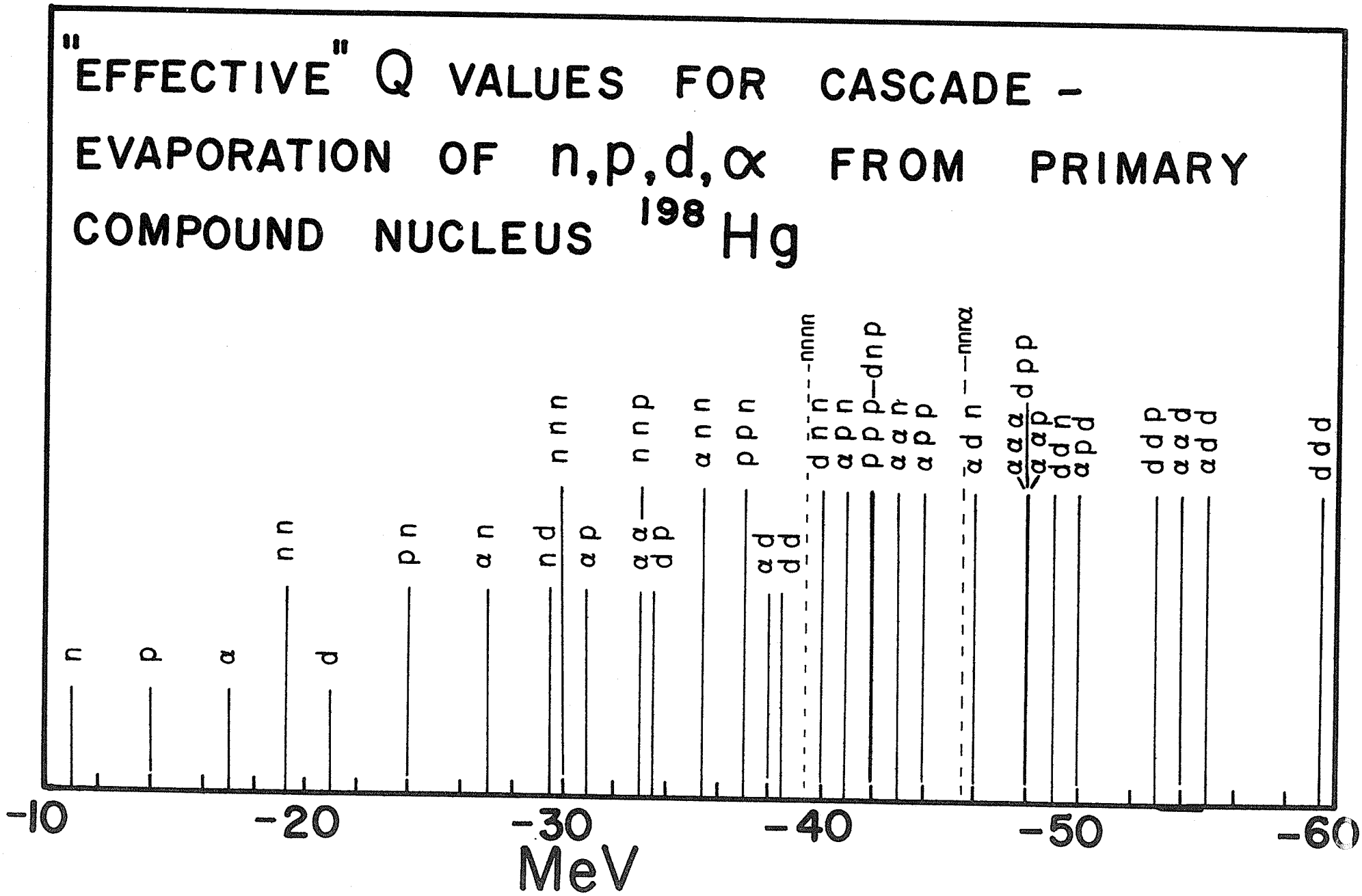
"EFFECTIVE" Q VALUES FOR CASCADE - EVAPORATION OF n,p,d,α FROM PRIMARY COMPOUND NUCLEUS 198Hg
n
p
α
nn
d
pn
αn
nd
αp
nnn
αα
dp
npp
ann
ppn
αd
dd
d n n n
nnnn
dnnp
αpn
ppp
dnpp
ααn
αpp
αd n
nnnα
ααα
dpp
αdp
ddn
αpd
ddp
ααd
ddd
-10
-20
-30
-40
-50
-60
MeV

we have "NORMAL" pairing energies and for the case where we have set all the pairing energies equal to zero. The effect of the pairing energies is to change the relative importance of successive "showers". Thus for example, we see from Tables 5.2 and 5.6 that for E_p=32 MeV , using "NORMAL" pairing energies, the 3rd shower contributes $\approx$2% to the total alpha spectrum while it contributes $\approx$6% when all the pairing energies were set to zero. Reactions such as (p,$\alpha\alpha$) and (p,dα) which just exceed the "Effective" Q values for E_p=32 MeV are expected to be more sensitive to the values of the corresponding pairing energies and this can be seen to be the case on comparing the corresponding yields shown in Tables 5.2 and 5.6 .

From Table 5.1-5.8 one can note that the predominant contributions to the second and third showers are the nα and nnα cascades respectively. This is consistent with the tabulated "Effective" Q values of Figure 5.5. Tables 5.1-5.8 also give the level density parameter (in MeV^{-1}) extracted by matching the theoretical and experimental alpha particle yield obtained by bombarding ^{197}Au with protons having the four energies investigated.

Figures 5.6-5.12 show the relative importance of the various "showers" to the energy spectra for α=A/10. MeV^{-1} and α=A/8. MeV^{-1} for E_p=23 MeV, 32 MeV, 41.3 MeV and 56.3 MeV ("NORMAL" δ_s'). From these figures one can readily observe that

a) Contributions from <u>all</u> showers increase with

FIGURE 5.6

Contributions from 1st and 2nd "showers" to the alpha particle energy spectrum resulting from 23 MeV proton bombardment of ^{197}Au

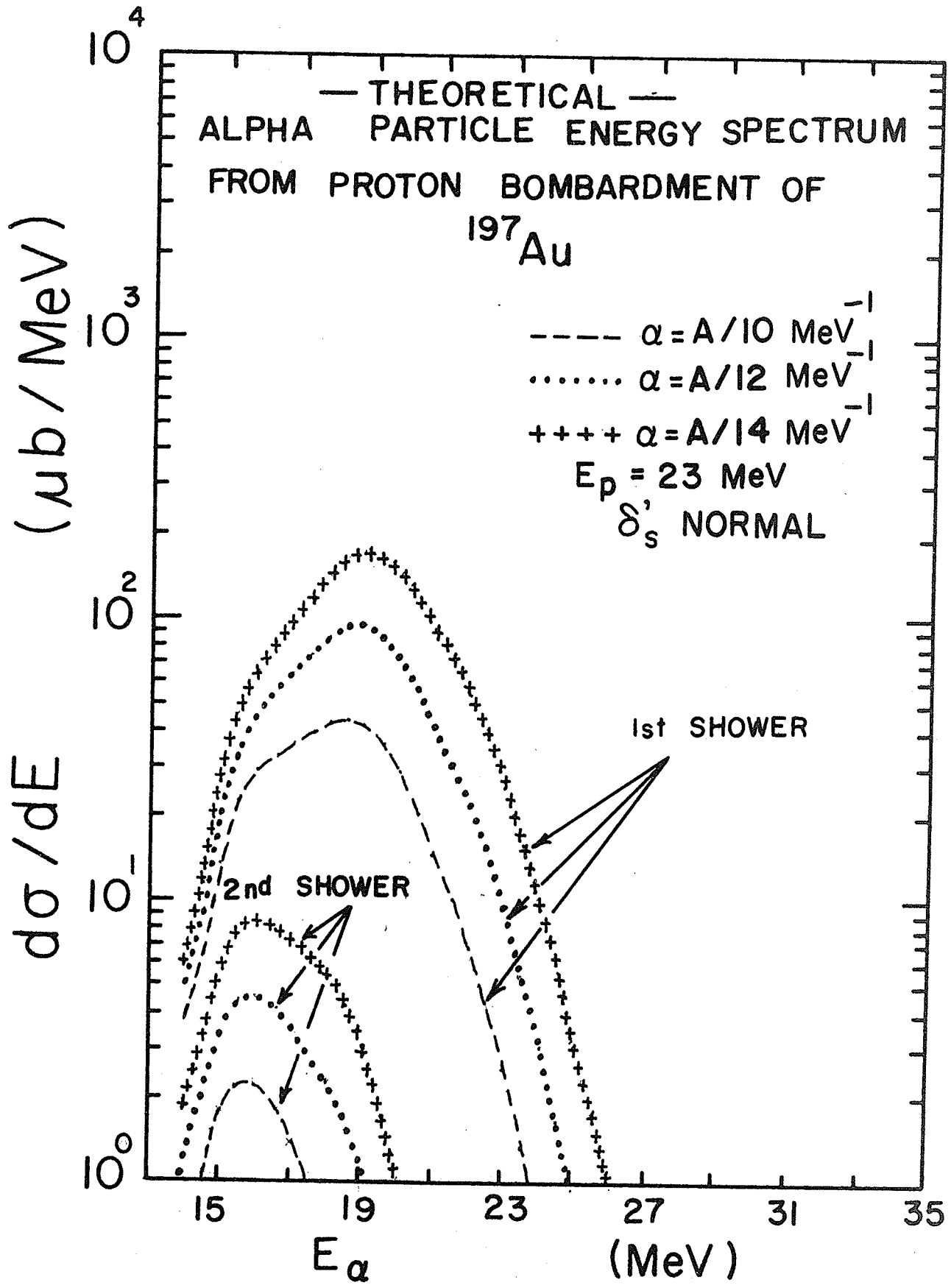
— THEORETICAL —
ALPHA PARTICLE ENERGY SPECTRUM
FROM PROTON BOMBARDMENT OF
197Au
---- α = A/10 MeV-1
..... α = A/12 MeV-1
++++ α = A/14 MeV-1
Ep = 23 MeV
δ's NORMAL
1st SHOWER
2nd SHOWER
dσ/dE (μb/MeV)
Eα (MeV)
10^4
10^3
10^2
10^1
10^0
15
19
23
27
31
35

FIGURE 5.7

Contributions, from the various showers, to the theoretical alpha particle energy spectrum resulting from 32 MeV proton bombardment of ^{197}Au

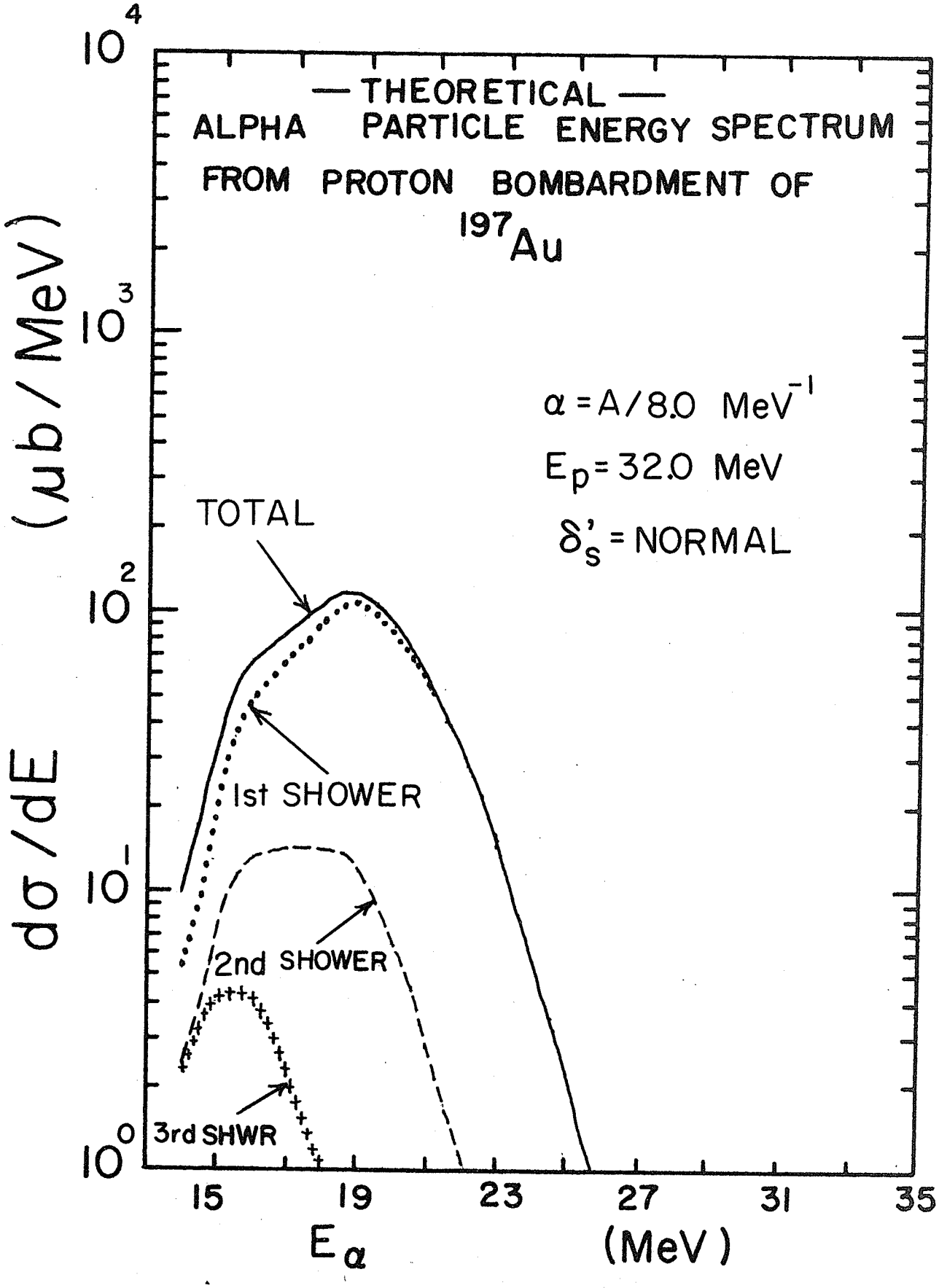
— THEORETICAL —
ALPHA PARTICLE ENERGY SPECTRUM
FROM PROTON BOMBARDMENT OF
197Au
α = A/8.0 MeV-1
Ep = 32.0 MeV
δ's = NORMAL
TOTAL
1st SHOWER
2nd SHOWER
3rd SHWR
dσ/dE (μb/MeV)
Eα (MeV)
10^4
10^3
10^2
10^1
10^0
15
19
23
27
31
35

FIGURE 5.8

Contributions, from the various showers, to the theoretical alpha particle energy spectrum resulting from 32 MeV proton bombardment of ^{197}Au

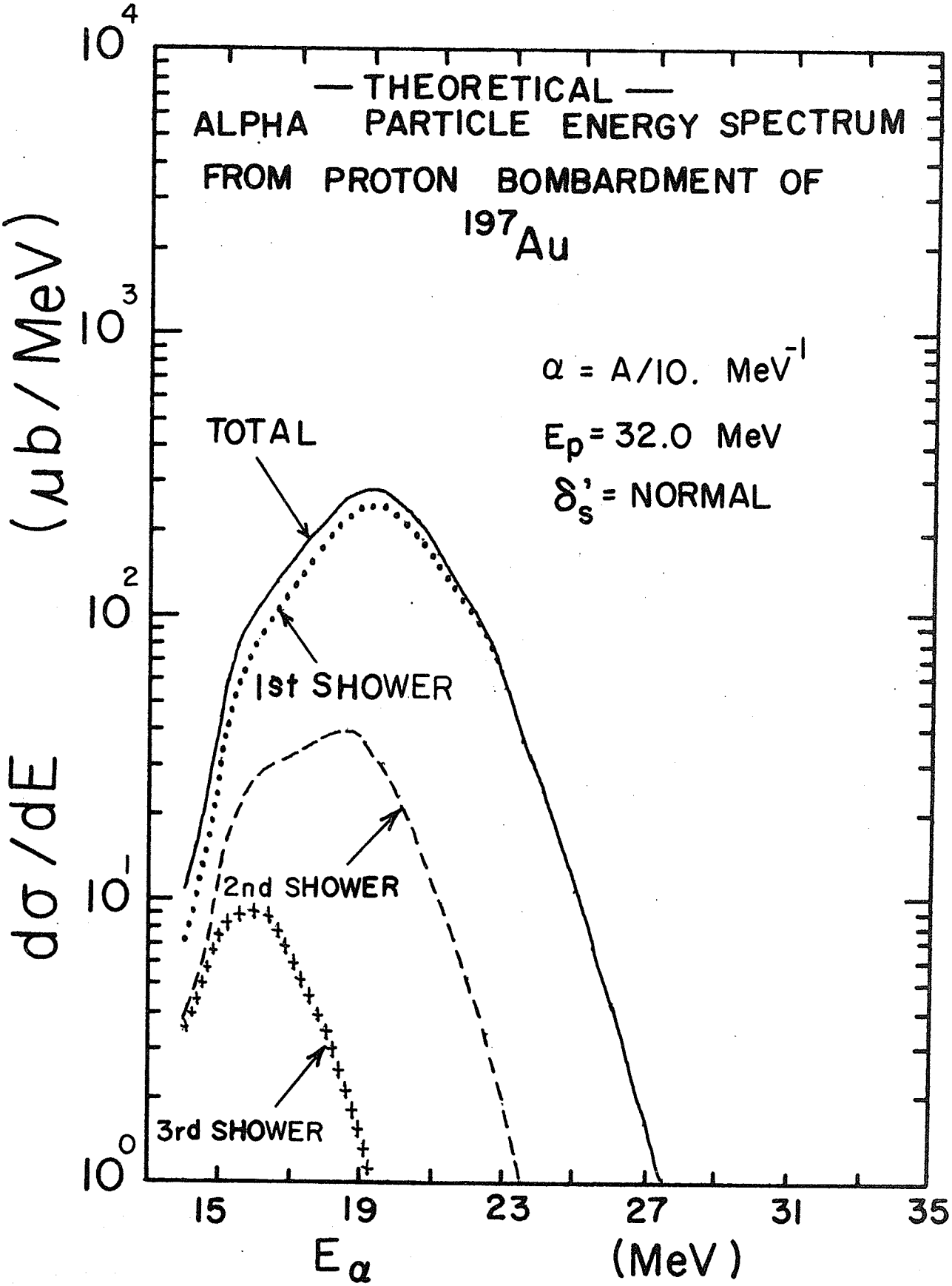
— THEORETICAL —
ALPHA PARTICLE ENERGY SPECTRUM
FROM PROTON BOMBARDMENT OF
197Au
α = A/10. MeV-1
Ep = 32.0 MeV
δs' = NORMAL
TOTAL
1st SHOWER
2nd SHOWER
3rd SHOWER
dσ/dE (μb/MeV)
Eα (MeV)
10^4
10^3
10^2
10^1
10^0
15
19
23
27
31
35

FIGURE 5.9

Contributions, from the various showers, to the theoretical alpha particle energy spectrum resulting from 41.3 MeV proton bombardment of ^{197}Au

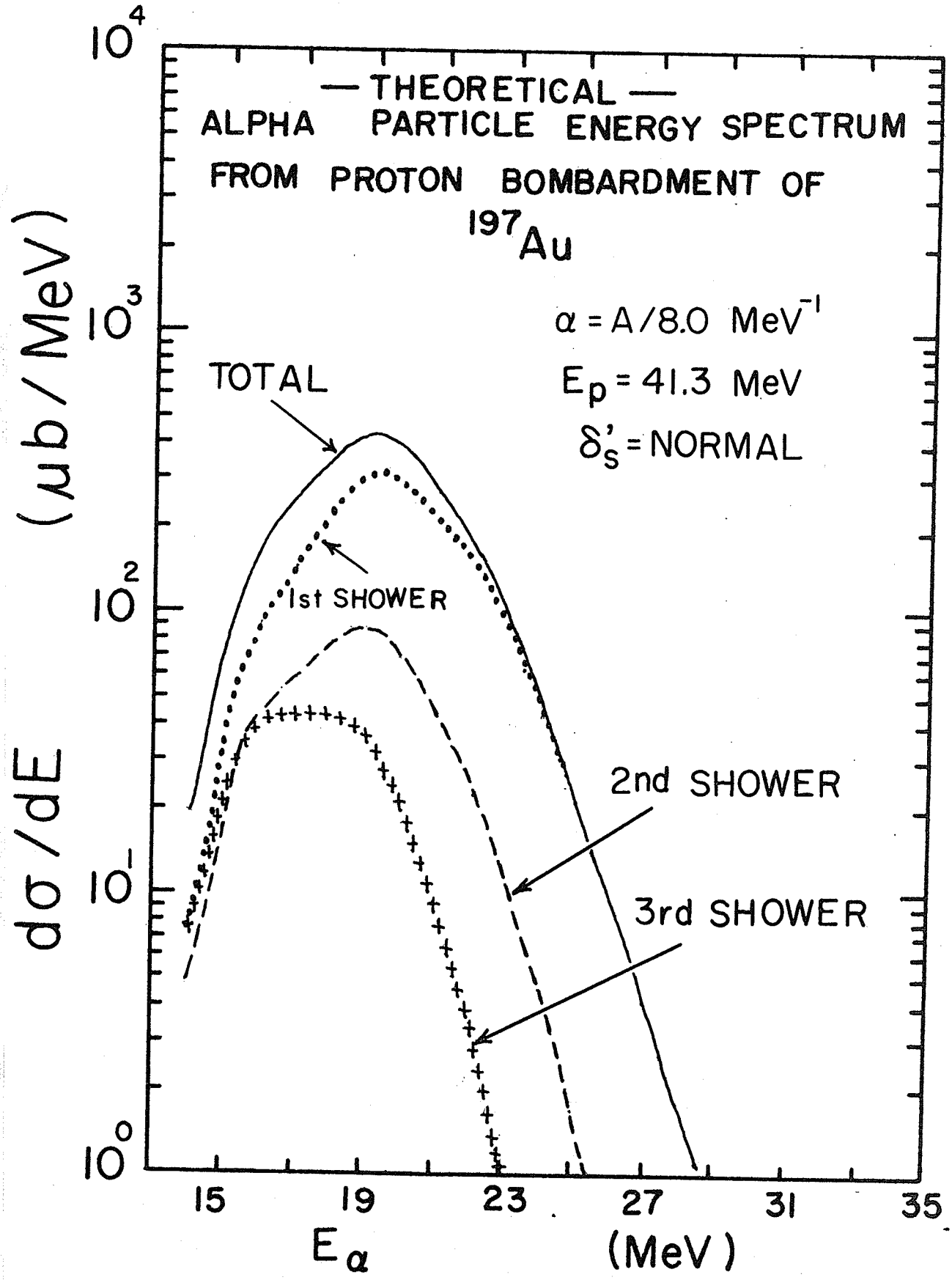
— THEORETICAL —
ALPHA PARTICLE ENERGY SPECTRUM
FROM PROTON BOMBARDMENT OF
197Au
α = A/8.0 MeV-1
Ep = 41.3 MeV
δ's = NORMAL
TOTAL
1st SHOWER
2nd SHOWER
3rd SHOWER
dσ/dE (μb/MeV)
Eα (MeV)
10^4
10^3
10^2
10^1
10^0
15
19
23
27
31
35

FIGURE 5.10

Contributions, from the various showers, to the theoretical alpha particle energy spectrum resulting from 41.3 MeV proton bombardment of ^{197}Au

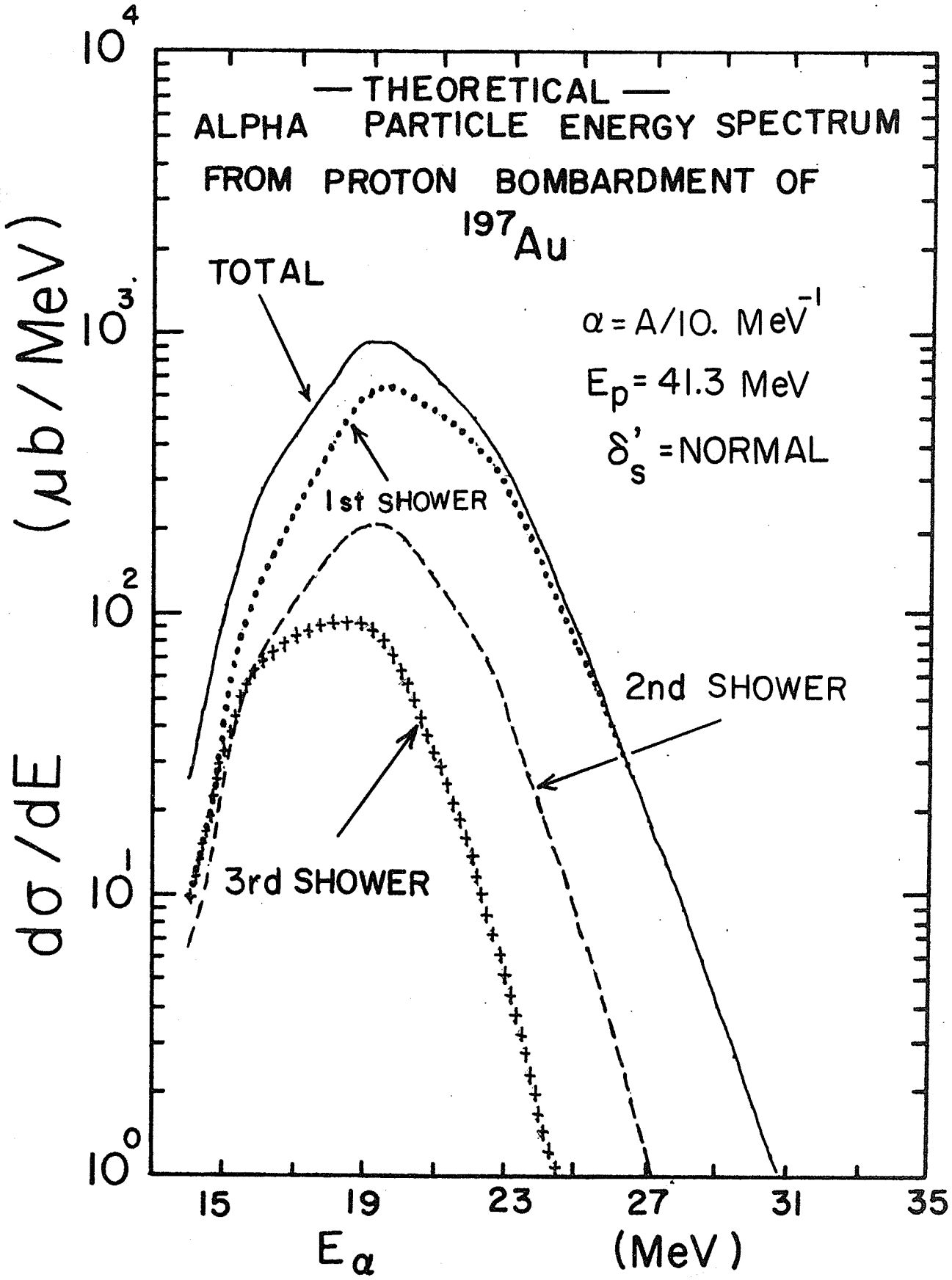
— THEORETICAL —
ALPHA PARTICLE ENERGY SPECTRUM
FROM PROTON BOMBARDMENT OF
197Au
TOTAL
α = A/10. MeV-1
Ep = 41.3 MeV
δ's = NORMAL
1st SHOWER
2nd SHOWER
3rd SHOWER
dσ/dE (μb/MeV)
Eα (MeV)
10^4
10^3
10^2
10^1
10^0
15
19
23
27
31
35

FIGURE 5.11

Contributions, from the various showers, to the theoretical alpha particle energy spectrum resulting from 56 MeV proton bombardment of ^{197}Au

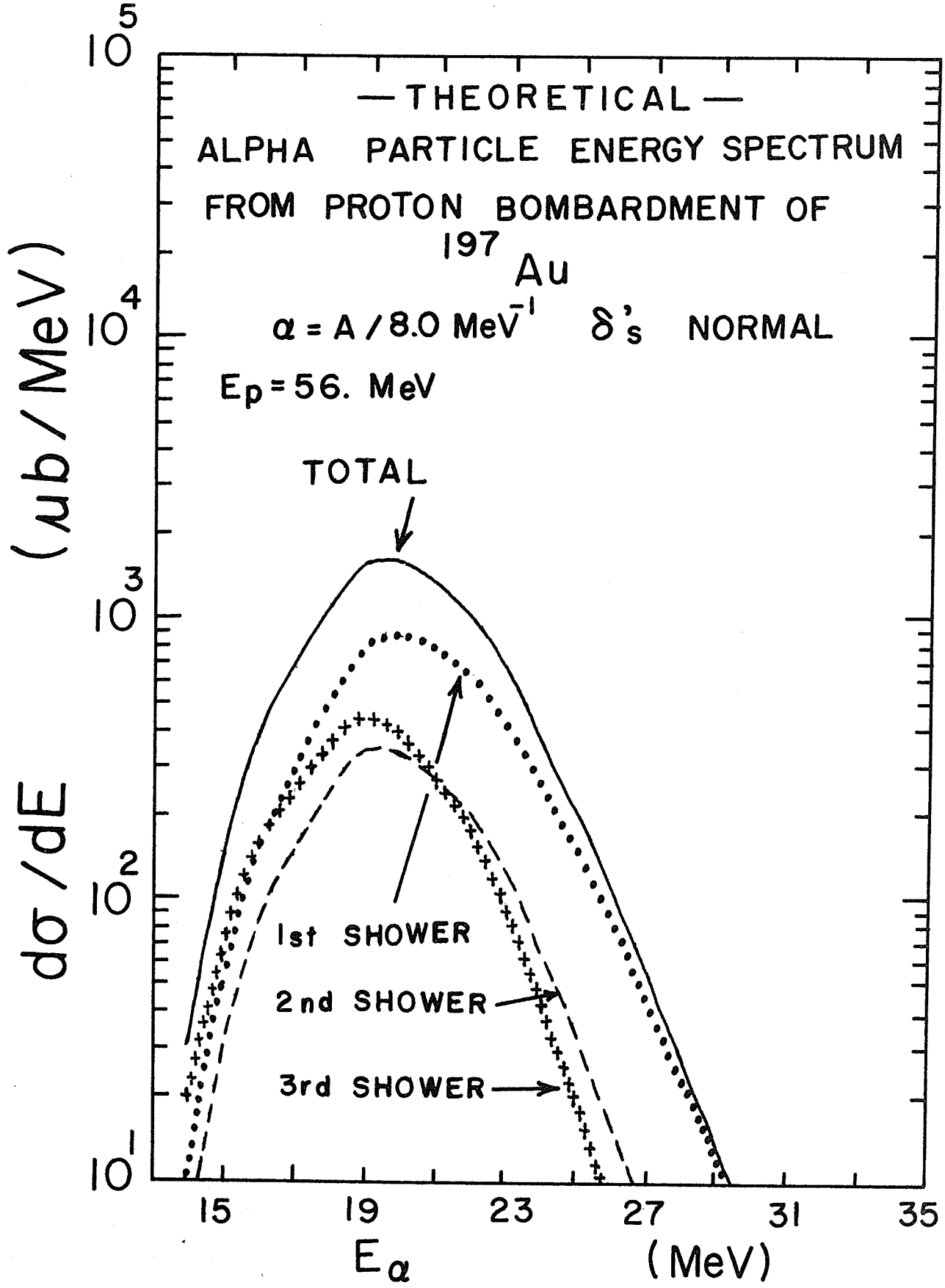
— THEORETICAL —
ALPHA PARTICLE ENERGY SPECTRUM
FROM PROTON BOMBARDMENT OF
197 Au
α = A / 8.0 MeV⁻¹ δ's NORMAL
Ep = 56. MeV
TOTAL
1st SHOWER
2nd SHOWER
3rd SHOWER
dσ/dE (μb/MeV)
Eα (MeV)
10⁵
10⁴
10³
10²
10¹
15
19
23
27
31
35

FIGURE 5.12

Contributions, from the various showers, to the theoretical alpha particle energy spectrum resulting from 56 MeV proton bombardment of ^{197}Au

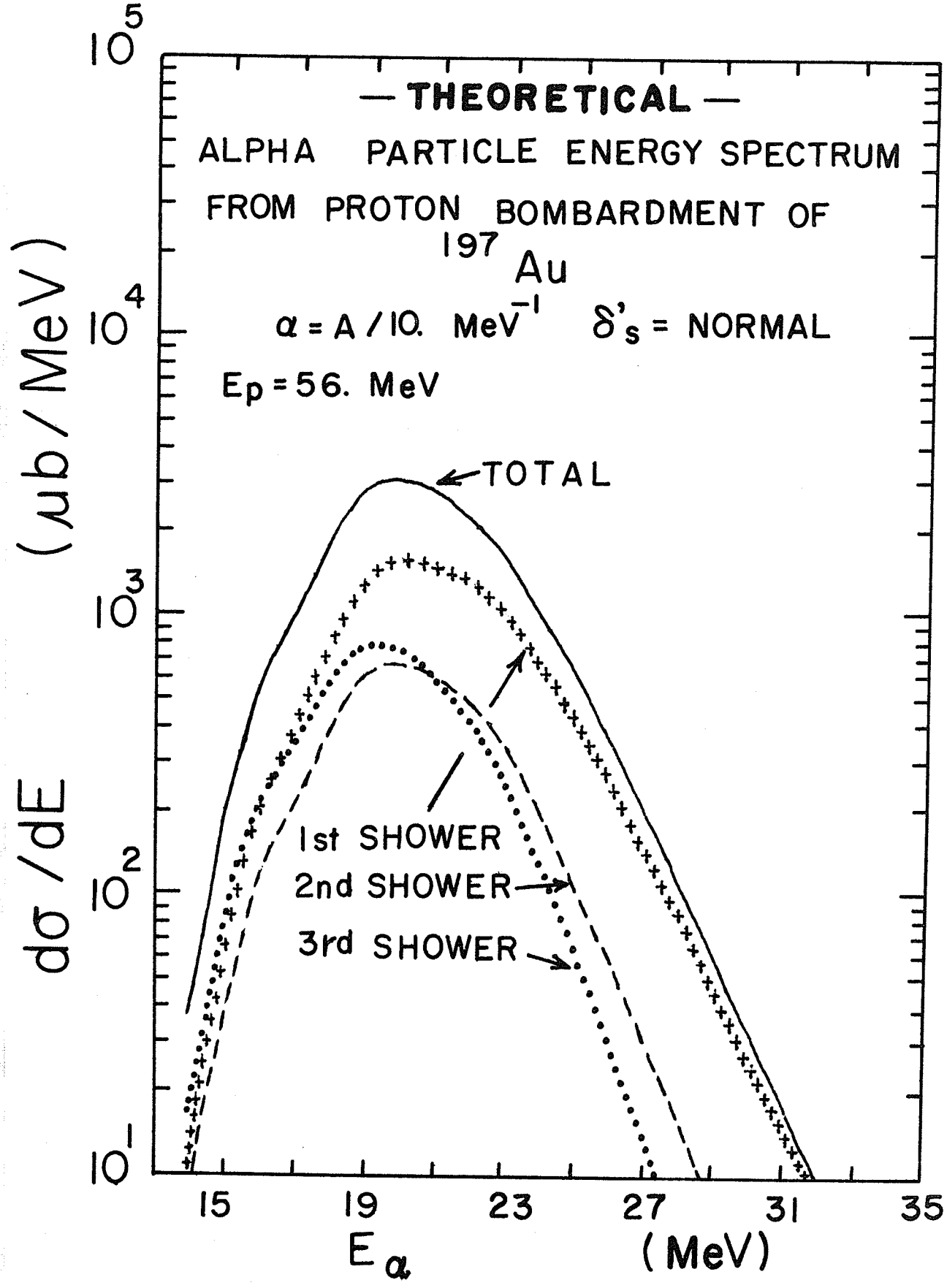
— THEORETICAL —
ALPHA PARTICLE ENERGY SPECTRUM
FROM PROTON BOMBARDMENT OF
197 Au
α = A / 10. MeV⁻¹ δ's = NORMAL
Ep = 56. MeV
TOTAL
1st SHOWER
2nd SHOWER
3rd SHOWER
dσ/dE (μb/MeV)
Eα (MeV)
10⁵
10⁴
10³
10²
10¹
15
19
23
27
31
35

increasing E_p.

b) The contributions from all showers increases as the level density parameter a is reduced.

c) The energy of the peak in the energy spectra increases with decreasing a.

d) The relative contributions from successive "showers" increases with increasing E_p. That is, as the excitation of the primary compound nucleus increases the third shower say, becomes more and more important relative to the preceding shower(s) .

Figures 5.13-5.16 show the variation of the "TOTAL" (sum of the contributions from all the showers) energy spectra for various a and compares them to the experimentally obtained energy spectra.

We can readily observe that successive showers have their greatest influence on the lower energy part of the alpha energy spectrum. The peak of each successive shower also shifts to lower energies. Although as a decreases these successive showers become more important the average energy cf all showers increases , with the net result that for the proton range 20-60 MeV the average alpha particle energy increases somewhat with decreasing level density parameter a.

For the four proton energies 23 MeV, 32 MeV, 41.3 MeV and 56.3 MeV we have extracted the level density parameter in two ways:

i) Varying a until one obtains agreement between the theoretical and experimental alpha particle yield. The values

FIGURE 5.13

Variation, with level density parameter α, of the theoretical alpha particle energy spectrum resulting from 23 MeV proton bombardment of ^{197}Au

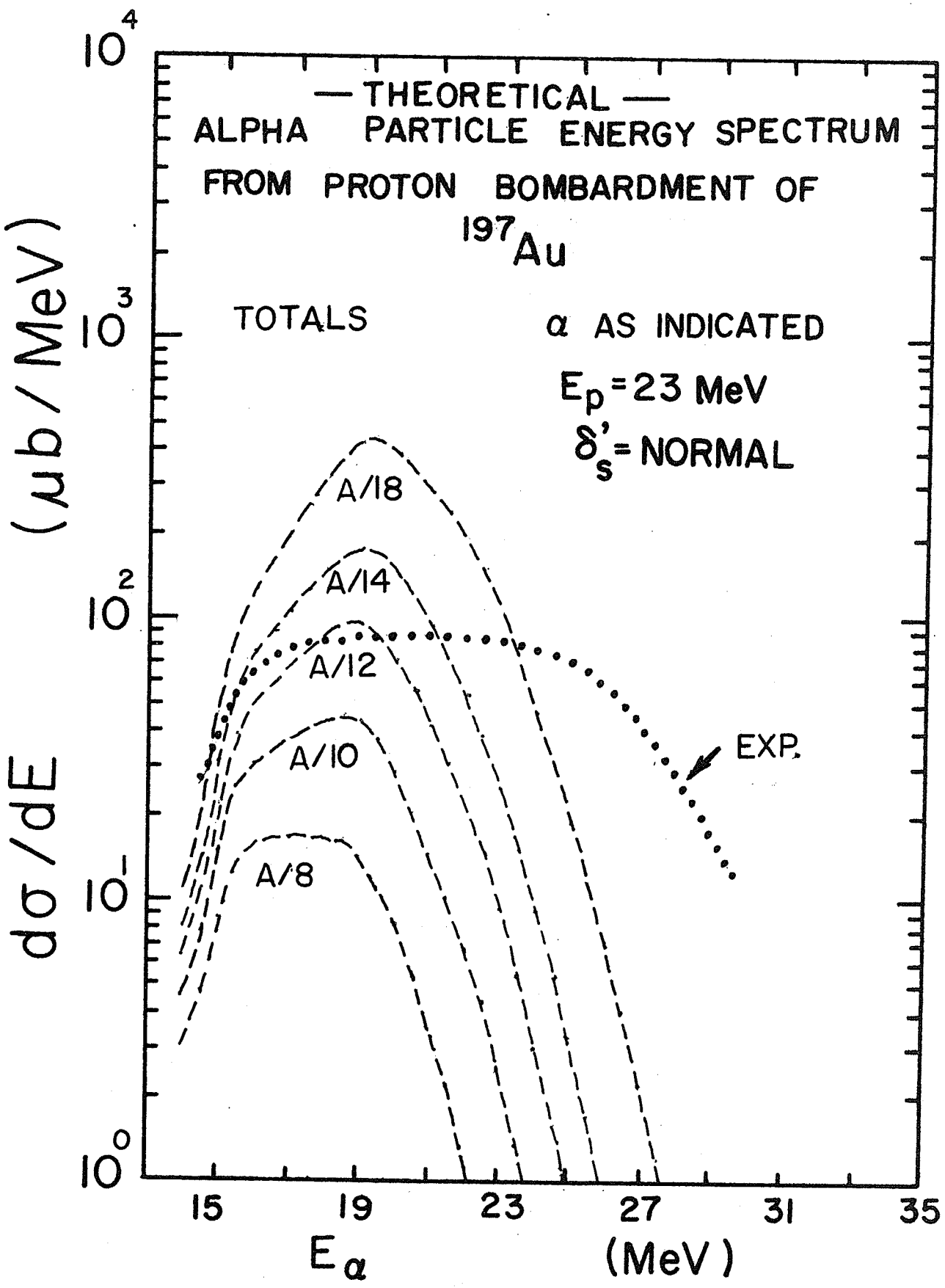
— THEORETICAL —
ALPHA PARTICLE ENERGY SPECTRUM
FROM PROTON BOMBARDMENT OF
197Au
TOTALS
α AS INDICATED
Ep = 23 MeV
δ's = NORMAL
A/18
A/14
A/12
A/10
A/8
EXP.
dσ/dE (μb/MeV)
Eα (MeV)
10^4
10^3
10^2
10^1
10^0
15
19
23
27
31
35

FIGURE 5.14

Variation, with level density parameter α, of the theoretical alpha particle energy spectrum resulting from 32 MeV proton bombardment of ^{197}Au

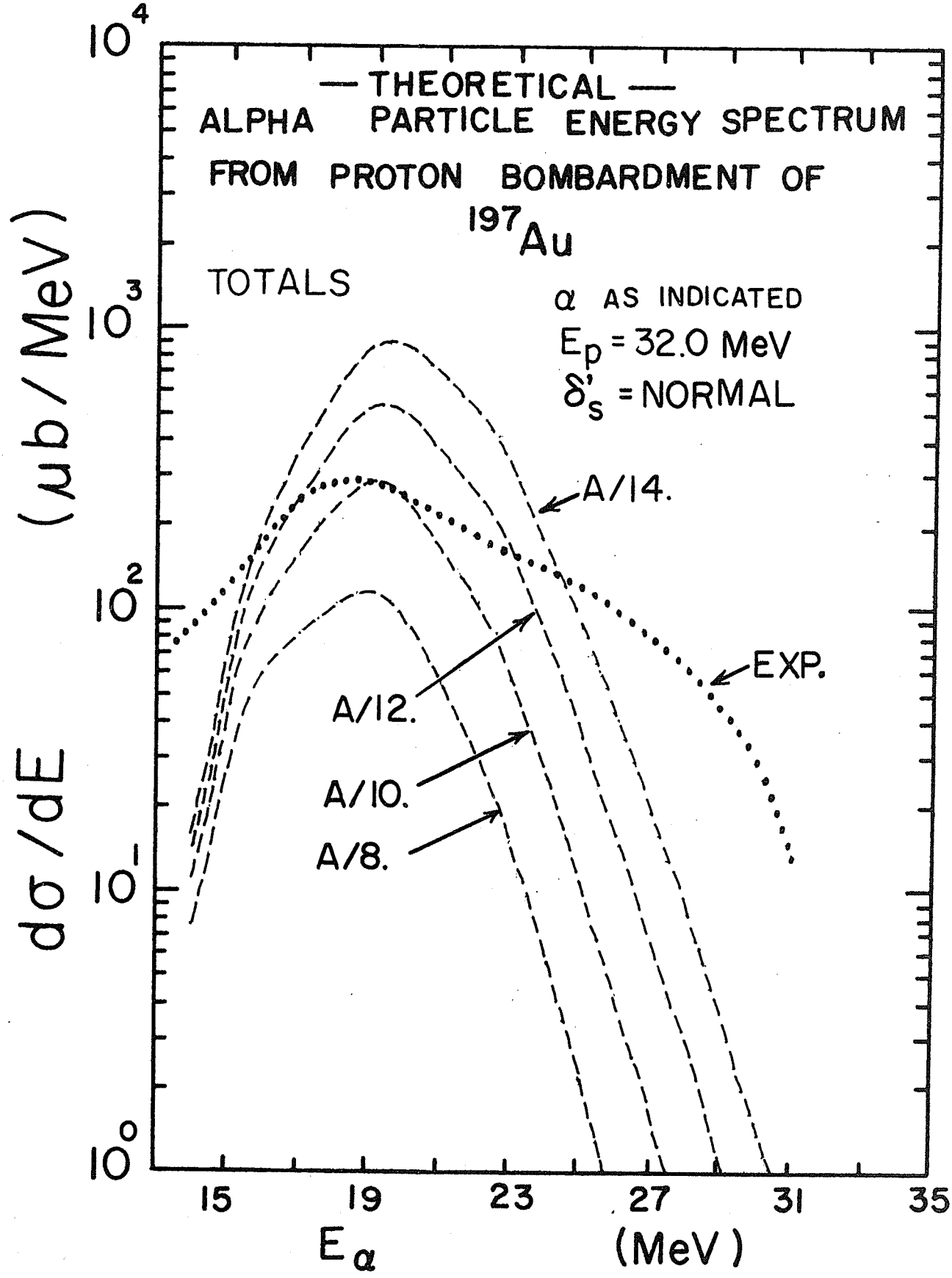
— THEORETICAL —
ALPHA PARTICLE ENERGY SPECTRUM
FROM PROTON BOMBARDMENT OF
197Au
TOTALS
α AS INDICATED
Ep = 32.0 MeV
δ's = NORMAL
A/14.
EXP.
A/12.
A/10.
A/8.
dσ/dE (μb/MeV)
Eα (MeV)
10^4
10^3
10^2
10^1
10^0
15
19
23
27
31
35

FIGURE 5.15

Variation, with level density parameter α, of the theoretical alpha particle energy spectrum resulting from 41.3 MeV proton bombardment of ^{197}Au

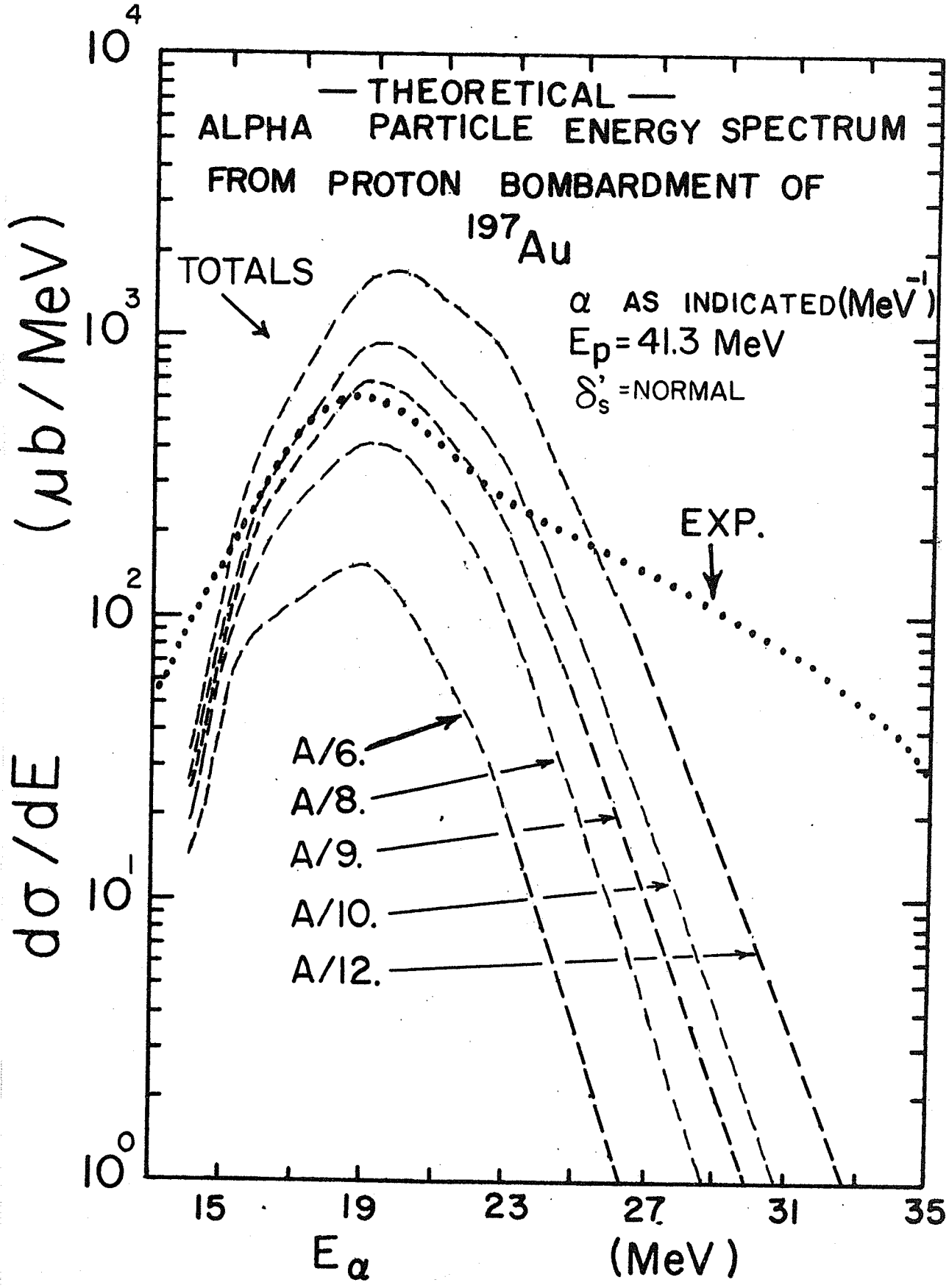
— THEORETICAL —
ALPHA PARTICLE ENERGY SPECTRUM
FROM PROTON BOMBARDMENT OF
197Au
TOTALS
α AS INDICATED (MeV-1)
Ep = 41.3 MeV
δs' = NORMAL
EXP.
A/6.
A/8.
A/9.
A/10.
A/12.
dσ/dE (μb/MeV)
Eα (MeV)
10^4
10^3
10^2
10^1
10^0
15
19
23
27
31
35

FIGURE 5.16

Variation, with level density parameter α, of the theoretical alpha particle energy spectrum resulting from 56.3 MeV proton bombardment of ^{197}Au

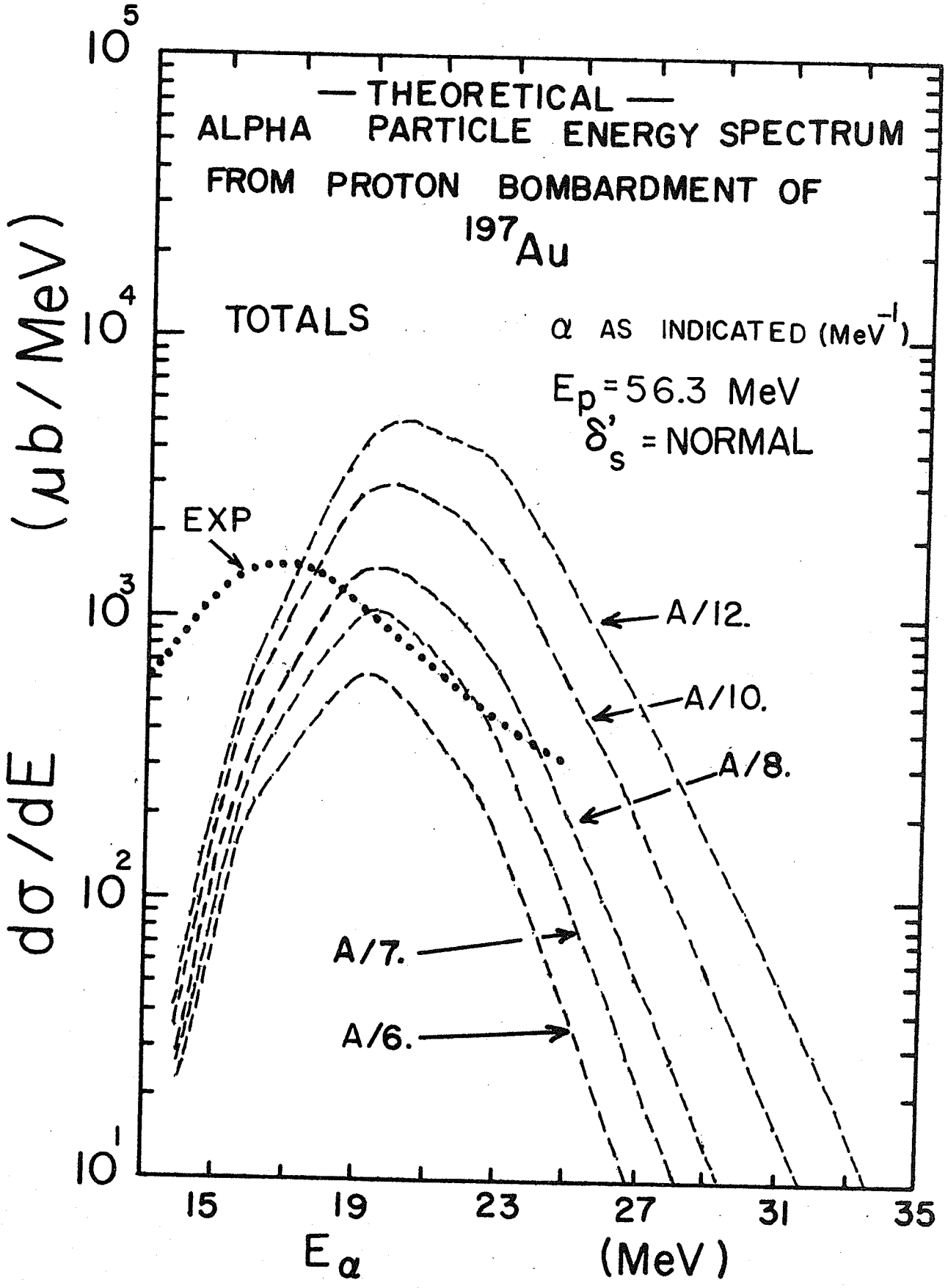
— THEORETICAL —
ALPHA PARTICLE ENERGY SPECTRUM
FROM PROTON BOMBARDMENT OF
197Au
TOTALS
α AS INDICATED (MeV-1)
Ep = 56.3 MeV
δ's = NORMAL
EXP
A/12.
A/10.
A/8.
A/7.
A/6.
dσ/dE (μb/MeV)
Eα (MeV)
10^5
10^4
10^3
10^2
10^1
15
19
23
27
31
35

of α so extracted are given in Tables 5.1-5.8 .

ii) Varying α so as to increase the theoretical alpha particle yield to the point where any part of the energy differential alpha particle yield exceeds the experimental yield (this is henceforth denoted as "matching of energy spectra"). The resultant values of α thus extracted are shown in Figure 5.17 along with those given by method i.

Clearly one can see that the level density parameters extracted by these methods are not constant with proton energy.

Figures 5.18-5.28 show the analogous results with all the pairing energies set to zero. The values of the extracted level density parameters obtained by the previously described technique are also shown in Figure 5.17 .

This variation of level density parameter with incident proton energy in addition to the fact that we cannot obtain any reasonable agreement in shape between the theoretical and experimental alpha particle energy spectra supports the conclusion that even for extremely backward angle measurements there exists an overwhelmingly large contribution to the alpha particle energy spectrum which resulted from non-statistical processes.

Angular Momentum effects are not expected to be responsible for this variation of α with bombarding energy. This has been noted by other authors[72,37].

A comparison of the proton yield, obtained from inelastic proton scattering from ^{197}Au for E_p=31 MeV as measured by Eisberg et al[75], with the theoretical yield (using α=A/10 MeV^{-1})

FIGURE 5.17

Variation of the level density parameter yielding agreement with the experimental results (assuming the extreme backward angle measurements are predominantly due to the evaporation mechanism)

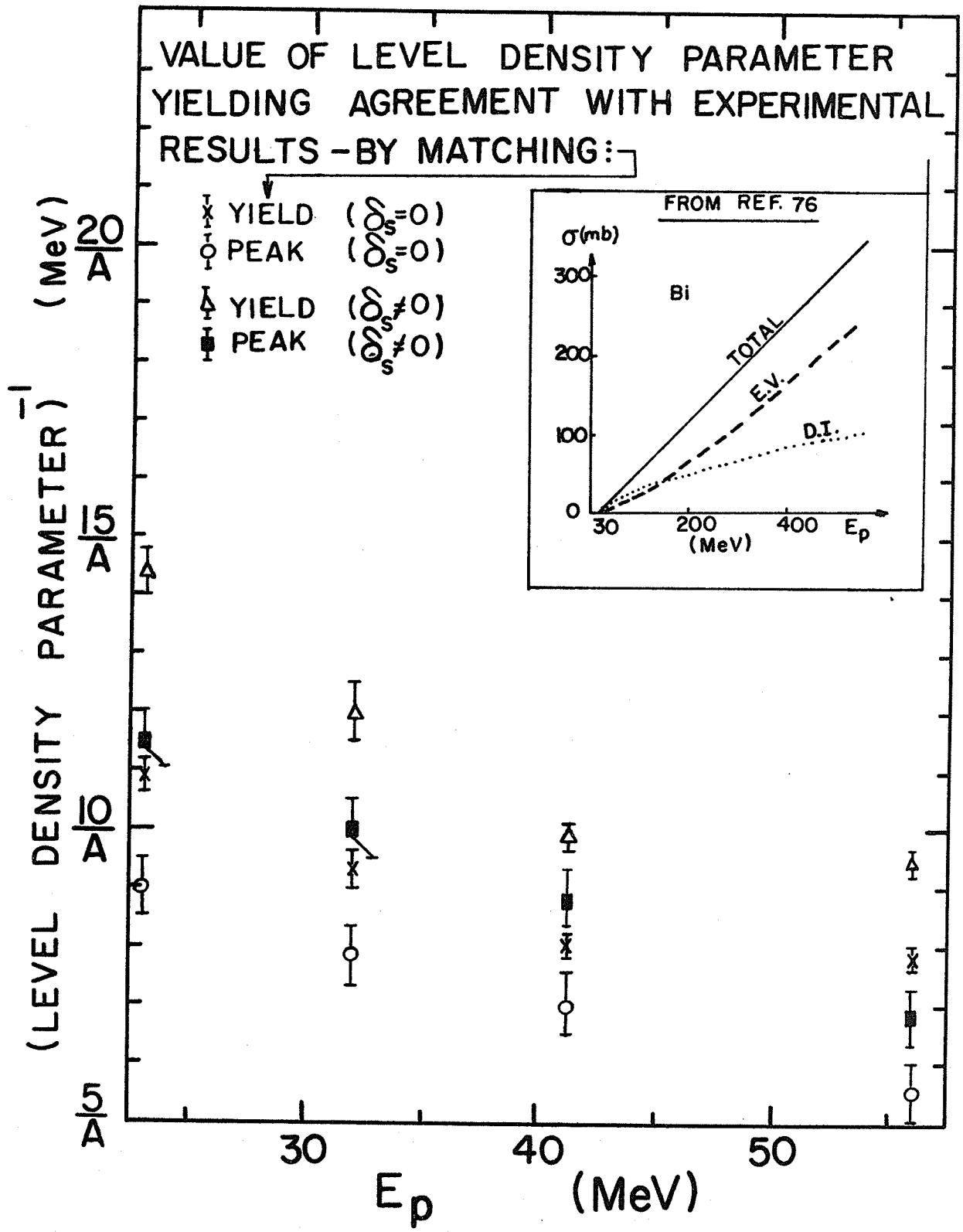
VALUE OF LEVEL DENSITY PARAMETER YIELDING AGREEMENT WITH EXPERIMENTAL RESULTS - BY MATCHING:
YIELD ($\delta_s=0$)
PEAK ($\delta_s=0$)
YIELD ($\delta_s\neq0$)
PEAK ($\delta_s\neq0$)
FROM REF. 76
σ(mb)
300
200
100
0
Bi
TOTAL
E.V.
D.I.
30
200
400
E_p
(MeV)
(LEVEL DENSITY PARAMETER)$^{-1}$ (MeV)
20/A
15/A
10/A
5/A
30
40
50
E_p (MeV)

FIGURE 5.18

Variation of the first shower partial width with E_p and the level density parameter α for the various product particles

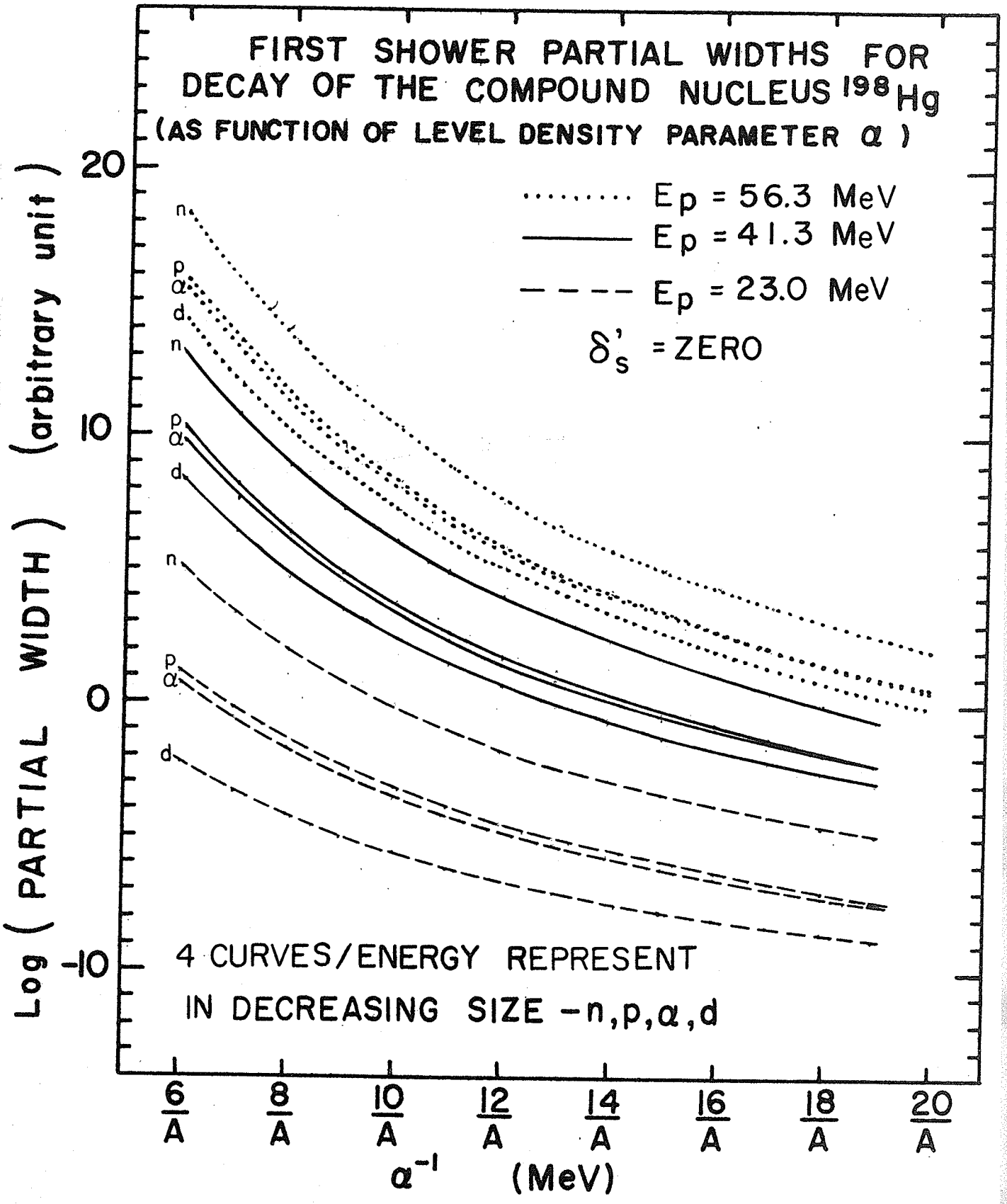
FIRST SHOWER PARTIAL WIDTHS FOR
DECAY OF THE COMPOUND NUCLEUS 198Hg
(AS FUNCTION OF LEVEL DENSITY PARAMETER α)
Ep = 56.3 MeV
Ep = 41.3 MeV
Ep = 23.0 MeV
δ's = ZERO
Log (PARTIAL WIDTH) (arbitrary unit)
20
10
0
-10
n
p
α
d
4 CURVES/ENERGY REPRESENT
IN DECREASING SIZE -n,p,α,d
6/A
8/A
10/A
12/A
14/A
16/A
18/A
20/A
α-1 (MeV)

FIGURE 5.19

Contributions, from the various showers, to the theoretical alpha particle energy spectrum resulting from 23 MeV proton bombardment of ^{197}Au

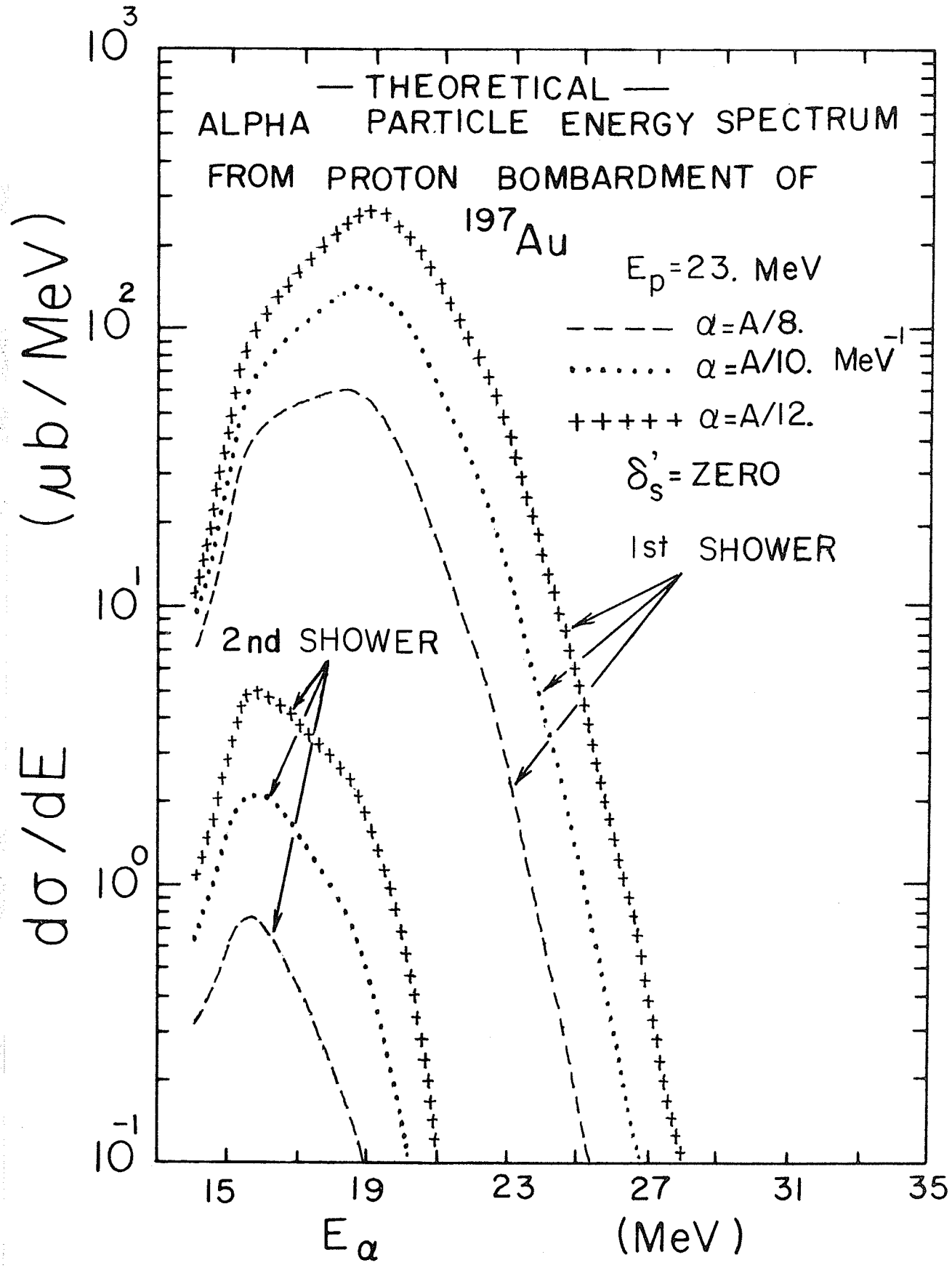
— THEORETICAL —
ALPHA PARTICLE ENERGY SPECTRUM
FROM PROTON BOMBARDMENT OF
197Au
Ep=23. MeV
α=A/8.
α=A/10. MeV-1
α=A/12.
δs'= ZERO
1st SHOWER
2nd SHOWER
dσ/dE (μb/MeV)
Eα (MeV)
10^3
10^2
10^1
10^0
10^-1
15
19
23
27
31
35

FIGURE 5.20

Variation, with level density parameter α, of the "total" theoretical alpha particle energy spectrum resulting from 23 MeV proton bombardment of ^{197}Au

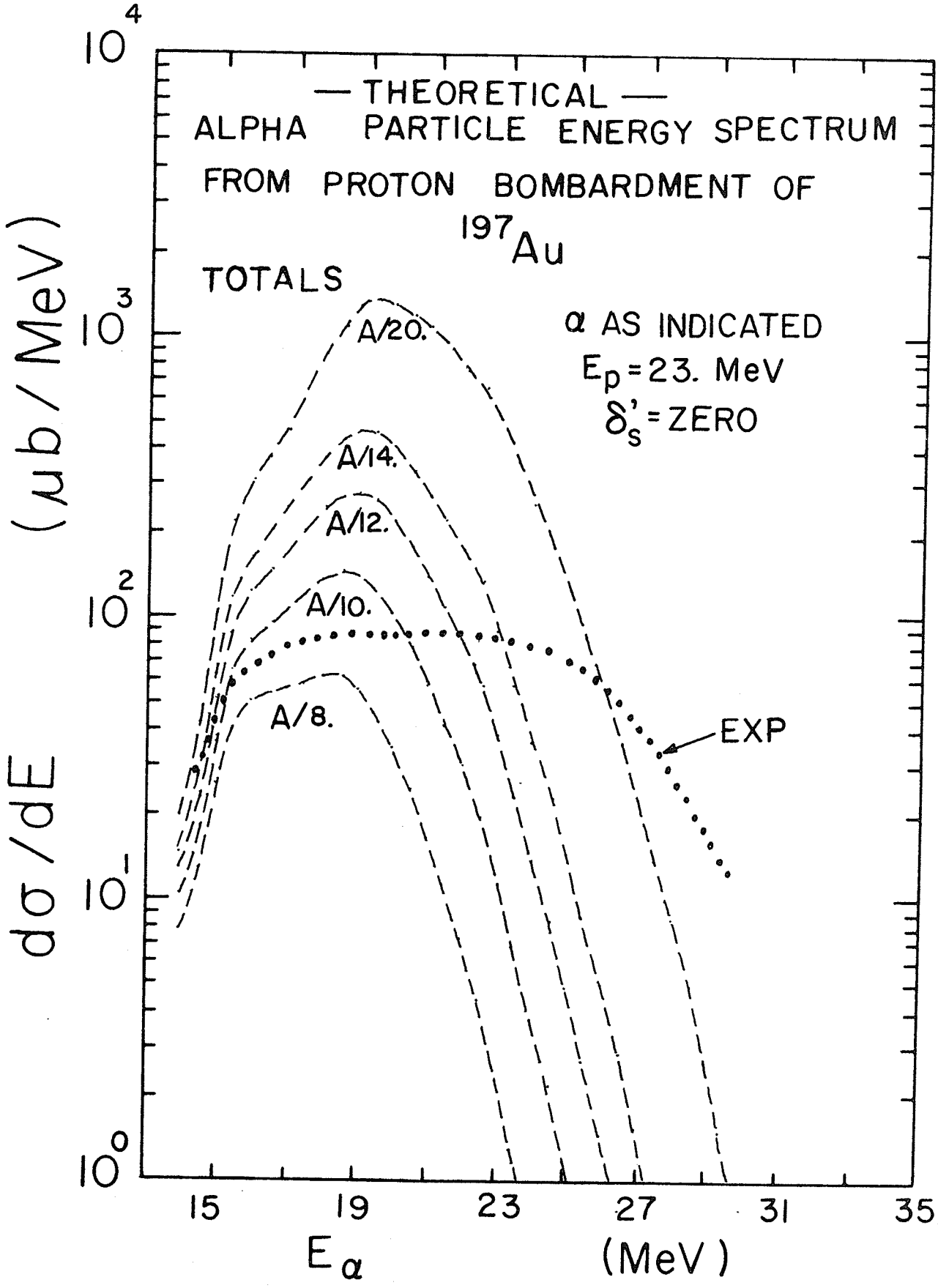
— THEORETICAL —
ALPHA PARTICLE ENERGY SPECTRUM
FROM PROTON BOMBARDMENT OF
197Au
TOTALS
α AS INDICATED
Ep = 23. MeV
δ's = ZERO
A/20.
A/14.
A/12.
A/10.
A/8.
EXP
dσ/dE (μb/MeV)
Eα (MeV)
10^4
10^3
10^2
10^1
10^0
15
19
23
27
31
35

FIGURE 5.21

Contributions, from the various showers, to the theoretical alpha particle energy spectrum resulting from 32 MeV proton bombardment of ^{197}Au

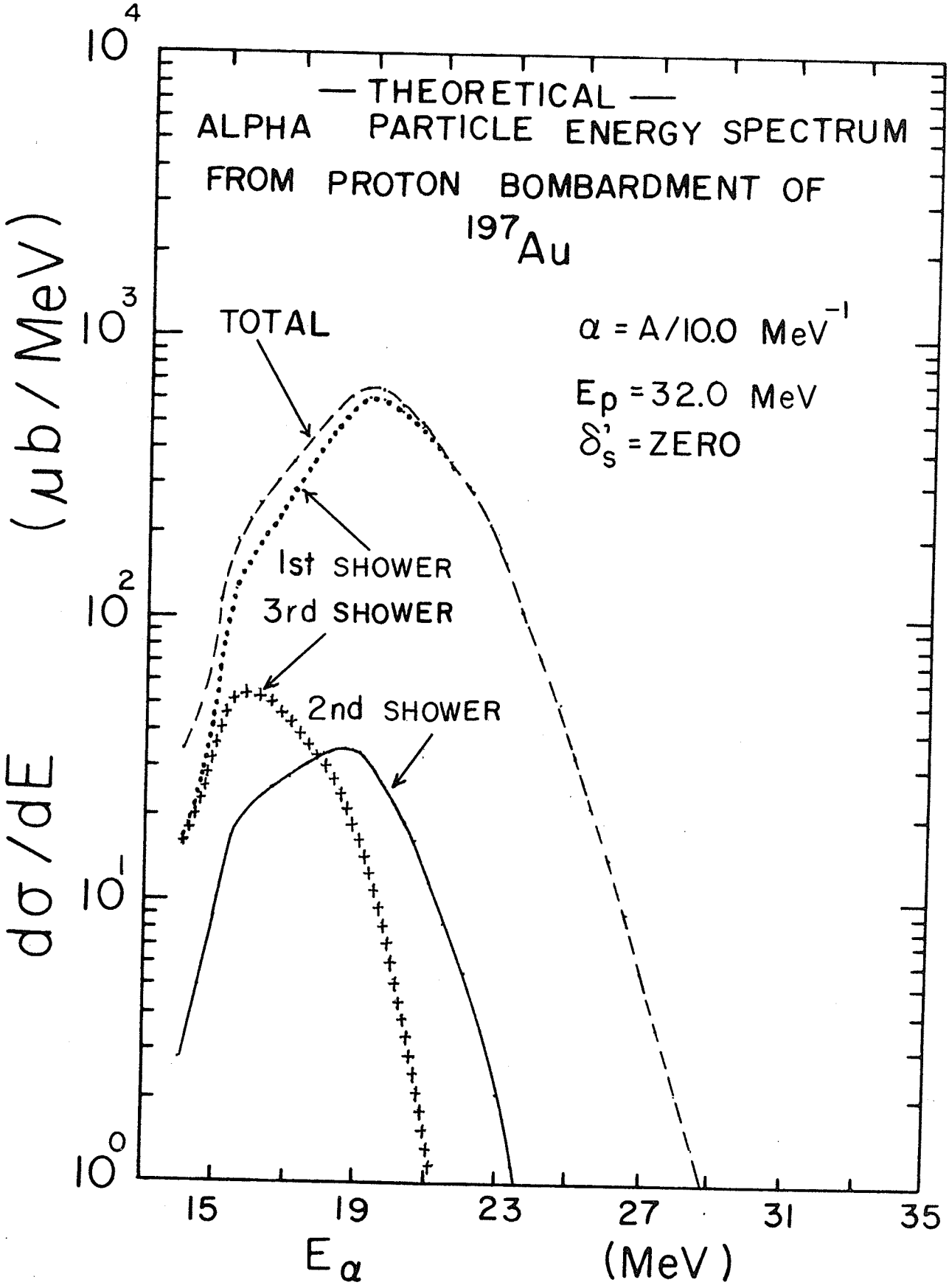
— THEORETICAL —
ALPHA PARTICLE ENERGY SPECTRUM
FROM PROTON BOMBARDMENT OF
197Au
TOTAL
α = A/10.0 MeV-1
Ep = 32.0 MeV
δ's = ZERO
1st SHOWER
3rd SHOWER
2nd SHOWER
dσ/dE (μb/MeV)
Eα (MeV)
10^4
10^3
10^2
10^1
10^0
15
19
23
27
31
35

FIGURE 5.22

Contributions, from the various showers, to the theoretical alpha particle energy spectrum resulting from 32 MeV proton bombardment of ^{197}Au

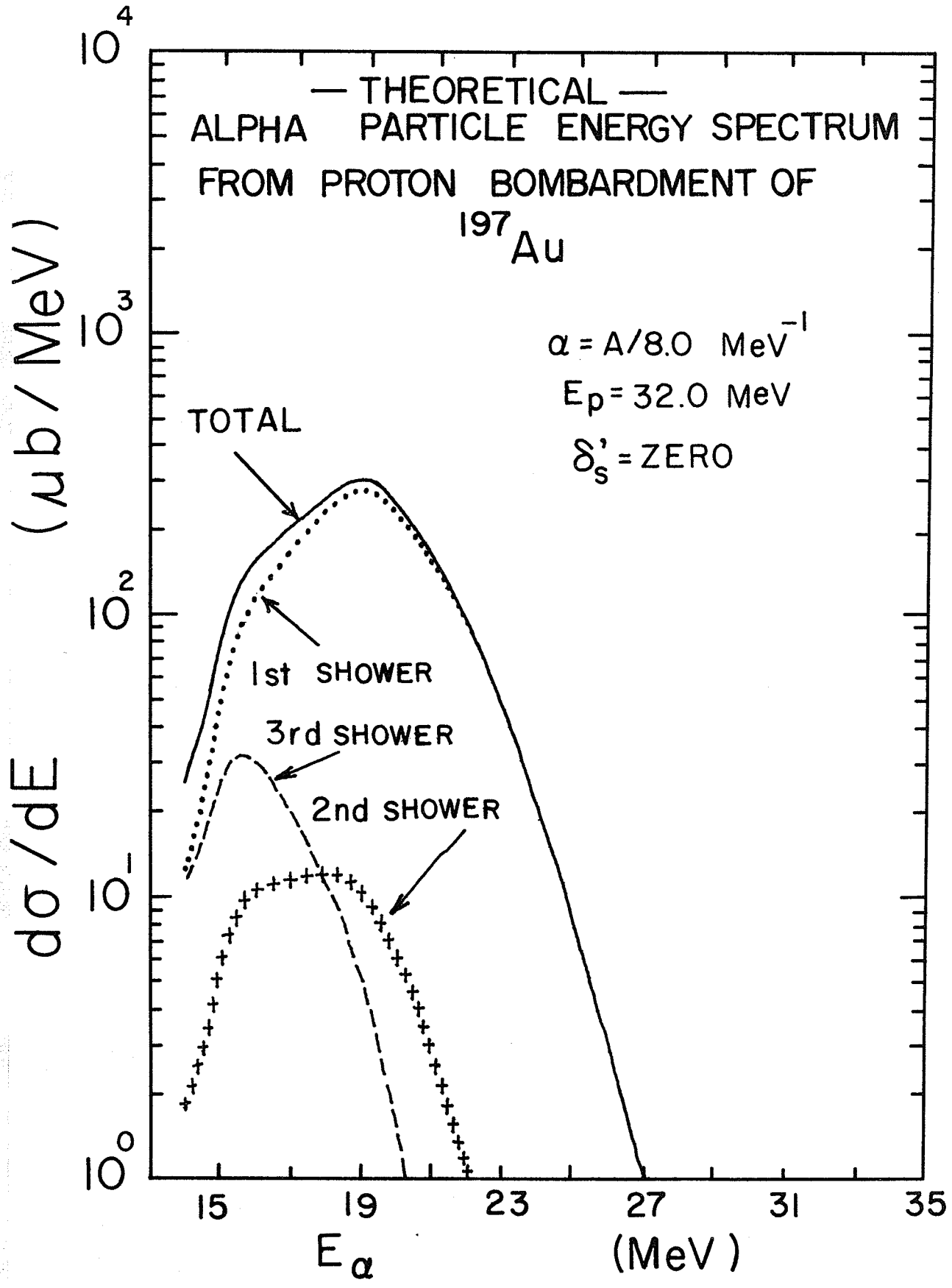
— THEORETICAL —
ALPHA PARTICLE ENERGY SPECTRUM
FROM PROTON BOMBARDMENT OF
197Au
α = A/8.0 MeV-1
Ep = 32.0 MeV
δs' = ZERO
TOTAL
1st SHOWER
3rd SHOWER
2nd SHOWER
dσ/dE (μb/MeV)
Eα (MeV)
10^4
10^3
10^2
10^1
10^0
15
19
23
27
31
35

FIGURE 5.23

Variation, with level density parameter α, of the "total" theoretical alpha particle energy spectrum resulting from 32 MeV proton bombardment of ^{197}Au

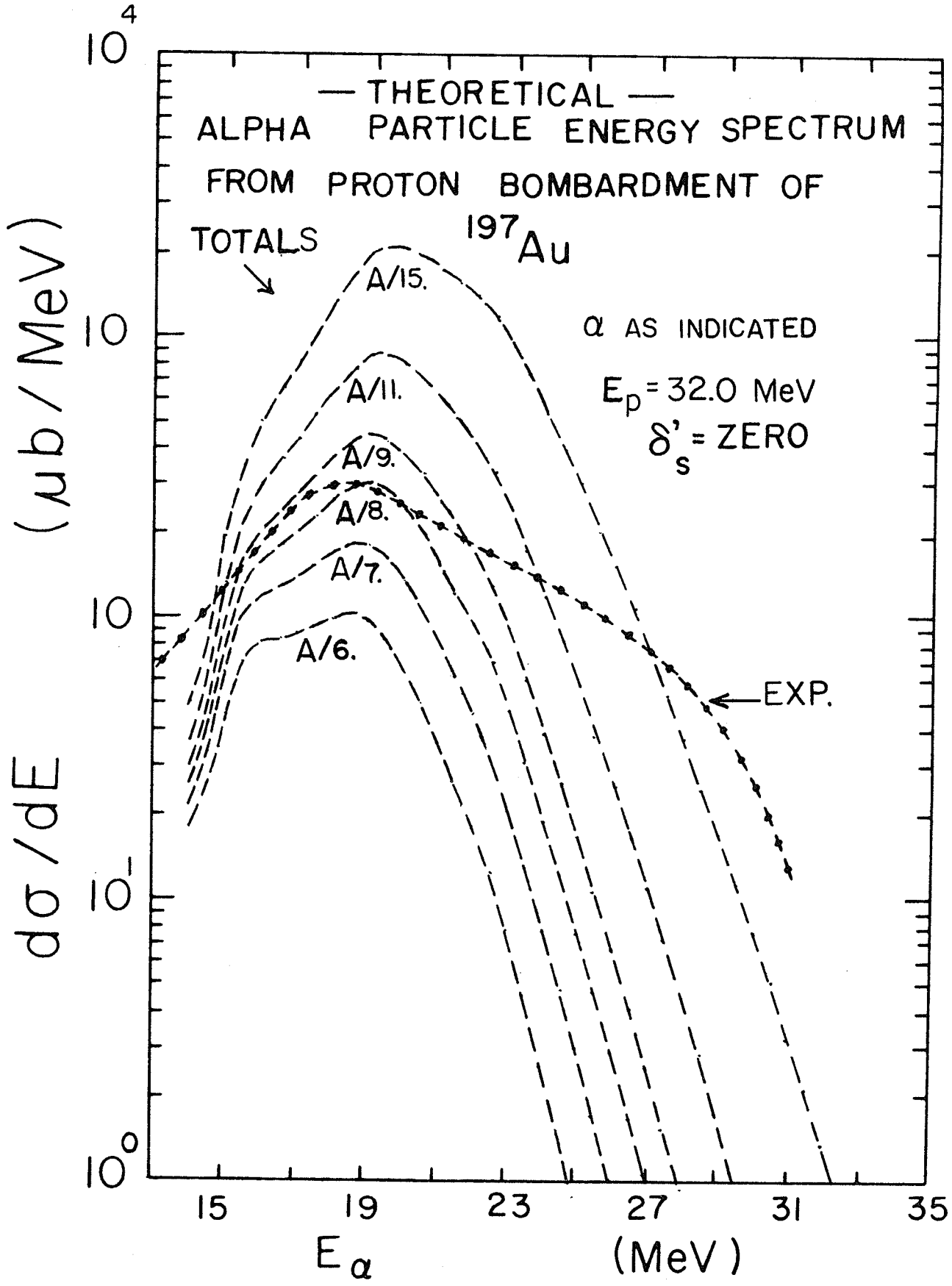
— THEORETICAL —
ALPHA PARTICLE ENERGY SPECTRUM
FROM PROTON BOMBARDMENT OF
197Au
TOTALS
A/15.
A/11.
A/9.
A/8.
A/7.
A/6.
α AS INDICATED
Ep = 32.0 MeV
δ's = ZERO
EXP.
dσ/dE (μb/MeV)
Eα (MeV)
10^4
10
10
10^-
10^0
15
19
23
27
31
35

FIGURE 5.24

Contributions, from the various showers, to the theoretical alpha particle energy spectrum resulting from 41.3 MeV proton bombardment of ^{197}Au

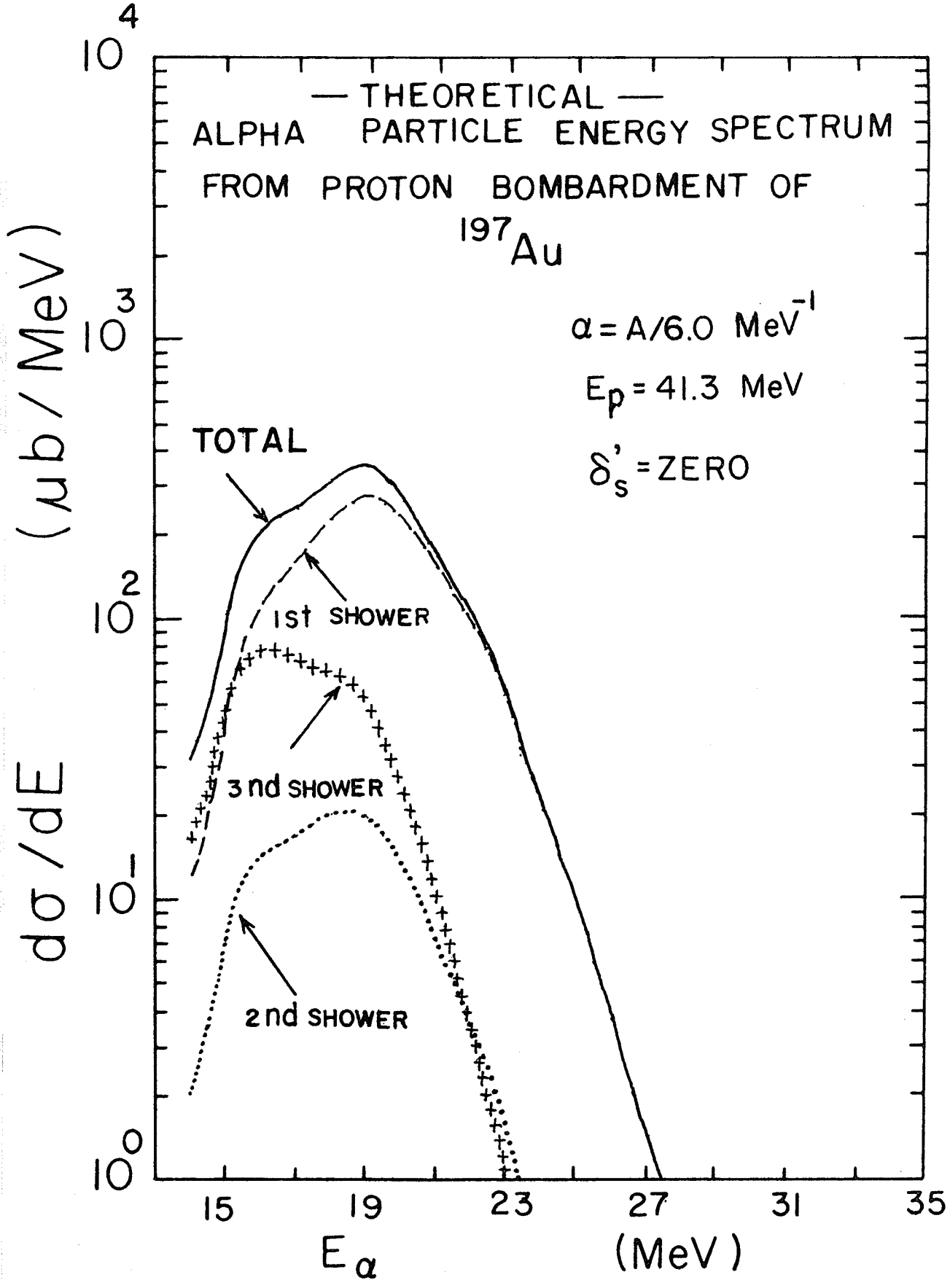
— THEORETICAL —
ALPHA PARTICLE ENERGY SPECTRUM
FROM PROTON BOMBARDMENT OF
197Au
α = A/6.0 MeV-1
Ep = 41.3 MeV
δ's = ZERO
TOTAL
1st SHOWER
3nd SHOWER
2nd SHOWER
dσ/dE (μb/MeV)
Eα (MeV)
10^4
10^3
10^2
10^1
10^0
15
19
23
27
31
35

FIGURE 5.25

Contributions, from the various showers, to the theoretical alpha particle energy spectrum resulting from 41.3 MeV proton bombardment of ^{197}Au

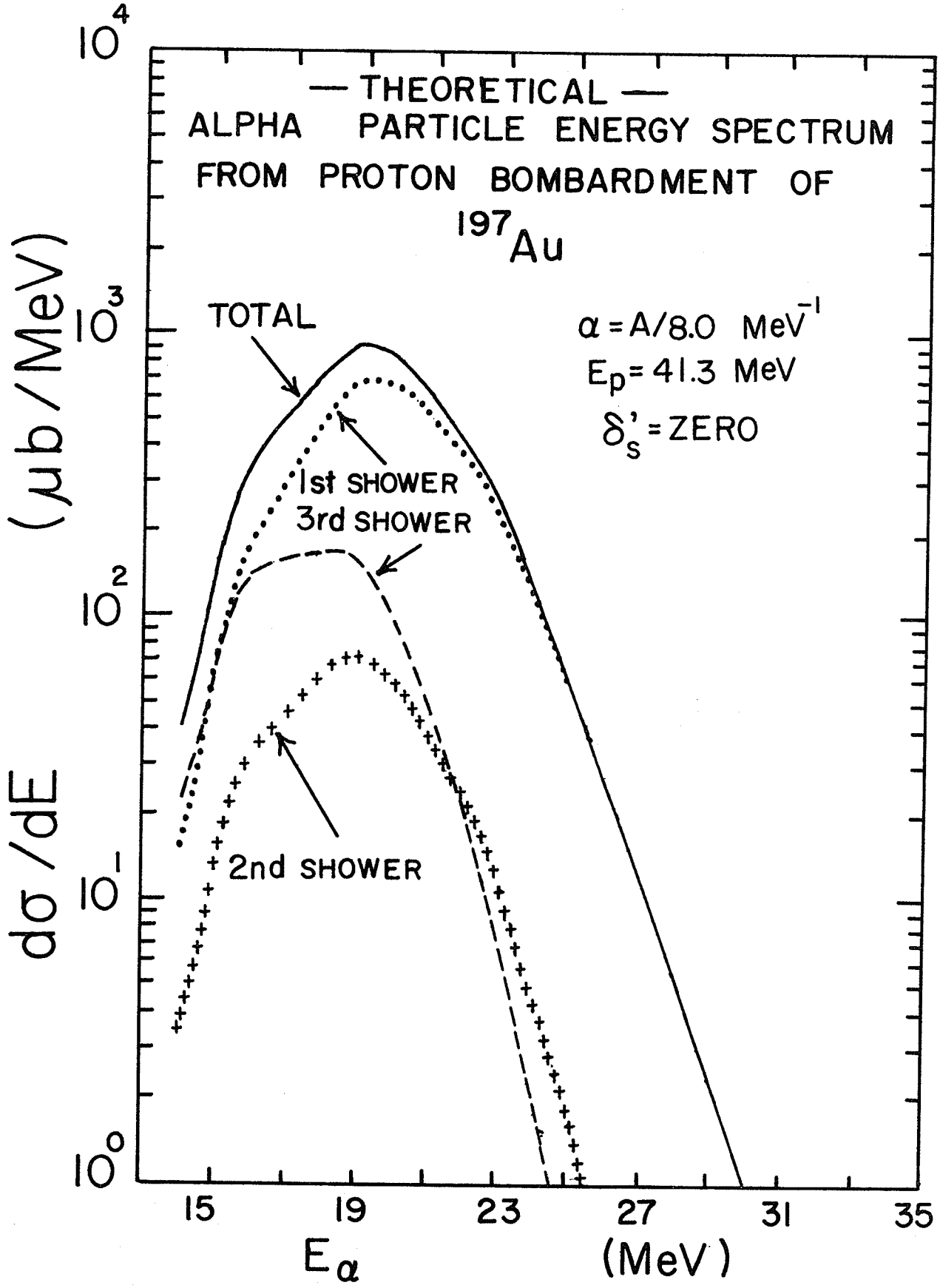
— THEORETICAL —
ALPHA PARTICLE ENERGY SPECTRUM
FROM PROTON BOMBARDMENT OF
197Au
TOTAL
1st SHOWER
3rd SHOWER
2nd SHOWER
α = A/8.0 MeV-1
Ep = 41.3 MeV
δs' = ZERO
dσ/dE (μb/MeV)
Eα (MeV)
10^4
10^3
10^2
10^1
10^0
15
19
23
27
31
35

FIGURE 5.26

Variation, with level density parameter α, of the "total" theoretical alpha particle energy spectrum resulting from 41.3 MeV proton bombardment of ^{197}Au

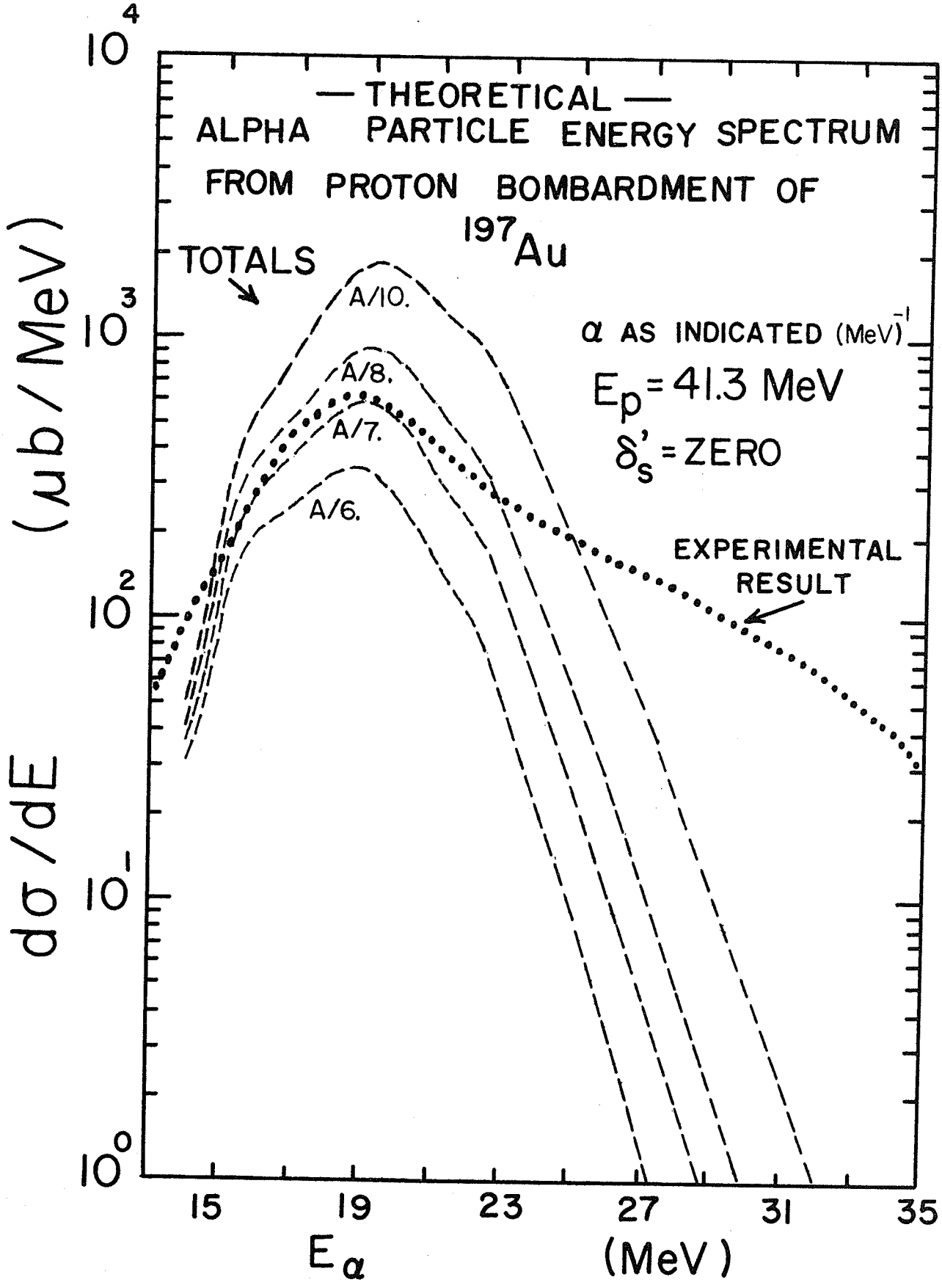
— THEORETICAL —
ALPHA PARTICLE ENERGY SPECTRUM
FROM PROTON BOMBARDMENT OF
197Au
TOTALS
A/10.
A/8.
A/7.
A/6.
α AS INDICATED (MeV)-1
Ep = 41.3 MeV
δ's = ZERO
EXPERIMENTAL RESULT
dσ/dE (μb/MeV)
Eα (MeV)
10^4
10^3
10^2
10^1
10^0
15
19
23
27
31
35

FIGURE 5.27

Contributions, from the various showers, to the theoretical alpha particle energy spectrum resulting from 56.3 MeV proton bombardment of ^{197}Au

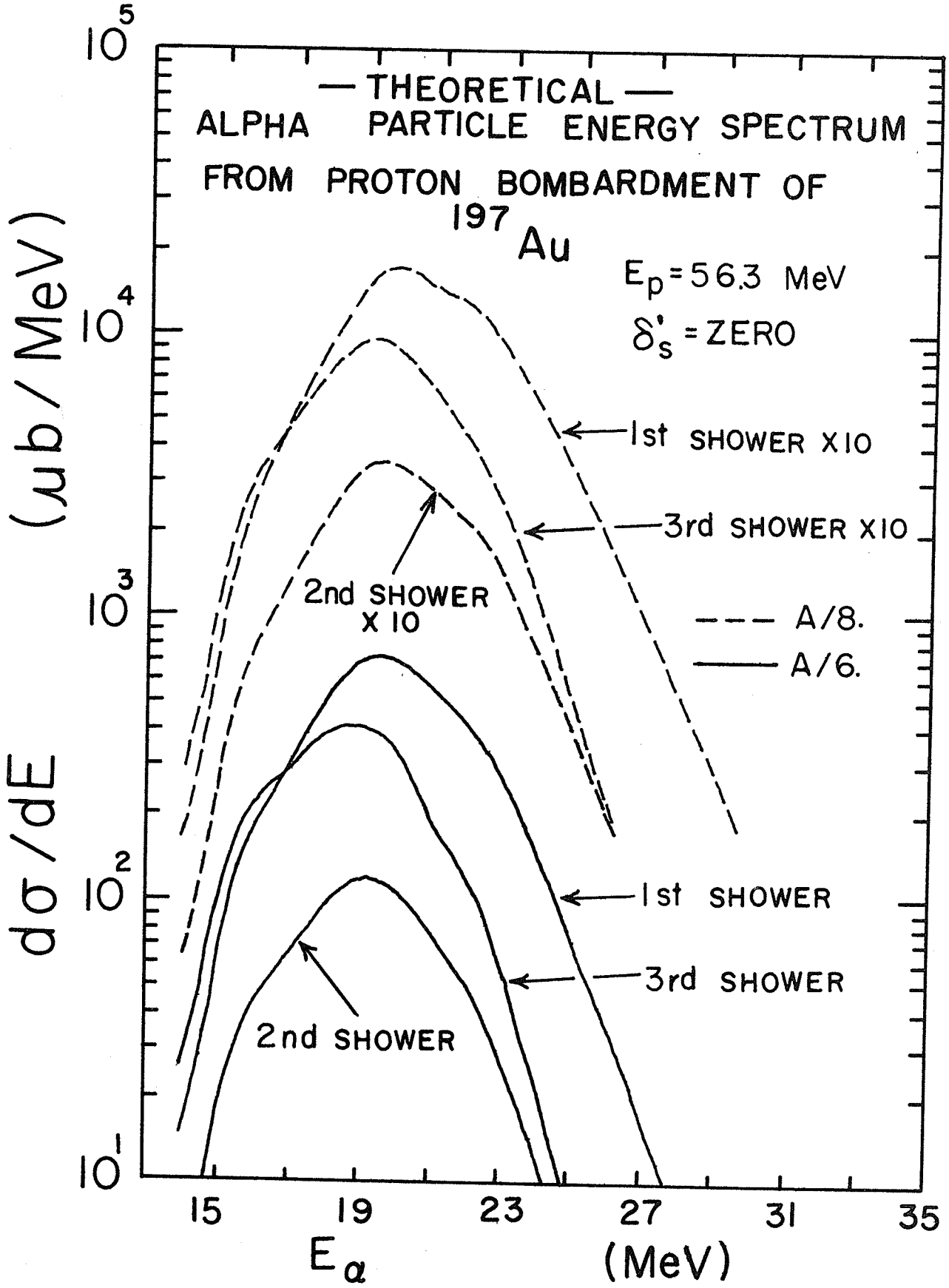
— THEORETICAL —
ALPHA PARTICLE ENERGY SPECTRUM
FROM PROTON BOMBARDMENT OF
197 Au
E_p = 56.3 MeV
δ_s' = ZERO
1st SHOWER X10
3rd SHOWER X10
2nd SHOWER X 10
A/8.
A/6.
1st SHOWER
3rd SHOWER
2nd SHOWER
$d\sigma/dE$ (μb / MeV)
10^5
10^4
10^3
10^2
10^1
15
19
23
27
31
35
E_α (MeV)

FIGURE 5.28

Variation, with level density parameter α, of the "total" theoretical alpha particle energy spectrum resulting from 56.3 MeV proton bombardment of ^{197}Au

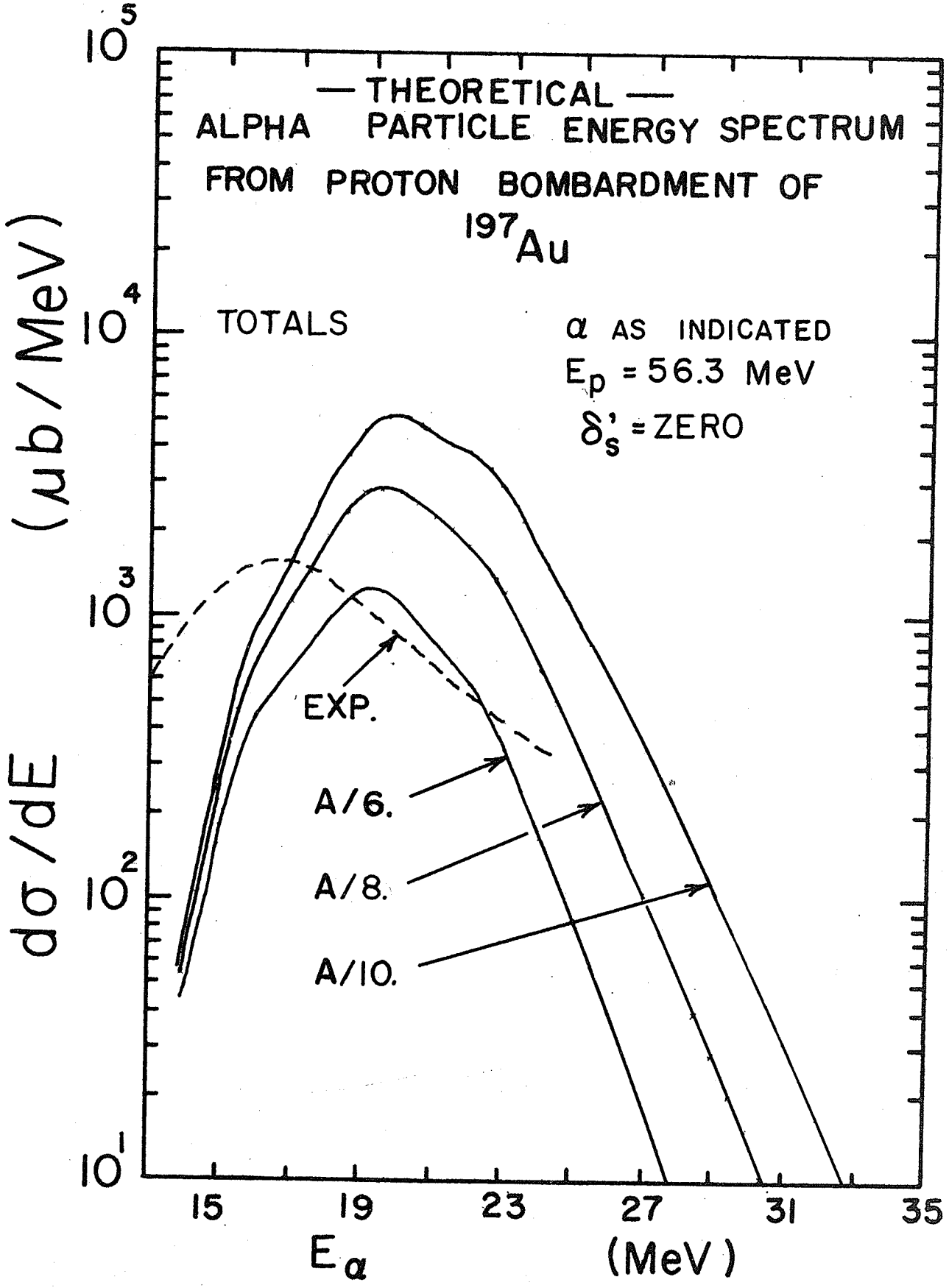
— THEORETICAL —
ALPHA PARTICLE ENERGY SPECTRUM
FROM PROTON BOMBARDMENT OF
197Au
TOTALS
α AS INDICATED
Ep = 56.3 MeV
δs' = ZERO
EXP.
A/6.
A/8.
A/10.
dσ/dE (μb/MeV)
Eα (MeV)
10^5
10^4
10^3
10^2
10^1
15
19
23
27
31
35

gave the result that the theoretical yield was only 1/4 the yield extracted from reasonable extrapolation of the experimental cross-section to 180 multiplied by 4π. This again indicates that particle emission appears to be occuring before thermal equilibrium is established that is, direct interactions predominate at all emission angles.

Now since σ(SUM) increases as a is decreased and we have found that by comparing either theoretical and experimental yields or "matching of energy spectrum" the level density parameter a increases with increasing E_p we can conclude that non-evaporation processes (for measurements taken in the extreme backward angles) are becoming less predominant as E_p increases. This is consistent with the observation of Dubost et al[76]. They concluded that for the emission of alpha particles from Bismuth (similar results would be expected from all the heavy nuclei) the cross section could be broken up into an direct interaction component and an evaporation component (for convenience we reproduce their results, based on the works of M. Lefort et al[77] as an insert into Figure 5.17) where the evaporation component exceeds the direct interaction component when $E_p \gtrsim 150$ MeV.

CHAPTER VI

CONCLUSIONS

A. Statistical Model

We have seen that the alpha spectra from proton bombardment of ^{197}Au all have forward-peaked angular distributions. This is characteristic of some sort of direct interaction mechanism. Even if it is assumed that the spectra observed in the extreme backward angles are predominantly due to the evaporation mechanism the disagreement in shape between the experimental and theoretical alpha spectra as well as the variation of the level density parameter with incident proton energy indicates that this is just not so. That is, direct interaction mechanisms seem to predominate at all angles for (p,α) reactions on ^{197}Au (and presumably for all heavy nuclei).

We can conclude however that since the level density parameter, required to "fit" either the "yield" or the "peak" of the experimental alpha spectra of these backward angles, decreases with increasing proton energies the non-statistical processes are becoming less predominant as the projectile energy is increased. This is in agreement with the higher (up to 550 MeV) projectile energy work reported by Lefort et al [77].

The conclusions as to the theoretical importance of multiple-particle emission on the alpha spectrum observed from 20-60 MeV proton bombardment of ^{197}Au can be conveniently summarized as shown in Figure 6.1. Here we have plotted the % of the yield due to each shower as a function of the incident

Figure 6.1

Theoretical % of alpha particle yield of the various showers, using level density parameters for the different proton energies which gave agreement with the experimental alpha particle yield observed from backward angle measurements.

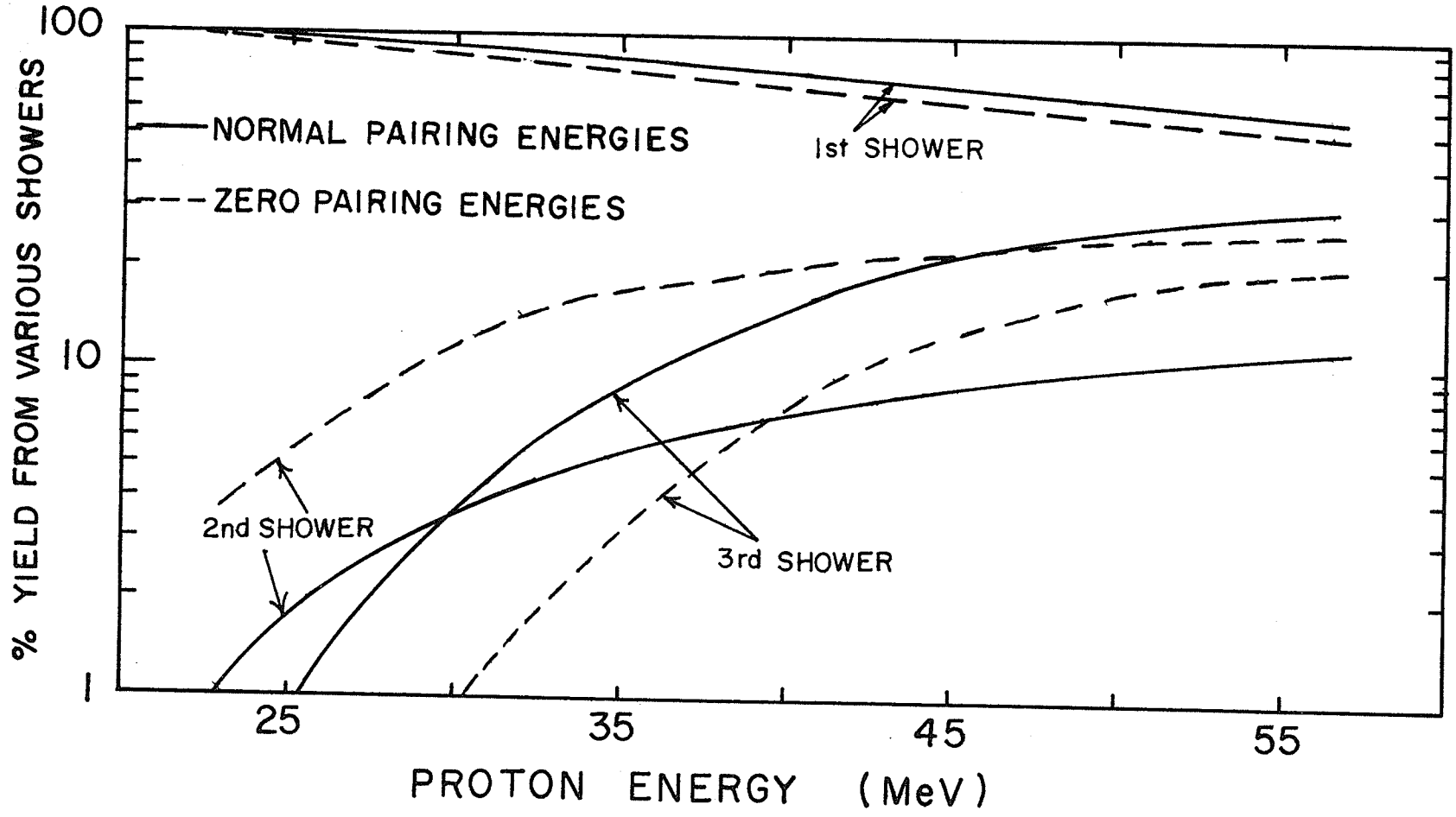
100
10
1
% YIELD FROM VARIOUS SHOWERS
NORMAL PAIRING ENERGIES
ZERO PAIRING ENERGIES
1st SHOWER
2nd SHOWER
3rd SHOWER
25
35
45
55
PROTON ENERGY (MeV)

proton energy . The value of the level density parameter used were those which gave the same "yield" as was experimentally observed in the (extrapolated) extreme backward angle measurements. One can readily observe the effect of the pairing energies on the relative importance of the various showers and how, as one would expect, the contributions from all the showers become of equal importance in the high energy limit. This is expected to occur when $E_p >> Q$ values for the various reactions involved in each shower. The effect of multiple-particle emission depends on which part of the "total" theoretical alpha spectrum one examines. The successive generations of emission have the greatest effect on reshaping the lower parts of the alpha energy spectra. The highest energy parts were always influenced most by the first "shower".

Clearly there is a need to take account of multiple-particle emission in order to make a proper evaluation of the compound nuclear statistical model. However the usefulness of taking account of successive emissions will only become apparent when it can be applied to analogous reactions which are not predominated by direct-interactions. Perhaps its application to lighter targets, where compound nuclear effects are known to be relatively more important [79] would be more suitable. Unfortunately some of the approximations used in the calculation of multiple-particle emission would then no longer hold as well as they do for the heavy nuclei. However further investigation along this line should prove interesting and fruitful. To make a substantially greater use of the multiple-particle emission

code measurements of all the possible reaction products would be of interest since one can then check for consistency in the application of this model.

B. Validity of Pick-up Mechanism in (p,α) Reactions.

We have seen how, using reasonable parameters for the optical parameters in the DWBA code, a more or less unique and satisfactory theoretical fit could be obtained to the (p,α) experimental angular distribution of ^{23}Na and ^{27}Al. In addition we obtained, for these unique (best) fits, quantitative agreement (within experimental errors) between the theoretical and experimental spectroscopic factors. We thus conclude that the triton pick-up mechanism is the predominant reaction mechanism for these reactions.

The fit to ^{58}Ni was quite reasonable and yielded an experimental spectroscopic factor of 1.08. The theoretical spectroscopic factor was not calculated.

The systematic application of the DWBA code proceeded as follows. One obtains a number of sets of optical model parameters from theoretical elastic scattering fits to the suitable elastic scattering data pertaining to the entrance and exit channels of the (p,α) reaction. Using realistic values for the bound state parameters (as obtained from ^{3}H or ^{3}He elastic scattering from the residual nucleus) we removed the degeneracies (almost identical theoretical angular distributions) of the proton parameters in combination with the sets of alpha parameters. Usually this means that there will remain two sets

of proton parameters (those with the best χ^2 in the elastic fitting routine), one with pure surface absorption and the other with pure volume absorption. There should usually remain six sets of alpha parameters, one with pure volume and the other with pure surface absorption, for each of the three real well depths $\approx$140 MeV, $\approx$200 MeV and $\approx$260 MeV. A clear choice of which proton set- alpha set of parameters gives the most reasonable shape should then become evident. If not, then one needs to carry out a two-dimensional search over a reasonable range of the bound state parameters (r_t, a_t) for these 12 combinations of proton-alpha sets of parameters. Stressing a fit to the forward angles ($\theta \lesssim 90^\circ$) one should then obtain a more or less unique fit. If more than one good fit were obtained for the forward angles, use the backward angles to decide which is more suitable. Extract the spectroscopic factors for the best and next best fits using the ratio of the experimental to theoretical partial cross- sections.

APPENDIX 3.A

THE VALIDITY OF THE ASSUMPTION OF INFINITE MOMENT OF INERTIA

The assumption that the moment of inertia of the target nucleus was infinite was necessary in order to study the multiple-particle emission process since the inclusion of angular momentum into the formalism would increase computational times by several orders of magnitude thus making them impractical. In any case, the inclusion of angular momentum effects would only introduce more uncertainties into the calculations since even less is known about the inverse partial cross-sections than is known about the inverse total reaction cross section.

The number of states with angular momentum J is, for the Fermi-gas model, given by [24,35]

$$\omega(E,J) = \frac{(2J+1)^2}{\sqrt{\pi}\,(2c\tau)^{3/2}} \exp\left[-(J+1/2)^2/2c\tau\right]\omega(E)$$

where $c\hbar^2$ = moment of inertia of nucleus, τ = nuclear temperature defined by

$$\frac{1}{\tau} = \frac{d \log \omega(E)}{dE} = \sqrt{\frac{a}{E}} - \frac{5}{4}\left[\frac{1}{E+t}\right] \quad \text{where}$$

$$t = \frac{.5}{a}\left(1 + \sqrt{1+4aE}\right)$$

The moment of inertia of the nucleus, $c\hbar^2$, can be shown [24,31,43] to be equal to the rigid body moment of inertia ($\frac{2}{5}$ MAR^2) for nucleons moving independently in a central potential (Fermi-gas).

For a Fermi-gas $a = 2\left(\frac{\pi}{3}\right)^{4/3} \frac{m r_o^2}{\hbar^2} A$

which for r_o = 1.4 fm yields $\alpha = A/10.\ (MeV)^{-1}$

Figure 3.Ai shows the value of $\frac{1}{\tau}$ as a function of the excitation energy E (under the assumption $\alpha \approx \frac{A}{10.} \approx 20$)

We will now justify the assumption that

$$\exp\left[-\ (J+1/2)^2 \hbar^2 /2I\tau\right] \approx 1$$ for all J values of interest. Classically $l_{max} = \frac{m'\ V\ R}{\hbar}$ where m' is mass of projectile V is its velocity and R is the interaction range of the target nucleon potential. Now $I = \frac{2}{5}\ M\ A\ R^2$, hence setting $l_{max} = J + 1/2$

$\frac{(J+1/2)^2\hbar^2}{2I} \approx \frac{m'^2V^2}{.8\ m\ A}$; if the projectile is a proton m = m'

and hence we have

$\exp\left[\frac{-mv^2}{.8A\tau}\right]$: For the maximum excitation of 50 MeV the argument is (referring to Fig. 3.Ai for $1/\tau$) = -.375. For 40, 30, 20, 10 MeV they are -.325, -.293, -.233 and -.178 respectively.

Thus

$$.68 \lesssim \exp\left[-(J + 1/2)^2\hbar^2 /2I\tau\right] \leq 1$$

and we have justified our assumption to a fairly high degree of accuracy. The more realistic assumption that the spin of the compound nucleus is less than l_{max} lends even greater support to the above approximation.

Figure 3.A1

Variation of (nuclear temperature)$^{-1}$

with excitation energy

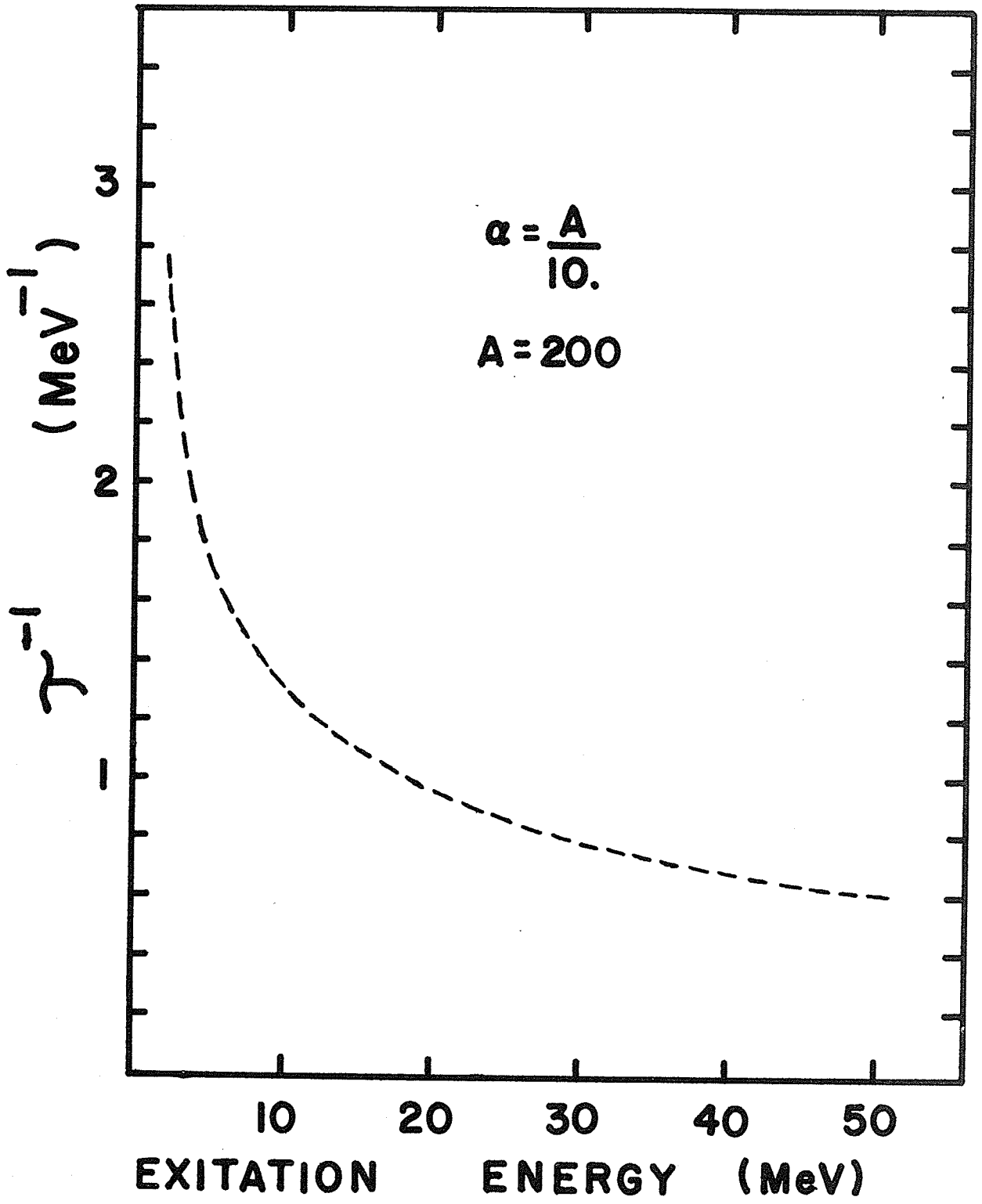
$\alpha = \frac{A}{10.}$
A = 200
γ^{-1} (MeV^{-1})
1
2
3
10
20
30
40
50
EXITATION ENERGY (MeV)

APPENDIX 4 A

Determination of RADNOD

The DWBA computor code requires as input the radial quantum number N (which is called RADNOD) for the centre-of-mass motion of the three picked-up mucleons cluster.

RADNOD is determined as follows. One must assume knowledge of the single particle states (n,l) of the three picked-up nucleons. Denote these as n_1l_1, n_2l_2, n_3l_3.

Assuming that the central potential can be approximated by a harmonic oscillator potential one can re-couple the single particle states into a cluster c.m. motion and an internal motion to obtain [68]

For two particles

$$\underbrace{(2n_1 + l_1) + (2n_2 + l_2)}_{\text{(single particle states)}} = \underbrace{(2N' + L')}_{\text{(cluster c.m.)}} + \underbrace{(2n' + l')}_{\text{(Internal motion}}$$

where N' = cluster radial quantum number , L' = cluster angular momentum, n' = relative radial quantum number and l' = relative angular momentum.

Similarly for three particles

(cluster c.m.) + (Internal motion) + $(2n_3 + l_3)$

$$= \underbrace{(2N + L)}_{\text{3 particle cluster c.m.}} + \underbrace{(2n'' + l'')}_{\substack{\text{Internal motion of} \\ \text{2 particle cluster} \\ \text{with 3rd}}} + \underbrace{(2n' + l')}_{\substack{\text{2 particle} \\ \text{internal} \\ \text{motion}}}$$

In the DWBA code FLTRIT ≡ L , the (triton) cluster c.m. angular momentum.

Hence

$$(2n_1 + l_1) + (2n_2 + L_2) + (2n_3 + L_3)$$
$$= (2N + L) + (2n'' + l'') + (2n' + l')$$

If in addition we assume that all three particles of the triton are in an l s state the internal motion of any two particles has $n' = l' = 0$ and the internal motion of the two particle cluster with the third particle also has $n'' = l'' = 0$

Hence

$$N \equiv \text{RADNOD} = \frac{(2n_1 + l_1) + (2n_2 + l_2) + (2n_3 + l_3) - L}{2}$$

APPENDIX 4B

We derive here a simple relativistically-correct expression for the time reversed (α,p) laboratory energy of the light outgoing product (α) yielding the same center of mass energy as does the forward (p,α) reaction.

Assume the forward reaction has the form $m_2(m_1, m_3)m_4 + Q$ with F the laboratory kinetic energy of m_1, while its inverse $m_4(m_3, m_1)m_2-Q$ has a laboratory kinetic energy of R of m_3 yielding the same center of mass energy.

Since the square of the four-vector momentum is an invarient $(\bar{p}_1+\bar{p}_2,\ i(E_1+E_2)\ )^2 = (\bar{p}_1'+\bar{p}_2',\ i(E_1'+E_2')\ )^2$ where the primed co-ordinates denotes c of mass. Thus since $\bar{p}'_1+\bar{p}'_2 = 0$, $(\bar{p}_1+\bar{p}_2,\ i(E_1+E_2)\ )^2_{FORWARD} = -(\text{c. of mass energy})^2$ similarly

$(\bar{p}_3+\bar{p}_4,\ i(E_3+E_4)\ )^2_{REVERSED} + -(\text{C. of mass energy})^2$

Hence since $(E_2)_f = m_2$, $(E_4)_r = m_4$, $(\bar{p}_2)_f = 0$ and $(\bar{p}_4)_r = 0$

$$(p_1^2-E_1^2-m_2^2-2\ m_2E_1)_{FORWARD} = (p_3^2-E_3^2-m_4^2-2E_3m_4)_{REVERSED}$$

Since $p_1^2=E_1^2-m_1^2$, $E_1 = F+m_1$, $p_3^2=E_3^2-m_3^2$ and $E_3=R+m_3$ we have upon substituting and cancelling

$$m_1^2+m_2^2+ 2m_1m_2 + 2Fm_2 = m_3^2+m_4^2+ 2m_3m_4 + 2Rm_4$$

$$\text{Thus}\quad R = \frac{m_2}{m_4}F + \frac{(m_1+m_2)^2-(m_3+m_4)^2}{2m_4}$$

Since $(m_1+m_2)^2-(m_3+m_4)^2 = ((m_1+m_2)+(m_3+m_4))\overbrace{((m_1+m_2)-(m_3+m_4))}^{Q}$

$$R = \left[\frac{m_1+m_2+m_3+m_4}{2m_4}\right] Q \quad +m_2 \quad F$$

$$\frac{}{m_4}$$

REFERENCES

1. J. J. Burgerjon, Nucl. Instr. Meth. 43 (1966) 381
2. T. Y. Li, Ph.D. Thesis, (1966), University of Manitoba, Canada
3. F. S. Goulding, D. A. Landis, J. Cerny, R. H. Pehl, Nucl. Instr. 31 (1964) 1
4. D. G. Douglas, private communication
5. V. Shkolnick and N. M. Hintz, University of Minnesota Annual Report, John H. Williams Lab. of Nuclear Physics (1967) pp. 58 - 66
6. S. Micheletti, private communication to R. M. Craig
7. P. E. Cavanagh, C. F. Coleman, G. A. Gard, D. A. Boyce, P.L.A. Progress report (1963) - Rutherford High Energy Laboratory - England
8. C. B. Fulmer, C. D. Goodman, Phys. Rev. 117 (1960) 1339
9. J. Muto et al. Nucl. Phys. 47 (1963) 19
10. M. Lefort, R. D. Silveira, Nucl. Phys. 75 (1966) 641
11. I. Dostrovsky, Z. Fraenkel, L. Winsberg, Phys. Rev. 118 (1960) 781
12. C. Hurwitz et al, Nucl. Phys. 54 (1964) 65
13. D. V. Reames, Phys. Rev. 137 (2B) (1965) 332
14. R. Sherr, F. P. Brady, Phys. Rev. 124 (1961) 1928
15. C. B. Fulmer, C. D. Goodman, Phys. Rev. 117 (1960) 1339
16. R. M. Eisberg, G. Igo, Phys. Rev. 93 (1954) 1039
17. D. B. Beard, A. McLellan, Phys. Rev. 131 (1963) 2664
18. D. B. Beard, A. McLellan, Phys. Rev. 140 (1965) 888
19. I. M. Turkiewicz et al, Nucl. Phys. 77 (1966) 276
20. K. Tsukada et al, Nucl. Phys. 78 (1966) 369
21. R. Chasman, Phys. Rev. 122 (1961) 902

22. W. Hauser, H. Feshbach, Phys. Rev. 87 (1952) 366

23. I. Dostrovsky et al. Phys. Rev. 116 (1959) 683

24. T. Ericson, Advances in Physics, 9 (1960) 426

25. M. Lefort, R. Da Silveira, Nucl. Phys. 75 (1966) 641

26. Programmed by C. A. Miller, private communication

27. J. R. Huizenga, G. Igo, Nucl. Phys. 29 (1962) 462

28. G. Igo, Phys. Rev. 115 (1959) 1665

29. M. M. Shapiro, Phys. Rev. 90 (1953) 171

30. A. G. W. Cameron, Can. J. Phys. 36 (1958) 1040

31. H. Bethe, Rev. Mod. Phys. 9 (1937) 69

32. H. Buttner et al., Nucl. Phys. 63 (1965) 615

33. J. Picard, C. F. Williamson, Nucl. Phys. 63 (1965) 673

34. J. M. Blatt and V. F. Weisskopf, Theoretical Nuclear Physics (John Wiley and Sons, Inc., New York, 1952), p. 336 - 378

35. J. M. B. Lang, K. J. Le Couteur, Proc. Phys. Soc. 67A (1954) 586

36. T. D. Thomas, Nucl. Physics 53 (1964) 558, (egn. 3.7)

37. D. Bodansky, Ann. Revs. Nucl. Sci. 12 (1962) 84

38. T. D. Newton, Can. J. Phys. 34 (1956) 804

39. E. T. Bramlitt, R. W. Fink, Phys. Rev. 131 (1963) 2642

40. C. Brun, B. Gatty, M. Lefort, X. Tarrago, Nucl. Physics A116 (1968) 177

41. J. H. E. Mattauch, W. Thiele, A. H. Wapstra, Nucl. Physics 67 (1965) 1

42. D. W. Lang, Nucl. Physics 26 (1961) 434

43. C. Bloch, Phys. Rev. 93 (1954) 1094

44. C. J. Kost, C. A. Miller, University of Manitoba Cyclotron - Internal Report

45. B. Hird and T. Y. Li, Can. J. Phys. 46 (1968) 1273

46. R. H. Bassel, R. M. Drisko, G. R. Satchler, ORNL-3240, UC-34-Physics (1962)

47. G. R. Satchler, "Some Topics in the Theory of Direct Nuclear Reactions",

LECTURES IN THEORETICAL PHYSICS (1965) VOL. VIII C, University of Colorado Press

48. L. N. Blumberg, E. E. Gross, A. Van Der Woude, A. Zucker and R. H. Bassel, Phys. Rev. 147 (1966) 812

49. Report C.E.A. - R3147 - Centre, D 'etudes Nucléaires De Saclay

50. D. J. Baugh et al, Nucl. Physics A95 (1967) 115.

51. M. P. Fricke and G. R. Satchler, Phys. Rev. 139B (1965) 567

52. J. R. Rook, Nucl. Phys. 61 (1965) 219

53. P. E. Hodgson, Advances in Physics 15 (1966) 329

54. L. McFadden, G. R. Satchler, Nucl. Phys. 84 (1966) 177

55. C. B. Fulmer and J.B. Ball, Phys. Rev. 140 (1965) B330

56. O.R.N.L. Report # 4122 (Specific use is made of 40 MeV fit to ^{28}Si)

57. V. E. Lewis, E. J. Burge, A. A. Rush and D. A. Smith, Nucl. Phys. A101 (1967) 589 (Specific use is made of 50 MeV protons on ^{24}Mg)

58. H. D. Holmgren and C.B. Fulmer, Phys. Rev. 132 (1963) 2644

59. B. Hird and D. Y. M. Tseng, Unpublished and private communication

60. N. M. Hintz - Private communication

61. A A. Rush, E. J. Burge, V. E. Lewis and D. A. Smith, Nucl. Physics A104 (1967) 340

62. B. G. Harvey et al, Private communication of Berkeley data to 70°. G. B. Shook, Phys. Rev. 114 (1959) 310 used to extend data to 133° (43 MeV alphas)

63. A. Springer, UCRL - 11681 (Ph.D. Thesis) - obtained in private communication with B. G. Harvey

64. D. Dehnhard, C. Mayer-Böricke, Nucl. Phys. A97 (1967) 164

65. R. J. Griffiths, Nucl. Phys. A102 (1967) 329

66. Revisions were programmed by C.A. Miller - Private communication.

67. R. H. Bassel et al, ORNL-3940 UC-34-Physics p.11

68. A. De-Shalit and I. Talmi, Nuclear Shell Theory, Academic Press, New York, 1963 p.238

69. D. W. Lang, Nucl. Physics 77 (1966) 545

70. D. V. Reames, Phys. Rev. 137(2B) (1965) B332

71. U. Facchini et al, Nucl. Physics 51 (1964) 460

72. T. D. Thomas, Nucl. Physics 53 (1964) 558

73. B. Hird and T. Y. Li - private communication.

74. N. Auerbach, Nucl. Physics 76 (1966) 321

75. R. M. Eisberg, G. Igo, Phys. Rev. 93 (1954) 1039

76. H. Dubost et al, Phys. Rev. 136(6B) (1964) B1618

77. M. Lefort et al, Nucl. Phys. 46, (1963) 161

78. G. L. Stobel and B. L. Scott, Phys. Rev. 140 (1965) B311

79. C. B. Fulmer and B. L. Cohen, Phys. Rev. 112 (1958) 1672

Glossary of Abbreviations

DWBA ... DISTORTED WAVE BORN APPROXIMATION

N.M.R. . NUCLEAR MAGNETIC RESONANCE

ORNL.... OAK RIDGE NATIONAL LABORATORY -
Oak Ridge, Tennessee, U.S.A.

I.B.M... INTERNATIONAL BUSINESS MACHINES COMPANY LIMITED

C.M..... CENTER OF MASS

LAB..... LABORATOTY